UDK 669+666+678+53

ISSN 1580-2949
MTAEC9, 49(3)311–477(2015)

MATER. TEHNOL.	LETNIK VOLUME 49	ŠTEV. NO. 3	STR. P. 311–477	LJUBLJANA SLOVENIJA	MAY–JUNE 2015

VSEBINA – CONTENTS

PREGLEDNI ČLANEK – REVIEW ARTICLE

IZVIRNI ZNANSTVENI ČLANKI – ORIGINAL SCIENTIFIC ARTICLES

STROKOVNI ČLANKI – PROFESSIONAL ARTICLES

IN MEMORIAM

UDK 531.43:539.92:621.793/.795
Review article/Pregledni članek

ISSN 1580-2949
MTAEC9, 49(3)313(2015)

WEAR MECHANISMS AND SURFACE ENGINEERING OF FORMING TOOLS

OBRABNI MEHANIZMI IN INŽENIRING POVRŠINE PREOBLIKOVALNIH ORODIJ

Bojan Podgornik, Vojteh Leskovšek

Institute of Metals and Technology, Lepi pot 11, 1000 Ljubljana, Slovenia
bojan.podgornik@imt.si

Prejem rokopisa – received: 2015-01-05; sprejem za objavo – accepted for publication: 2015-03-02

doi:10.17222/mit.2015.005

The manufacturing of parts is faced with ever-increasing demands for higher strength (hardness) and toughness of the work material, as well as higher productivity and environmental concerns. At the same time, the quality requirements are high and will continue to grow in the future. This leads to restrictions in terms of the type and use of lubricants and especially to increased requirements relating to the wear and fatigue resistance of tools.

The main focus on improving the wear resistance and tribological properties of forming tools has mainly been on developing tool steels with an improved fracture toughness and then modifying the lubricants for better retention and permeability at the tool/work-piece contact area. Nevertheless, the wear resistance of forming tools can also be successfully improved by surface-engineering techniques. In recent years, hard coatings in particular have shown enormous potential for improving the tribological properties of contact surfaces.

This paper reviews the wear mechanisms encountered in forming processes, as well as various surface-engineering techniques designed to improve the wear resistance and the anti-sticking properties of forming tools. The possible benefits and restrictions of different surface-engineering techniques are presented for the example of sheet-metal forming, fine blanking and forging.

Keywords: surface engineering, forming, hard coatings, topography, friction, wear

Preoblikovalna industrija se spopada z nenehno naraščajočimi zahtevami po višji trdnosti (trdoti) in žilavosti preoblikovanih materialov, kakor tudi večji produktivnosti in skrbi za okolje. Istočasno se povečujejo zahteve po kvaliteti izdelkov, kjer predvsem kvaliteta površine postaja vedno bolj pomembna. To pomeni omejitve pri uporabi maziv ter seveda večje zahteve po obrabni odpornosti in vzdržljivosti preoblikovalnih orodij.

Do nedavnega je izboljševanje obrabne obstojnosti in triboloških lastnosti preoblikovalnih orodij temeljilo predvsem na razvoju bolj žilavih in čistejših orodnih jekel ter modifikaciji maziv z boljšimi mazalnimi lastnostmi. V zadnjih letih pa tudi na področju preoblikovalnih orodij tehnike inženiringa površin, še posebej nanos trdih zaščitnih prevlek, omogočajo nadaljnje izboljšanje triboloških lastnosti kontaktnih površin.

V prispevku so tako predstavljeni obrabni mehanizmi, ki so jim izpostavljena preoblikovalna orodja, kakor tudi različne tehnike inženiringa površine, namenjene izboljšanju obrabne obstojnosti in tornih lastnosti preoblikovalnih orodij. Problemi in prednosti uporabe inženiringa površine so poudarjene na primeru hladnega preoblikovanja pločevine, štancanja in kovanja.

Ključne besede: inženiring površin, preoblikovanje, trde prevleke, topografija, trenje, obraba

1 INTRODUCTION

The forming industry is confronted with ever-increasing demands to form low-weight, high- and ultra-high-strength materials, as well as with higher productivity and environmental concerns.[1] Simultaneously, we are increasing the requirements on the quality of the formed parts, especially in terms of surface quality.[2–4] All these lead to restrictions regarding the use of the type and quality of the lubricants and to increased demands on the wear and fatigue resistance of the tool.

The wear resistance and the efficiency of forming tools are limited for different reasons, including thermal and mechanical fatigue and cracking, erosion, corrosion, abrasive and adhesive wear, and galling.[5,6] In addition to that, tool replacement and reconditioning often depends on the surface quality of the formed parts.[3,7,8] A smooth, defect-free surface represents a competitive market advantage, but mostly it is more favourable contact conditions and a better wear resistance. The main obstacles to obtaining smooth surfaces are the increased surface roughness and the wear of the tool, especially the adhesive wear and the galling.[9,10] On the other hand, tool wear and galling also lead to increased contact pressures and unstable friction in the forming process.

Traditionally, improving the tribological properties and the wear resistance of forming tools was mainly based on the increased cleanliness, hardness and fracture toughness of the tool steel, as well as on the better lubricity and stability of the forming lubricants. However, wear and galling resistance can also be very successfully reduced with a proper modification or surface engineering of the tool surface.[2,11] Commonly applied surface-engineering processes, found in many tool applications, are the thermo-chemical treatments, ranging from basic surface hardening and plasma nitriding to more recent processes of deep cryogenic treatment and laser-surface remelting.[12–16] However, in the past two decades, surface coating processes are gaining an advantage, including PVD, CVD and PACVD techniques. Thin, hard coatings

with excellent tribological properties, like TiN, TiAlN, CrN, etc., have already outperformed and successfully replaced traditional high-speed steel tools in the majority of cutting operations.[17,18] Despite this, the majority of forming tools are still uncoated. Besides the complex geometry, which makes it difficult to obtain uniform coating deposition, commercial hard wear-resistant coatings show a relatively high coefficient of friction and a high tendency for galling against typical formed materials.[19–21] Typical tool steels also have a lower load-carrying capacity than high-speed steel, ceramics and hard metals. As such, tool steels do not provide sufficient support for very thin, hard and brittle coatings. However, in recent years a lot of new deposition methods and coating types have been developed, which show excellent adhesion, as well as mechanical and tribological properties.[22] In order to exploit the full potential of hard coatings in terms of improving the tribological properties of forming tools, coated surfaces must primarily be able to sustain high-impact dynamic loading without cracking, debonding or spallation. The improved load-carrying capacity of coated systems can be obtained by increasing the thickness of the coating, which is not easy to achieve due to the high residual stresses, by employing support layers, which increases costs, or through the most efficient duplex technique, combining a classic thermo-chemical treatment of the steel substrate and PVD or PACVD deposition of the protective coat ing.[19,23,24]

Another option for improving the tribological properties, mainly the friction behaviour of the forming tools, either coated or un-coated, is through a surface-roughness and topography optimization. Proper selection and preparation of the surface topography, using techniques like polishing, shot-peening and laser surface texturing, can greatly improve the performance and galling resistance of the forming tools, and thus reduce or even eliminate the need for lubrication.[7,25,26]

2 WEAR MECHANISMS IN FORMING APPLICATIONS

Different materials can be formed in a desired shape or product using different processes, like casting, metal forming and machining. Metal forming is further divided into rolling, drawing, extrusion, sheet-metal forming, die casting and forging.[27] During forming the tool surface is subjected to a sliding contact with the formed material, to high contact stresses and often to elevated temperatures, which all lead to tool wear. The wear mechanisms that can be found in forming applications include abrasive and adhesive wear, mechanical and thermal fatigue, plastic deformation and corrosion.[27,28] Certainly, different wear mechanisms require different properties of the tool material and especially of the tool surface. However, in general, the surface of the tool should be hard and should maintain this hardness at high temperatures to reduce the abrasive wear. Furthermore, the tool material should be tough in order to limit or reduce the fatigue and be heat resistant with a high thermal resistivity. Typical wear mechanisms found in different forming operations and being responsible for tool wear are summarized in **Table 1**.

2.1 Cold forming

In the case of cold forming the tool failure is caused by five main wear mechanisms, which are a consequence of the high contact pressure and the relative motion between the tool surface and the formed material (**Figure 1**).[29] The main wear and damage mechanisms in cold forming are:

- abrasive wear
- adhesive wear
- low-cycle fatigue
- crack propagation
- plastic deformation

The most dominant wear mechanism, found in all cold-forming operations, is adhesive wear. However, normally more than just one wear mechanism takes place, often even all of them can be observed, which depends on the forming process and the work material. In the case of punching and fine blanking, characterized by sharp edges and high impact loads, adhesion is accompanied by fatigue and chipping, and for drawing and extrusion, with abrasive wear. On the other hand, in the cold forming of harder and thicker materials, abra-

Table 1: Wear mechanisms in forming processes
Tabela 1: Obrabni mehanizmi v preoblikovalnih procesih

	abrasion	adhesion	low cycle fatigue	high cycle fatigue	thermal* fatigue	corrosion	plastic deformation
Punching, Fine blanking	x	x	x	x			x
Deep drawing	x	x					
Sintering	x	x		x			
Rolling	x	x	x	x	x	x	x
Extrusion Drawing	x	x	x	x	x		x
Forging	x	x	x	x	x	x	x
Injection moulding	x	x			x	x	
Die casting	x	x			x	x	

* valid for processes at elevated temperatures

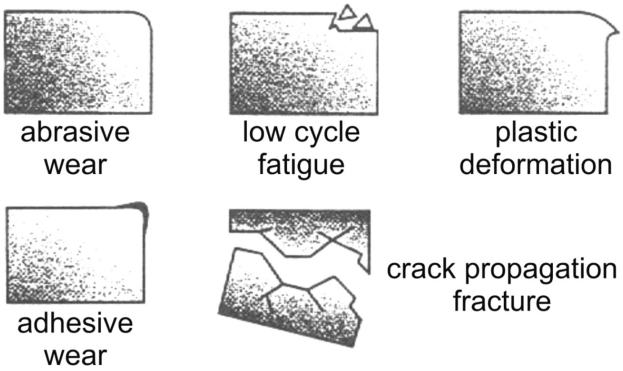

Figure 1: Wear mechanisms found in cold-forming processes[29]
Slika 1: Obrabni mehanizmi, značilni za procese hladnega preoblikovanja[29]

sive wear and plastic deformation will dominate, while for softer materials it is adhesive wear, known also as galling.

Adhesive wear as the prevailing wear mechanism can be found in the cold forming of softer metals, like aluminium, titanium, copper, austenitic stainless steel, etc., and is especially critical in sheet-metal forming. The adhesive wear of forming tools is a result of local micro welds between the surface of the tool and the work-piece followed by the gradual transfer and accumulation of the work material on the tool surface, known also as galling.[30] The transferred material causes unstable friction as well as scratching and a poor, uneven surface of the work-piece. Removal of the transferred work material can even cause abrasive wear of the tool surface. For good adhesive wear resistance the tool surface should be hard but with sufficient ductility, as smooth as possible and have low friction against the work material. In practice, adhesion or galling problems are mostly tackled by the application of different lubricants. However, the use of lubricants requires additional cleaning procedures and presents environmental concerns.

Abrasive wear dominates when forming hard materials or multiphase materials with hard particles (oxides, carbides, etc.) which scratch the tool surface and lead to tool wear. However, as already mentioned, abrasive wear can also be a result of adhesive wear. During forming the transferred and adhered work material becomes work hardened and when detached from the surface it represents a hard abrasive particle, which can cause three-body abrasive wear of the tool surface. Abrasive wear can be found in punching, fine blanking, drawing, extrusion and forging. The improved abrasive wear resistance of forming tools is mainly achieved by increasing the tool-surface hardness, either through thermo-chemical treatments or the deposition of hard, wear-resistant coatings.

Low-cycle fatigue is typical for punching, stamping and fine blanking, where the cutting edges are subjected to repeated high contact stresses. The repeated impact loading, sliding motion and local plastic deformation result in crack initiation and propagation, which finally leads to chipping. Due to this chipping the cutting edges become blunt and, consequently, this leads to increased stresses, unfavourable sliding conditions between the tool surface and the work-piece, and to adhesive wear. The resistance to low-cycle fatigue can be improved by increasing the ductility but without sacrificing the tool hardness.

In contrast to other wear mechanisms found in cold forming, crack propagation leads to instantaneous failure or even to the fracture of the tool, which is very hard to predict. Crack propagation is a consequence of stress concentrations, cracks initiation and the tensile stress field in the tool material. Since the majority of cracks start and propagate below the surface, the most important properties in terms of crack-propagation resistance are the properties of the base or substrate tool material. It has to possess high toughness, which on the other hand also means reduced hardness. Therefore, a suitable compromise between the increased toughness and the reduced tool hardness needs to be obtained.

Plastic deformation, caused by high contact pressures, is a common problem in many cold-forming operations. When the compressive stress exceeds the yield strength of the tool material, the tool geometry becomes distorted and this is often also coupled with imprints on the tool surface. The tool-geometry distortion means an incorrect shape of the formed part, while the presence of imprints leads to a poor surface quality. In terms of the resistance to plastic deformation, the most critical tool property is the hardness of the tool surface.

2.2 Hot forming

In hot-forming processes, including die casting, injection moulding and hot forging, the wear of the tool is caused by four types of loading:[31]

- thermal,
- mechanical,
- tribological,
- chemical.

Thermal loads are caused by repeated heat transfer from the work-piece and the repeated cyclic heating and cooling of the tool surface. High-temperature exposure leads to a reduced tool hardness as well as cyclic heating and cooling, leading to thermal fatigue. In the same way as in cold forming, also for hot forming, especially in the case of hot forging, mechanical loads may result in fatigue and plastic deformation. However, the tribological conditions in the case of hot forming are much more complex. Oxide layers formed on the work-piece surface are hard and brittle and as such result in the generation of hard, abrasive particles, which often cause abrasive wear of the tool surface. On the other hand, contact temperatures during hot forming often exceed 700 °C, thus affecting the hardness and adhesive properties of the

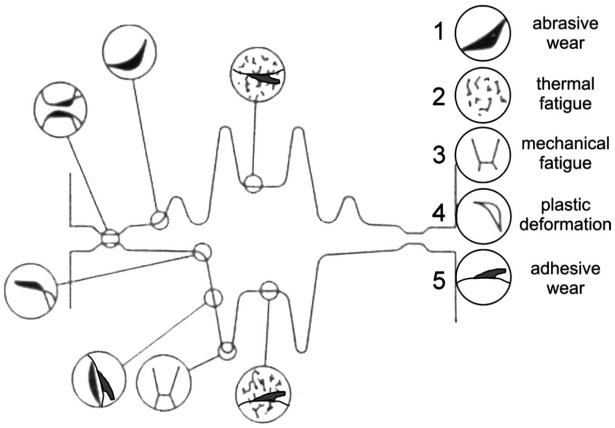

Figure 2: Typical wear mechanisms in hot forming[32]
Slika 2: Obrabni mehanizmi, prisotni pri vročem preoblikovanju[32]

contact surfaces. The higher is the temperature, the larger will be the drop in the surface hardness and more reactive is the surface, resulting in more intense abrasive wear and galling. The situation becomes even worse due to the constant flow of hot-work material into the contact with the tool surface. On the other hand, high temperatures also result in chemical loads on the tool, which may cause different chemical reactions on the tool surface, i.e., oxidation.

Different parts of hot-forming tools are subjected to different and quite specific combinations of loads and consequently display different wear mechanisms, as shown in **Figure 2**.[32] The surfaces exposed to the highest temperature changes are subjected to thermal fatigue, and the surfaces with the highest stress concentrations, to mechanical fatigue. Furthermore, in processes with high thermal loads (die casting and injection moulding) an increased surface reactivity leads to adhesive wear and galling. However, in highly loaded tools for hot forging and extrusion, more than 70 % of all tool failures are caused by abrasive wear of the tool surface.

3 SURFACE ENGINEERING FOR IMPROVED TRIBOLOGICAL PROPERTIES OF FORMING TOOLS

3.1 Cold sheet-metal forming

Failure and the replacement of tools for cold sheet-metal forming is mainly caused by adhesive wear and galling, which is followed by abrasive wear. An improvement in the abrasive wear is directly related to an increased hardness of the surface, achieved through different thermo-chemical treatments and hard-coating deposition techniques.[12] Galling problems and unstable friction, on the other hand, are mainly addressed by the use of highly additivated and environmentally hazardous lubricants, which should provide proper lubrication between the tool and the work-piece surface. The improved tribological properties in sheet-metal forming processes can also be achieved through the proper surface engineering of the tool.[2,33] The first group are the thermo-chemical treatments (nitriding, boriding, vanadizing), the second is surface texturing and the third is the deposition of low-friction coatings.

Investigations in the field of thermo-chemical treatments have shown that increased hardness of the surface and microstructure refinement obtained through a deep-cryogenic treatment can effectively improve the galling resistance of tool steel.[16] On the other hand, the best results are obtained using plasma nitriding.[25,34] The plasma nitriding of tool steel gives up to 40 % lower friction against austenitic stainless steel and up to 50 % better galling resistance, as compared to hardened tool steel, as shown in **Figure 3**. However, the selection of the proper plasma-nitriding parameters and post-treatment conditions is crucial.[25,35] The presence of a compact γ' (Fe_4N) compound layer may enhance the galling resistance against stainless steel, while a combination of porous ε ($Fe_{2\text{-}3}N$) and γ' compound layer and the use of a non-polished, nitrided surface have a detrimental effect (**Figure 3**).

More important than the selection of the thermo-chemical treatment is the proper preparation of the tool

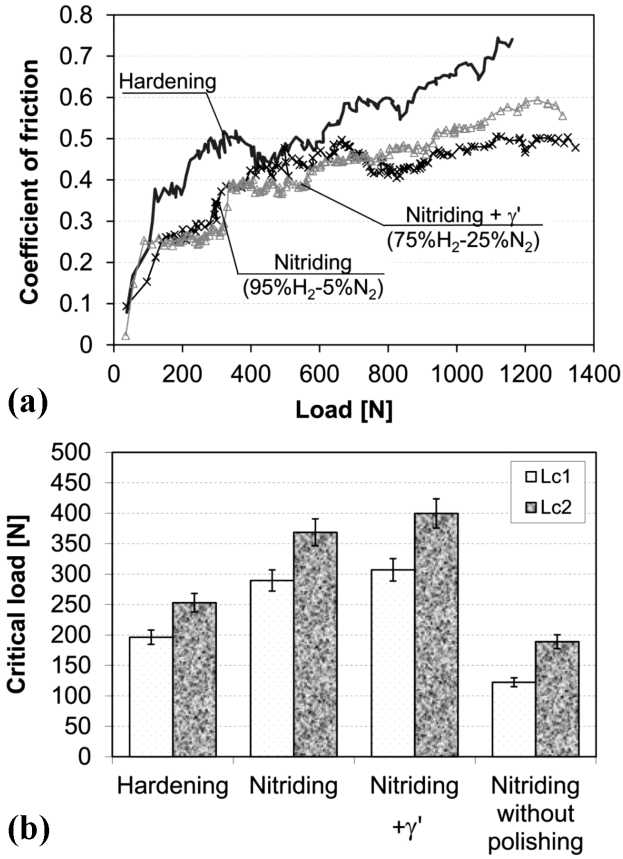

Figure 3: a) Coefficient of friction and b) critical loads for galling initiation (L_{c1}) and transfer layer build up (L_{c2}) for different surface treatments of tool steel[35]
Slika 3: a) Potek koeficienta trenja in b) kritična obremenitev začetka prenosa (L_{c1}) ter tvorjenja plasti nerjavnega jekla (L_{c2}) v odvisnosti od kemo-termične priprave površine orodnega jekla[35]

surface.[7,26] As shown in **Figure 4**, even with just simple polishing of the tool surface, a low and stable coefficient of friction can be achieved, and the galling resistance can be greatly improved. Rough surfaces (R_a > 0.25 μm) result in high and unstable friction, but above all in the almost immediate transfer of work material to the tool surface. By reducing the surface roughness below 0.05 μm, low and stable friction and excellent galling resistance across a broad load range can be achieved, even with reduced lubrication, the use of less additivated lubricants or without any lubrication (**Figure 4**).

A microscopic analysis of the contact surfaces of the tools for cold forming has revealed that galling and the transfer of work material is initiated at scratches, irregularities and asperities on the tool surface,[36] as shown in **Figure 5a**. During forming and load increases the transferred material becomes accumulated around the initial galling points, forming a thick, transferred layer on the tool surface (**Figure 5b**). Therefore, every imperfection on the tool surface represents a potential initial point for the beginning of the galling and the work-material transfer. Polishing the surface, on the other hand, removes and smoothens the scratches and imperfections caused during tool manufacturing, thus greatly reducing the risk of adhesive wear. In forming processes, where lubricants and lubrication cannot be eliminated, more favourable tribological properties and a reduced amount of lubricants can be achieved through the surface texturing.[37–39] Surface structures in the form of channels or dimples with the proper size and density (**Figure 6**) may act as mini-reservoirs, which can effectively feed the lubricant into the contact and prevent, or at least reduce, galling.[26]

The third option for improving the tribological properties of tools for cold sheet-metal forming is the

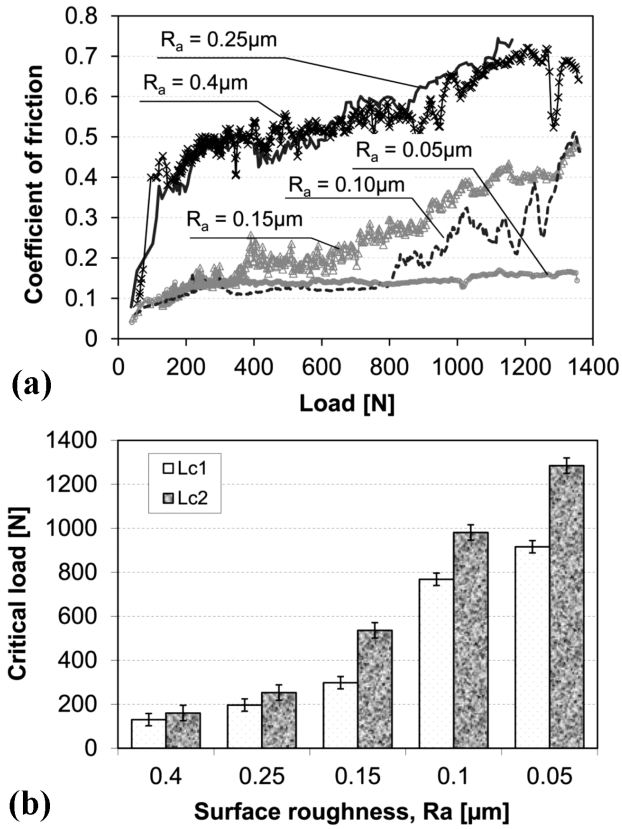

Figure 4: Effect of surface roughness on: a) the coefficient of friction and b) the critical loads for stainless-steel transfer[7]

Slika 4: Vpliv hrapavosti površine na: a) potek koeficienta trenja in b) kritično obremenitev prenosa nerjavnega jekla[7]

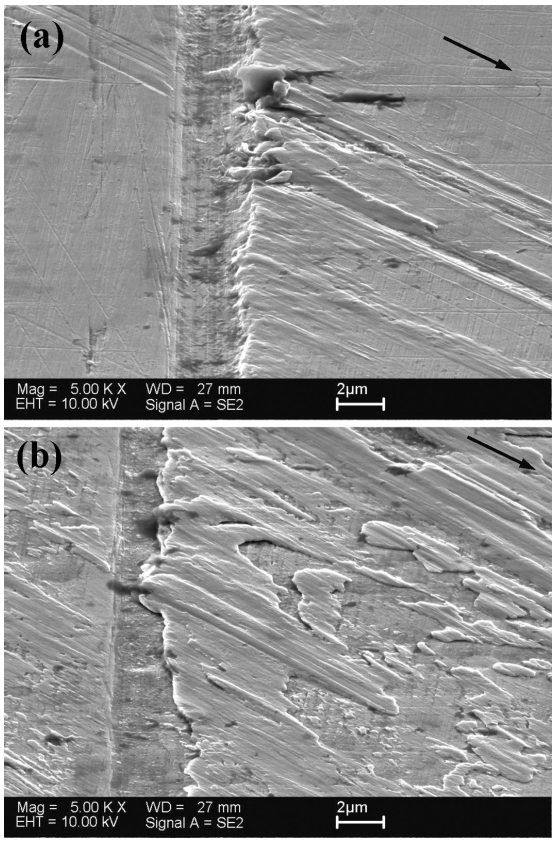

Figure 5: a) Beginning of galling and b) accumulation of thick transferred layer of work material on the tool surface

Slika 5: a) Začetek adhezije preoblikovanega materiala na površino orodja in b) akumulacija in tvorjenje plasti prenesenega materiala

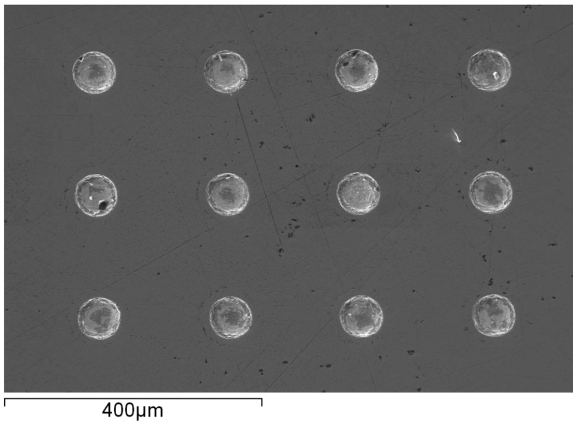

Figure 6: Surface-textured tool surface

Slika 6: Obličena kontaktna površina

deposition of a hard protective coating. In the case of cutting tools, hard ceramic coatings, i.e., TiN, TiAlN, AlCrN, etc., successfully replace classic materials, giving a greatly improved abrasive wear resistance and productivity and, in some cases, even allowing for dry cutting.[40] However, the requirements for the successful implementation of hard coatings on forming tools are much tougher and more complex. Besides the more complex geometry of forming tools and the limited load-carrying capacity of the tool-steel substrate, typical commercial hard coatings for cutting applications show a high friction and a strong tendency to pick up work material. Therefore, coating selection in the forming operations mainly depends on the material to be formed and the coating galling tendency against it.[2,32,41]

In the case of stainless steel a TiN coating gives a similar friction to un-coated cold-work tool steel, but almost instantaneous adhesion and galling. As shown in **Figure 7**, similar properties with a high galling tendency against stainless steel are also displayed by other hard ceramic coatings. On the other hand, carbon-based coatings, either amorphous diamond-like-carbon coatings (DLC) or metal-doped carbon-based coatings (W-C, Ta-C, etc.) provide low and stable friction, even under dry-sliding conditions.[42] At the same time, DLC coatings considerably increase the critical loads for galling initiation and transfer-layer build up when it comes to the forming of stainless steel (**Figure 7b**).

Although polishing of the contact surface greatly improves the tribological properties of tool steel, highly additivated lubricants are still required to prevent galling and transfer-layer build up when forming stainless steel. Switching to pure base oil does not allow more than 10 forming cycles, which are more or less limited to low loads and low deformation rates before adhesion and galling take place (**Figure 8a**). However, with the application of DLC coatings we can effectively prevent adhesive wear and provide a stable tribological contact with a low coefficient of friction (≈ 0.1) with a more environmentally friendly base lubricant without any additives,[7] as shown in **Figure 8b**.

When forming aluminium and aluminium alloys, galling and adhesion to hardened tool steel take place immediately and at very low loads if the contact is not

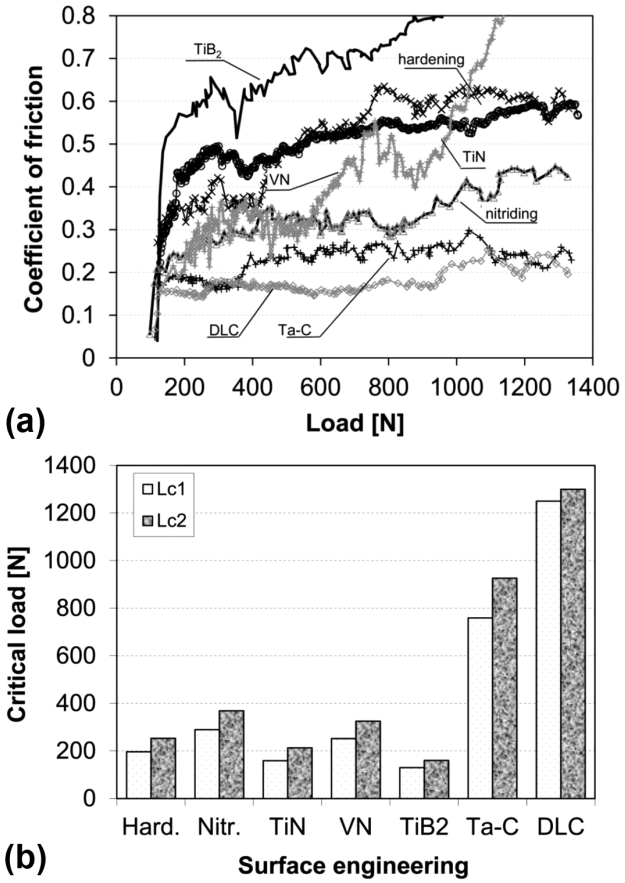

Figure 7: a) Coefficient of friction and b) critical loads for galling initiation and transfer-layer build up for different hard coatings tested against stainless steel[35]

Slika 7: a) Potek koeficienta trenja in b) kritične obremenitve prenosa nerjavnega jekla pri suhem drsnem kontaktu različnih prevlek[35]

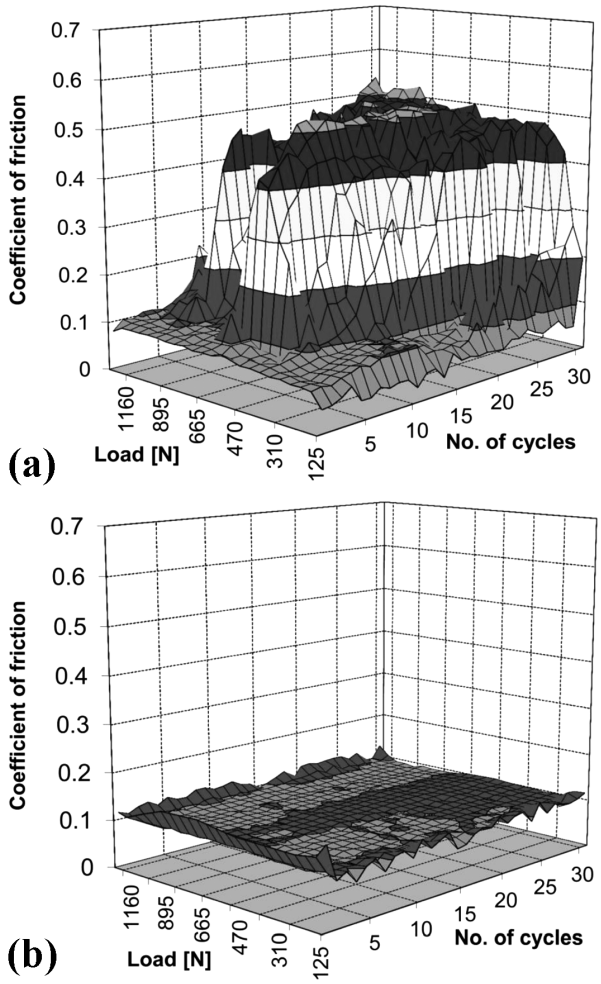

Figure 8: Friction maps for: a) polished tool steel and b) DLC-coated surface-lubricated with pure PAO8 base oil[7]

Slika 8: Karte koeficienta trenja za: a) polirano orodno jeklo in b) površino, prekrito z DLC-prevleko; bazno olje PAO8[7]

lubricated. Even through surface engineering (polishing, nitriding, hard coating) galling resistance cannot be improved to any great extent. However, the proper selection of surface-engineering technique affects the coefficient of friction and the critical loads for aluminium transfer-layer build up. In contrast to stainless steel, DLC coatings show no beneficial effect when it comes to forming aluminium alloys. However, the galling performance of DLC coatings also depends on the coating and the aluminium-alloy type.[43–45] In the case of aluminium alloys a certain reduction in the coefficient of friction and increased critical loads for the transfer-layer build up can be expected with the application of nitride-type coatings (TiN, VN, CrN, etc.) and by nitriding the tool-steel surface, as shown in **Figure 9a**. Even smaller differences between different surface-engineering techniques in terms of galling resistance are found for titanium and titanium alloys, where plasma nitriding shows the greatest potential (**Figure 9b**).

3.2 Punching and fine blanking

In punching and fine blanking the cutting elements of the tool are subjected to high impact loads as well as to a sliding contact. Impact loads lead to low-cycle fatigue and the chipping of the cutting edges, while sliding against steel sheet material causes galling and abrasive wear. An improvement in the abrasive wear resistance as well as in the galling resistance can be achieved through the deposition of hard coatings. At the same time, a substrate material with a high toughness is required in order to postpone the low-cycle fatigue and the chipping of the cutting edge. This, on the other hand, means insufficient load-carrying capacity, which often results in coating cracking and delamination[46]. And the harder is the coating, the higher is the risk of coating failure. For the coating to show its full potential in reducing friction and increasing surface wear resistance, we primarily have to provide sufficient load-carrying capacity for the substrate. This can be achieved by combining a thermochemical treatment of the substrate and hard-coating deposition, called a duplex treatment.[19,47] As shown in **Figure 10a**, by plasma nitriding the load-carrying capacity of the tool steel can be increased by up to three times. However, improper preparation of the substrate (the presence of a γ' compound layer, a high roughness) or insufficient coating adhesion (TaC) will lead to immediate flaking of the coating (**Figure 10b**), regardless of the substrate's properties.

Besides the load-carrying capacity, the tribological properties and the resistance of the coated surfaces to

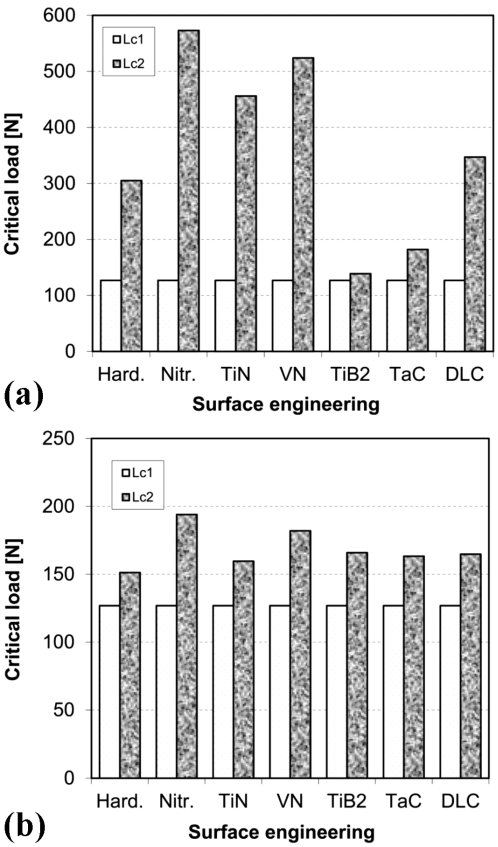

Figure 9: Critical loads for galling against: a) aluminium alloy and b) titanium alloy[35]

Slika 9: Kritične obremenitve prenosa materiala za: a) aluminijevo in b) titanovo zlitino[35]

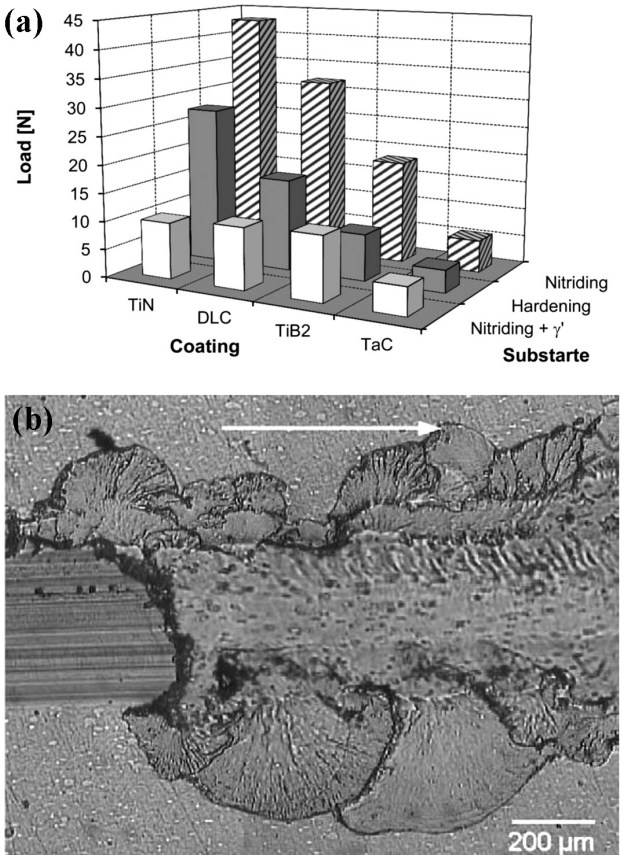

Figure 10: a) Effect of substrate treatment on the load-carrying capacity of coated tool steel and b) flaking of the TaC coating[19]

Slika 10: a) Vpliv kemo-termične priprave podlage na nosilnost oplaščenih površin in b) luščenje prevleke TaC[19]

dynamic loading also depend on the coating type and the properties of the substrate material,[48] as shown in **Figure 11**. The best resistance is achieved by multilayer coatings composed of a base, load-carrying ceramic layer (TiAlN, CrN, etc.) and top, low-friction layer (DLC, Me-C:H, MoS_2, etc.). Multilayer coatings are followed by gradient coatings (i.e., TiCN), while the lowest resistance to dynamic loading is displayed by monolayer coatings of TiN, AlCrN, etc. (**Figure 11**). In terms of substrate material, due to the poor adhesion and a high flaking tendency, tungsten carbide is not the most suitable for coated tools subjected to high dynamic impact loading. The best substrate material, regardless of the coating used, is fine-grained, micro-clean tool steels produced by powder metallurgy (P/M) processes.[49,50] In order to provide a high load-carrying capacity combined with a superior impact, a wear-resistant tool-steel substrate should have a hardness of at least 64–65 HRc and a fracture toughness above 12 MPa $m^{1/2}$.[51] Although plasma nitriding provides the highest static load support, its negative effect on the surface ductility greatly reduces the resistance of the coated surface on the crack initiation and propagation,[52,53] as shown in **Figure 12**.

The purpose of hard coatings in punching and fine blanking is not only to increase the wear resistance of the tool but also to reduce or even eliminate the lubrication. As shown in **Figure 13**, regardless of the substrate material used, the lowest coefficient of friction (≈ 0.15) and the highest potential are shown by carbon-based or diamond-like-carbon coatings (DLC). On the other hand, harder ceramic coatings, especially nitride-type multilayer coatings, display a much higher friction (> 0.3), but when deposited on a suitable substrate up to 10 times less wear (**Figure 13**).

Experiments with coated punching and fine-blanking tools have shown that although coatings can greatly

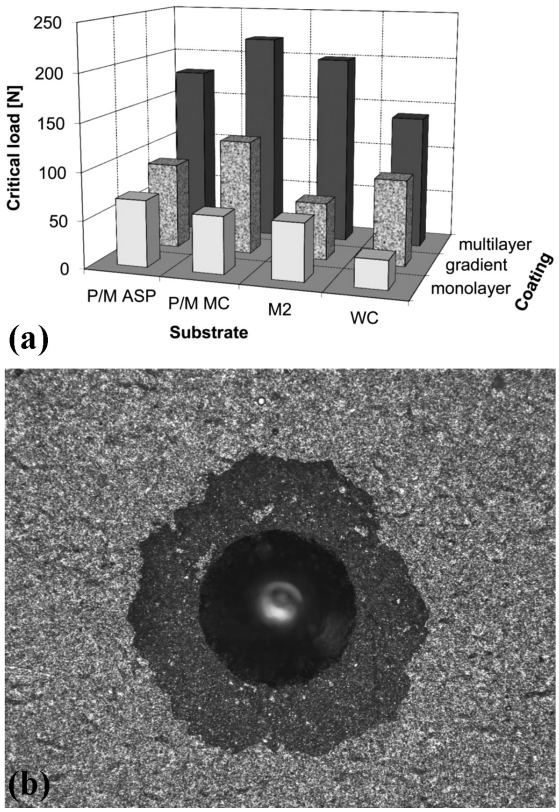

Figure 11: a) Effect of substrate material and coating type on the load-carrying capacity and b) example of poor coating adhesion in the case of tungsten carbide substrate[48]

Slika 11: a) Vpliv materiala podlage in tipa prevleke na nosilnost oplaščene površine ter b) primer neustrezne oprijemljivosti na podlago karbidne trdine[48]

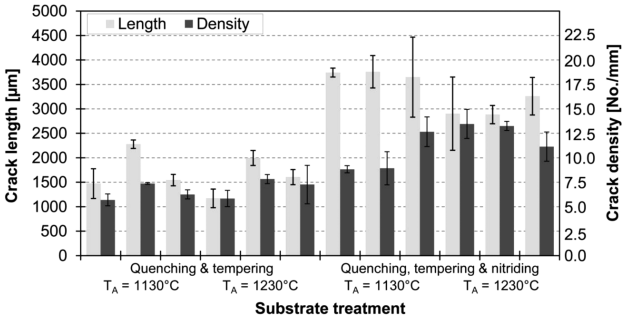

Figure 12: Effect of substrate treatment type on the crack length and the density in a gradient TiCN coating deposited on fine-grained micro-clean P/M tool steel and subjected to a sliding contact at 3500 N[52]

Slika 12: Vpliv postopka priprave podlage na dolžino in gostoto razpok v gradientni TiCN-prevleki, naneseni na finozrnato orodno jeklo P/M in izpostavljeno drsnemu kontaktu pri 3500 N[52]

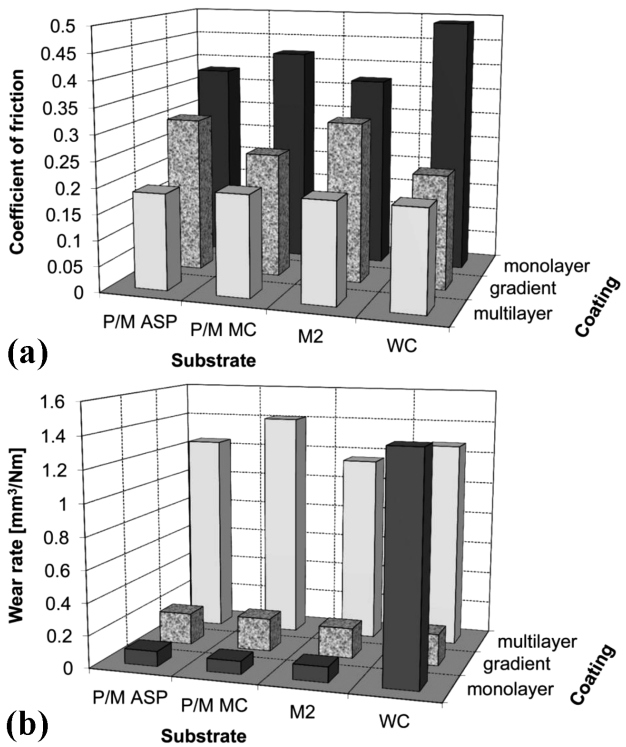

Figure 13: a) Effect of substrate material and coating type on: a) coefficient of friction and b) wear rate in a dry-sliding contact[48]

Slika 13: a) Vpliv materiala podlage in tipa prevleke na: a) koeficient trenja in b) stopnjo obrabe pri suhem drsnem kontaktu[48]

increase the tools' performance and wear resistance, neither coating group and type allow the complete elimination of lubrication.[48,54] In the case of hard ceramic coatings, high friction leads to the adhesion of the work material to the tool surface and consequently for up to three times higher extraction forces and even up to ten times higher punching forces, which then lead to coating cracking and flaking (**Figure 14**). On the other hand, for DLC coatings, although initially reducing the punching forces, a high coating-wear rate in just a few strokes leads to failure of the cutting elements. However, the combination of minimum lubrication, a suitable fine-grained-steel substrate and its heat treatment, and a hard, wear-resistant coating can result in the greatly improved resistance of both sliding surfaces and cutting edges of the punching and fine blanking tools.

3.3 Hot forging

Tools for hot forging are exposed to the widest and most demanding loading and contact conditions, which result in the most severe wear of the tool surface. Besides the adhesive and abrasive wear, the contact surfaces are exposed to mechanical and thermal fatigue, as well as to plastic deformation.[31,46] Traditionally, forging dies are subjected to different thermo-chemical treatments, mostly to nitriding in order to improve their wear resistance and lifetime.[55] However, due to the very high contact temperatures, all these treatments have only a limited effect.[46] On the other hand, investigations with hard coatings, including TiN, TiCN, CrN, TiB_2, etc., show very promising results.[56,57] Coatings prevent thermal fatigue and the formation of intermetallic alloys on the tool surface, while at the same time they protect the substrate material from thermal shocks and softening. Furthermore, with a high hardness, which can be maintained even at very high temperatures, coatings also improve the tool's abrasive and erosive wear resistance.

As shown in **Figure 15**, the deposition of gradient or multilayer coatings can significantly improve the wear resistance of hot-forging die inserts. When they are only nitride, the surface hardness of the inserts will drop by more than 15 % in less than 15000 strokes, eventually resulting in severe plastic deformation and wear of the inserts. On the other hand, a combination of plasma nitriding and a hard PACVD coating was found to prevent a drop in the surface hardness and almost eliminated the wear of the contact surfaces.[56] As shown in **Figure 15**, even after about 15000 strokes the coated inserts were able to maintain their initial geometry.

Although the coatings have exceptional thermal and anti-wear properties, coating deposition on an improperly prepared substrate will lead to a deterioration rather than an improvement in the performance of forging dies. Insufficient hardness and a too rough substrate will cause coating cracking and delamination (**Figure 16a**), which even accelerates the abrasive wear of the die. Furthermore, the use of hardened hot-work tool steel with a coarse microstructure greatly increases the likelihood of cracks initiation and propagation, thus reducing the tool's fatigue resistance.[5] As in the case of punching tools, the best results are obtained through duplex technology, combining plasma nitriding of the tool-steel substrate and PVD or PACVD coating deposition.[57,58] However, besides the substrate hardness, a very important substrate property is its fracture toughness.[59] A dense

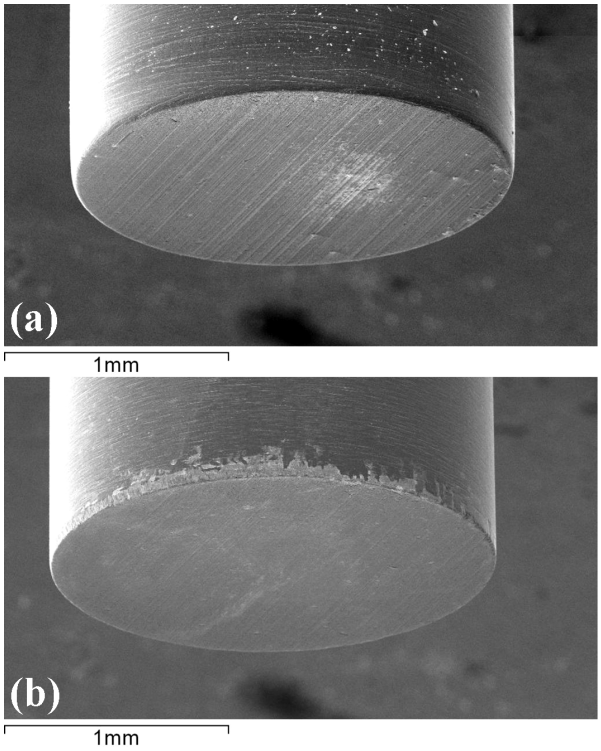

Figure 14: Contact surface of punching tool coated with monolayer AlCrN coating after 4000 strokes: a) fine-grained micro-clean P/M tool steel substrate and b) WC substrate[48]

Slika 14: Površina štancnega noža, prekritega z AlCrN-prevleko, po 4000 udarcih; podlaga iz: a) visokokvalitetnega jekla P/M in b) karbidne trdine[48]

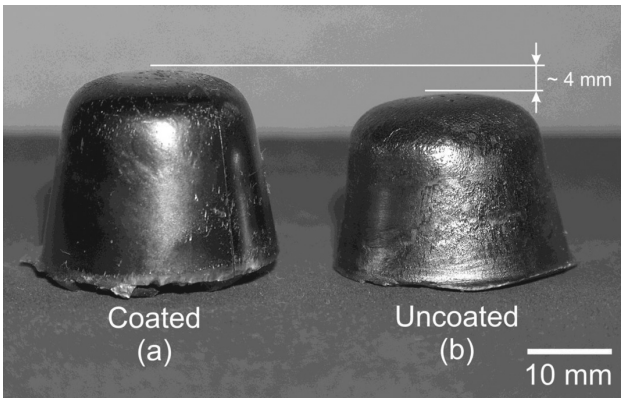

Figure 15: Forging die insert after 13500 strokes: a) Duplex – TiCN + nitriding, b) only nitrided[56]

Slika 15: Vložek kovaškega utopa po 13500 udarcih: a) Duplex – TiCN + nitriranje, b) nitriran[56]

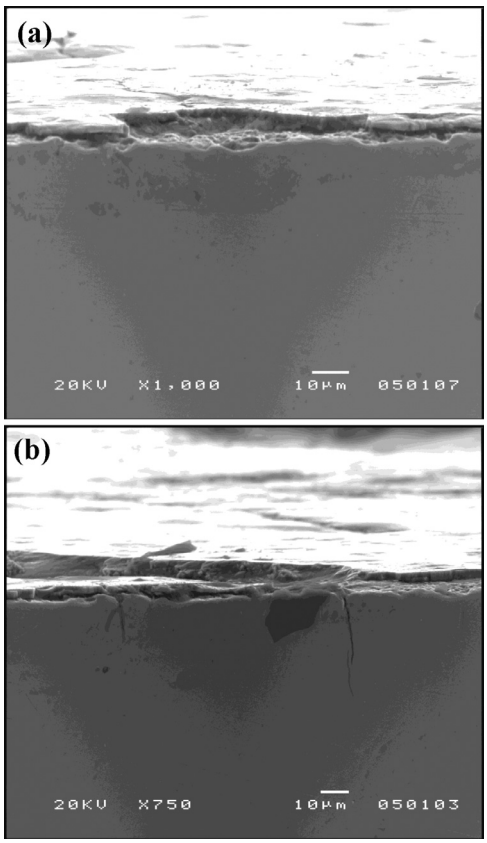

Figure 16: Failure of the coated die insert: a) flaking and b) crack initiation and propagation
Slika 16: Poškodba oplaščenega kovaškega orodja: a) luščenje in b) nastanek ter širjenje razpok

γ' compound layer may act as an additional support interlayer, but its brittleness leads to a reduced coating-cracking resistance as soon as the substrate core hardness is reduced below 50 HRc. Even for a compound-layer-free nitrided substrate a high core-hardness level is the main requirement in providing good load support, but it needs to be supported by a sufficient fracture-toughness level[53] (**Figure 17**).

4 CONCLUSIONS

The first step in improving the tribological properties and galling resistance of forming tolls is reducing the surface roughness. Surface polishing smoothens and removes the surface irregularities and thus eliminates potential spots for galling initiation. Increasing surface hardness or the deposition of a hard coating, although improving the abrasive wear resistance, exaggerates the effect of the surface roughness.

In cold sheet-metal forming the main wear mechanism responsible for tool failure is adhesive wear or galling. The selection of a surface-engineering technique aimed at improving the anti-galling properties mainly depends on the material to be formed. In the case of stainless steel, low and stable friction as well as complete protection of the tool surface against galling under

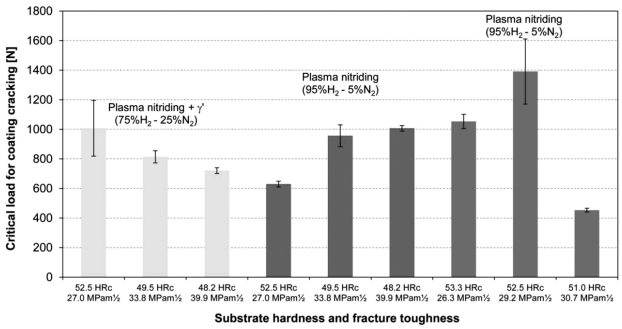

Figure 17: Effect of substrate hardness and fracture toughness on the load-carrying capacity of TiN/TiB_2-coated hot-work tool steel[53]
Slika 17: Vpliv trdote in lomne žilavosti orodnega jekla za delo v vročem na kritično obremenitev nastanka razpok v TiN/TiB_2-prevleki[53]

high loads and boundary lubrication is provided by carbon-based or diamond-like-carbon coatings. Nitride-type coatings, on the other hand, are more suitable for the cold forming of aluminium and aluminium alloys, and plasma-nitrided tool steel for titanium alloys.

For the successful use of hard coatings and improved tool performance in punching and fine blanking operations, first of all the substrate needs to have a sufficient load-carrying capacity. Besides that, a high hardness should be coupled with a sufficient fracture toughness. The best results are obtained when using multilayer coatings on fine-grained micro-clean P/M tool steels. P/M tool steels give good impact and fatigue resistance, while an optimal thermo-chemical treatment provides a superior load support. Although the complete elimination of lubrication in punching and fine blanking is not yet possible, the superior wear resistance and friction performance of hard coatings allow a reduction in the lubrication quantity and the amount of additives.

Due to the combined mechanical and thermal loads of hot-forging dies the proper selection and optimal parameters of substrate thermo-chemical treatment are crucial for the proper performance of the coated tools. Instead of the expected improvement an improper combination of substrate hardness and toughness can lead to increased wear and accelerated crack initiation and propagation. The highest potential for improving the performance of hot-forging dies is shown by the combination of a plasma-nitrided tool-steel substrate coated with a multilayer nano-composite coating. However, before the coating the substrate needs to be polished and increased substrate hardness combined with sufficient fracture toughness.

5 REFERENCES

[1] P. Groche, M. Christiany, Evaluation of the potential of tool materials for the cold forming of advanced high strength steels, Wear, 302 (**2013**), 1279–1285, doi:10.1016/j.wear.2013.01.001

[2] B. Podgornik, S. Hogmark, Surface modification to improve friction and galling properties of forming tools, Journal of Materials Processing Technology, 174 (**2006**), 334–341, doi:10.1016/j.jmatprotec.2006.01.016

[3] C. Mitterer, F. Holler, C. Lugmair, R. Nobauer, R. Kullmer, C. Teichert, Optimization of plasma-assisted chemical vapour deposition hard coatings for their application in aluminium die-casting, Surface and Coatings Technology, 142-144 (**2001**), 1005–1011, doi:10.1016/S0257-8972(01)01065-9

[4] A. Attanasio, E. Ceretti, C. Giardini, L. Mazzoni, Asymmetric two points incremental forming: Improving surface quality and geometric accuracy by tool path optimization, Journal of Materials Processing Technology, 197 (**2008**), 59–67, doi:10.1016/j.jmatprotec.2007.05.053

[5] A. Persson, J. Bergstrom, S. Hogmark, Influence of surface engineering on the performance of tool steels for die casting, 6th International Tooling Conference, Karlstad, Sweden, 2002, 841–854

[6] R. Jervis, B. Johnson, L. A. Norstrom, O. Sandberg, Properties profile of a new presswork tool steel, International Conference on Tooling Materials, Interlaken, Switzerland, 1992, 49–64

[7] B. Podgornik, S. Hogmark, O. Sandberg, Influence of surface roughness and coating type on the galling properties of coated forming tool steel, Surface and Coatings Technology, 184 (**2004**), 338–348, doi:10.1016/j.surfcoat.2003.11.002

[8] D. Wang, H. Li, H. Yang, J. Ma, G. Li, Tribological evaluation of surface modified H13 tool steel in warm forming of Ti–6Al–4V titanium alloy sheet, Chinese Journal of Aeronautics, 27 (**2014**), 1002–1009, doi:10.1016/j.cja.2014.03.030

[9] S. R. Schmid, W. R. D. Wilson, Tribology in manufacturing, In: B. Bhushan (Ed.), Modern Tribology Handbook, CRC Press, NY 2000

[10] S. Gulizia, M. Z. Jahedi, Evaluation of PVD coatings for industrial applications, 6th International Tooling Conference, Karlstad, Sweden, 2002, 739–748

[11] Y. Hou, W. Zhang, Z. Yu, S. Li, Selection of tool materials and surface treatments for improved galling performance in sheet metal forming, The International Journal of Advanced Manufacturing Technology, 43 (**2009**), 1010–1017, doi:10.1007/s00170-008-1780-2

[12] B. Bhushan, B. K. Gupta, Handbook of Tribology: Materials, Coatings and Surface Treatments, McGraw-Hill, NY 1991

[13] H. Paschke, M. Weber, G. Braeuer, T. Yilkiran, B. A. Behrens, H. Brand, Optimized plasma nitriding processes for efficient wear reduction of forging dies, Archives of Civil and Mechanical Engineering, 12 (**2012**), 407–412, doi:10.1016/j.acme.2012.06.001

[14] S. J. Bull, R. I. Davidson, E. H. Fisher, A. R. McCabe, A. M. Jones, A simulation test for the selection of coatings and surface treatments for plastics injection moulding machines, Surface and Coatings Technology, 130 (**2000**), 257–265, doi:10.1016/S0257-8972(00)00697-6

[15] B. Podgornik, V. Leskovšek, J. Vizintin, Influence of deep-cryogenic treatment on tribological properties of P/M high-speed steel, Materials and Manufacturing Processes, 24 (**2009**), 734–738, doi:10.1080/10426910902809339

[16] B. Podgornik, F. Majdic, V. Leskovsek, J. Vizintin, Improving tribological properties of tool steels through combination of deep-cryogenic treatment and plasma nitriding, Wear, 288 (**2012**), 88–93, doi:10.1016/j.wear.2011.04.001

[17] K. L. Rutherford, S. J. Bull, E. D. Doyle, I. M. Hutchings, Laboratory characterisation of the wear behaviour of PVD-coated tool steels and correlation with cutting tool performance, Surface and Coatings Technology, 80 (**1996**), 176–180, doi:10.1016/0257-8972(95)02706-8

[18] M. Stoiber, M. Panzenbock, C. Mitterer, C. Lugmair, Fatigue properties of Ti-based hard coatings deposited onto tool steels, Surface and Coatings Technology, 142–144 (**2001**), 117–124, doi:10.1016/S0257-8972(01)01220-8

[19] B. Podgornik, S. Hogmark, O. Sandberg, V. Leskovsek, Wear resistance and anti-sticking properties of duplex treated forming tool steel, Wear, 254 (**2003**), 1113–1121, doi:10.1016/S0043-1648(03)00322-3

[20] V. Imbeni, C. Martini, E. Lanzoni, G. Poli, I. M. Hutchings, Tribological behaviour of multi-layered PVD nitride coatings, Wear, 251 (**2001**), 997–1002, doi:10.1016/S0043-1648(01)00706-2

[21] J. Heinrichs, S. Jacobson, Mechanisms of Transfer of Aluminium to PVD-Coated Forming Tools, Tribology Letters, 46 (**2012**), 299–312, doi:10.1007/s11249-012-9952-5

[22] C. Donnet, A. Erdemir, Tribology of diamond-like carbon films: Fundamentals and Applications, Springer, 2008

[23] B. Podgornik, J. Vižintin, O. Wänstrand, M. Larsson, S. Hogmark, H. Ronkainen, K. Holmberg, Tribological properties of plasma nitrided and hard coated AISI 4140 steel, Wear, 249 (**2001**), 254–259, doi:10.1016/S0043-1648(01)00564-6

[24] I. Ebrahimzadeh, F. Ashrafizadeh, High temperature wear and frictional properties of duplex-treated tool steel sliding against a two phase brass, Ceramics International, 40 (**2014**), 16429–16439, doi:10.1016/j.ceramint.2014.07.151

[25] B. Podgornik, J. Vizintin, S. Hogmark, Improvement in galling performance through surface engineering, Surface Engineering, 22 (**2006**), 235–238, doi:10.1179/174329406X122946

[26] B. Podgornik, J. Jerina, Surface topography effect on galling resistance of coated and uncoated tool steel, Surface and Coatings Technology, 206 (**2012**), 2792–2800, doi:10.1016/j.surfcoat.2011.11.041

[27] J. A. Schey, Tribology in Metalworking: Friction, Lubrication and Wear, ASM, Ohio 1984

[28] C. Subramanian, K. N. Strafford, T. P. Wilks, L. P. Ward, On the design of coated systems: metallurgical and other considerations, Journal of Materials Processing Technology, 56 (**1996**), 385–397, doi:10.1016/0924-0136(95)01852-2

[29] L. Norstrom, B. Johansson, Selection of tool steels for cold-work applications, International Conference on Tooling, Bochum, Germany, 1989, 193–208

[30] A. Gåård, Influence of tool microstructure on galling resistance, Tribology International, 57 (**2013**), 251–256, doi:10.1016/j.triboint.2012.08.022

[31] R. Seidel, H. Luig, Friction and wear processes in hot die forging, International Conference on Tooling Materials, Interlaken, Switzerland, 1992, 467-480

[32] O. Barrau, C. Boher, C. Vergne, F. Rezai-Aria, Investigations on friction and wear mechanisms of hot forging tool steels, 6th International Tooling Conference, Karlstad, Sweden, 2002, 81–94

[33] P. Carlsson, M. Olsson, PVD coatings for sheet metal forming processes – a tribological evaluation, Surface and Coatings Technology, 200 (**2006**), 4654–4663, doi:10.1016/j.surfcoat.2004.10.127

[34] H. Paschke, M. Weber, P. Kaestner, G. Braeuer, Influence of different plasma nitriding treatments on the wear and crack behavior of forging tools evaluated by Rockwell indentation and scratch tests, Surface and Coatings Technology, 205 (**2010**), 1465–1469, doi:10.1016/j.surfcoat.2010.07.053

[35] B. Podgornik, J. Vižintin, Galling properties of forming tool steels - How to determine and improvements through surface engineering, International Conference on Tribology in Manufacturing Processes, Yokohama, Japan, 2007, 195–202

[36] A. Gåård, R. M. Sarih, Influence of Tool Material and Surface Roughness on Galling Resistance in Sliding Against Austenitic Stainless Steel, Tribology Letters, 46 (**2012**), 179–185, doi:10.1007/s11249-012-9934-7

[37] M. Geiger, U. Popp, U. Engel, Excimer Laser Micro Texturing of Cold Forging Tool Surfaces - Influence on Tool Life, Manufacturing Technology, 51 (**2002**), 231–234, doi:10.1016/S0007-8506(07)61506-6

[38] T. D. Ling, P. Liu, S. Xiong, D. Grzina, J. Cao, Q. J. Wang, Z. C. Xia, R. Talwar, Surface Texturing of Drill Bits for Adhesion Reduction and Tool Life Enhancement, Tribology Letters, 52 (**2013**), 113–122, doi:10.1007/s11249-013-0198-7

[39] B. Podgornik, M. Sedlaček, Performance, characterization and design of textured surfaces, Journal of Tribology, 134 (**2012**), 041701/1–041701/7, doi:10.1115/1.4007108

[40] L. Lu, Q. M. Wang, B. Z. Chen, Y. C. Ao, D. H. Yu, C. Y. Wang, S. H. Wu, K. H. Kim, Microstructure and cutting performance of CrTiAlN coating for high-speed dry milling, Transactions of Nonferrous Metals Society of China, 24 (**2014**), 1800–1806, doi:10.1016/S1003-6326(14)63256-8

[41] B. Podgornik, S. Hogmark, O. Sandberg, Proper coating selection for improved galling performance of forming tool steel, Wear, 261 (**2006**), 15–21, doi:10.1016/j.wear.2005.09.005

[42] A. Ghiotti, S. Bruschi, Tribological behaviour of DLC coatings for sheet metal forming tools, Wear, 271 (**2011**), 2454–2458, doi:10.1016/j.wear.2010.12.043

[43] T. Horiuchi, S. Yoshihara, Y. Iriyama, Dry deep drawability of A5052 aluminum alloy sheet with DLC-coating, Wear, 286–287 (**2012**), 79–83, doi:10.1016/j.wear.2011.07.005

[44] J. Heinrichs, M. Olsson, S. Jacobson, Initiation of Galling in Metal Forming: Differences Between Aluminium and Austenitic Stainless Steel Studied In Situ in the SEM, Tribology Letters, 50 (**2013**), 431–438, doi:10.1007/s11249-013-0139-5

[45] J. Heinrichs, S. Jacobson, Mechanisms of Transfer of Aluminium to PVD-Coated Forming Tools, Tribology Letters, 46 (**2012**), 299–312, doi:10.1007/s11249-012-9952-5

[46] G. Hakansson, Experiences of surface coated tools, International Conference on Recent Advances in Manufacture & Use of Tools & Dies and Stamping of Steel Sheets, Olofstrom, Sweden, 2004, 245–254

[47] B. Podgornik, J. Vižintin, V. Leskovšek, O. Wänstrand, M. Larsson, S. Hogmark, Wear properties of plasma nitrided and hard coated 42CrMo4 steel, Mater. Tehnol., 34 (**2000**) 1–2, 17–21

[48] B. Podgornik, B. Zajec, N. Bay, J. Vižintin, Application of hard coatings for blanking and piercing tools, Wear, 270 (**2011**), 850–856, doi:10.1016/j.wear.2011.02.013

[49] P. Jurči, B. Šuštaršič, V. Leskovšek, Fracture characteristics of the Cr-V ledeburitic steel Vanadis 6, Mater. Tehnol., 44 (**2010**) 2, 77–84

[50] P. Karlsson, A. Gåård, P. Krakhmalev, Influence of tool steel microstructure on friction and initial material transfer, Wear, 319 (**2014**), 12–18, doi:10.1016/j.wear.2014.07.002

[51] B. Podgornik, M. Sedlaček, V. Leskovšek, Surface engineering of fine blanking tool inserts, Project report, Institute of Metals and Technology, Ljubljana, 2014

[52] B. Podgornik, V. Leskovšek, B. Arh, The effect of heat treatment on the mechanical, tribological and load-carrying properties of PACVD-coated tool steel, Surface and Coatings Technology, 232 (**2013**), 528–534, doi:10.1016/j.surfcoat.2013.06.019

[53] B. Podgornik, V. Leskovšek, F. Tehovnik, J. Burja, Vacuum heat treatment optimization for improved load carrying capacity and wear properties of surface engineered hot work tool steel, Surface and Coatings Technology, 261 (**2015**), 253–261, doi:10.1016/j.surfcoat.2014.11.021

[54] M. Çöl, D. Kir, E. Erişir, Wear and blanking performance of AlCrN PVD-coated punches, Materials Science, 48 (**2013**), 514–520

[55] M. Bayramoglu, H. Polat, N. Geren, Cost and performance evaluation of different surface treated dies for hot forging process, Journal of Materials Processing Technology, 205 (**2008**), 394–403, doi:10.1016/j.jmatprotec.2007.11.256

[56] V. Leskovšek, B. Podgornik, M. Jenko, A PACVD duplex coating for hot-forging applications, Wear, 266 (**2009**), 453–460, doi:10.1016/j.wear.2008.04.016

[57] E. Doege, E. Westkamper, R. Seidel, C. Romanowski, G. Andreis, O. Morlok, Combined surface treatment of forging tools by plasma nitriding and PACVD, Progress in tool steels, Bochum, Germany, 1996, 373–384

[58] P. Panjan, I. Urankar, B. Navinšek, M. Terčelj, R. Turk, M. Čekada, V. Leskovšek, Improvement of hot forging tools with duplex treatment, Surface and Coatings Technology, 151–152 (**2002**), 505–509, doi:10.1016/S0257-8972(01)01634-6

[59] V. Leskovšek, B. Podgornik, Multi-functional KIc-test specimen for the assessment of different tool- and high-speed-steel properties, Mater. Tehnol., 47 (**2013**) 3, 273–283

UDK 677.017:519.233.4
Original scientific article/Izvirni znanstveni članek

ISSN 1580-2949
MTAEC9, 49(3)325(2015)

PREDICTING THE PHYSICAL PROPERTIES OF DRAWN NYLON-6 FIBERS USING AN ARTIFICIAL-NEURAL-NETWORK MODEL

NAPOVEDOVANJE FIZIKALNIH LASTNOSTI VLEČENIH VLAKEN IZ NAJLONA 6 Z UPORABO MODELA UMETNE NEVRONSKE MREŽE

Ruhollah Semnani Rahbar[1], Morteza Vadood[2]

[1]Department of Textile and Leather, Faculty of Chemistry and Petrochemical Engineering, Standard Research Institute (SRI), Karaj, P. O. Box 31745-139, Iran
[2]Department of Textile Engineering, Amirkabir University of Technology, Tehran, Iran
semnani@standard.ac.ir

Prejem rokopisa – received: 2013-08-13; sprejem za objavo – accepted for publication: 2014-07-11

doi:10.17222/mit.2013.128

Low-oriented nylon-6 fibers were drawn in a multistage drawing process, during which the number of drawing steps and the temperature of each step were changed. The physical properties of these fibers were measured and compared with the values predicted by a multiple-linear-regression model. Moreover, six input variables and four output variables were used in an artificial neural network (ANN) to establish the logical relationships between the inputs and outputs. Attempts were also made to determine the effective parameters for each physical property and explain the observed trends. The results showed that the models based on the ANN performed well and provided stable responses in predicting combined interactions between independent variables.

Keywords: drawing process, artificial neural network, modeling, physical properties

Malo orientirana vlakna najlon 6 so bila vlečena z večstopenjskim postopkom, pri čemer se je pri vsakem vleku spreminjala stopnja vlečenja in temperatura. Izmerjene vrednosti teh vlaken so bile primerjane z vrednostmi, napovedanimi z modelom multivariantne linearne regresije. Poleg tega je bilo v umetni nevronski mreži (ANN) uporabljenih šest vhodnih spremenljivk in štiri izhodne, da bi ugotovili logične odvisnosti med vhodnimi in izhodnimi spremenljivkami. Poskušalo se je ugotoviti učinkovite parametere za vsako fizikalno lastnost in razložiti opažene tendence. Rezultati so pokazali, da so modeli na osnovi ANN dobri in ponujajo stabilne odgovore pri predvidevanju kombiniranih interakcij neodvisnih spremenljivk.

Ključne besede: postopek vlečenja, umetna nevronska mreža, modeliranje, fizikalne lastnosti

1 INTRODUCTION

Synthetic-fiber drawing is a critical process to obtain fibers with desired properties for final applications. There are various parameters in this process that should be controlled to yield a fiber with acceptable technical specifications. These variables include the draw ratio, the drawing temperature, the number of drawing steps, the drawing speed and the distribution of draw ratio in the multistage drawing[1]. Because of the complex relationships between the fiber properties and the drawing-process variables, there is a need for a sound experimental design and a careful analysis of the experimental results. In this way, the relationships between a measured characteristic of a drawn fiber and the influencing factors can be identified and optimized. The understanding of these relationships reduces the processing cost and provides for reproducibility in a day-to-day production. Moreover, the risk of excessive downtime for trials is reduced[2–5].

Due to their simplicity, regression-based models and statistical analyses were extensively used to solve textile technological problems[2–4,6–9]. However, they have certain limitations as they require a specialized knowledge of both the statistical methods and techniques of experimental design. Moreover, the prediction ability of the regression analysis may be limited in the case of an analysis of multidimensional technical problems[10,11].

In recent years, artificial neural network (ANN) has been used as an alternative modeling method in many different engineering fields to predict the properties of materials. ANN can be considered as a black box consisting of a series of complex equations for estimating the outputs on the basis of a given series of input values. The advantage of ANNs is the ability of representing complex relationships directly from the data being modeled, while their representation (modeling) is always nonlinear[12–14].

Many researches were done in the textile industry to predict the properties of yarns, woven and nonwoven fabrics and many other characteristics of textile materials[10,13–25]. Among these, just few studies are devoted to melt spinning and drawing of synthetic fibers. It seems that there is a lack of information concerning the appli-

cation of ANN for predicting fiber properties during multistage drawing. Therefore, in this paper, an ANN model was used to predict some physical properties of drawn nylon-6 fibers upon multistage drawing.

2 EXPERIMENTAL WORK

2.1 Materials and methods

A low-oriented nylon-6 multifilament yarn, 340 dtex, 24 filaments, was kindly supplied by Alyaf Co. (Iran). Nylon 6 (polyamide 6) is made up of linear macromolecules whose structural units are linked with an amide linkage (-NH-CO-group). This synthetic fiber is used for a variety of different applications ranging from garments to industrial usages.

Fiber samples were prepared by melt spinning and the take-up speed of 800 m/min. The undrawn multifilament yarn had a polymerization degree of 148. The drawing process was performed on an industrial Zinser draw-twisting machine (Germany), type 520-2. The details of the drawing process were explained in the previous work[26]. The fixed drawing conditions are listed in **Table 1**.

Table 1: Fixed operating conditions of the drawing experiments
Tabela 1: Pogoji obratovanja pri preizkusih vlečenja

Temperature of the feeding roller (°C)	Temperature of the third godet roller (°C)	Drawing speed (m/min)	Intermingling jet pressure (bar)	Spindle speed (r/min)
Room temperature	Room temperature	400	2	4000

Six process parameters of drawing trials included the first-stage draw ratio (*FSDR*), the second-stage draw ratio (*SSDR*), the third-stage draw ratio (*TSDR*), the first-godet temperature (*FGT*), the block-heater temperature (*BHT*), and the second-godet temperature (*SGT*). In the trials, one-, two- and three-stage drawn fibers and also the fiber heat-treated without drawing were produced to have a broad range of fibers with different structures. A total of 61 different fibers were prepared and the drawing trials are reported in **Table 2**.

Table 2: Experimental array for the drawing process
Tabela 2: Pogoji eksperimenta pri postopku vlečenja

Run	First-stage draw ratio, *FSDR*	Second-stage draw ratio, *SSDR*	Third-stage draw ratio, *TSDR*	First-godet temperature (°C), *FGT*	Block-heater temperature (°C), *BHT*	Second-godet temperature (°C), *SGT*
1	1.1	4.126	1.3	100	170	170
2	2.098	1.611	1.626	100	170	170
3	2.8	1.621	1.3	100	170	170
4	1.755	1.5	1.3	100	170	170
5	1.755	2.586	1.3	100	170	170
6	1.615	1.884	1.939	100	170	170
7	1.1	2.488	1.3	100	170	170
8	1.1	2.551	2.102	100	170	170
9	1.1	1.5	1.3	100	170	170
10	1.315	2.074	1.564	100	170	170
11	1.755	1.97	1.3	100	170	170
12	1.348	1.611	2.53	100	170	170
13	1.8	1.5	2.185	100	170	170
14	1.1	1.5	2.102	100	170	170
15	1.1	1.5	3.4	100	170	170
16	1.637	1.5	1.792	150	170	170
17	1.1	1.739	2.3	150	170	170
18	1.1	1.5	1.729	150	150	150
19	1.1	1.615	2.3	30	30	30
20	1.1	3.077	1.3	150	150	150
21	1.1	2.313	1.729	30	170	170
22	1.253	1.975	1.676	60	80	80
23	1.1	3.077	1.3	90	170	170
24	2.1	1.612	1.3	150	170	170
25	1.1	1.5	1.3	30	30	30
26	1.1	1.5	1.3	30	170	170
27	1.1	2.148	1.3	150	150	150
28	1.1	1.5	1.3	90	90	90
29	2.1	1.5	1.397	30	30	30
30	1.1	3.077	1.3	30	170	170
31	1.637	1.5	1.792	30	170	170
32	1.275	1.5	2.3	30	100	100
33	1.52	1.5	1.3	30	170	170
34	1.732	1.591	1.506	90	110	110
35	1.52	2.227	1.3	30	30	30
36	1.1	1.5	1.3	150	170	170
37	2.1	1.612	1.3	30	170	170
38	1.1	1.5	2.3	30	170	170
39	1.1	3.077	1.3	30	30	30
40	1.637	1.5	1.792	30	30	30
41	1.275	1.5	2.3	90	90	90
42	1.1	1.5	1	100	170	170
43	1.1	4.2	1	100	170	170
44	1.1	4.2	1.3	100	170	170
45	2.8	1	1	30	30	30
46	2.8	1	1	100	30	30
47	1.1	4.126	1.3	100	30	170
48	1.1	4.126	1.3	100	60	170
49	1.1	4.126	1.3	100	100	170
50	1.1	4.126	1.3	100	150	170
51	1.008	4.6	1	100	170	170
52	1.1	4.215	1	100	170	170
53	1.1	3.242	1.3	100	170	170
54	2.8	1.648	1.3	100	170	170
55	2.8	1.506	1.3	100	170	170
56	1.187	1.5	2.5	30	30	30
57	2.1	1.564	1.3	30	30	30
58	1.579	1.5	1.879	30	30	30
59	1.1	1	1	30	30	30
60	1.1	1	1	100	30	30
61	1	1	1	100	30	30

The yarn linear density (expressed in dtex) was determined in accordance with ASTM D 1577-96. The mean value is the average of five measurements.

Stress-strain curves were obtained with an EMT-3050 tensile testing machine (Elima Co., Iran). The initial lengths of the fibers and cross-head speeds were 300 mm and 500 mm/min, respectively. From the stress-strain plots, the initial modulus, the tenacity and the specific work of rupture were evaluated. The reported values for all the mechanical properties were averaged over at least ten independent measurements.

Yarn-shrinkage measurements were made according to DIN 53840 at 130 °C for 10 min. The initial and final lengths were measured at room temperature and the total shrinkage was defined as the fraction of the initial sample length remaining after the exposure to the elevated temperature. The reported values are the average of eight tests.

2.2 Artificial neural network

Neural networks are mainly composed of the processing elements called neurons with interconnections. The exclusive structure of an ANN makes it very appropriate for modeling a complex system with nonlinear relations between the parameters. Generally, an ANN can be made of many layers, namely the input, output and several hidden layers. The neurons in each layer are connected with the associated weights to the other neurons in the next layer. The input layer receives the input parameters and, through the hidden layers based on Equation (1), the output can be calculated in the output layer[19]. **Figure 1** indicates the topology of an ANN with one hidden layer:

$$y_k = f\left(\sum_{j=1}^{m} w_{jk} f\left(\sum_{i=1}^{n} w_{ij} x_i + b_{1j}\right) + b_{2k}\right) \quad (1)$$

Here w_{ij}, w_{jk}, b_{1j} and b_{2k} are the weight between the ith input neuron and the jth hidden neuron, the weight between the jth hidden neuron and the kth output neuron, the bias for the jth hidden neuron and the bias for the kth output neuron, respectively. The $f(x)$ is the activation function[27,28]. All the data is divided into three groups known as the training, validation and testing sets. The first group is used to train the ANN. When the network begins to overfit the data, the training is stopped for a specified number of iterations (maximum number of fails) and the weights and biases are returned with the minimum error on the validation set. The testing group is used to control the error after the training process[21]. In this study, to apply ANNs, the Matlab R2008 software was used. The ANNs were trained on the basis of the error back-propagation algorithm using the "Trainlm" function to avoid an over-fitting error. The activation functions for all the hidden and output layers were considered as the hyperbolic tangent and linear function, respectively (this type of ANN is called the perceptron).

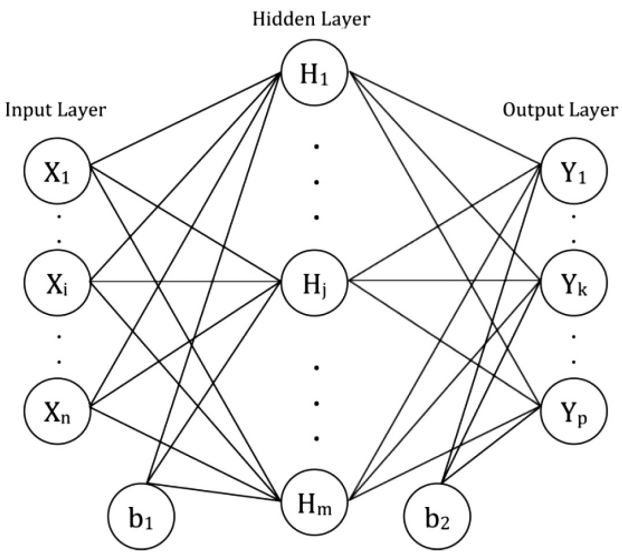

Figure 1: ANN with one hidden layer
Slika 1: ANN z eno skrito plastjo

3 RESULTS AND DISCUSSION

3.1 Linear regression model

In this research, multiple linear regression (MLR) was employed to evaluate the performance of different models. In order to determine the variables that can directly affect the physical properties, as well as decreasing the number of variables, a traditional linear-regression model at the 90 % confidence level was accomplished. This procedure was only used for three variables including the *FSDR*, *SSDR* and *TSDR* because they were varied at multiple levels. The *FSDR*, *SSDR* and *TSDR* were changed at the 18th, 21st and 17th levels, respectively. Moreover, theses parameters were individually considered with respect to the responses of the linear-regression model. **Table 3** shows the Pearson correlation coefficient (*PCC*) and the corresponding *P*-value between the measured parameters (*FSDR*, *SSDR* and *TSDR*) and the physical properties.

Table 3: *PCC* and *P*-value between the measured parameters and physical properties
Tabela 3: *PCC* in *P*-vrednost med izmerjenimi parametri in fizikalnimi lastnostmi

	Shrinkage		Specific work of rupture		Tenacity		Initial modulus	
	PCC	*P*-value	*PCC*	*P*-value	*PCC*	*P*-value	*PCC*	*P*-value
FSDR	0.23	0.08	–0.25	0.05	0.23	0.08	0.25	0.06
SSDR	–0.19	0.14	–0.49	0.00	0.59	0.00	0.31	0.01
TSDR	0.38	0.00	–0.32	0.01	0.14	0.29	0.36	0.00

The *PCC* varies between –1 and 1; the more absolute value of the *PCC* indicates the existence of a strong relation between two parameters. *P*-values are used for testing the hypothesis of no correlation. Each *P*-value is the probability of getting a correlation as large as the observed value by random chance when the true correlation is zero. If a *P*-value is less than 0.1, the corresponding

correlation is significant. But the data for the *FGT*, *BHT* and *SGT* were different and they were varied only at the 5th, 9th and 7th levels, respectively. Hence, a one-way ANOVA was used to evaluate their effects on the physical properties and the results are listed in **Table 4**. The confidence level was 90 %. As mentioned before, the parameters with the *P*-value below 0.1 have a significant effect on the physical parameters. The greater the *F*-value, the greater are the influence and the relevance of the source factor.

Table 4: ANOVA results identifying the statistical significance of *FGT*, *BHT*, and *SGT* for the physical properties

Tabela 4: Rezultati ANOVA prikazujejo statistično pomembnost *FGT*, *BHT* in *SGT* na fizikalne lastnosti

		Shrinkage	Specific work of rupture	Tenacity	Initial modulus
FGT	*SSE*	103.202	62.662	4003.172	386497.497
	DF	4.000	4.000	4.000	4.000
	MSE	25.801	15.665	1000.793	96624.374
	F	3.480	0.703	5.435	2.339
	P	0.013	0.593	0.001	0.066
BHT	*SSE*	185.671	240.453	3159.013	710707.421
	DF	8.000	8.000	8.000	8.000
	MSE	23.209	30.057	394.877	88838.428
	F	3.627	1.461	1.841	2.323
	P	0.002	0.194	0.090	0.033
SGT	*SSE*	176.808	235.435	3412.317	694829.932
	DF	6.000	6.000	6.000	6.000
	MSE	29.468	39.239	568.720	115804.989
	F	4.659	1.971	2.817	3.119
	P	0.001	0.086	0.019	0.011

SSE: sum of squares, *DF*: degree of freedom, *MSE*: mean squared error, *F*: *F*-statistic (the ratio of the mean squares), *P*: *P*-value

According to **Tables 3** and **4**, the effective factors for each physical property were determined and shown in **Table 5**.

Table 5: Parameters affecting the physical properties

Tabela 5: Parametri, ki učinkujejo na fizikalne lastnosti

	Shrinkage	Specific work of rupture	Tenacity	Initial modulus
FSDR	+	+	+	+
SSDR	–	+	+	+
TSDR	+	+	–	+
FGT	+	–	+	+
BHT	+	–	+	+
SGT	+	+	+	+

+ : effective, – : non-effective

After determining the effective parameters, multiple-linear-regression (MLR) analyses based on **Table 5** were performed. The results (**Figure 2**) indicated that the developed MLR models provided different predictions for the physical properties.

According to **Figure 2**, MLR can predict the specific work of rupture and the shrinkage with the highest and

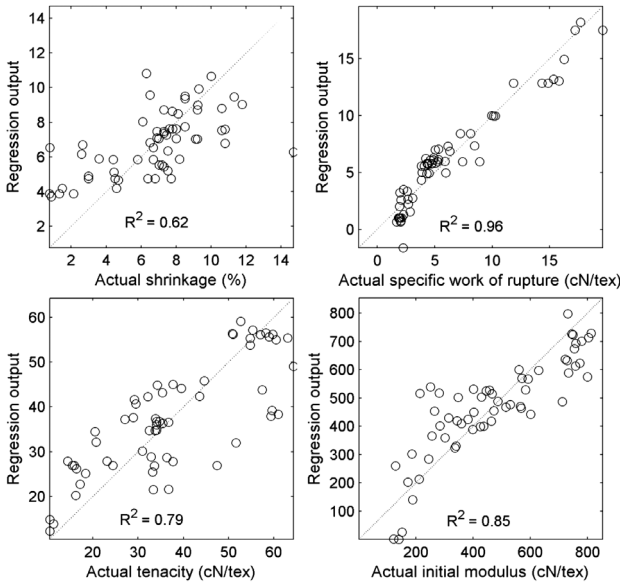

Figure 2: Results of the MLR prediction for various physical properties ($R^2 = PCC$)

Slika 2: Rezultati MLR-napovedovanja različnih fizikalnih lastnosti ($R^2 = PCC$)

the lowest accuracies, respectively. **Table 6** shows the coefficients of MLR for predicting physical properties. Actually, each coefficient in MLR is a partial derivative of the model response with respect to the variable of that coefficient. So, the contribution of each variable in predicting the model response can be assessed by checking the coefficient values.

Referring to **Table 6**, the *TSDR* and the *SGT* have the highest and the lowest effects on the shrinkage, respectively. A similar trend was observed for the specific work of rupture. Moreover, for the tenacity and the initial modulus, the *FSDR* and the *TSDR* play the main roles, respectively. Also, the *BHT* and the *FGT* have the lowest effects on the tenacity and the initial modulus, respectively. Although increasing the order of the regression equation gives better results, it makes the regression equation more complicated. For example, using a quadratic regression including linear, interaction and square terms to predict the initial modulus increases the number of coefficients up to 28. Therefore, using an ANN model in this situation can be very beneficial. The ANN contains various parameters such as the number of hidden layers and the number of neurons in each hidden layer that directly affect the output of the ANN. Hence, to determine the best set of the ANN parameters, the trial-and-error method was applied. The numbers of hidden layers and neurons in each hidden layer were considered to be between 1 to 5 and 1 to 6, respectively. In this study the stopping criteria for the ANN training were the following three options: the training tolerance level (0), the maximum number of fails (6 iterations) or the total number of iterations for training (1000 iterations). The experimental data were used to train the network; 37, 12 and 12 data sets were randomly chosen for the training,

validation and testing groups, respectively. To evaluate the accuracy of the developed ANN, the absolute value of the *PCC* between the ANN outputs and the actual values for the testing set was calculated. A higher *PCC* indicates a higher accuracy of the ANN. To remove the effects of the initial weights and biases on the ANN output, each ANN structure was created five times with the weights and biases chosen randomly and the ANN with the highest absolute value of the *PCC* was considered for that structure.

Table 6: Coefficients of MLR models for predicting the physical properties
Tabela 6: Koeficienti MLR-modela za napovedovanje fizikalnih lastnosti

	Shrinkage	Specific work of rupture	Tenacity	Initial modulus
Constant	1.777	36.461	–14.612	–697.759
FSDR	1.688	–6.795	15.768	251.684
SSDR	–	–4.518	10.865	115.788
TSDR	2.899	–6.892	–	270.758
FGT	0.008	–	–0.014	0.347
BHT	–0.023	–	–0.010	–1.231
SGT	0.003	–0.002	0.065	2.084

Unlike the regression method, an ANN can predict physical properties simultaneously with four neurons in the output layer, but such results showed an insufficient accuracy. In this way the prediction ability of an ANN for each output neuron only involves the weights between the last hidden layer and the output layer; so, considering separate ANNs for each physical property (one neuron in the output layer) would give a higher accuracy in the prediction. As the ANN calculations using computers can be performed quickly, to consider all the terms of the effects, such as linear terms or interactions, all the input parameters were considered for the ANN models. As expected, it was found that the structure of the neural network for each physical property was different and exhibited a high prediction performance of the models in terms of the *PCC*, as given in **Table 7**. The individual values of the predictions of the models, along with the experimental values, are shown in **Figure 3**. By comparing **Table 7** and **Figure 2**, it can be found that the prediction potential of the ANN models is superior to that of the MLR. This means that removing some input variables could not enhance the quality of the MLR predictions as compared to the ANN models.

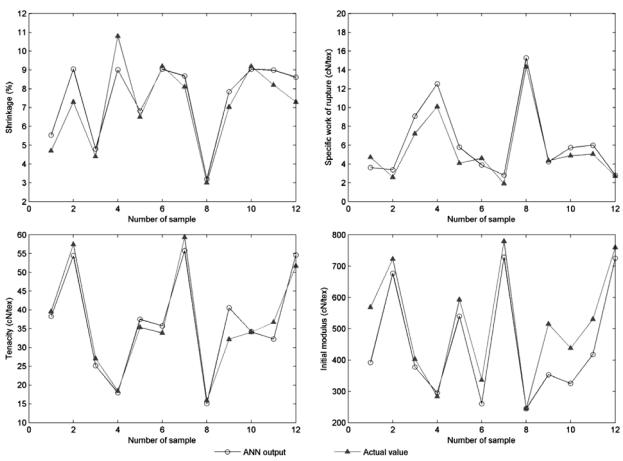

Figure 3: Predictions of ANN models for the testing group
Slika 3: Napovedi ANN-modelov za preizkušeno skupino

Table 7: Best ANN structure for predicting various mechanical properties
Tabela 7: Najboljša struktura ANN za napovedovanje različnih mehanskih lastnosti

Physical property	Maximum *PCC*	Hidden layer
Shrinkage	0.9182	[1-1-2]
Specific work of rupture	0.9907	[3]
Tenacity	0.981	[3-4-2]
Initial modulus	0.9917	[2-1-3]

In **Table 7**, [1-1-2] in the hidden-layer column means that the ANN contains three hidden layers with 1, 1 and 2 neurons in the first, second and third hidden layers, respectively. As can be seen in **Figure 2**, the *PCC* value for the specific work of rupture modeled with MLR is 0.96, indicating that the relation between this parameter and its effective variables is not complicated. Also, according to **Table 7**, a simple ANN can model the specific work of rupture with the *PCC* value of almost 1 which indicates a perfect prediction. As observed from **Table 7**, there is an increase in the *PCC* values for the shrinkage, tenacity and initial modulus compared to the values of the MLR predictions as shown in **Figure 2**. This means that the relations between the parameters are no longer linear and the MLR prediction is not reliable any more, whereas the ANN using multilayers could predict these responses very well.

3.2 Sensitivity analysis of the ANN model

Because of the complex and nonlinear form of the ANN analysis, a sensitivity analysis was conducted to study the influence of the input variables on the output. As a matter of fact, the aim of this analysis was to evaluate the effects of the changes in each input on the ANN output. In this process, the value of one input variable from the initial condition is slightly changed (10–50 %) and then the output value is predicted, while all the other variables are set to the selected constant values. This process is repeated for all the input variables. The robustness of the model is determined by examining how well the predictions compare with the available structural knowledge. **Figure 4** shows the effects of the changes in the input variables from –50 % to +50 % in the scale of 0.1 for the physical properties. It is evident from **Figure 4a** that the shrinkage initially increases with the *TSDR* and then reaches a constant value as the *TSDR* moves toward higher values. The changes in the other input variables have no significant

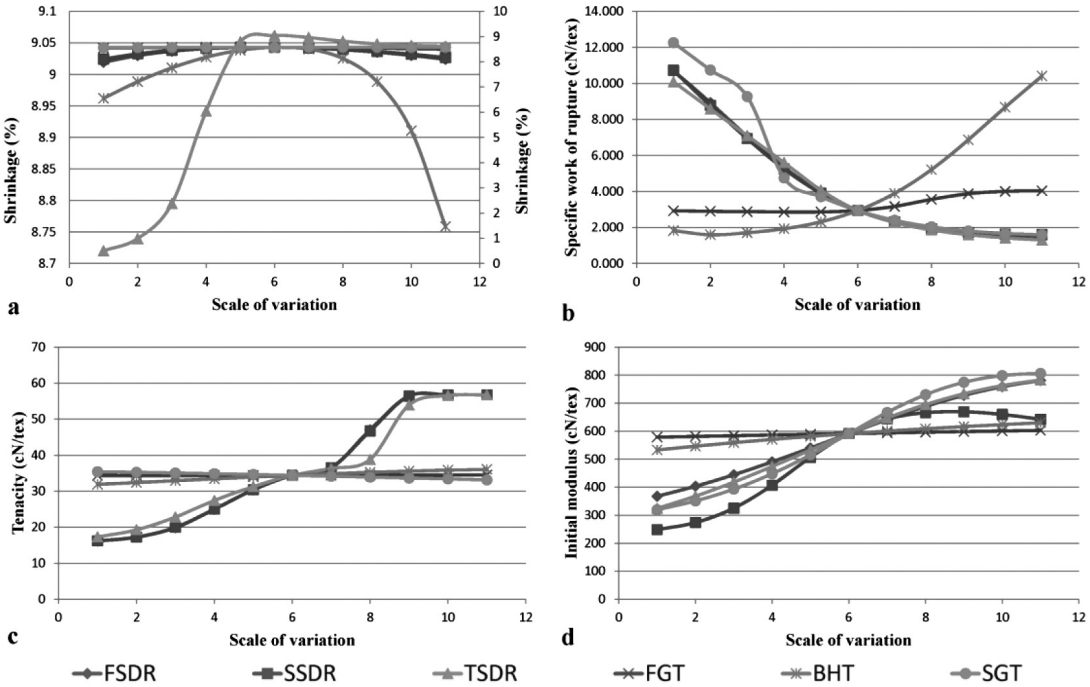

Figure 4: Effects of the changing input variables on the mechanical properties: a) shrinkage, b) specific work of rupture, c) tenacity, d) initial modulus. Since the variation of *TSDR* is higher than the ones of the other parameters, it is shown on the right vertical axis in **Figure 4a**.

Slika 4: Vpliv spremenjenih vhodnih spremenljivk na mehanske lastnosti: a) krčenje, b) specifično delo pri pretrgu, c) trdnost, d) začetni modul. Ker je spreminjanje *TSDR* večje od drugih parametrov, je to prikazano na desni vertikalni osi na **sliki 4a**.

effect on the shrinkage. The internal stress achieved with the third-stage draw ratio increases the fiber shrinkage. This is related to the absence of heat in the third stage of drawing. A further crystallization after a critical *TSDR*, along with an increase in the orientation of the amorphous region, led to a negligible change in the shrinkage value. According to **Figure 4b**, the effects of the *FSDR*, *SSDR* and *TSDR* on the specific work of rupture are the same and the effect of the *SGT* is also very similar to them. By increasing these parameters, a decrease in the specific work of rupture can be achieved. But the *BHT* has an opposite effect on this parameter and an increase in the *BHT* gives rise to an increase in the specific work of rupture. After a critical *BHT*, a reorientation begins which is accompanied by a decrease in the orientation and confirmed by a significant increase in the specific work of rupture. Moreover, the *FGT* has no appreciable effect on the specific work of rupture.

Based on **Figure 4c** and considering the tenacity variation, the variables can be divided into effective/non-effective categories; the *FGT*, *BHT* and *SGT* are categorized as the non-effective group, while the *FSDR*, *SSDR*, and *TSDR* are considered as the effective group. By increasing the values of the effective group, the tenacity increases, and with even higher values the tenacity almost reaches the plateau. As shown in **Figure 4d**, the initial modulus increases due to the increased *FSDR*, *SSDR*, *TSDR* and *SGT*, while the *FGT* and *BHT* have no visible effect on the initial modulus. It seems that the temperature of the block heater mainly affects the crystalline structure of the fibers that restricts the chain orientation in the third stage of drawing. This explains why the initial modulus did not change significantly as the *BHT* increased.

3.3 Important index analysis of the ANN model

To study the contributions of different input variables to the ANN output model, various methods were introduced, like the weights method[29,30]. A modified weights method was introduced by Gevrey et al.[31] and their results are very close to the weights method. In this study, the modified weights method was implemented to determine the percentage contribution of each input variable to the physical properties. Referring to the modified weight method and **Figure 1**, the relative importance (*RI*) is calculated through Equations (2) and (3):

$$Q_j = \frac{\left|w_{ij}\right|}{\sum_{i=1}^{n}\left|w_{ij}\right|}, \; j = 1, 2, ..., m \tag{2}$$

$$RI_i = \frac{\sum_{j=1}^{m} Q_{ij}}{\sum_{j=1}^{m}\sum_{i=1}^{n} Q_{ij}} \times 100 \tag{3}$$

It must be noted that only the first hidden layer is considered in the modified weights method. The *RI* values for all the input variables were obtained and shown in **Figure 5**.

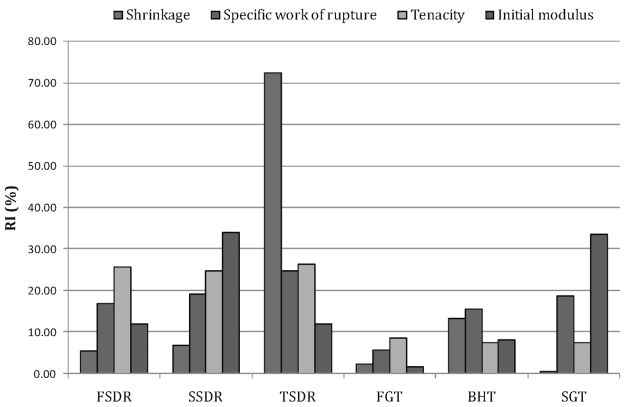

Figure 5: *RI* for all the input variables versus the physical properties
Slika 5: *RI* vseh vhodnih spremenljivk proti fizikalnim lastnostim

Figure 5 indicates that the main effect of the *TSDR* is more pronounced on the shrinkage than the other factors and that among the temperature variables, the *BHT* plays the main role. In the case of the tenacity, although all the draw ratios and temperatures influence this mechanical property, the tenacity of drawn fibers is primarily governed by the draw ratios. The initial modulus and the specific work of rupture correlate with all the variables except for the *FGT*. Among them, the second-stage drawing variables have significant effects on the initial modulus.

4 CONCLUSION

The results of this investigation suggest that an ANN can be used quite effectively for a prediction of the physical properties of drawn fibers. The ANN approach was better at fitting the measured response in comparison to the regression model. According to the obtained results, it can be seen that, though only a limited number of samples were available for the training and testing, the overall prediction capabilities of the models were good and would be very useful for optimizing the hot multi-stage drawing process with regard to the time, quality and price.

Among the variables, the first-godet temperature had no significant effect on the physical properties. The shrinkage was governed by the third-stage draw ratio and the draw ratios were the variables affecting the tenacity. The second-stage drawing variables played the main roles in determining the initial modulus, while the specific work of rupture was governed by the draw ratios and the second-godet temperature.

5 REFERENCES

[1] D. R. Salem (Ed.), Structure formation in polymeric fibers, Hanser Publishers, Munich 2000, 118–184

[2] R. Yang, R. R. Mather, A. F. Fotheringham, Processing, structure, and mechanical properties of as-spun polypropylene filaments – A systematic approach using factorial design and statistical analysis, Journal of Applied Polymer Science, 96 (**2005**) 1, 144–154, doi:10.1002/app.21416

[3] R. Yang, R. R. Mather, A. F. Fotheringham, The influence of processing parameters on the structural and mechanical properties of drawn polypropylene fibres: A factorial design approach, Journal of Applied Polymer Science, 124 (**2012**) 5, 3606-3616, doi:10.1002/app.34738

[4] R. D. Yang, R. R. Mather, A. F. Fotheringham, The application of factorial experimental design to the processing of polypropylene fibres, Journal of Materials Science, 36 (**2001**) 13, 3097–3101, doi:10.1023/A:1017909630132

[5] B. Younes, A. Fotheringham, R. Mather, Statistical analysis of the effect of multi-stage hot drawing on the thermal shrinkage and crystallographic order of biodegradable aliphatic-aromatic co-polyester fibres, Fibers and Polymers, 12 (**2011**) 6, 778–788, doi:10.1007/ s12221-011-0778-9

[6] F. Arain, A. Tanwari, T. Hussain, Z. Malik, Multiple response optimization of rotor yarn for strength, unevenness, hairiness and imperfections, Fibers and Polymers, 13 (**2012**) 1, 118–122, doi:10.1007/s12221- 012-0118-8

[7] K. Yildirim, Y. Ulcay, O. Kopmaz, Forming Regression-based Mathematical Models to Predict PET POY Yarn Properties in the Case of Changing Production Parameters, Textile Research Journal, 80 (**2010**) 5, 411–421, doi:10.1177/0040517509346437

[8] B. Younes, A. Fotheringham, H. M. El-Dessouky, G. Hadda, A Statistical Analysis of the Influence of Multi-Stage Hot-Drawing on the Overall Orientation of Biodegradable Aliphatic-Aromatic Co-Polyester Fibers, Journal of Engineered Fibers and Fabrics, 8 (**2013**) 1, 6–16

[9] M. D. Teli, R. Chakrabarti, Use of Statistical Methods to Understand the Effect of Yarn and Fabric Parameters on Desizing Efficiency, Fibres & Textiles in Eastern Europe, 16 (**2008**) 2, 95–100

[10] L. J. Strumillo, D. Cyniak, J. Czekalski, T. Jackowski, Neural Model of the Spinning Process Dedicated to Predicting Properties of Cotton-Polyester Blended Yarns on the Basis of the Characteristics of Feeding Streams, Fibres & Textiles in Eastern Europe, 16 (**2008**) 1, 28–36

[11] A. Moghassem, A. Fallahpour, M. Shanbeh, An intelligent model to predict breaking strength of rotor spun yarns using gene expression programming, Journal of Engineered Fibers and Fabrics, 7 (**2012**) 2, 1–10

[12] A. A. Gharehaghaji, M. Shanbeh, M. Palhang, Analysis of two modeling methodologies for predicting the tensile properties of cotton-covered nylon core yarns, Textile Research Journal, 77 (**2007**) 8, 565–571, doi:10.1177/0040517507078061

[13] C. F. J. Kuo, K. I. Hsiao, Y. S. Wu, Using neural network theory to predict the properties of melt spun fibers, Textile Research Journal, 74 (**2004**) 9, 840–843, doi:10.1177/004051750407400914

[14] G. Allan, R. Yang, A. Fotheringham, R. Mather, Neural modelling of polypropylene fibre processing: Predicting the structure and properties and identifying the control parameters for specified fibres, Journal of Materials Science, 36 (**2001**) 13, 3113–3118, doi:10.1023/a:1017913731041

[15] G. Yao, J. Guo, Y. Zhou, Predicting the warp breakage rate in weaving by neural network techniques, Textile Research Journal, 75 (**2005**) 3, 274–278, doi:10.1177/004051750507500314

[16] O. Balcı, R. Tuğrul Oğulata, Prediction of the changes on the CIELab values of fabric after chemical finishing using artificial neural network and linear regression models, Fibers Polym, 10 (**2009**) 3, 384–393, doi:10.1007/s12221-009-0384-2

[17] A. Rawal, A. Majumdar, S. Anand, T. Shah, Predicting the properties of needlepunched nonwovens using artificial neural network, Journal of Applied Polymer Science, 112 (**2009**) 6, 3575–3581, doi:10.1002/app.29687

[18] M. M. Yazdi, D. Semnani, M. Sheikhzadeh, Moisture and heat transfer in hybrid weft knitted fabric with artificial intelligence, Journal of Applied Polymer Science, 114 (**2009**) 3, 1731–1737, doi:10.1002/app.30685

[19] M. Vadood, D. Semnani, M. Morshed, Optimization of acrylic dry spinning production line by using artificial neural network and genetic algorithm, Journal of Applied Polymer Science, 120 (**2011**) 2, 735–744, doi:10.1002/app.33252

[20] O. N. Hung, L. J. Song, C. K. Chan, C. W. Kan, C. W. M. Yuen, Using artificial neural network to predict colour properties of laser-treated 100% cotton fabric, Fibers Polym, 12 (**2011**) 8, 1069–1076, doi:10.1007/s12221-011-1069-1

[21] D. Semnani, M. Vadood, Improvement of intelligent methods for evaluating the apparent quality of knitted fabrics, Engineering Applications of Artificial Intelligence, 23 (**2010**) 2, 217–221, doi:10.1016/j.engappai.2009.08.003

[22] P. Unal, M. Üreyen, D. Mecit, Predicting properties of single jersey fabrics using regression and artificial neural network models, Fibers Polym, 13 (**2012**) 1, 87–95, doi:10.1007/s12221-012-0087-y

[23] K. Nasouri, H. Bahrambeygi, A. Rabbi, A. M. Shoushtari, A. Kaflou, Modeling and optimization of electrospun PAN nanofiber diameter using response surface methodology and artificial neural networks, Journal of Applied Polymer Science, 126 (**2012**) 1, 127–135, doi:10.1002/app.36726

[24] T. Chen, C. Zhang, L. Li, X. Chen, Simulating the drawing of spunbonding nonwoven process using an artificial neural network technique, Journal of The Textile Institute, 99 (**2008**) 5, 479–488, doi:10.1080/00405000701608631

[25] P. Soltani, M. Vadood, M. Johari, Modeling spun yarns migratory properties using artificial neural network, Fibers Polym, 13 (**2012**) 9, 1190–1195, doi:10.1007/s12221-012-1190-9

[26] R. Semnani Rahbar, M. R. M. Mojtahedi, Influence of hot multistage drawing on structure and mechanical properties of nylon 6 multifilament yarn, Journal of Engineered Fibers and Fabrics, 6 (**2011**) 2, 7–15

[27] L. Fausett, Fundamentals of neural networks, Prentice Hall, New Jersey 1994

[28] I. Belič, Neural Networks and Static Modelling, In: M. ElHefnawi, M. Mysara (Eds.), Recurrent Neural Networks and Soft Computing, InTech [online]. 2012, 1, 1–21. Available from: http://www.intechopen.com/books/recurrent-neural-networks-and-soft-computing/neural-networks-and-static-modelling

[29] A. T. C. Goh, Back-propagation neural networks for modeling complex systems, Artificial Intelligence in Engineering, 9 (**1995**) 3, 143–151, doi:10.1016/0954-1810(94)00011-S

[30] G. D. Garson, Interpreting neural network connection weights, Artificial Intelligence Expert, 6 (**1991**) 4, 46–51

[31] M. Gevrey, I. Dimopoulos, S. Lek, Review and comparison of methods to study the contribution of variables in artificial neural network models, Ecological Modelling, 160 (**2003**) 3, 249–264, doi:10.1016/S0304-3800(02)00257-0

UDK 536.2:536.28
Original scientific article/Izvirni znanstveni članek

ISSN 1580-2949
MTAEC9, 49(3)333(2015)

INFLUENCE OF THE IMPACT ANGLE AND PRESSURE ON THE SPRAY COOLING OF VERTICALLY MOVING HOT STEEL SURFACES

VPLIV VPADNEGA KOTA IN TLAKA NA OHLAJANJE Z BRIZGANJEM NA VERTIKALNO PREMIKAJOČE SE VROČE POVRŠINE JEKLA

Milan Hnízdil, Martin Chabičovský, Miroslav Raudenský

Heat Transfer and Fluid Flow Laboratory, Brno University of Technology, Technicka 2896/2, 616 69 Brno, Czech Republic, European Union
hnizdil@fme.vutbr.cz

Prejem rokopisa – received: 2013-10-09; sprejem za objavo – accepted for publication: 2014-09-04

doi:10.17222/mit.2013.239

The cooling of vertically moving strips is used very often to obtain the required material properties. Water spray cooling has to be used when a high cooling intensity is needed.
Our Heat Transfer and Fluid Flow Laboratory is equipped with a testing device which allows vertical movement of a heated experimental plate (sheet). Two different sizes of flat-jet nozzles were tested with different water pressures and angles of the water impact (inclination angles of the spraying bar). The water-pressure range was between 2 bar and 9.3 bar and the angle of the water impact changed from 20 ° to 40 °.
The dependence of the heat-transfer coefficient on the surface temperature was evaluated for each experiment. Interesting results were obtained from the comparison of these experimental results, showing that the heat-transfer coefficient and the Leidenfrost temperature increase with the increasing water pressure. Very interesting results were obtained during the tests with different inclination angles. The highest heat-transfer coefficient was obtained for the angle of 20 ° and the lowest value of the heat-transfer coefficient was obtained for the angle of 40 ° at the surface temperatures of around 200 °C.

Keywords: spray cooling, flat-jet nozzles, impact angle, water impingement density, Leidenfrost temperature

Ohlajanje vertikalno premikajočih se trakov se pogosto uporablja za zagotovitev zahtevanih lastnosti materiala. Kadar je potrebna velika intenzivnost hlajenja, se uporablja ohlajanje z brizganjem vode.
Laboratorij za prehajanje toplote in tok fluidov je opremljen s preizkusno napravo, ki omogoča vertikalno premikanje eksperimentalne plošče (jeklo). Preizkušeni sta bili dve različni dimenziji šob pri različnih tlakih vode in različnih kotih pršenja vode (nagibni kot palice za brizganje). Območje tlaka vode je bilo med 2 bar in 9,3 bar, kot vodnega curka pa med 20 ° in 40 °.
Za vsak poskus je bila ocenjena odvisnost koeficienta prehajanja toplote od temperature površine. Dobljeni so bili zanimivi rezultati iz primerjave eksperimentalnih podatkov, ki kažejo, da koeficient prehajanja toplote in Leidenfrostova temperatura naraščata z večanjem tlaka vode. Zanimive rezultate smo dobili tudi pri poskusih z različnimi vpadnimi koti. Najvišji koeficient prehajanja toplote je bil dosežen pri kotu 20 °, najnižja vrednost koeficienta prehajanja toplote pa je bila dosežena pri kotu 40 ° pri temperaturi površine okrog 200 °C.

Ključne besede: hlajenje z brizganjem, šobe s ploščatim curkom, vpadni kot curka, gostota udarca vode, Leidenfrostova temperatura

1 INTRODUCTION

Vertically moving strips are cooled by spraying water when a high cooling intensity (the heat-transfer coefficient) is needed. The cooling of these strips has to be homogeneous to avoid thermal deformation. Falling reflected water has a significant influence on the cooling homogeneity[1]. It can cause local thermal stresses in a strip and its deformation. The heat-transfer coefficient is influenced by many parameters such as water pressure, nozzle distance, water impingement density, water temperature, etc.[2–4]

A special cooling system which sprays water at a prescribed inclination angle to avoid the falling of the reflected water (**Figure 1**) was tested and the influence of the impact angle and the pressure on the heat-transfer coefficient was investigated during the cooling of a stainless-steel sheet at the initial temperature of 900 °C.

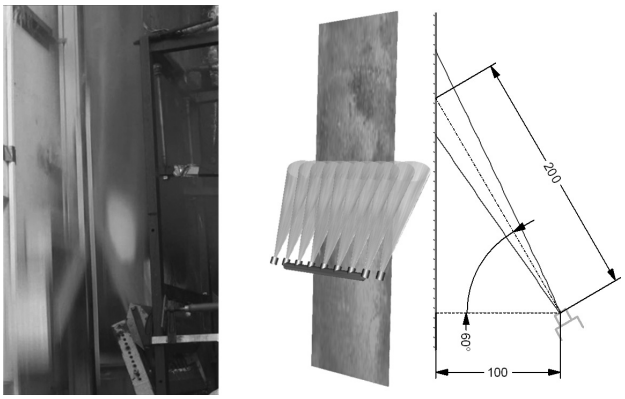

Figure 1: Cooling system (inclination angle of 30 °, distance to the surface is 100 mm)

Slika 1: Sistem ohlajanja (vpadni kot 30 °, razdalja do površine 100 mm)

2 LABORATORY STAND, EXPERIMENTAL PROCESS AND CONFIGURATION

An experimental apparatus developed for the vertical moving of a hot stainless-steel test sheet was used in the experiments (**Figure 2**). An electrical furnace which heated the experimental sheet to its initial temperature was positioned in the upper part of the testing bench. This sheet was made of thick austenitic stainless steel 1.5 mm. Five thermocouples were welded to the rear side of the sheet and they were positioned in the center line, perpendicular to the direction of the movement of the sheet. The test sheet was fixed on the trolley which moved repeatedly through the water spray. The temperatures were recorded by a data logger with a frequency of 320 Hz for each thermocouple.

The experiments started by heating the sheet in an inert atmosphere to the initial temperature (900 °C). Then the required water pressure was set. The data logger was switched on and it started to record the temperatures. Then the test sheet repeatedly moved through the spray till the surface temperature was less than 200 °C.

The recorded data were transferred to a computer and the inverse task[5] was used to compute the surface temperature, the heat flux and the heat-transfer coefficient, which is usually used as a boundary condition[6].

The influence of the water pressure was investigated. Five tests, each with a different water pressure (2, 4, 6, 8 and 9.3) bar, were conducted. Commercially available flat-jet nozzles were fixed in a single row with the same offset angle. The distance between the nozzles was 55 mm. The distance of the nozzle orifices to the test sheet was 100 mm and the inclination angle was 20 ° during these tests.

Further, three tests, each with a different inclination angle (20 °, 30 ° and 40 ° from the vertical direction, **Figure 1**) were conducted to investigate the influence of the inclination angle. These nozzles had a larger size of the orifice than the nozzles used for the tests with different water pressures. The distance between the nozzles was 100 mm. The distance of the nozzle orifices to the test sheet was 100 mm and the water pressure was 4 bar during these experiments. All the experiments were conducted with the velocity of the movement of 3 m/s.

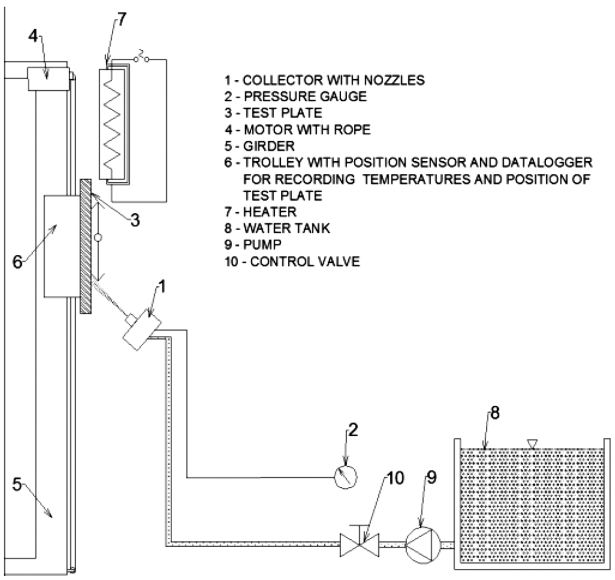

Figure 2: Testing bench for experimental tests of cooling vertically moving strips (1 – collector with nozzles; 2 – pressure gauge; 3 – test plate; 4 – motor with rope; 5 – girder; 6 – trolley with position sensor and data logger for recording temperatures and position of the test plate; 7 – heater; 8 – water tank; 9 – pump; 10 – control valve)

Slika 2: Preizkusna klop za preizkušanje ohlajanja vertikalno premikajočih se trakov (1 – nosilec s šobami; 2 – merilnik tlaka; 3 – preizkusna plošča; 4 – motor z vrvjo, 5 – nosilec; 6 – voziček s senzorjem pozicije in "data logger" za registracijo temperature ter pozicije preizkusne plošče; 7 – grelnik; 8 – vodni rezervoar; 9 – črpalka; 10 – kontrolni ventil)

3 RESULTS

The results shown in this part are the average values of the heat-transfer coefficient in the impact area computed for the positions of 0 mm to 600 mm (**Figure 3**). The measured dependences of the heat-transfer coefficient on the surface temperature are shown for different water pressures (**Figure 4a**) and for different inclination angles (**Figure 4b**).

It is evident that the heat-transfer coefficient increases with the increasing water pressure (an increase in the water pressure also causes an increase in the water impingement density $\dot{m}_L$). Also, the Leidenfrost temperature (T_{Leid} (°C)), which is defined as the temperature at which the heat flux reaches its minimum (or the temperature, at which the film-boiling regime changes to the transition-boiling regime), increases with the increase in the pressure (**Figure 5**). The measured Leidenfrost temperatures are higher than the ones predicted

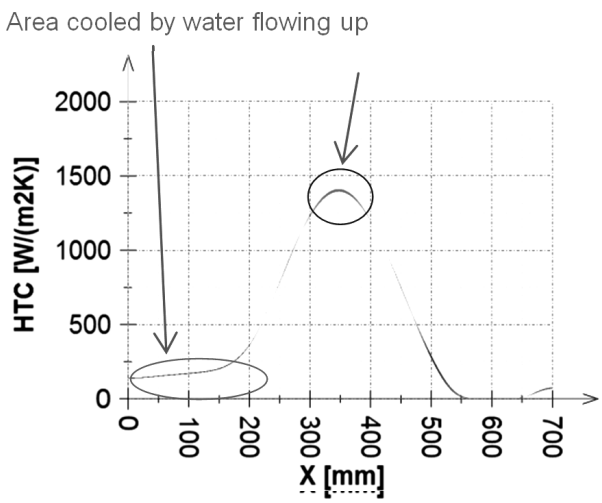

Figure 3: Dependence of the HTC on the position, for the surface temperature of 800 °C – evaluating area of 0–600 mm

Slika 3: Odvisnost HTC od položaja pri temperaturi površine 800 °C – področje ocenjevanja 0–600 mm

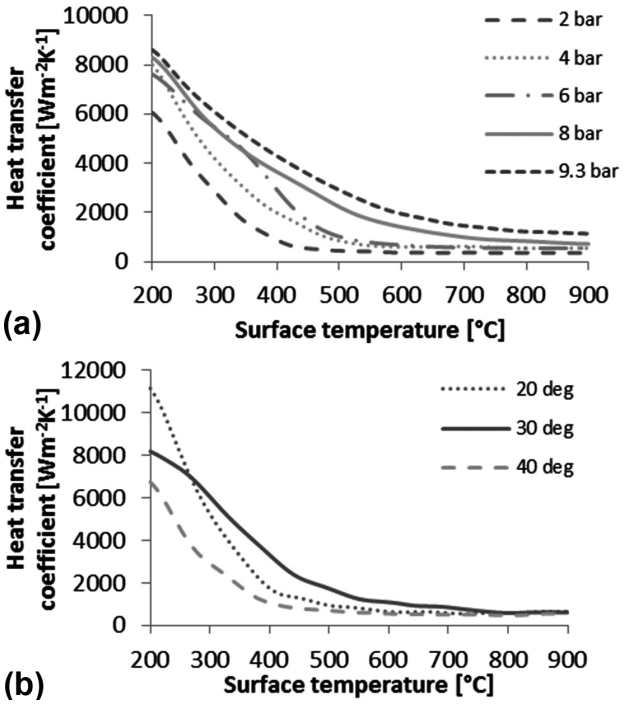

Figure 4: Dependence of the heat-transfer coefficient on the surface temperature for the: a) increasing water pressure and b) increasing inclination angle

Slika 4: Odvisnost koeficienta prehoda toplote od temperature površine pri: a) naraščajočem tlaku vode in b) naraščajočim vpadnim kotom

with the common prediction equations that use the water impingement density[7,8]:

$$T_{\mathrm{Leid}} = 339.604 \dot{m}_{\mathrm{L}}^{0.19} \quad (1)$$

$$T_{\mathrm{Leid}} = 1400 \frac{\dot{m}_{\mathrm{L}}^{2} d_{32}^{0.13}}{\rho \sigma} \quad (2)$$

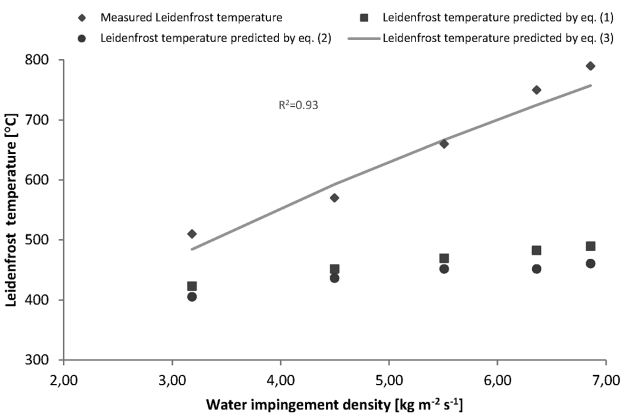

Figure 5: Comparison of the measured Leidenfrost temperature with the existing predictions and the new modified prediction of the Leidenfrost temperature (corresponding water impingement densities for water pressures of (2, 4, 6, 8 and 9.3) bar are (3.18, 4.5, 5.51, 6.36 and 6.86) kg m^{-2} s^{-1})

Slika 5: Primerjava izmerjene Leidenfrostove temperature z obstoječim predvidevanjem in novo modificirano predvidevanje Leidenfrostove temperature (ustrezne gostote vodnega curka pri tlakih vode (2, 4, 6, 8 in 9,3) bar so (3,18, 4,5, 5,51, 6,36 in 6,86) kg m^{-2} s^{-1})

where $\dot{m}_{\mathrm{L}}$ is the water impingement density (kg m^{-2} s^{-1}), d_{32} is the Sauter mean diameter (m) of water droplets, ρ is the density (kg m^{-3}) and σ is the surface tension (N m^{-1}).

The comparison of the measured Leidenfrost temperatures and the ones predicted with Eqs. (2) and (3) is shown in **Figure 5**. The error of prediction with Eqs. (2) and (3) is growing with the increase in the pressure. This shows that the water pressure must be taken into account when an accurate prediction of the Leidenfrost temperature is necessary. The increase in the pressure increases the exit velocity of the water from a nozzle and this leads to destroying the vapour layer at higher surface temperatures. The new prediction of the Leidenfrost temperature based on Eq. (1) that takes the pressure into account is:

$$T_{Leid} = 339.604 (\dot{m}_{\mathrm{L}}\, p)^{0.19} \quad (3)$$

where $\dot{m}_{\mathrm{L}}$ is the water impingement density (kg m^{-2} s^{-1}) and p is the water pressure (bar).

The comparison of the new prediction with the measured data and the other predictions is shown in **Figure 5**.

The second part of the experiments was focused on the influence of the water impact angle on the cooling intensity. As it is shown in **Figure 4b**, the heat-transfer coefficient and the Leidenfrost temperature are influenced by the change in the impact angle. The Leidenfrost temperature is the highest for the impact angle of 30 ° (800 °C) and the lowest for the impact angle of 40 ° (540 °C). The Leidenfrost temperature for the impact angle of 20 ° is 610 °C. The heat-transfer coefficient in the area of stable film boiling (the surface temperatures are higher than the Leidenfrost temperature – higher than 800 °C) is almost the same for all the impact angles. The main effect of the inclination angle on the heat-transfer coefficient occurs at low surface temperatures (approximately 200 °C), where the heat-transfer coefficient is the highest at the angle of 20 ° and the lowest at 40 °.

4 CONCLUSION

Two kinds of tests were done to find the influence of the water pressure (the flow rate) and the impact angle on the heat-transfer coefficient. It is evident (from the results) that the cooling intensity increases with the increasing water-flow rate (the water pressure). Also, the Leidenfrost temperature is dependent on the water pressure – a higher water pressure means a higher leidenfrost point. Different spray impact angles cause changes in the heat-transfer coefficient at low surface temperatures and the Leidenfrost temperature also depends on the impact angle. A new correlation for the prediction of the leidenfrost temperature was found.

Acknowledgement

This work is an output of research and scientific activities of the project LO1202 with financial support of the MEYS under the programme NPU I and the internal grant of the Brno University of Technology focused on specific research and development No. FSI-S-14-2437 and by the project No. CZ.1.07/2.3.00/20.0188, HEATEAM - Multidisciplinary Team for Research and Development of Heat Processes.

5 REFERENCES

[1] M. Chabicovsky, M. Raudenský, Experimental investigation of spray cooling of horizontally and vertically oriented surfaces, Conference proceedings of 22nd Conference on metallurgy and materials 1, Ostrava, 2013, 102–107

[2] M. Chabicovsky, M. Raudenský, Experimental Investigation of the Heat Transfer Coeficient, Mater. Tehnol., 47 (**2013**) 3, 395–398

[3] M. Raudenský, M. Hnízdil, P. Kotrbáček, Why oxides intensify spray cooling, 30th International Steel Industry Conference, Paris, 2012, 92–337

[4] M. Hnízdil, M. Raudenský, Influence of Water Temperature on the Cooling Intensity during Continuous Casting and Hot Rolling, Conference METAL 2012, Brno, 2012, 1–6

[5] M. Raudenský, Heat Transfer Coefficient Estimation by Inverse Conduction Algorithm, International Journal of Numerical Methods for Heat and Fluid Flow, 3 (**1993**) 3, 257–266, doi:10.1108/eb017530

[6] J. Stetina, F. Kavicka, T. Mauder, Heat Transfer Coefficients Beneath the Water Cooling Nozzles of a Billet Caster, 18th International Conference on Metallurgy and Materials, Hradec Nad Moravici, 2009

[7] H. Muller, R. Jeschars, Wärmeübergang bei der Spritzwasserkühlung von Nichteisenmetallen, Metallkunde, 1983, 257–264

[8] S. Yao, T. L. Cox, A general heat transfer correlation for impacting water sprays on high-temperature surfaces, Experimental Heat Transfer, 15 (**2002**) 4, 207–219, doi:10.1080/08916150290082649

UDK 621.77:536.28
Original scientific article/Izvirni znanstveni članek

ISSN 1580-2949
MTAEC9, 49(3)337(2015)

TECHNIQUES OF MEASURING SPRAY-COOLING HOMOGENEITY

TEHNIKE MERJENJA HOMOGENOSTI HLAJENJA Z BRIZGANJEM

Martin Chabičovský, Miroslav Raudenský

Heat Transfer and Fluid Flow Laboratory, Faculty of Mechanical Engineering, Brno University of Technology, Technická 2, 616 69 Brno, Czech Republic
chabicovsky@LPTaP.fme.vutbr.cz

Prejem rokopisa – received: 2013-10-18; sprejem za objavo – accepted for publication: 2014-07-14

doi:10.17222/mit.2013.253

The cooling homogeneity is one of the most important factors that must be considered in the design of cooling sections for the hot rolling of thin sheets. Inhomogeneous cooling can lead to undesirable thermal distortion. The cooling homogeneity is mainly influenced by the water distribution of the cooling section. And so, one way to measure the cooling homogeneity is to measure the impact-pressure distribution of the cooling section. Another way is to measure the surface-temperature distribution of a steel sample during the cooling process. There are two ways to measure the surface temperature and the temperature field: the contact and non-contact measurements. The contact measurement can be performed with thermocouples and the non-contact method is an optical measurement like the one using an infrared scanner. Each of these methods has their advantages and disadvantages. Their comparison was made during an experimental measurement of the cooling of a stainless steel sheet using full-cone water nozzles and a special linear pneumatic sprayer.

Keywords: cooling homogeneity, full-cone nozzles, linear pneumatic sprayer, heat-transfer coefficient

Homogenost ohlajanja je med najpomembnejšimi dejavniki, ki ga je treba upoštevati pri načrtovanju ohlajevalnega področja pri vročem valjanju tankih pločevin. Nehomogeno ohlajanje lahko povzroči neželeno toplotno izkrivljanje. Homogenost ohlajanja je predvsem odvisna od razporeditve vode v območju ohlajanja. Ena od možnosti merjenja homogenosti ohlajanja je merjenje razporeditve tlaka udarca v območju ohlajanja. Druga možnost je merjenje razporeditve temperature na površini vzorca iz jekla med postopkom ohlajanja. Obstajata dva načina za merjenje temperature površine in temperaturnega polja: kontaktno in nekontaktno. Kontaktno merjenje se lahko izvrši s termoelementi, nekontaktno pa z optično meritvijo, kot je na primer infrardeče vrstično tipalo. Vsaka od teh metod ima svoje prednosti in slabosti. Izvršena je bila eksperimentalna primerjava merjenja ohlajanja pločevine iz nerjavnega jekla v območju vodnih šob in s posebnim linearnim pnevmatskim brizgalnikom.

Ključne besede: homogenost ohlajanja, območje s šobami, linearni pnevmatski brizgalnik, koeficient prehoda toplote

1 INTRODUCTION

The intensive cooling of thin sheets during hot rolling or heat treatment is mainly conducted with water. Cooling with water provides high cooling rates compared to gas cooling, but these can be associated with undesirable problems of the homogeneity of cooling. Inhomogeneous cooling can lead to non-homogeneous material properties and also to thermal distortion. The cooling homogeneity is one of the most important factors that must be considered in the design of water-cooling sections for the hot rolling or the heat treatment of thin sheets.

Cooling hot surfaces with water is associated with different regimes of boiling. The film-boiling regime occurs when the surface temperature is higher than the Leidenfrost temperature[1] (**Figure 1**). The surface is covered with a vapor layer which protects the surface and lowers the cooling intensity during the film-boiling regime. When the surface temperature drops below the Leidenfrost temperature, the vapor layer is broken and the transient and nucleate boiling regime occurs, which is characterized by high cooling intensities. A large inhomogeneity of the surface-temperature distribution can mostly be observed when the temperature of one part of the cooled surface is below the Leidenfrost temperature and another is above the Leidenfrost temperature. This is well demonstrated in **Figure 1**. The temperature record at time *T*1 corresponds to the heat-transfer coefficient *HTC T*1. This heat-transfer coefficient has a Leidenfrost

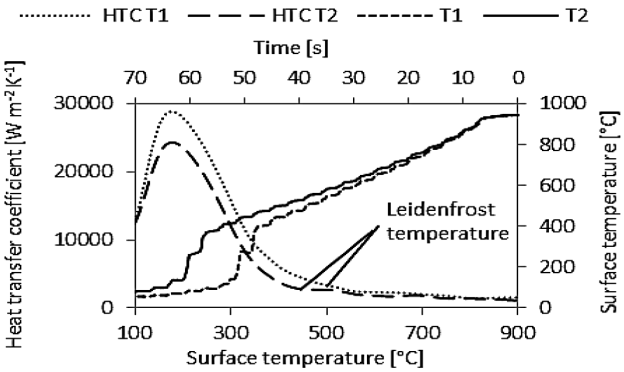

Figure 1: Simulation of the cooling process
Slika 1: Simulacija postopka ohlajanja

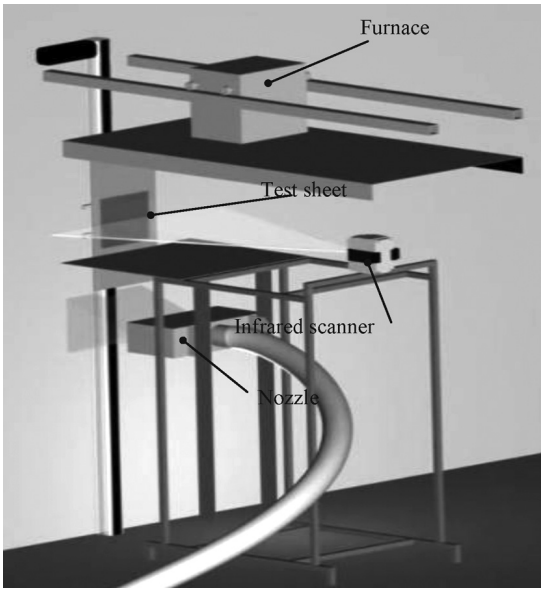

Figure 2: Experimental apparatus for measuring cooling homogeneity with thermocouples and an infrared scanner

Slika 2: Eksperimentalna naprava za merjenje homogenosti ohlajanja s termoelementi in infrardečim vrstičnim tipalom

temperature of approximately 500 °C. And so the intensive cooling caused by the breaking up of the vapor layer starts at a time of 44 s. The distribution of the heat-transfer coefficient *HTC T*2 has a Leidenfrost temperature of 450 °C. This temperature relates to the start of a rapid decrease in temperature *T*2 at a time of 50 s. This is why the difference in the temperature is almost 300 °C between 50 s and 60 s although the difference between the heat-transfer coefficients is small, especially for the surface temperatures higher than 500 °C.

The best way of measuring the cooling inhomogeneity during the cooling of thin sheets is to do it in the plant. However, because this method is very expensive, laboratory experimental methods simulating the plant conditions should be taken into account. With the reported technique we simulated a cooling process involving a small sheet, and measured the distribution of surface temperatures during the cooling process either with the contact method using thermocouples or the non-contact method using an infrared scanner. As the cooling intensity is mainly influenced by the water distribution and impact velocity[2,3] the cooling homogeneity can be evaluated by measuring the impact-pressure distribution of the cooling section. The experimental methods for the measurement of the cooling inhomogeneity are described below.

2 EXPERIMENT

2.1 Measurement of spray-cooling homogeneity

An experimental study was performed to compare three different methods of measuring the cooling homogeneity. The homogeneity of cooling was measured during the cooling process with thermocouples and an infrared scanner. The cooling homogeneity was also investigated during cold tests when the impact pressure was measured.

The experiments for this comparison were conducted with three different nozzle configurations, which provided three different levels of cooling homogeneity.

The configuration with a very good cooling homogeneity (Configuration 1) was composed of a row of full-cone nozzles. The distance between the full-cone nozzles was 80 mm and the distance from the nozzle orifices to the test sheet was 250 mm. The water pressure was 130 kPa. The spray angle was 60 ° and the water impingement density in the impact area was 12.07 kg m^{-2} s^{-1}. Configuration 2 was a configuration with a medium cooling homogeneity and Configuration 3 provided very inhomogeneous cooling. Configurations 2 and 3 were composed of a special linear pneumatic spray box which is well described in[4].

The distance between the nozzle orifice and the test sheet was 250 mm and the spray angle was 60 °. The water pressure was 130 kPa for Configuration 2 and 600 kPa for Configuration 3. The air pressure was 8.5 kPa for Configuration 2 and 10.5 kPa for Configuration 3.

The water impingement density was 9.76 kg m^{-2} s^{-1} for Configuration 2 and 20.64 kg m^{-2} s^{-1} for Configuration 3.

One way to measure the temperature is using the thermocouples welded onto the rear side of the test sheet which, with the help of inverse methods, determines the surface temperatures. The other method uses an infrared scanner for a direct measurement of the surface temperatures during the cooling process. The apparatus for measuring the temperatures using an infrared scanner and thermocouples is shown in **Figure 2**. Details of the experimental apparatus and the experimental set-up are described in[5,6]. Hot tests were conducted with the austenitic stainless-steel sheets with a thickness of 2 mm, a height of 300 mm and a width of 320 mm. A test sheet was heated in a furnace with a protective atmosphere at a temperature of 950 °C. After the heating, the test sheet moved down with a velocity of 3 m s^{-1} and passed through the cooling section. Then it moved up through the cooling section and stopped for 1.5 s above the cooling section. During this time the infrared scanner measured the surface temperature. Then the test sheet moved down and repeated the previous steps until it was cooled to a temperature of 200 °C. During the experiment, the temperature of the sheet was measured with five type-K thermocouples with a frequency of 320 Hz. The thermocouples were welded onto the rear side of the test sheet. One thermocouple was welded in the center of the test sheet and the distance between the thermocouples was 20 mm (for more details see reference[5]). The distance between the infrared scanner and test sheet was 1500 mm. The frequency of the measurement was 36 Hz and the resolution was 1024 points per line.

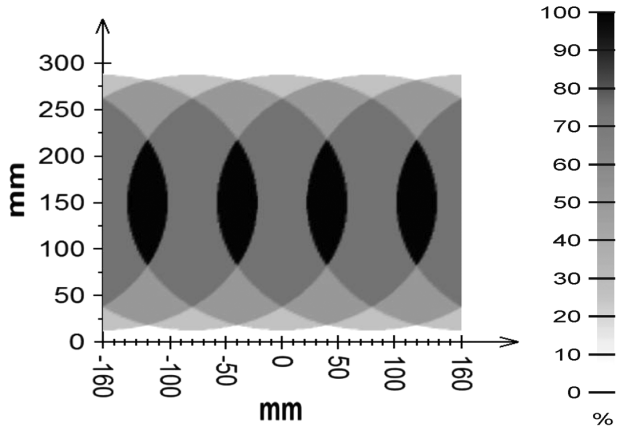

Figure 3: Water distribution for Configuration 1
Slika 3: Razporeditev vode pri postavitvi 1

Impact-pressure tests were conducted with a pressure sensor with a diameter of 12 mm and during the test the impact pressure was measured on the whole area that was influenced by the spraying nozzles, with a step of 10 mm in the direction of the *X*-axis and 20 mm in the direction of the *Y*-axis.

3 RESULTS AND DISCUSSION

3.1 Thermocouples

The use of thermocouples for measuring the cooling homogeneity has some restrictions. Thermocouples can be placed only in a finite number of positions. So, it is necessary to know the positions, in which inhomogeneity can be expected. The water distribution can serve as the first source of information about the expected cooling homogeneity. An example of the computed water distribution is shown in **Figure 3**. The information about the water distribution is necessary when deciding where to place the thermocouples. The thermocouples were installed in positions of 0 mm and 40 mm (**Figure 3**) for Configuration 1. The position of 40 mm corresponds to the position with the highest water impingement density and the position of 0 mm is the position with the lowest water impingement density. The measured temperatures are shown in **Figure 4**. The temperatures are almost the same for the positions of 0 mm and 40 mm. The surface

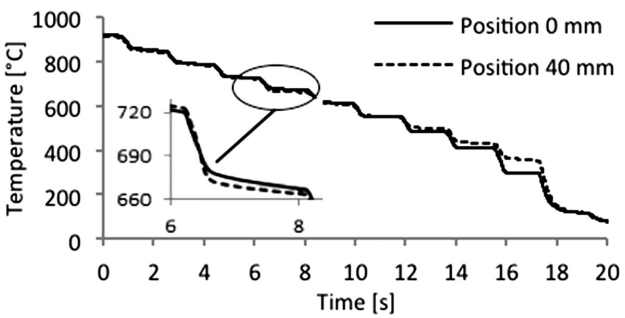

Figure 4: Measured temperatures for Configuration 1
Slika 4: Izmerjene temperature pri postavitvi 1

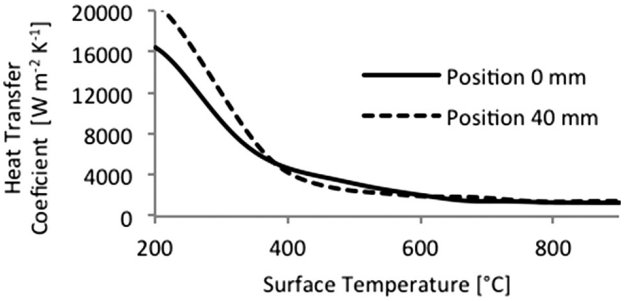

Figure 5: Heat-transfer coefficient for Configuration 1
Slika 5: Koeficient prehoda toplote pri postavitvi 1

temperatures and the heat-transfer coefficients can be computed at these positions using inverse methods.[7–9] The computed dependence of the heat-transfer coefficient on the surface temperature is shown in **Figure 5**. The dependence of the heat-transfer coefficient on the surface temperature also shows a very good homogeneity of the cooling, obviously for the surface temperatures higher than 600 °C.

3.2 Infrared scanner

Although the measurement with an infrared scanner provides information about the surface temperature of the overall surface area, and these measured temperatures can be directly used for the evaluation of the cooling homogeneity, this method of measuring the cooling homogeneity needs a more complicated experimental set-up. The precision of the non-contact measurement is not as good as in the case of thermocouples. There are several factors that have a considerable influence on the quality of measurement. One of them is emissivity. Information about emissivity is necessary for obtaining surface temperatures. Emissivity depends on the properties of the surface (material, temperature, presence of oxides and others) and the surface properties change during the cooling process. If a sheet is heated in a protective atmosphere and removed from the furnace, its surface is like a mirror and the emissivity is lower than during the cooling process due to different surface temperatures and the presence of scales on the surface. The scales on the surface enhance the emissivity. Uneven

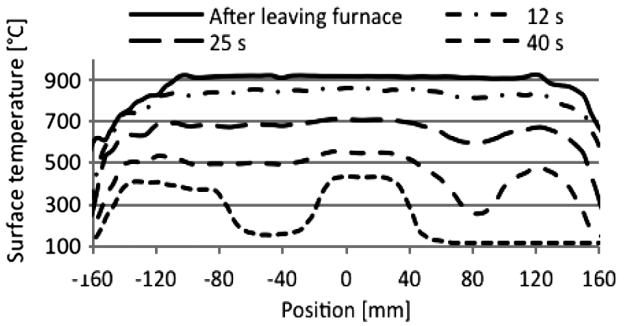

Figure 6: Surface temperatures at given times for Configuration 2
Slika 6: Temperature površine pri danih časih pri postavitvi 2

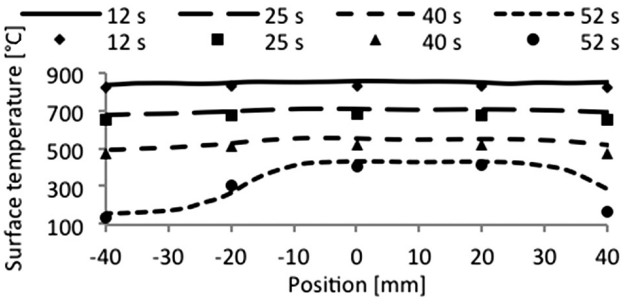

Figure 7: Comparison of the surface temperatures measured with the infrared scanner (lines) and with the thermocouples (marks: ♦, ■, ▲ and ●)

Slika 7: Primerjava temperature na površini, izmerjene z infrardečim vrstičnim tipalom (polna črta) in izmerjene s termoelementi (oznake: ♦, ■, ▲ in ●)

scale coverage of the surface is a problem and can lead to errors in the measurement of the surface temperatures and an incorrect conclusion regarding the cooling homogeneity.

The temperature that is measured can also be influenced by the presence of water droplets and vapor in the air between the sheet and the infrared scanner. The water remaining on the sheet and the radiation from the surroundings also prevent the measured temperatures from reflecting the reality. The presence of vapor and water droplets in the air or a water layer on the surface can smooth a low temperature inhomogeneity or cause the measured temperatures to be lower or higher than the real temperatures. The radiation from the surroundings can cause the temperatures measured in some positions to be higher than in reality. All the above factors should be considered during the measurement preparation to obtain realistic results. An example of the temperatures measured with the infrared scanner is shown in **Figure 6**. The position of 0 mm was in the center of the test sheet with a width of 320 mm and the temperatures were measured in the centerline of the test sheet. The temperature was also measured with five thermocouples during the cooling process and the comparison is shown in **Figure 7**. The thermocouples were welded on at the positions of (–40, –20, 0, 20 and 40) mm. The surface temperatures that were measured with the thermocouples and computed with an inverse task were slightly lower

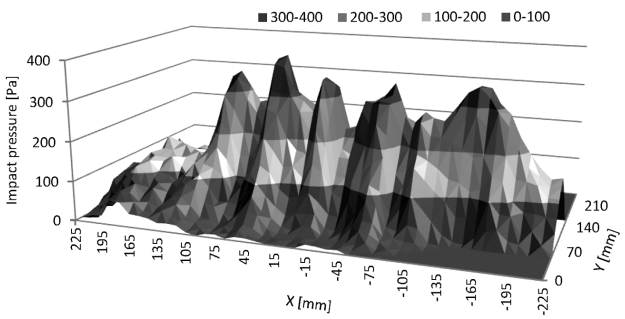

Figure 8: Impact-pressure distribution for Configuration 2

Slika 8: Razporeditev dinamičnega tlaka pri postavitvi 2

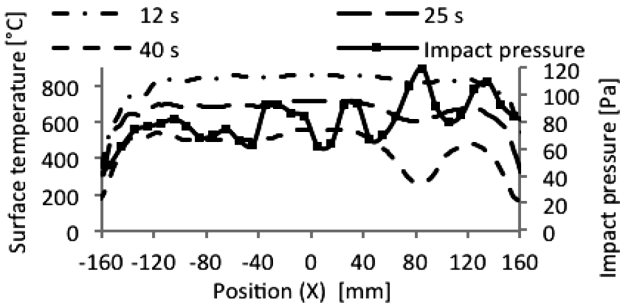

Figure 9: Comparison of the impact pressure with the measured surface temperatures for Configuration 2

Slika 9: Primerjava dinamičnega tlaka pri izmerjeni temperaturi površine pri postavitvi 2

than the temperatures measured with the infrared scanner. There is only one big difference between the temperatures measured with the infrared scanner and those measured with the thermocouples. It is found in the position of 40 mm at a time of 52 s. The difference is approximately 120 °C. It can be explained with the water layer on the surface in this position. The homogeneity of cooling is almost the same with both methods.

3.3 Impact pressure

The measurement of the impact pressure is an indirect method for measuring the cooling homogeneity because the real surface temperature is not measured during the cooling process. An example of the measured impact-pressure distribution is shown in **Figure 8**. Its average value over the width of the spray configuration (*Y*-axis) of Configuration 2 is compared with the surface temperatures measured for this configuration with the infrared scanner in **Figure 9**.

Although the impact-pressure distribution looks inhomogeneous, the surface temperatures at the times of 12 s and 25 s look homogeneous except at the position of 80 mm. This is why the surface temperatures are higher than the Leidenfrost temperature and the vapor layer protects the surface and only a significant inhomogeneity of the impact pressure is observed during the real cooling. This was confirmed during the experiment with Configuration 3 (**Figure 10**). The surface temperatures

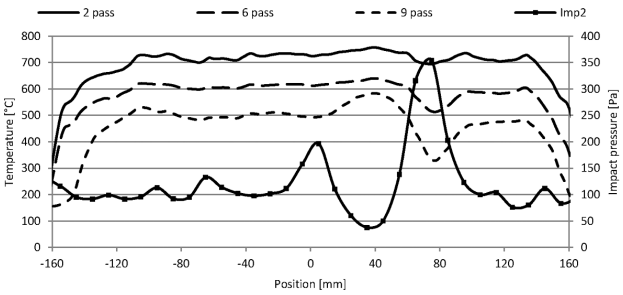

Figure 10: Comparison of the impact pressure with the surface-temperature distribution for Configuration 3

Slika 10: Primerjava dinamičnega tlaka z razporeditvijo temperature pri postavitvi 3

after the second pass through the cooling section (pass 2) fit well with the impact-pressure distribution (Imp. 2) only at the position of 80 mm. When the surface temperature is lower than the Leidenfrost temperature (pass 9) almost every increase or decrease in the impact pressure is reflected in the surface-temperature distribution.

4 CONCLUSIONS

The thermocouples provided accurate and reliable information about the cooling homogeneity, though only in a finite number of positions. The benefit of the infrared scanner was that the cooling homogeneity was measured on all the surface area; but to obtain accurate values of the measurement, a demanding measurement preparation was necessary. The homogeneity of the impact-pressure distribution corresponded with the homogeneity of the measured surface temperatures only for the surface temperatures below the Leidenfrost temperature. During the test with a hot test plate, a large inhomogeneity of the impact pressure was observed only for the surface temperatures higher than the Leidenfrost temperature.

Acknowledgement

This work is an output of research and scientific activities of this project LO1202 with financial support of the MEYS under the programme NPU I and the internal grant of the Brno University of Technology focused on specific research and development No. FSI-S-14-2437.

5 REFERENCES

[1] S. Nukiyama, The Maximum and Minimum Values of the Heat Q Transmitted from Metal to Boiling Water Under Atmospheric Pressure, International Journal of Heat and Mass Transfer, 9 (**1966**) 12, 1419–1433, doi:10.1016/0017-9310(66)90138-4

[2] J. Wendelstorf, K. H. Spitzer, R. Wendelstorf, Spray water cooling heat transfer at high temperatures and liquid mass fluxes, International Journal of Heat and Mass Transfer, 51 (**2008**) 19–20, 4902–4910, doi:10.1016/j.ijheatmasstransfer.2008.01.032

[3] S. C. Yao, T. L. Cox, A general heat transfer correlation for impacting water sprays on high-temperature surfaces, Experimental Heat Transfer, 15 (**2002**) 4, 207–219, doi:10.1080/08916150290082649

[4] J. Rivallin, S. Viannay, General principles of controlled water cooling for metallurgical on-line hot rolling processes: forced flow and sprayed surfaces with film boiling regime and rewetting phenomena, International Journal of Thermal Sciences, 40 (**2001**) 3, 263–272, doi:10.1016/S1290-0729(00)01216-3

[5] M. Chabicovsky, M. Raudensky, Experimental Investigation of a Heat Transfer Coefficient, Mater. Tehnol., 47 (**2013**) 3, 395–398

[6] M. Chabičovský, M. Raudenský, Experimental investigation of spray cooling of horizontally and vertically oriented surfaces, Proc. of the 22nd International Conference on Metallurgy and Materials METAL 2013, Brno, 2013, 198–202

[7] M. Raudensky, Heat Transfer Coefficient Estimation by Inverse Conduction Algorithm, International Journal of Numerical Methods for Heat and Fluid Flow, 3 (**1993**) 3, 257–266, doi:10.1108/eb017530

[8] M. Pohanka, K. A. Woodbury, A Downhill Simplex method for computation of interfacial heat transfer coefficients in alloy casting, Inverse Problems in Engineering, 11 (**2003**) 5, 409–424, doi:10.1080/1068276031000109899

[9] M. Pohanka, P. Kotrbáček, Design of Cooling Units for Heat Treatment, In: F. Czerwinski (ed.), Heat Treatment – Conventional and Novel Applications, chapter 1, InTech, 2012, 1–20, doi:10.5772/50492

UDK 66.046.58
Original scientific article/Izvirni znanstveni članek

ISSN 1580-2949
MTAEC9, 49(3)343(2015)

MINERALOGICAL AND GEOCHEMICAL CHARACTERIZATION OF ROMAN SLAG FROM THE ARCHAEOLOGICAL SITE NEAR MOŠNJE (SLOVENIA)

MINERALOŠKA IN GEOKEMIČNA KARAKTERIZACIJA RIMSKE ŽLINDRE Z ARHEOLOŠKEGA NAJDIŠČA PRI MOŠNJAH (SLOVENIJA)

Sabina Kramar[1], Judita Lux[2], Helmut Pristacz[3], Breda Mirtič[4], Nastja Rogan - Šmuc[4]

[1]Slovenian National Building and Civil Engineering Institute, Dimičeva 12, 1000 Ljubljana, Slovenia
[2]Institute for the Protection of Cultural Heritage of Slovenia, Preventive Archaeology Department, Tomšičeva 7, 4000 Kranj, Slovenia
[3]University of Vienna, Institute of Mineralogy and Crystallography, Althanstrasse 14, 1090 Vienna, Austria
[4]University of Ljubljana, Faculty of Natural Sciences and Engineering, Department of Geology, Aškerčeva 12, 1000 Ljubljana, Slovenia
sabina.kramar@zag.si

Prejem rokopisa – received: 2013-12-02; sprejem za objavo – accepted for publication: 2014-07-25

doi:10.17222/mit.2013.299

Roman slag from the archaeological site near Mošnje (NW Slovenia) was studied with respect to its mineralogical and geochemical characteristics. Samples were analysed with light microscopy, X-ray powder diffraction (XRD), scanning electron microscopy with an energy dispersive spectrometer (SEM-EDS) and Raman microspectroscopy. A chemical investigation was carried out using inductively coupled plasma-atomic emission spectroscopy (ICP-ES) to determine the major elements. The investigated slags are recognized as iron slags, grouped into two main classes according to their chemical and mineralogical compositions. The first group is characterized by high Fe_2O_3 and low SiO_2 contents and the second by high CaO and SiO_2 and low Fe_2O_3 contents. The phase occurrence obviously depends on the chemical composition as the first group mainly consists of fayalite, wüstite and magnetite, and the second one of augite, leucite, hedenbergite, monticellite and kirschsteinite.

Keywords: slag, archaeometallurgy, iron slag, Roman slag, archaeological site near Mošnje (Slovenia)

V prispevku je obravnavana rimska žlindra z arheološkega najdišča Mošnje (SZ Slovenija), pri kateri smo določili mineralno in kemijsko sestavo. Vzorci so bili analizirani s svetlobno mikroskopijo, rentgensko praškovno difrakcijo, SEM-EDS in ramansko mikrospektroskopijo. Kemijska sestava glavnih elementov je bila določena z ICP-ES. Preiskana žlindra dokazuje, da izvira iz pridelave železa na tem področju. Glede na mineraloško in kemijsko sestavo lahko delimo žlindro na dve skupini. Za prvo skupino je značilna visoka vsebnost Fe_2O_3 in nizka vsebnost SiO_2, za drugo pa visoki vsebnosti SiO_2 in CaO ter nizka vsebnost Fe_2O_3. Kemijska sestava vpliva na mineralne faze; tako je za prvo skupino značilen fajalit, wustit in magnetit, za drugo pa avgit, levcit, hedenbergit, monticelit in kirschsteinit.

Ključne besede: žlindra, arheometalurgija, železova žlindra, rimska žlindra, arheološko najdišče pri Mošnjah (Slovenija)

1 INTRODUCTION

The archaeological site near Mošnje with a Roman *villa rustica* is located in the northwestern region of Slovenia. Five masonry structures, incorporated in an embankment, were recognized. The main structure represents a residential building with seven rooms, including baths, decorated with a floor mosaic and wall paintings. The discovery of small finds such as coins, jewellery, elements of costume and fragments of pottery within closed stratigraphic layers suggests that the Roman *villa rustica* was inhabited during the first and second centuries AD and was already in ruins by the third century, whereas the archaeological finds from the mixed layers indicate that this area has been inhabited since the early Iron Age[1]. Excavation also provides evidence of prehistoric metallurgical activities as numerous slag occurrences – almost 400 pieces of slag – were evidenced at the mentioned location.

Slags form as by-products of metallurgical processes and they often represent the only relics of prehistoric metallurgical activities at certain archaeological sites[2–4]. Slags vary in terms of size, shape, and chemical and mineralogical compositions as a consequence of the technological process. In particular, the compositions and properties of metallurgical slags are influenced by the types of ores, the fluxes added, the furnace construction material (the lining), the use of charcoal and the cooling conditions[5]. Iron slags are routinely discovered at almost all archaeological sites throughout Slovenia[6–9] and occasionally blacksmiths' hearths or smelting furnaces are also found[10].

Preliminary analyses revealed that the archaeometallurgical samples from the archaeological site near Mošnje (Slovenia) differentiated in their mineralogical and chemical compositions[11]. Consequently, in this study, detailed mineralogical and geochemical characteristics of the slag from the Roman *villa rustica* were

investigated in order to obtain information on the metallurgical operation and, thus, contribute to better knowledge and evidence of metallurgical activities.

2 EXPERIMENTAL WORK

2.1 Materials

A set of 12 archaeometallurgical samples were selected for the study. Information regarding the samples is provided in **Table 1**. Samples of the slag were selected from the closed stratigraphic units of the *villa rustica* (**Figure 1**). Thus, the slags from the stratigraphic units that were determined as antique (i.e., SU 280, SU 337 inside the object or SU 281) or presumably antique (SU 367) and the layers that periodically contained different finds (from the Roman and recent periods, i.e., SU 126, SU 38) were sampled and compared. Additionally, various layers from the inside objects, such as rubble layers (SU 337) or different coat layers (SU 280, SU 281, SU 126, 38, 367), fill layers (SU 296) and hearth remnants (SU 285) from the outside objects were selected. This selection enabled us to obtain a variety of samples that provided information regarding the diversity of the finds.

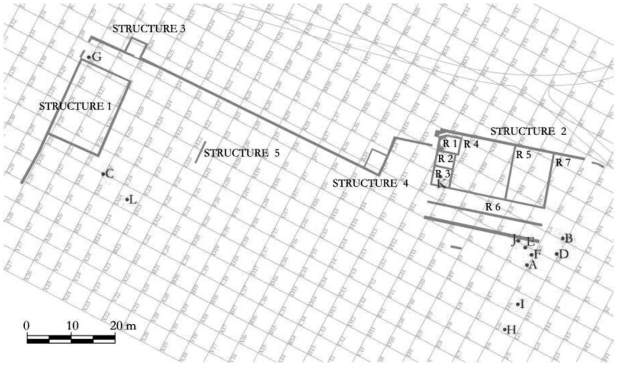

Figure 1: Plan of the *villa rustica* near Mošnje with marked sampling locations
Slika 1: Načrt vile rustike pri Mošnjah z označenimi vzorčnimi mesti

2.2 Methods

Polished cross-sections of the samples were studied with light microscopy using a Zeiss AX 10 equipped with an AxioCam MRc5 digital camera.

The mineral composition of the slag samples was determined with X-ray powder diffraction (XRD), using a Philips PW3710 X-ray diffractometer equipped with Cu-$K\alpha$ radiation and a secondary graphite monochromator. Data were collected at 40 kV and a current of 30 mA in the range from $2\theta = 2\,°$ to $70\,°$ with a speed of 3.4 r/min. The results were analyzed with the EVA diffraction software v12 using ICSD powder diffraction files. For the purpose of the XRD analysis, the samples were milled in an agate mortar to a particle size of less than 50 µm.

Polished cross-sections of the samples were examined in the back-scattered-electron (BSE) imaging mode of low-vacuum scanning electron microscopy (SEM) and the energy dispersive X-ray (EDS) technique using a JEOL 5500 LV instrument.

Table 1: Summary of the investigated samples, their locations and mineral compositions
Tabela 1: Sinteza preiskanih vzorcev z njihovo lokacijo in mineralno sestavo

Sample	Location	Stratigraphy	Dating	Mineral composition
A (6597)	J/6,7	280	Layer, Roman period; 1st–3rd c. AD	Fayalite, wüstite
B (1499)	L6	126	Layer, mixed, prehistoric–recent	Fayalite, wüstite, magnetite, quartz, goethite, α-Fe?
C (2630)	D, E/25, 26	38	Layer, mixed, Roman period–recent	Wustite, magnetite, quartz, goethite, lepidocrocite
D (1580)	K6	126	Layer, mixed, prehistoric–recent	Fayalite, wüstite, quartz, dolomite, magnetite, lepidocrocite, graphite?
E (4193)	J7	281	Layer, Roman period, 1st, 2nd c. AD	Magnetite, goethite, quartz, fayalite, wüstite
F (5006)	J7	281	Layer, Roman period	Magnetite, quartz, augite, leucite, fayalite, wüstite, kirschsteinite, akermanite?
G (5129)	I/28, 29	367	Villa's entrance, layer, Roman period?	Quartz, augite, kirschsteinite?, fayalite, leucite, cristobalite, hercynite, monticellite, magnetite, maghaemite?
H (3531)	G6	296	Fill layer, Roman period	Quartz, cristobalite, augite, leucite, hedenbergite, monticellite
I (3823)	H6	285	Hearth, Roman period	Wuestite, kirschsteinite, pyrolusite, akermanite?, leucite
J (1999)	K7	194	Layer, Roman period, 1st–3rd c. AD	Quartz, augite, anorthite, hedenbergite
K (4100)	K, L/12	0337	Object 2, room 1, layer, Roman period, 1st–2nd c. AD	Quartz - mullite 3 : 2, cordierite, α-Fe?, magnetite, wüstite
L (2641)	D24	38	Layer, mixed, Roman period–recent	Quartz, diopside, anorthite, leucite, akermanite?, olivine

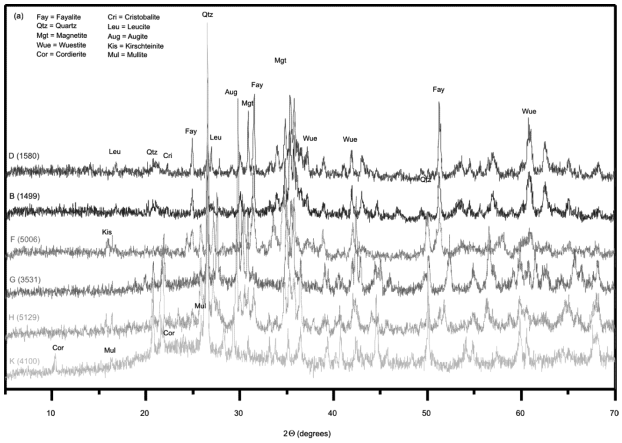

Figure 2: X-ray powder diffraction patterns of the selected samples
Slika 2: Rentgenogrami izbranih vzorcev

Raman spectra of the phases were obtained on the polished cross-sections with a Horiba Jobin Yvon LabRAM HR800 Raman spectrometer equipped with an Olympus BXFM light microscope. The measurements were made using a 633 nm laser excitation line (6.6 mW measured behind the objective) and a Leica 100 ° objective was used. The wavenumber accuracy was better than 1 cm^{-1} and the spectral resolution was about 2.5 cm^{-1}.

The samples were analysed for their major chemical components (SiO_2, Al_2O_3, Fe_2O_3, MgO, CaO, Na_2O, K_2O, TiO_2 and P_2O_5) in an accredited commercial Canadian laboratory (Acme Analytical Laboratories, Vancouver, B.C., Canada) after fusion with a mixture of lithium metaborate/tetraborate and dissolution in nitric acid using inductively coupled plasma emission spectroscopy (ICP-ES). The accuracy and precision of the slag analysis were assessed using the reference material CCRMR SO-18 CSC. The analytical precision and accuracy were better than ± 5 % for the investigated elements. This was indicated by the results of duplicate measurements in 12 slag samples as well as duplicate measurements of the standards.

To identify distinct groupings of the investigated samples, a hierarchical cluster analysis was applied using Ward's method and squared Euclidean distance. The basic statistical parameters for each element and the calculations mentioned above were computed using the statistical software program Statistica VII.

3 RESULTS AND DISCUSSION

3.1 Mineral composition

The mineral compositions of the samples were determined by combining various methods and they are given in **Table 1**. For instance, using Raman microspectroscopy, tiny crystals that could not be analysed with XRD due to their small quantity were also detected. The X-ray powder-diffraction patterns of the selected slag samples are shown in **Figure 2**.

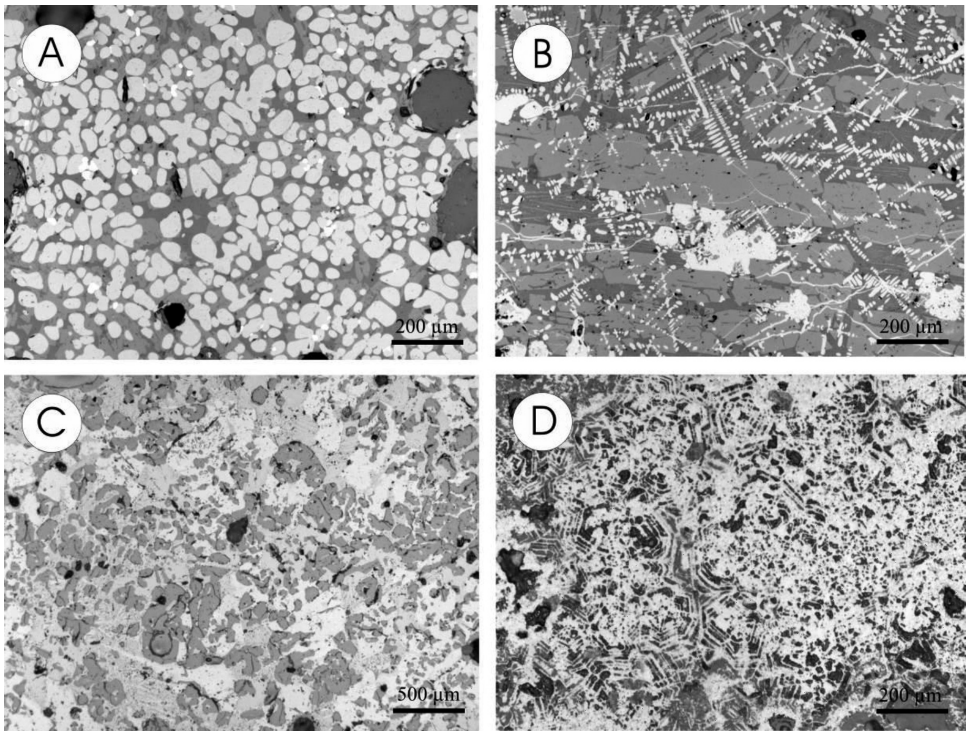

Figure 3: Microphotographs of the investigated samples: a) globular wüstite, sample A, b) dendritic wüstite and lamellar fayalite, sample D, c) abundant leucite in sample G, d) preserved carbonate structure indicating siderite ore, sample I

Slika 3: Mikroposnetki preiskanih vzorcev: a) globularni wüstit, vzorec A, b) dendritski wüstit in lamelarni fajalit, vzorec D, c) levcit, ki se pojavlja v večjih količinah, v vzorcu G, d) ohranjena karbonatna struktura, ki nakazuje sideritno rudo, vzorec I

The investigated samples were distinguished by their mineral compositions and different distributions of the phases, most probably reflecting different stages of the iron production. The samples were recognized as the iron slags that could be grouped, in general, into two main classes according to the mineral composition.

Wüstite and fayalite are the most abundant phases in the samples of the first group (A–E). Wüstite is particularly abundant in sample A, where it occurs as globular grains (**Figure 3a**). Dendritic wüstite is often observed (**Figure 3b**). A common feature of fayalite (**Figure 4a**) is idiomorphic lath crystals. Besides, goethite and lepidocrocite as the weathering products or magnetite could also be detected in those samples. Quartz is present in some samples, probably from the smith's hearth, and dolomite is identified in sample D. The glassy matrix is mostly formed of Si, Al, and Fe; small quantities of K, Na, Ca, and P are also present, as determined with SEM-EDS. Samples B, C, D and E also contain the remnants of charcoal particles, which were incorporated into the slag at the smithing hearth. Larger areas of metallic iron, somewhat limonitized, are observed in samples B, C, and E, which could be part of refined bloom – gromp[12].

Concerning the second group of samples (F–L), the more abundant slag phases are represented by the pyroxenes augite and hedenbergite, and Ca-rich olivine monticellite, followed by leucite (**Figures 3c** and **4b**). Leucite, which is especially abundant in sample G, shows that the melt contains enhanced quantities of Al and K with respect to the melt of the samples within the first group. The samples are depleted in iron oxide, which was also noted in their microstructure, due to the absence of wüstite. While wüstite and olivine minerals predominate within the first group, in the samples of the second group they are present in small quantities or absent. Often two generations of fayalite are observed. Cordierite, mullite, cristobalite, pyrolusite and akermanite are also found, indicating furnace or smith's hearth linings. These are the minerals that were formed by firing at over 900 °C in the solid state and/or partly liquid state from the melt. However, as observed with the microscope, in those samples, slag is adhered to the ceramic (samples H, J and K). The melt of the slag is surrounded by partially reacted quartz grains; in some samples (sample H) the grains of quartz sand transformed into the high-temperature-modified cristobalite during the firing, which suggests a temperature of 1200 °C. According to the SEM-EDS analyses the glassy phase within this group contains rather smaller amounts of Fe (up to amount fractions 2 %) and larger amounts of Mg (about amount fractions 3 %) with respect to the first group. Furthermore, compared with the olivine of the first group, olivine laths contain a higher amount fractions of Mg (8 %) and less Fe (16 %). Hedenbergite and monticellite also crystallized in some samples that incorporated enhanced values of Ca (around 6.5 %). Ca-rich minerals, such as augite, hedenbergite and monticellite, formed due to the enhanced Ca content in the melt, which could have originated from several sources such as ore, ash, furnace lining or an addition of lime fluxes[13]. The use of sideritic ore for the iron production was proved by the preserved carbonate structures in sample I (**Figure 3d**). The siderite ore known from the vicinity of the archaeological site, i.e., Savske jame, Jesenice, occurring as veins between dolomite and limestone[14] could have eventually contributed to the higher lime levels. Concerning the furnace or smith's hearth linings, a lime-rich furnace lining might have resulted in the formation of lime-rich slag even if the smelted ore contained little lime[13]. A high quantity of pores is characteristic for the samples within the group.

3.2 Chemical analysis

The major elements of the 12 investigated samples along with their mean and standard deviations are presented in **Table 2**. The samples have heterogenic chemical compositions.

The amount fractions of SiO_2 ranges from 5.79 % to 65.24 % in the samples. The highest SiO_2 concentrations are detected in the samples of the second group (F–L).

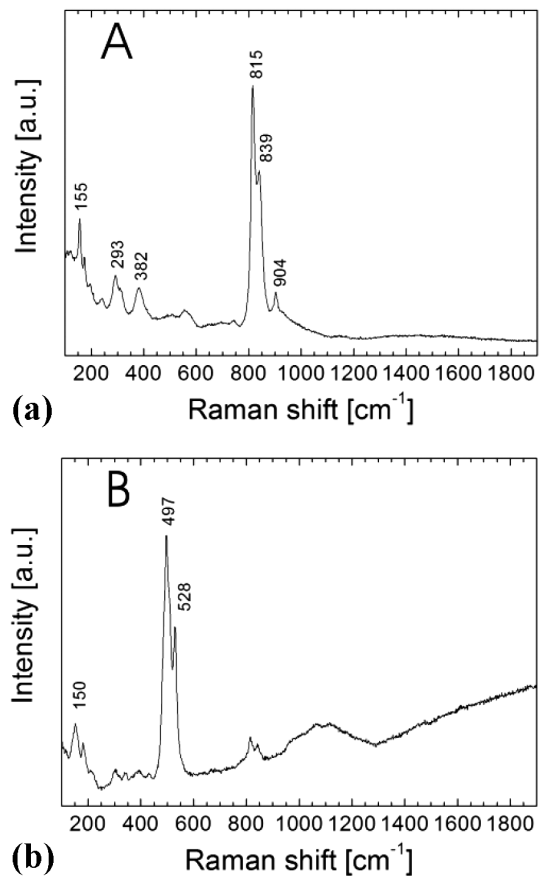

Figure 4: Raman spectra of the slag minerals of: a) fayalite (sample D) and b) leucite (sample G)

Slika 4: Ramanski spekter mineralov žlindre: a) fajalit (vzorec D) in b) levcit (vzorec G)

Table 2: Chemical compositions (mass fractions, *w*/%) of the samples
Tabela 2: Kemijska sestava (masni deleži, *w*/%) vzorcev

Sample	SiO_2	Al_2O_3	Fe_2O_3	MgO	CaO	Na_2O	K_2O	TiO_2	P_2O_5	MnO
A	11.20	3.16	87.30	1.00	2.56	0.07	0.62	0.16	0.58	0.16
B	15.43	3.92	72.77	0.66	1.44	0.16	0.68	0.22	0.42	0.15
C	11.16	2.90	68.98	0.48	2.17	0.17	0.75	0.15	0.59	0.15
D	17.36	4.40	70.23	0.83	1.90	0.18	0.82	0.25	0.25	0.18
E	5.79	1.23	77.93	0.27	0.98	0.05	0.16	0.07	0.58	0.10
F	33.11	7.03	46.68	2.70	8.85	0.64	2.60	0.38	0.47	0.16
G	57.62	14.32	14.27	1.93	4.61	0.95	4.16	0.73	0.20	0.08
H	52.76	11.91	10.03	5.13	11.81	0.61	2.74	0.56	0.69	0.15
I	25.49	7.06	39.64	2.78	14.42	0.48	3.17	0.36	2.53	0.38
J	54.77	14.33	6.18	6.21	10.76	0.61	1.82	0.77	0.54	0.13
K	65.24	17.36	7.73	2.06	1.47	0.74	3.80	1.10	0.32	0.16
L	56.49	10.87	17.50	1.54	6.44	2.48	1.81	0.46	1.04	0.16
Min	5.79	2.90	6.18	0.27	1.44	0.07	0.16	0.07	0.20	0.08
Max	65.24	17.36	87.30	6.21	11.81	2.48	4.16	1.10	2.53	0.38
Mean	33.87	8.21	43.27	2.13	5.62	0.60	1.93	0.43	0.68	0.16
SD	22.06	5.37	31.15	1.86	4.73	0.66	1.35	0.31	0.62	0.07

Iron (Fe_2O_3) and alumina (Al_2O_3) concentrations range from 6.18 % to 87.30 % and from 2.90 % to 17.36 %, respectively. The highest Fe_2O_3 concentrations are determined in samples A–E (the first group), which are mostly associated with different types of iron oxides and hydroxides (weathering) and the presence of wüstite and fayalite in these samples. According to the increased abundance of alumosilicates (augite, leucite, cordierite, mullite, and anorthite) in the studied samples, the samples of the second group contain the highest amount of Al_2O_3. Alkalis have moderate concentrations (0.05–2.48 % for Na_2O and 0.16–4.016 % for K_2O). The highest potassium amounts are observed in the samples of the second group, which are associated with the higher leucite amounts in the mentioned samples. In addition, the glassy matrix also hosts the elements that do not enter crystalline silicates, such as potassium originating from the charcoal[15]. MgO ranges between 0.27 % and 6.21 % (the highest values in the samples of the second group might be related to the occurrence of the Mg-rich olivine and Mg-enriched glassy matrix), while the CaO content varies between 0.28 % and 14.42 % and is enhanced in the samples of the second group where it is sometimes incorporated in the Ca-rich olivine and hedenbergite. Titanium (TiO_2) and phosphorous (P_20_5) concentrations range from 0.07 % to 1.10 % and from 0.20 % to 2.53 %, without significant variations amongst the analysed samples.

The major elemental compositions generally confirm the mineral compositions of the slag samples. Additionally, the chemical compositions of the major elements were subjected to a multivariate analysis in order to distinguish individual groups among the samples studied. **Figure 5** shows the results of the multivariate analysis.

Two features became evident from the evaluation of **Figure 5**. First, two samples, F and I, are placed as outliers within the first group. This could be because of the absence or a small quantity of the slag minerals. Second, the remaining 10 samples are clustered into two different groups according to the prevailing component: Fe-minerals or alumosilicates. The first group includes five samples (A–E) characterized by high Fe_2O_3 and low SiO_2 contents. The second group comprises five samples (G, L, K, H, and J) characterized by high SiO_2 contents, most probably derived from quartz.

The enhanced Al_2O_3 values result in the crystallization of plagioclases and other alumosilicates. In the samples of the second group Mg is enhanced and it is incorporated in the glassy phase, especially in samples H and J. In addition, olivine minerals are also enriched in Mg in these samples, as identified with SEM-EDS. The samples of the second group have enhanced values of Ca in the glassy phase. The enhanced Ca values in the samples of the second group allow the occurrence of Ca-rich olivines – kirschsteinite and monticellite – and Ca-rich pyroxene hedenbergite, and Ca is incorporated in the glassy phase. The Na values are enhanced in the samples of the second group and could be incorporated in the augite minerals, which was proved with the XRD analy-

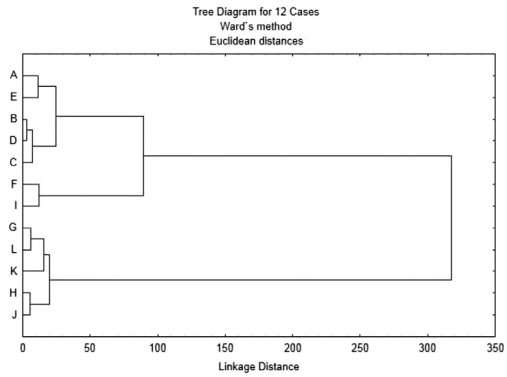

Figure 5: Investigated-sample dendrogram
Slika 5: Dendrogram preiskanih vzorcev

sis of the samples in the second group. Potassium is sourced from the charcoal and is enhanced in the samples of the second group, where it could be incorporated in the leucite mineral and the glassy matrix. K and Na are correlated, which could indicate that Na and K were derived together from wood or charcoal.

4 CONCLUSIONS

The obtained results showed that the investigated samples from the archaeological site near Mošnje (Slovenia) indicate an iron production.

The samples are recognized as iron slags that can be grouped into two main slag classes according to their mineral compositions, representing different stages of the iron processes. The first group is characterized by high Fe_2O_3 and CaO and low SiO_2 contents. The second group is characterized by high SiO_2 contents. The phase occurrence obviously depends on the chemical composition as the first group consists of fayalite, wüstite and magnetite and the second of augite, hedenbergite, monticellite and kirschsteinite. The slag in some samples of the second group is adhered to the ceramic, indicating smelting or smith's hearth lining, which could have been the source of the enhanced CaO values of those samples. The preserved carbonate structures indicating roasted siderite ore prove the use of the local siderite ore for the iron production.

The results showed that samples A (SU 280), G (SU 367) and L (SU 38) are very particular due to their surface textures or mineral compositions. Sample C from SU 38 belongs to a similar group of samples (B, D, and E), which were found in SU 126 and 281. The second group of similar samples (F, H, I, J and K) was found in Roman layers SU 194, 281, 296, 285 and 337. Thus, the groups established on the basis of the chemical-mineralogical analyses are not in complete accordance with the grouping of the samples based on their stratigraphy. For instance, among slag samples C, B, D and E, only one example (E) was found in the layer that is dated to the Roman period, while the rest are dated to a longer period – from prehistory to the modern era. However, the results indicate general varieties in the types of the slag from the archaeological site of Mošnje that can be defined in more detail only with a further study.

Acknowledgements

The above analyses were conducted as part of the post-excavation process and the study of the archaeological site of Mošnje – Pod cesto (EŠD 10036). This work was financially supported by ARRS Programme Group P2-0273 and Programme Group P1-0195.

5 REFERENCES

[1] J. Lux, M. Sagadin, Emona between Aquileia and Pannonia, Symposium in memory of Ljudmila Plesničar Gec, City Museum of Ljubljana, Slovenia, 2010, 27–28

[2] M. L. Wayman, Mater. Charact., 45 (**2000**), 259–267, doi:10.1016/S1044-5803(00)00108-X

[3] R. Pleiner, Iron in Archaeology: The European Bloomery Smelters, Archaeological Institute of the Academy of Sciences, Praha 2000, 418

[4] R. Pleiner, Iron in Archaeology: Early European Blacksmiths, Archaeological Institute of the Academy of Sciences, Praha 2006, 379

[5] V. F. Buchwald, Iron and Steel in Ancient Times, Royal Danish Academy of Sciences and Letters, Copenhagen, 29 (**2005**), 372

[6] N. Zupančič, M. Mišič, RMZ – Mater. Geoenviron., 48 (**2001**) 3, 447–457 (in Slovene)

[7] L. Orengo, P. Fluzin, Iron metallurgical remnants from Trnava, Trnava, ZVKDS, Ljubljana 2006, 62–66 (in Slovene)

[8] J. Lamut, J. Medved, Analyses of slag, Sela pri Dobu, ZVKDS, Ljubljana 2007, 63–66 (in Slovene)

[9] S. Kramar, V. Tratnik, I. M. Hrovatin, A. Mladenović, H. Pristacz, N. Rogan Šmuc, Archaeometry, (**2014**), doi:10.1111/arcm.12116

[10] M. Horvat, Sela pri Dobu, ZVKDS, Ljubljana 2007, 68 (in Slovene)

[11] U. Umek, Mineralogical characterization of Roman slag from archaeological site Mošnje, Diplomsko delo, Ljubljana, 2011, 162 (in Slovene)

[12] E. M. Nosek, The metallography of gromps, La sidéurgie ancienne de l´Est de la France dans son cintexte Européen, Ann. Litt. Univ. Besançon, 536 (**1994**), 65–73

[13] S. Paynter, Archaeometry, 48 (**2006**), 271–292, doi:10.1111/j.1475-4754.2006.00256.x

[14] B. Berce, Pregled železovih nahajališč LR Slovenije (Review of iron ore deposits in P. R. Slovenia), Prvi jug. Geol. Kongr., Ljubljana, 1956, 235–259 (in Slovene)

[15] A. Manasse, M. Mellini, J. Cult. Herit., 3 (**2002**), 187–198, doi:10.1016/S1296-2074(02)01176-7

UDK 519.61/.64:621.77
Original scientific article/Izvirni znanstveni članek

ISSN 1580-2949
MTAEC9, 49(3)349(2015)

REYNOLDS DIFFERENTIAL EQUATION SINGULARITY USING PROCESSES OF SMALL STRAINING WITH LUBRICATION

REYNOLDSOVA DIFERENCIALNA ENAČBA PRI PROCESIH MAJHNE DEFORMACIJE Z MAZANJEM

Dušan Ćurčija[1], Franc Vodopivec[2], Ilija Mamuzić[1]

[1]Croatian Metallurgical Society, Berislavićeva 6, Zagreb, Croatia
[2]Institute of Metals and Technology, Lepi pot 11, 1000 Ljubljana, Slovenia
ilija.mamuzić@public.carnet.hr

Prejem rokopisa – received: 2014-02-01; sprejem za objavo – accepted for publication: 2014-09-03

doi:10.17222/mit.2014.025

Frequently, simplified partial differential equations include transcendental functions with analytical solutions based on a singularity. Such solutions are characteristic for numerical analyses with strong Solvers and several programs singularities in the processes of dressing rolling mills with lubrication. The devised dynamical model includes the variability of the gripping angle and of the rolls radius in a section of continuous rolling. Below the real lubricant layer, in the analysis two apparent lubricant layers are presumed. The solution of the differential equation of the lubricant layer with the singularity is obtained using standard mathematical solutions for apparent lubricant layers. On the ring diagram, the transfer over the singularity shows a stronger disorder, i.e., disharmony, than the transfer over the transcendental point.

Keywords: Reynolds differential equation, singularity, dressing rolling mill, lubrication, geometrical centre

Pogosto poenostavljene diferencialne enačbe vključujejo transcendentne funkcije z analitičnimi rešitvami na podlagi singularne točke. Take rešitve so značilne za numerične analize z zmogljivimi reševalci in več singularnimi točkami v programih pri procesih dresirnih valjarn z mazanjem. Predlagan dinamičen model vključuje različnost prijemnega kota in premera valjev na delu kontinuirne valjalne proge. Pod realno plastjo maziva sta v analizi predpostavljeni dve navidezni plasti maziva. Rešitev diferencialne enačbe plasti maziva s točko singularnosti je dosežena z uporabo standardnih matematičnih metod za navidezni plasti maziva. Na krožnem diagramu prenos preko singularnosti pokaže večji nered oziroma disharmonijo, kot je prenos preko transcendentne točke.

Ključne besede: Reynoldsova diferencialna enačba, točka singularnosti, dresirna valjarna, mazanje, geometrična sredina

1 INTRODUCTION

The Reynolds[1] differential equation[2,3] is used for the analysis of the processes of the lubricated low reduction of metals (dressing, cold rolling and drawing) and a simplified equation is used[4,5]:

$$\frac{\mathrm{d}p}{\mathrm{d}x}=\frac{6\cdot\mu(v_0+v_\mathrm{R})}{\varepsilon^2(x)}-\frac{12\cdot\mu\cdot Q}{\varepsilon^2(x)} \tag{1}$$

The approximate solution using the transcendent equation is:

$$A=\frac{-\alpha}{2\varepsilon_0\cdot\psi}+\left(\frac{\Omega}{R\cdot\psi\cdot\xi^{0.5}}\right)+\frac{3\alpha}{2R\cdot\psi^2}-\left(\frac{3\varepsilon_0\cdot\Omega}{2R^2\cdot\psi^2\cdot\xi^{0.5}}\right) \tag{2}$$

$$\Omega=\ln\left(\frac{-\alpha-\xi^{0.5}}{-\alpha+\xi^{0.5}}\right)\quad \xi=-\psi\quad \psi=\frac{2}{R}\varepsilon_0-\alpha^2$$

$$A=\frac{1-\exp(-\gamma\cdot p_0)}{6\mu\cdot\gamma(v_0+v_\mathrm{R})} \tag{3}$$

where A is a technological parameter, R is the rolls radius, μ is the lubricant dynamical viscosity, v_0 and v_R are the rolling and circumferential rolls velocity, α is the rolling angle, $\varepsilon(x)$ is the geometry of the lubricant layer in the deformation zone, Q is the lubricant consumption, $\mathrm{d}p/\mathrm{d}x$ is the axial stressing gradient x, ε_0 is the thickness of the lubricant layer of the entry section of the deformation zone, γ is the piezo-coefficient of the lubricant viscosity and p_0 is the rolling pressure.

The entry roll in Section I has the radius R_1, the gripping angle α_1 and forms a lubricant layer with the thickness ε_1 (**Figure 1**). The exchange parameter ω in

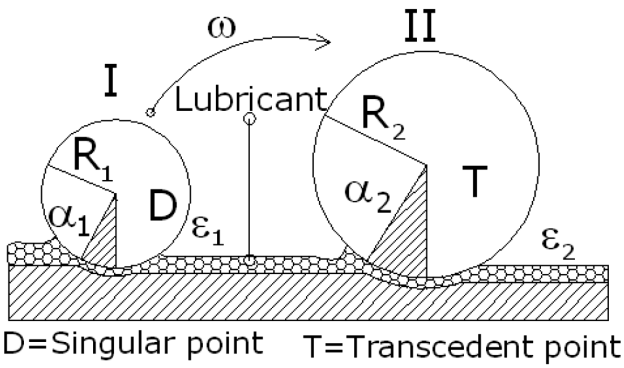

Figure 1: Scheme of the calculation of lubricant layer between two rolling stands. The entry roll I joins in the singularity, i.e., the transcedency point.

Slika 1: Shema izračuna plasti maziva med dvema valjalnima ogrodjema. Vstopni valj I doseže singularno točko oz. transcendentno točko.

Section II changes these parameters, either as: $R_2 = \omega^3 \cdot R_1$, $\alpha_2 = \alpha_1/\omega$ or $R_2 = R_1/\omega^3$, $\alpha_2 = \alpha_1 \cdot \omega$

The exit lubricant layer thickness ε_2 is calculated using the Solver solution of the transcendent Equation (2) and it is confirmed with a Monte Carlo numerical integration of Equation (1).

2 NUMERICAL ANALYSIS OF THE SINGULARITY *D* AND THE TRANSCENDENT POINT *T*

As a special case of the solution of the transcendent Equation (2) is the singularity solution acceptable for dressing processes. This solution[2,6] is:

$$\varepsilon_0^* = \frac{1}{2} R\dot{\alpha}^2 \qquad \dot{\alpha} = \sqrt[3]{\frac{8}{15R \cdot A}} \tag{4}$$

Figure 2 shows the occurrence of the singularity in the dressing process with respect to the lubricant-layer thickness and the gripping angle. With respect to the singularity, the transcendent point *T* is situated on the right-hand side.

The singularity creates a vicinity of unpredictable behaviour and the numerical analysis is spread around the singularity. The determinant (5) was used for the analysis:

$$\begin{bmatrix} \varepsilon_0^* & \varepsilon_0^{\mathrm{T}} \\ \varepsilon_0^{\mathrm{MS}} & \varepsilon_0^{\mathrm{MT}} \end{bmatrix} \tag{5}$$

where ε_0^* is the thickness of the lubricant layer for $\dot{\alpha}, \varepsilon_0^{\mathrm{MS}}$ is the thickness of lubricant layer according to the Mizuno-Grudev equation for α^*, $\varepsilon_0^{\mathrm{T}}$ is the thickness of the lubricant layer according to the transcendent Eq. (2) and $\varepsilon_0^{\mathrm{MT}}$ is the thickness of the lubricant layer according to the Mizuno-Grudev[6] equation $\alpha = \alpha^*/\varpi$ for $\alpha = \alpha^*/\omega$.

If the singularity is at the interaction of two points, the value of the determinant (5) tends to zero. In the absence of a singularity between the initial and the aimed for point, the value of the determinant (5) is zero. This allows us to describe all the aimed for points' values without a singularity using:

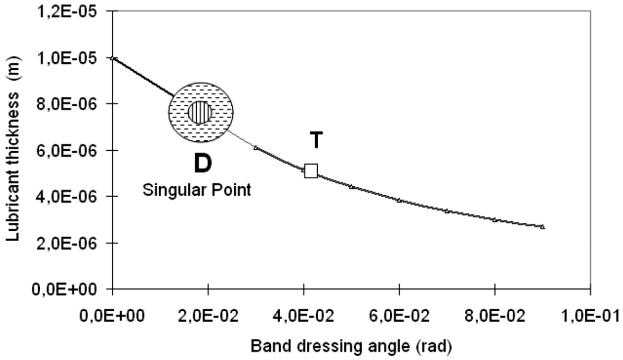

Figure 2: Vicinity of the singularity (singular point) $D(\dot{\alpha};\varepsilon_0^*)$ and the transcendent point *T*

Slika 2: Bližina singularne točke $D(\dot{\alpha};\varepsilon_0^*)$ in transcendentne točke *T*

$$\varepsilon_0^{\mathrm{Target}} = \frac{R \cdot \sqrt[3]{\left(\frac{8}{15R \cdot A}\right)^2}}{2\omega} \tag{6}$$

where ω is a proportionality constant in the technical signification equal to the deformation degree. In the analysis, the apparent lubricant layer ε_0 (column *J*) is divided by the aimed analysis into two pseudo layers (columns *H* and *I* in **Tables 1** and **2**).

3 SOLVER CALCULATION USING EQUATIONS (2) AND (6) WITH THE INITIAL ON THE SINGULARITY

The results of calculations using the Solver (MathCAD, EXCEL) after the commutation law of multiplication for the condition of the technological process are listed in **Table 1**. With respect to the commutation law of multiplication, the external ring *J* is the product of the inner two rings *H* and *I*. The imagined is the rolling line with rolling 10 cages with deformation degrees varying from cage to cage. The results of the calculations are listed in **Table 2** for increasing values of π.

The constructive coefficient of transfer between two rolling stands is $\alpha \cdot R = 0.22145 \cdot \omega^2$.

Table 1: Solver calculations for Eq. (2) for three singularity rings. The variability of ω influences the variability of the clutch angle α and the rolls radius *R*.

Tabela 1: Izračuni enačbe (2) z uporabo reševalca za tri singularne obroče. Variabilnost ω vpliva na variabilnost prijemnega kota α in polmera valjev *R*.

ω = 2.2	*H*	*I*	*J*
2	5.6881486648E-05	4.3089901167E-01	2.4510176379E-05
2.2	5.6754502094E-05	4.7504943260E-01	2.6961194017E-05
2.22	5.2837299927E-05	5.1490700355E-01	2.7206295781E-05
2.222	6.2070776615E-05	4.3870573952E-01	2.7230805957E-05
2.2222	5.4395165663E-05	5.4219876699E-01	2.9492991753E-05
2.22222	5.9160153196E-05	4.6033521899E-01	2.7233502077E-05
2.222222	5.2737233458E-05	5.1640036463E-01	2.7233526587E-05
2.2222222	5.4753146188E-05	4.9738747779E-01	2.7233529284E-05
2.22222222	4.7791846331E-05	5.6983630888E-01	2.7233529308E-05
2.222222222	5.6585859142E-05	4.8127800343E-01	2.7233529310E-05

Table 2: Solver calculations for three singularity rings using Eq. (2)
Tabela 2: Izračuni z uporabo reševalca za tri obroče singularnosti z enačbo (2)

$\omega = \pi$	H	I	J
3	9.0652411487E-01	4.0556839290E-05	3.6765752839E-05
3.1	7.2525287463E-01	5.2383491694E-05	3.7991277934E-05
3.14	9.9122718480E-01	3.8822066788E-05	3.8481487970E-05
3.141	6.2041700114E-01	6.2044951242E-05	3.8493742586E-05
3.1415	9.7002625173E-01	3.9689514361E-05	3.8499870849E-05
3.14159	8.4111868525E-01	4.5773532910E-05	3.8500973821E-05
3.141592	8.2952986160E-01	4.6413034797E-05	3.8500998332E-05
3.1415926	1.0885265884E+00	3.5369834871E-05	3.8501005684E-05
3.14159265	8.8297139988E-01	4.3603910956E-05	3.8501006297E-05
3.141592654	8.0201286093E-01	4.8005472508E-05	3.8501006346E-05

Figure 3 has a mark for the turn of the apparent lubricant rings H and I with the singularity as the initial point with respect to the fictive outer lubricant layer for the cage rolling for ten cages in the rolling line.

The transfer in **Figure 4** also indicates the discordance of the inner two rings as in **Figure 3**, where the transfer was achieved using the Solver.

4 APPARENT LUBRICANT LAYERS *H* AND *I*

The Solver solution of the transcendent equation, the apparent layers H and I may have different results for an equal degree of deformation, as listed in **Table 3**. The value of the lubricant layer $J = H * I$ is equal, as also shown by the solution of Eq. (1).

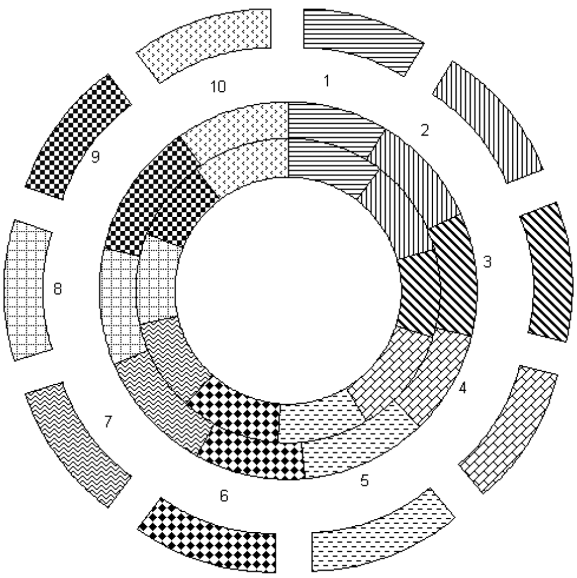

Figure 3: Aimed for transcendent point from the singularity after the Solver and Eq. (2) with: $\omega = 2.222222222$, $\alpha = 1.107262798/\omega$, $R = 0.2 \cdot \omega^3$, $A = 1965512\ \mathrm{m}^{-1}$, $R = 0.2$ m, $\alpha = 1.107402627$ rad, $\mu \cdot \gamma = 5.232 \cdot 10^{-9}$ and $p_0 \cdot \gamma = 4.36$ s

Slika 3: Ciljana točka transcendentnosti na podlagi singularnosti, izračunane z uporabo reševalca in enačbe (2) z : $\omega = 2{,}222222222$, $\alpha = 1{,}107262798/\omega$, $R = 0{,}2 \cdot \omega^3$, $A = 1965512\ \mathrm{m}^{-1}$, $R = 0{,}2$ m, $\alpha = 1{,}107402627$ rad, $\mu \cdot \gamma = 5{,}232 \cdot 10^{-9}$ in $p_0 \cdot \gamma = 4{,}36$ s

The constructive transfer coefficient between two rolling cages is $\alpha \cdot R = 0.22145/\omega^2$.

The data in **Table 3** are depicted in **Figure 5**.

The results of the investigation of the columns H and I are listed in **Table 4**. The geometrical average of the column J is obtained using the apparent lubricant layers K and I. The relation of the column J and the apparent lubricant columns K and I are also supported by the standard mathematical averages: arithmetic, harmonic, geometric, quadratic, etc.

Although having an equal value to the external, i.e., third ring J, the lower apparent rings H and I are in disharmony with the external ring, and only with values for $i = 1$ is the harmony achieved. The second series $i = 2$ creates the inversion of the two internal rings, while the series $i = 3$ supports the turn, i.e., with respect to the external ring J. As explained already, this is supported by

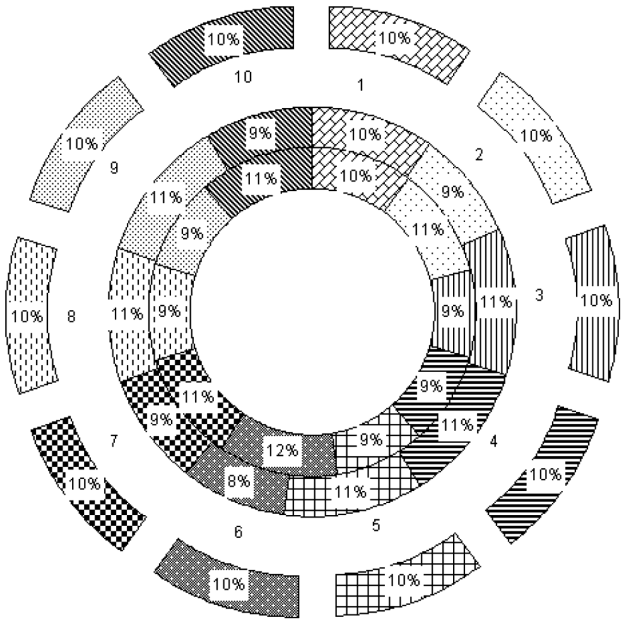

Figure 4: Transfer of similarity for the singularity to the transcendent point using Eq. (6)

Slika 4: Prenos podobnosti s točke singularnosti na točko transcendentnosti z enačbo (6)

Table 3: Different values in the columns *H* and *I* for the equal degree of deformation ω = 3
Tabela 3: Različne vrednosti v kolonah *H* in *I* za enako stopnjo deformacije ω = 3

i	ω = 3.0	*H*	*I*	*J*
1	3	3.6080500075E-05	1.1321986636E-01	4.0850293967E-06
2	3	3.6684996110E-05	1.1135422733E-01	4.0850293964E-06
3	3	4.4999094308E-05	9.0780258123E-02	4.0850293966E-06
4	3	4.5445189361E-05	8.9889148972E-02	4.0850293965E-06
5	3	5.1287540856E-05	7.9649547013E-02	4.0850293966E-06
6	3	6.1373811833E-05	6.6559812314E-02	4.0850293966E-06

Table 4: Geometrival averages of columns *H* and *I* in interval form
Tabela 4: Geometrična povprečja kolon *H* in *I* v intervalni obliki

Δi	*H*	*I*	*J*
i = 1 to 6	4.5193358310E-05	9.0390038477E-02	4.0850293966E-06
i = 2 to 6	4.5232311633E-05	9.0312196062E-02	4.0850293966E-06
i = 3 to 6	4.3833687801E-05	9.3193833361E-02	4.0850293966E-06
i = 4 to 6	3.9181673469E-05	1.0425867593E-01	4.0850293966E-06

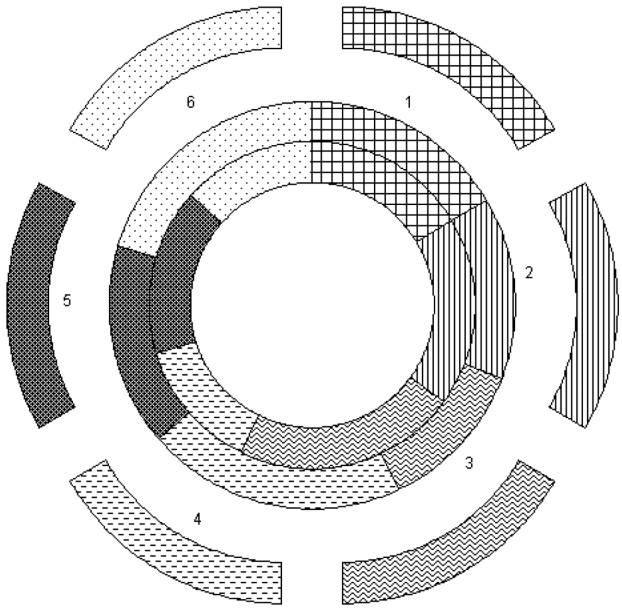

Figure 5: Ring diagram of **Table 3** calculated using the Solver from the initial singularity for two rolling stands
Slika 5: Krožni diagram **tabele 3**, izračunan z reševalcem od začetne točke singularnosti za dve valjalni ogrodji

the mathematical average and the law of commutation of the hyperbolic multiplication.

Further, the numbers in **Table 4** show that for the values of columns *J* (*J* = *H* * *I*):

$$G = A \cdot H \tag{7}$$

G is the geometrical average for column *J*
A is the arithmetic average for column *I*
H is the harmonic average for column *H*.

The numbers in column *J*, **Table 3** could also be obtained with the opposite values of the apparent lubricant layers *K* and *I*, e.g.:

$$G = \frac{H_6 + I_4}{2} \cdot \frac{2}{(1/H_4)+(1/I_6)} = 4.0850293966E-06 \tag{8}$$

The connection between the apparent layers is supported by the algebraic opposite identity of several possible and with respect to **Table 3**, on the hyperbole for the first step it is:

$$\sqrt[3]{\frac{(H_{i+1})^3+(I_i)^3}{2}} + \sqrt[3]{\frac{(H_{i+1})^3+(I_{i+1})^3}{2}} = 2\sqrt[3]{\frac{(H_{i+1})^3+(I_{i+2})^3}{2}} \tag{9}$$

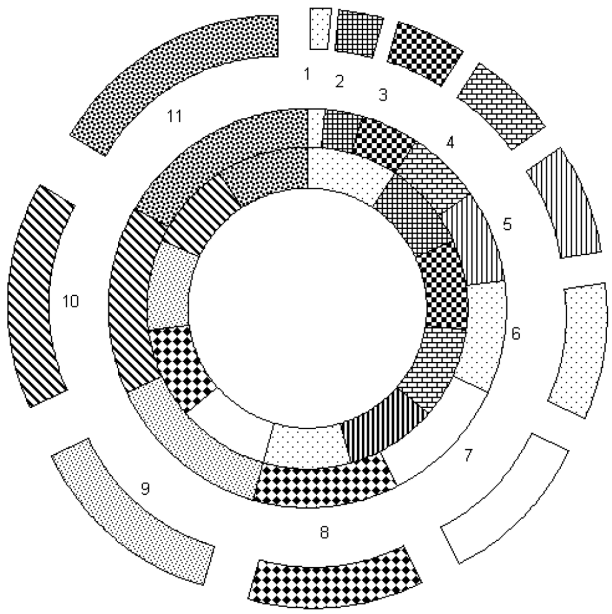

Figure 6: Disorder on the transcendent point by a large degree of metal deformation using the initial singularity calculated with the Solver
Slika 6: Nered na točki singularnosti pri veliki stopnji deformacije za začetno točko singularnosti, izračunano z reševalcem

Table 5: Solver calculation for large metal deformation from the singularity to the transcendent point
Tabela 5: Izračuni z uporabo reševalca za velike deformacije od točke singularnosti do točke transcendentnosti

	H	*I*	*J*
2	4.9140375541E-01	1.4369767894E-05	7.0613579075E-06
3	4.9140375543E-01	2.8739535788E-05	1.4122715816E-05
4	4.9140375554E-01	4.3109303672E-05	2.1184073723E-05
5	4.9140375543E-01	5.7479071576E-05	2.8245431631E-05
6	4.9140375544E-01	7.1848839468E-05	3.5306789539E-05
7	4.9140375585E-01	8.6218607289E-05	4.2368147446E-05
8	4.9140375543E-01	1.0058837526E-04	4.9429505355E-05
9	4.9140375543E-01	1.1495814315E-04	5.6490863261E-05
10	4.9140375543E-01	1.2932791105E-04	6.3552221172E-05
11	4.9140375543E-01	1.4369767894E-04	7.0613579078E-05
12	4.9140375543E-01	1.5806744683E-04	7.7674936983E-05

The singularity coexists with two apparent lubricant layers, which are in the ring diagram incongruous with respect to the external apparent lubricant layer *J* and the disharmony i.e., the disorder may be obtained. The internal apparent lubricant rings rotate with respect to the external fixed ring and neither are congruent.

5 LARGE METAL DEFORMATION

The calculation results are listed in **Table 5**. By transferring the similarity from cage to cage, the deformation coefficient varies strongly.

In **Figure 6** the data from **Table 5** are depicted as a ring diagram. The great rings disorder by the transfer of disharmony on the outer ring *J* was calculated using the transcendent Eq. (2). The results of this calculation[7] were confirmed by a numerical integration[7] Monte-Carlo of Eq. (1). The apparent column *H* is constant by rolling on a line with 11 rolling cages.

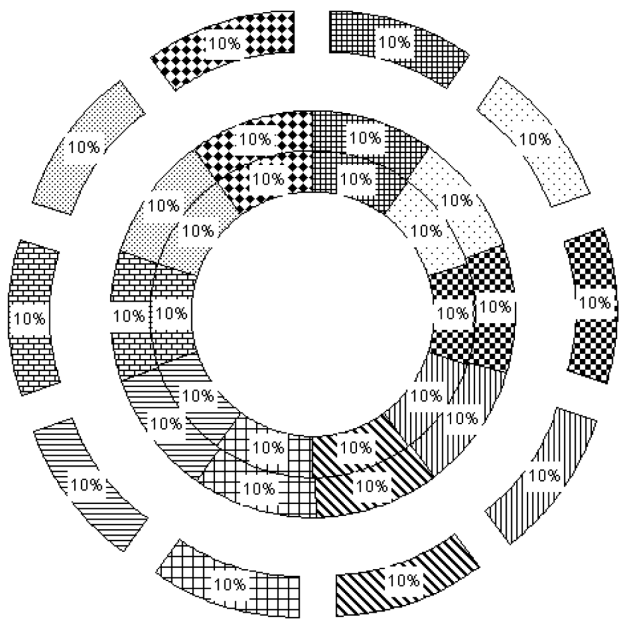

Figure 7: Example of rhythmics by ten cages
Slika 7: Primer ritmičnosti za deset ogrodij

6 TRANSFER TRANSCENDENT TO TRANSCENDENT POINT

The initial roll in **Figure 1** is on the transcendent point *T* in **Figure 2**. The Solver calculation of the lubricant layer between two connected cages shows great stability and rhythmics (**Figure 7**).

The apparent lubricant layers *K* and *I* turn within and unrelated to the external lubricant layer *J*. The congruency of all three rings is achieved without discordant inversions in rings *H* and *I*.

The transfer is:

$$R_{i+1} = \omega^3 R_i \qquad \alpha_{i+1} = \alpha_i / \omega \qquad \alpha_i = 3.141592654$$

Using ω = 1 no transfer of similarity coefficient should occur as both rolls in **Figure 1** are in the same position and no metal deformation occurs on the dressing line.

7 CONCLUSION

The mixing and penetration of the layers in the *H* and *I* rings by calculation using Eq. (6) are the evaluation of the stability of technological procedure of rolling on continuous lines with different degrees of deformation ω. The mixing is diminished essentially by Solver calculations, although the layer inversion could be obtained, also. Besides inversion, according to law commutation of multiplication, the layers are inclined to rotation at the singularity with respect to the outer layers. For proper use of the Solver program, experience is necessary. The apparent layers *H* and *I* are connected to the column *J* and the related geometrical average after Eq. (7) verified by numerical integration. It was shown that the data in column *J* in **Table 4** could also be calculated using Eq. (8), which was not generalised. Eq. (9) is a possible connection of apparent lubricant layers *K* and *I*. The transcendent point shows the marked order for the lubricant layer better than the singularity.

The results of the calculation of lubricant layer using the Reynolds equation agree well with experimental results for the processes of dressing of bands and cold

tube drawing[8,9] and by investigations of the contact friction[10].

Acknowledgements

The authors are indebted to prof. F. Vodopivec for useful comments and the Croatian-to-English translation of the manuscript.

8 REFERENCES

[1] D. Ćurčija, F. Vodopivec, I. Mamuzić, Mater. Tehnol., 47 (**2013**) 1, 53–57

[2] D. Ćurčija, I. Mamuzić, Mater. Tehnol., 41 (**2007**) 1, 21–27

[3] D. Ćurčija, I. Mamuzić, Mater. Tehnol., 42 (**2008**) 2, 59–63

[4] D. Ćurčija, I. Mamuzić, Metalurgija, 44 (**2005**) 3, 221–226

[5] D. Ćurčija, I. Mamuzić, Metalurgija, 44 (**2005**) 4, 295–300

[6] D. Ćurčija, Mater. Tehnol., 37 (**2003**) 5, 237–250

[7] M. I. Sobol, Die Monte Carlo Methode, Ver. H. Deutsch, Frankfurt a. Main 1986

[8] O. P. Maksimenko, A. A. Semenča, Issledovanie kontaktno-gidrodinamičeskoj smazki pri prokatke, Sučasni problemi metallurgii, 8 (**2005**), 99–103

[9] M. R. Jensen, L. Olovsson, J. Danckert, Numerical model for the oil pressure distribution in the hydromechanical deep drawing process, J. Mater. Process. Techn., 103 (**2000**) 1, 74–79, doi:10.1016/S0924-0136(00)00421-0

[10] P. Heyer, J. Läuger, Correlation between friction and flow of lubricating greases in new tribometer device, Lubrication Science, 21 (**2009**) 7, 253–268, doi:10.1002/ls.88

UDK 621.941:539.538:539.42
Original scientific article/Izvirni znanstveni članek

ISSN 1580-2949
MTAEC9, 49(3)355(2015)

PREDICTION OF THE CATASTROPHIC TOOL FAILURE IN HARD TURNING THROUGH ACOUSTIC EMISSION

NAPOVEDOVANJE KATASTROFIČNE POŠKODBE KERAMIČNIH VLOŽKOV PRI STRUŽENJU Z AKUSTIČNO EMISIJO

Mária Čilliková[1], Branislav Mičieta[1], Miroslav Neslušan[1], Robert Čep[2], Ivan Mrkvica[2], Jana Petrů[2], Tomáš Zlámal[2]

[1]University of Žilina, Faculty of Mechanical Engineering, Univerzitna 8215/1, 010 26 Žilina, Slovakia
[2]VŠB-Technical University of Ostrava, Faculty of Mechanical Engineering, 17. listopadu 15, 708 33 Ostrava, Czech Republic
maria.cilikova@fstroj.uniza.sk

Prejem rokopisa – received: 2014-02-07; sprejem za objavo – accepted for publication: 2014-09-03

doi:10.17222/mit.2014.029

The paper deals with a new concept for the detection and prediction of the catastrophic tool failure (CTF) of ceramic inserts using an acoustic emission (AE) technique and an associated analysis of the chip formation during hard turning of bearing steel 100Cr6. The suggested method is based on the application of two sensors and the ratios of parameters of the acoustic emission such as AE RMS, AE absolute energy, and AE strength. The specific character of the segmented chips during hard turning is associated with the raw acoustic signals as well as the extracted AE features. The paper indicates that the conventional data processing of acoustic emission signals enables the detection of CTF. Tool wear connected with the cutting edge micro-chipping is related to the slow increase of tool wear (mainly flank wear VB) and stable values of AE features in the normal phase of tool wear. The CTF alters the AE waveforms as well as the course of the AE features. Conventional AE signal processing enables the detection of tool breakage. However, approaching CTF itself cannot be reliably predicted. Hence, a new concept of AE processing based on the ratios of the extracted AE features obtained in the different frequency ranges is suggested.

Keywords: hard turning, acoustic emission, wear, prediction

Članek obravnava nov način odkrivanja in napovedovanja porušitve (CTF) keramičnih vložkov z uporabo tehnike akustične emisije (AE), povezano z analizo nastanka ostružka med struženjem jekla 100Cr6 za ležaje. Predlagana metoda temelji na uporabi dveh senzorjev in razmerij pri akustični emisiji, kot so AE RMS, absolutna energija AE in AE-moč. Specifična oblika delca ostružka med struženjem je povezana s surovim akustičnim signalom, kot tudi z ločenimi AE-lastnostmi. Članek obravnava, kako konvencionalna obdelava podatkov signalov akustične emisije omogoča določitev CTF. Obraba orodja je povezana s krušenjem rezilnega roba ter s počasnim povečanjem obrabe orodja (večinoma obrabe boka VB) in s stabilnimi vrednostmi AE-lastnosti pri normalni obrabi orodja. CTF spreminja obliko AE-valov, kot tudi AE-lastnosti. Konvencionalna obdelava AE-signalov omogoča odkritje loma orodja. Vendar pa napovedovanje nastanka CTF ni mogoče zanesljivo napovedati. Predlagan je torej nov način obdelave AE, ki temelji na izbranih AE-lastnostih, dobljenih pri različnih območjih frekvenc.

Ključne besede: struženje, akustična emisija, obraba, napovedovanje

1 INTRODUCTION

The hard tuning process has found great industrial relevance as a result of recent developments in machine tools (especially cubic boron nitride and ceramics). High flexibility, high removal rates, and the ability to manufacture a complex workpiece geometry in one set are the main advantages of hard turning operations compared to grinding[1]. Furthermore, hard turning makes it possible to avoid coolants and therefore can actually be regarded as an interesting alternative, even from the ecological point of view[1,2].

On the other hand, the main disadvantages of hard turning can be found in the formation of white layers induced in the early stages of tool wear and the high risk of unexpected catastrophic tool failures (CTFs) at the end of the normal phase of tool wear (especially in the case of ceramic inserts[3]). Macro-chipping of the cutting edge should be regarded as a serious problem. CTF can damage the machined surface or tool holder and dramatically alter the tool geometry and corresponding workpiece dimensions. Thus, hard turning operations need the incorporation of a properly proposed monitoring system for the detection or, much better, the prediction of CTF.

Lee, Dornfeld, and Wright[4] reported on a variety of sensors, each having a certain degree of applicability, for the monitoring of the cutting process. Monitoring techniques based on the implementation of dynamometers, accelerometers, laser interferometers, acoustic emission, and so on were proposed and properly integrated into machine control systems[5]. However, the specific mechanism of chip formation during hard turning means that specific requirements should be met to suggest the proper concept for monitoring hard turning operations.

It is well known that segmented chips are produced during hard turning[6,7] as a result of the poor plasticity and high hardness and strength of the work material. Thus, thermal softening dominates over strain hardening when the hardness of the work material attains a certain value. It should also be mentioned that the shear instability during chip segmentation is a function, not only of

the hardness of the work material, but also such aspects as cutting conditions or tool geometry[6,7]. **Figure 1** illustrates a segmented chip during the turning of hardened steel 100Cr6. Poulachon and Moisan[8] published an outstanding study of the different phases of chip segmentation as a series of micrographs. They clearly proved that segment formation starts with a crack initialization near the free surface and its propagation towards the tool tip of the cutting edge (zone Ib; **Figure 2**). However, crack propagation transforms into a plastically deformed zone where microcracks still occur (zone Ia, **Figure 2**). The variable chip cross-section is due to the sliding of a segment along the fully cracked surfaces as well as the thinning of the microcracked region during sliding.

Severe plastic deformation can also be found at the tool–chip interface. Thus, the segmented chip is a mixture of zones of extremely high intensity structural transformation located on segment boundaries (narrow white bands) and the nearly untouched structure inside the segment.

In the case of a continuous chip, the rapid shift of the plastic deformation from the actual shear plane to the adjacent plane of the incoming work material is driven by the strain hardening. Therefore, a more pronounced homogeneity of the continuous chip can be found. As a result of the different mechanism of chip formation, conventional soft turning is a process during which the energy needed for chip separation is continuously released, while the chip segmentation represents the cyclic process when the energy accumulated in front of the cutting edge is suddenly emitted when the shear strain near the free surface attains the value which the structure cannot afford to exceed[7].

This cyclic process is associated with the fluctuation of the cutting force and the corresponding segmentation frequency. This segmentation frequency is a function of the work material properties and the cutting conditions as well as the tool geometry. Shaw and Vyas[6] reported that the segmentation frequency is about 18 kHz for a cutting speed of 100 m min^{-1} and a feed of 0.28 mm, and the case of carburized steel with a hardness of 62 HRc. Neslušan[3] reported that the segmentation frequency is strongly dependent on the feed and cutting speed and can be found in the range of 14 kHz to 90 kHz. A dynamic analysis of the processes that fluctuate at a frequency over 25 kHz with the application of conventional accelerometers or dynamometers is difficult to carry out. On the other hand, acoustic emission (AE) techniques enable detection of processes that fluctuate at a frequency over several megahertz.

The AE technique can be successfully adapted for machining operations[9]. This technique is sensitive to events such as dislocation movements, deformation, inclusion fracture, crack propagation, and so on. The major AE sources[10] in a metal cutting process are the deformation and fracture of work materials in the cutting zone, deformation, and mainly the fracture of cutting tools, collisions, entanglement, and the breakage of chips.

AE signals can be classified[11,12] as being either continuous-type or burst-type AE signals. Continuous signals are usually associated with shearing in the primary zone and at the tool–chip and tool–workpiece interfaces, while burst-type AE signals are observed during crack growth in the material, tool fracture, or chip breakage. The major advantage of the AE technique is its high frequency range (much higher than that of the machine vibrations and environmental noises)[10].

AE techniques were adapted for monitoring turning[13], milling[14], drilling[15], grinding[16,17], and precision machining[18]. Suggested concepts based on the AE technique are based on the sensitivity of the AE signal to various contact areas and deformation regions. Jemielniak and Otman[19] reported that the skew and kurtosis extracted from the raw AE signal are more sensitive to CTF than conventional AE signals and AE features. Li and Yuan[20] gives a brief review of the acoustic emission methods for tool-wear monitoring during turning. Dolinšek and Kopač[21] investigated the AE signals and associated process

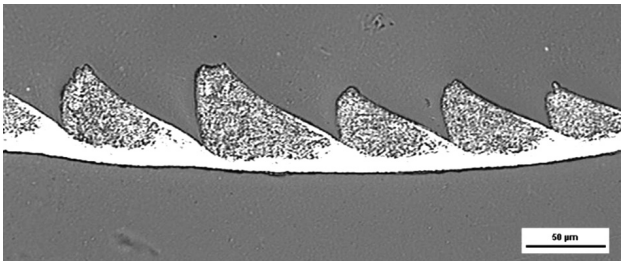

Figure 1: Segmented chip 100Cr6 (hardened 62 HRc), v_c = 100 m min^{-1}, f = 0.09 mm

Slika 1: Segmentirani ostružki 100Cr6 (trdota 62 HRc, v_c = 100 m min^{-1}, f = 0,09 mm

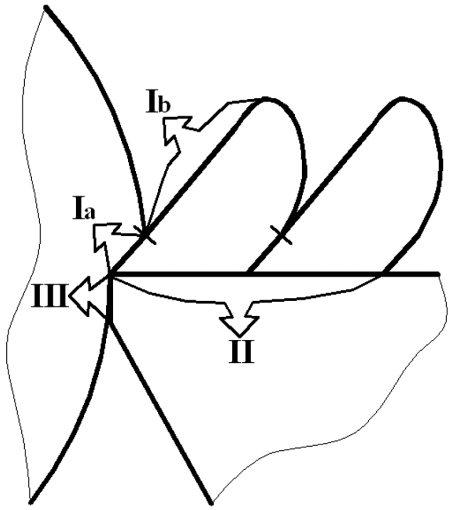

Figure 2: Cutting zone during hard cutting – brief sketch: Ia-microcracked and plastically deformed shear zone, Ib-cracked region, II-tool–chip contact, III-tool–workpiece contact

Slika 2: Območje rezanja med struženjem – shematsko: Ia-plastično deformirano področje striženja z mikrorazpokami, Ib-razpokano področje, II-stik orodje-ostružek, III-stik orodje-obdelovanec

of tool-wear monitoring. They noticed that tool wear is one of the most influential factors contributing to an increase in the energy of the AE signal. Govekar, Gradišek, and Grabec[22] suggested a system and methods for the extraction of useful information from signals of multiple sensors (including the AE technique). Inasaki[12] reported that continuous-type AE signals are associated with plastic deformations in ductile materials, while burst-type signals are observed during crack growth in the material. Also, many attempts to predict tool wear have been investigated, such as the pattern-classification methodology, fuzzy classifiers, neural networks, and sensor and data fusion methodology, overviewed in.[20]

It is well known that the structure of the workpiece strongly affects the mechanism of chip separation and the machinability of a job.[3,6,23,24] AE techniques adopted for discontinuous chips are less frequently reported. The chip formation during machining of hardened steel determines the criteria for crack initiation and propagation. Strong elastic waves related to the crack initiation and its propagation during the segment formation can be detected through the AE systems as well as the severe plastic deformation at the tool–chip and tool–workpiece interfaces. Furthermore, regarding segmentation frequencies, the AE technique is able to detect high-frequency processes emitted by the cutting zone. Therefore, the suggestion of using the AE technique to monitor hard turning operations seems to be reasonable.

Uehara[25] reported on remarkable patterns in the AE waveforms due to chip segmentation. The amplitude of the acoustic emission varies in accordance with the periodic change of the cutting force. Guo and Ammula[26] applied AE for real-time monitoring of the surface damage in hard machining. The results show that AE signals can be used to monitor surface integrity; specifically AE_{rms}, frequency, and count rate are sensitive to the existence of a white layer and the corresponding tool wear and surface roughness. Barry and Byrne[27] reported that in comparison to the AE_{rms} during continuous chip formation, which is between 0.05 V and 0.1 V, the AE_{rms} produced during segmented chip formation is at least one order of magnitude greater. In addition to the single AE sensor techniques, multi-sensing techniques were also developed. Axinte et al.[28] reported the application of the triangulation technique to arrays of acoustic emission sensors for the location of uneven events occurring during machining. The specific character of chip formation in hard turning connected with shear instability, its cyclic character, and mixed processes in the cutting zone (plastic deformation mixed with brittle cracking) suggest that the AE technique should be adapted. Two sensor techniques were suggested and verified.[29]

The application of two different AE sensors is connected with the frequency range of the different processes during the formation of a segmented chip. As was observed, chip formation during hard turning exhibits two different processes. The first is associated with crack initiation on the free surface and its prolongation towards the tool tip (zone Ib, **Figure 2**). The second type is represented by severe plastic deformation in the shear zone (zone Ia) and at the tool–chip (zone II) and tool–workpiece (III) interfaces. Conventional AE techniques (when turning soft steels) are usually carried out in the frequency ranges corresponding to the frequency range of the WD sensor. However, the process of plastic deformation in the cutting zone during the machining of hardened steel differs from a continuous chip. The cutting process is less stable with the characteristic segmentation frequency (accumulation of energy ahead of the cutting edge and its sudden relaxation in the form of a crack initiated on the free surface). As previously reported,[3,29,30] this segmentation frequency does not usually exceed 100 kHz and so it would be difficult to monitor the true dynamics of the cutting process via a WD sensor. Hence, the next D9241A sensor was integrated into the measuring system.

The preliminary studies[3,30] proved that this suggestion was reasonable. It was found that the peak frequency extracted from the raw AE signal recorded by the D9241A sensor is strongly correlated with the calculated segmentation frequencies and allows the true dynamic, reflecting the cracking process in the shear zone to be detected. The application of the WD sensor does not allow the segmentation frequencies to be detected because the detectable frequency spectrum of the WD sensor lies above all the segmentation frequencies. The instability of the cutting process connected with the chip segmentation (crack initiation and its propagation in the shear zone) does not interfere with AE signals detected by the WD sensor. However, while the character of the raw AE signal and also the values of the extracted AE features (such as AE_{rms}, $AE_{absolute}$ energy and $AE_{strength}$) obtained from the D9241A sensor stay nearly constant with varying cutting conditions, the magnitude of the AE signals for the WD sensor and the extracted AE features stated above are correlated with the release of energy accumulated ahead of the cutting edge and the corresponding intensity of the transformation processes in the white narrow bands and the more pronounced thinning region of a formed chip. These preliminary studies discussed earlier and carried out at varying cutting speeds (from 25 m min^{-1} to 200 m min^{-1}) and feeds (from 0.051 mm to 0.27 mm) indicate the correlation among the real intensity of the transformation processes, its dynamics (based on metallographic analyses of the formed chips), and the AE signals recorded by both AE sensors. These analyses also indicated parameters suitable for the evaluation of the deformation processes such as AE_{rms}, $AE_{absolute}$ energy and $AE_{strength}$.

As stated above, a specific mechanism of chip formation takes place during the hard turning. Thus, a specific character of the emitted acoustic waves should be expected. Furthermore, a suitable concept for the detection of the CTF or, much better, its prediction

should differ from the concept proposed for turning soft steel. Therefore, this paper discusses a specific aspect of AE signals during hard turning and suggests a suitable concept for the CTF prediction.

2 EXPERIMENTAL SETUP

The experimental setup is shown in **Figure 3**. Two commercial piezoelectric AE sensors (D9241A – frequency range from 15 kHz to 180 kHz; WD – frequency range from 100 kHz to 1000 kHz) from Physical Acoustics Corporation were mounted on the top of the tool holder (**Figures 3** and **4**). Semi-solid high-vacuum grease was used to maintain a good propagation of signals from the tool holder to the sensor. During the experiment, the AE signals were amplified, high passed at 15 kHz, low passed at 1000 kHz, and then sent through a preamplifier at a gain of 40 dB to the signal-processing software package. The signals were sampled in real-time, amplified, digitized, and then fed to the signal processing unit. The AE signals were post-processed using AE_{win}.

The experimental study was conducted on bearing steel 100Cr6 of hardness 62 HRc and external diameter 56 mm. The cutting and other conditions were as follows: v_c = 170 m min^{-1}, f = 0.09 mm, a_p = 0.25 mm, dry cutting, CNC Lathe Hurco TM8; the cutting tool was TiC reinforced Al_2O_3 ceramic inserts DNGA150408 (TiN coating).

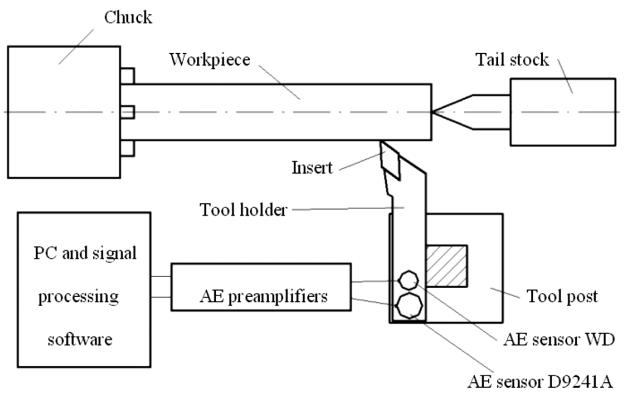

Figure 3: Schematic of the experimental setup
Slika 3: Shematski prikaz eksperimentalnega sestava

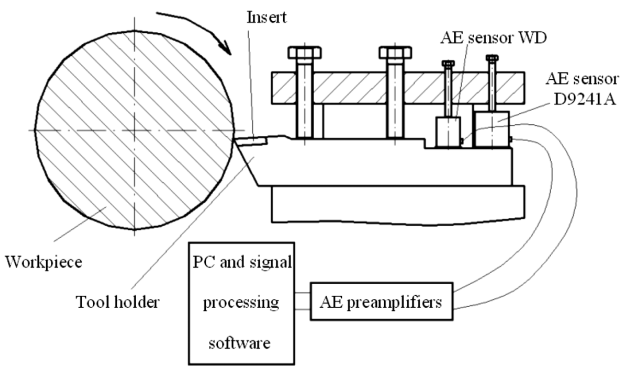

Figure 4: Detail of the sensor placement
Slika 4: Detajl namestitve senzorjev

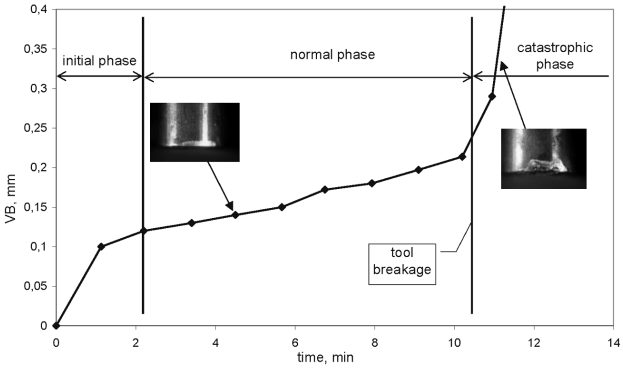

Figure 5: Different phases of tool wear
Slika 5: Različne faze obrabe orodja

3 RESULTS

The specific information connected with the application of two different sensors and their sensitivity to the different processes in the cutting zone can be applied for the monitoring of tool wear. Monitoring of the tool wear for ceramic inserts, especially the prediction of cutting-edge breakage, is a very sophisticated problem. Laboratory and also practical applications of these inserts indicated relatively stable and low-intensity tool wear in the normal phase of tool wear with the following unexpected CTF. The intensity of the tool wear is high in the initial and catastrophic phases of tool wear, as illustrated in **Figure 5**. While micro-chipping of the cutting edge is a dominant mechanism of tool wear in the initial and normal phases of tool wear, CTF represents tool wear in the form of massive breakage when the shape and tool geometry change dramatically in a very short time period. It is well known that the tool geometry strongly affects the stress and the temperature distribution in the cutting zone and therefore the corresponding chip form, as illustrated in **Figures 6** and **7**.

A segmented chip forms during the initial and normal phases of tool wear, as shown in **Figure 6**. It forms on

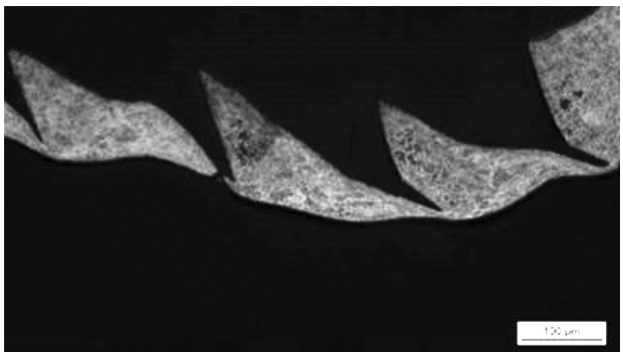

Figure 6: Segmented chip in the normal phase of tool wear
Slika 6: Segmentirani ostružki pri normalni fazi obrabe orodja

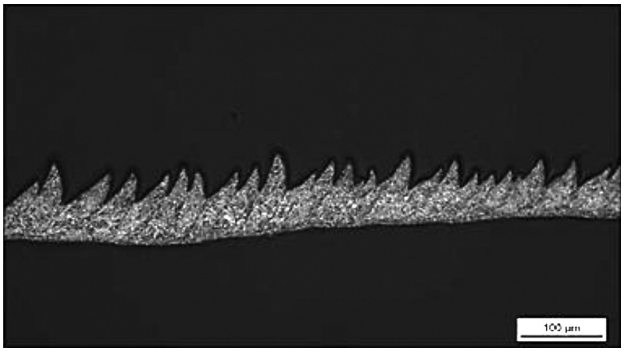

Figure 7: Segmented chip in the catastrophic phase of tool wear
Slika 7: Segmentirani ostružki pri katastrofični fazi obrabe orodja

the chamfer in the form of a radius with a highly negative geometry under the high normal stresses induced near the tool tip. In the early stages of tool wear a crater is formed on the tool radius with a rake angle between –7 ° and –10 °, as indicated in **Figure 8**. However, the CTF usually forms a mainly positive tool geometry and significantly alters the temperature and stress distribution in the cutting zone and the corresponding chip formation (**Figures 7** and **9**). High compressive stresses near the tool tip can be found when the chip is produced at the cutting-edge radius. The high compressive stresses ahead of the cutting edge obstruct the early crack initiation. A high portion of energy is accumulated ahead of the cutting edge. A crack on the free surface is initiated when the energy in front of the cutting edge attains its ultimate value. The high energy emitted during brittle cracking corresponds with a more pronounced region of thinning of the produced chip (a longer cracking zone, as illustrated in **Figure 6**) in the initial and also the normal phase of tool wear. However, the chip becomes more continuous when the tool geometry is strongly altered due to the CTF (**Figure 8**). The zone of crack propagation Ib is shorter and the thinning region is reduced.

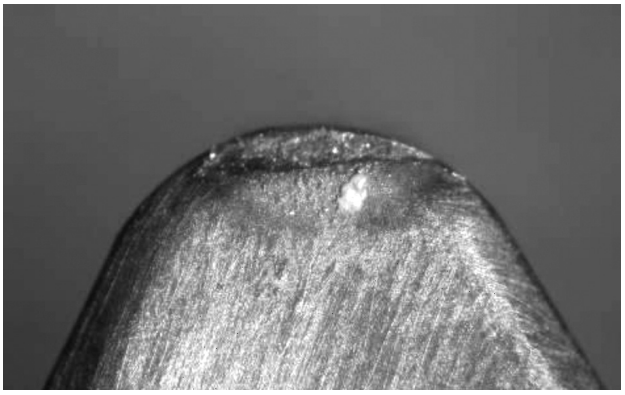

Figure 8: Crater on the cutting-insert radius formed in the initial phase of tool wear
Slika 8: Krater na rezalnem vložku, nastal v začetni fazi obrabe orodja

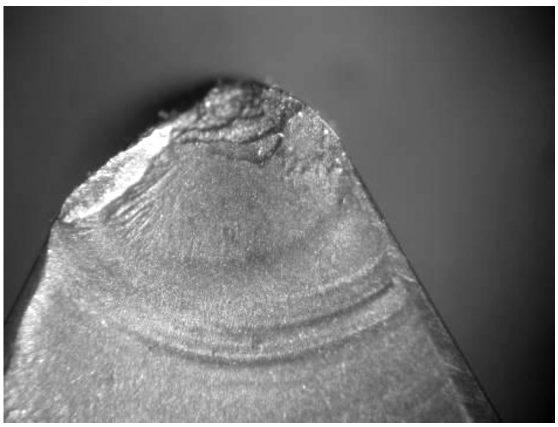

Figure 9: CTF of cutting insert
Slika 9: CTF rezalnega vložka

The character of the chip formed is strongly correlated with the AE signals and the extracted features (parameters). A conventional segmented chip is formed in the initial and normal phases of the tool wear. According to the theory of crack propagation and segment formation, the change in the amplitude of the acoustic emission indicates the change in the sliding velocity at the tool–chip interface and also different phases of the segment formation (the accumulation of energy ahead of the cutting edge and its sudden emission; **Figure 10**). The observed pulses of the AE signal correspond to the periodic fluctuation (relaxation character) of the cutting process. The signal level of the AE between these pulses is relatively small. During the segmented

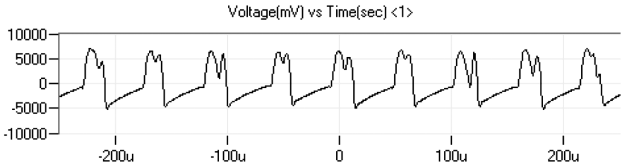

Figure 10: AE-signal in the normal phase of tool wear, D9241A-sensor
Slika 10: AE-signal pri normalni fazi obrabe orodja, D9241A-senzor

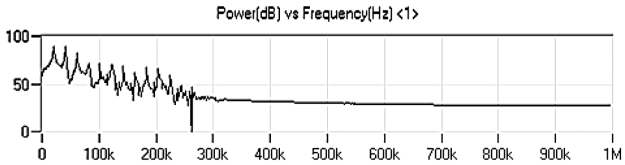

Figure 11: FFT-spectrum for D9241A-sensor in the normal phase of tool wear
Slika 11: FFT-spekter za D9241A-senzor pri normalni fazi obrabe orodja

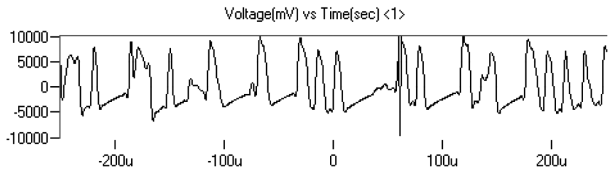

Figure 12: AE-signal in the catastrophic phase of tool wear, D9241A-sensor
Slika 12: AE-signal pri katastrofični fazi obrabe orodja, D9241A-senzor

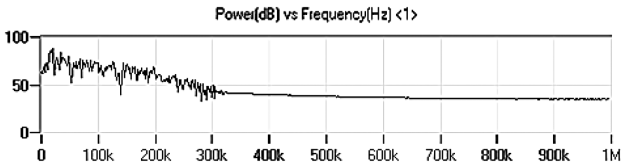

Figure 13: FFT-spectrum for D9241A-sensor in the catastrophic phase of tool wear
Slika 13: FFT-spekter za D9241A-senzor pri katastrofični fazi obrabe orodja

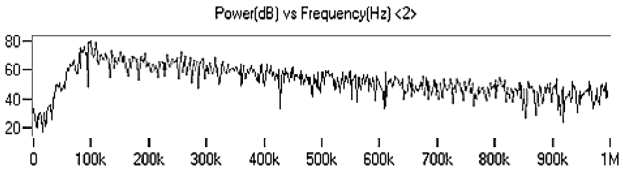

Figure 14: FFT-spectrum for WD-sensor in the normal phase of tool wear
Slika 14: FFT-spekter za WD-senzor pri normalni fazi obrabe orodja

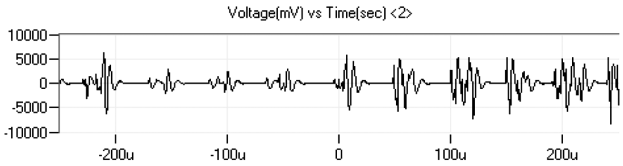

Figure 15: AE-signal in the normal phase of tool wear, WD-sensor
Slika 15: AE-signal pri normalni fazi obrabe orodja, WD-senzor

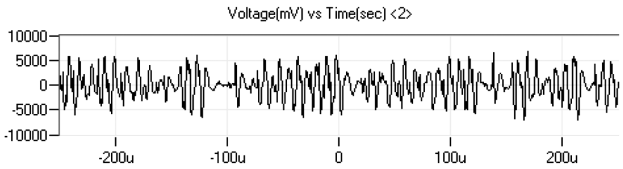

Figure 16: AE-signal in the catastrophic phase of tool wear, WD-sensor
Slika 16: AE-signal pri katastrofični fazi obrabe orodja, WD-senzor

chip formation, the chip slides over the rake face with varying speed.

Figure 10 shows this relaxing and periodic character of the signal in the normal phase of the tool wear and the related character of the FFT (Fast Fourier Transformation) spectrum (**Figure 11**) with the periodic peaks in this spectrum (overtones frequencies of the sensor resonance frequency). This character of the FFT spectrum confirms the dominant periodic character of the recorded signal and the ability of the D9241A AE sensor to detect the periodic process typical for the segmented chip formation proved by preliminary experiments.[31] On the other hand, **Figure 12** shows that the character of the AE signal in the catastrophic phase of tool wear is altered. This signal is partially deformed and the periodic character of the AE signal is violated. The irregular character of the AE signal corresponds with the irregular form of the segments produced after the CTF (**Figure 7**). Moreover, the FFT spectrum of the AE signal is peak-free (**Figure 13**).

Considering the WD AE sensor, all the segmentation frequencies lie outside the frequency range of this sensor and the relaxing character of the AE signal is missing. The FFT spectrum of the AE signal for the WD sensor is peak-free for all the formed chips (**Figure 14**). Furthermore, the transformation in the shear zone, where the cracking zone is suppressed and the shear zone is enlarged after the CTF, corresponds with the semi-continuous chip (**Figure 15**) and also the alteration in the appearance of the AE signal (**Figure 16**).

The AE features extracted from the raw AE signal plotted in the time scale are illustrated in **Figures 17** to **19**. The values of all the parameters for both sensors stay nearly constant in the initial and normal phases of tool wear. Wang and Liu[32] carried out the decomposition of the cutting force during hard turning with respect to the chip formation and flank wear. They reported a gradual increase of the shear and the normal force with increasing flank wear and a gentle drop in the forces associated with the chip formation. As the flank wear progresses, the change in the force becomes appreciable. **Figures 17** to **19** illustrate that AE_{rms}, $AE_{absolute}$ energy and $AE_{strength}$ vary only a little, despite a gradual increase in the flank wear VB. This indicates that the processes at the tool–workpiece interface play only a minor role

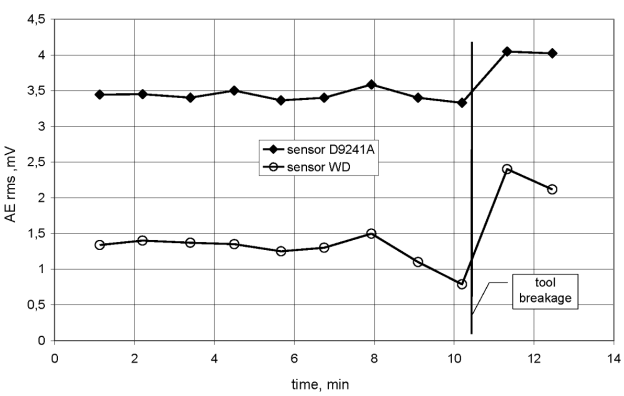

Figure 17: Influence of tool wear on RMS values of the AE
Slika 17: Vpliv obrabe orodja na vrednost RMS pri AE

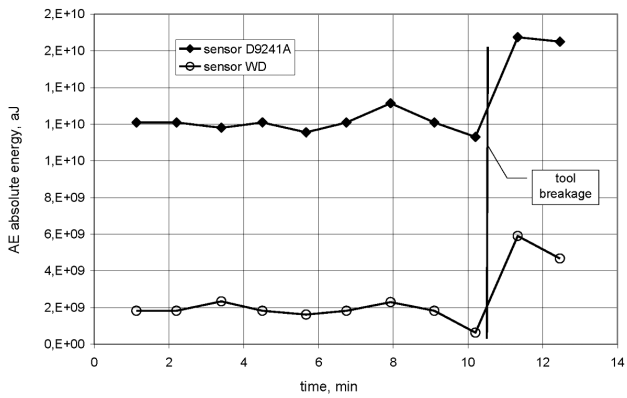

Figure 18: Influence of tool wear on absolute energy of the AE
Slika 18: Vpliv obrabe orodja na absolutno energijo AE

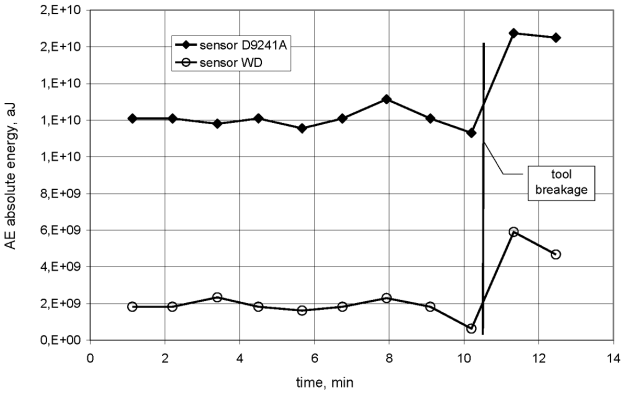

Figure 19: Influence of tool wear on signal strength of the AE
Slika 19: Vpliv obrabe orodja na moč signala AE

concerning the AE features and their contribution to the overall AE signals is low.

Since the CTF can be easily recognized (as shown in **Figures 17** to **19**) the gradual increase of flank wear and the associated process at the tool–workpiece interface are difficult to detect using the AE technique. Furthermore, the AE burst-type signal reflecting micro-chipping as a dominant mechanism of tool wear in the initial and normal phases of tool wear interferes with AE bursting due to cracking in the shear zone. Thus, an alternative approach to the prediction of the CTF has to be suggested. This suggestion can be based on the correlation between the chip form and the corresponding AE signal (as well as the extracted AE features) since the tool geometry strongly affects the stress and the temperature distribution in the cutting zone and, therefore, the chip appearance.

As illustrated in **Figures 17** and **18**, a certain fall of AE_{rms} and $AE_{absolute}$ energy can be viewed at the end of the normal phase with a subsequent abrupt increase after the tool breakage. On the other hand, the intensity of these changes differs between the two sensors. While a gentle decrease in the AE_{rms} value before the CTF for the 9241A sensor can be observed (in the time interval from 8 to 10 minutes), a more pronounced decrease is found for the WD sensor. Furthermore, while the increase in the AE_{rms} value after the CTF is only 21 % for the 9241A sensor, in the case of the WD sensor the CTF leads to AE_{rms} values that are twice as high. Thus, the idea of the signal ratio between the features extracted from the different sensors seems to be a suitable quantity that properly expresses the transformation processes in the cutting zone with respect to the tool wear.

Figure 20 indicates the transformation of the AE features' ratios between the sensors in connection with the transformation of processes in the cutting zone at the end of the normal phase of tool wear. The abrupt increase of the AE features allows the tool breakage itself to be detected. However, poor sensitivity with regard to the CTF prediction is also visible. A reliable CTF prediction can be suggested through a rationing of the extracted features, as indicated by Equations (1) and (2) and illustrated in **Figure 20**. The significant peaks occur before the tool breakage and these peaks warn of an imminent, approaching CTF. These peaks occur due to the unbalanced sensitivity to the different processes in the cutting zone between WD and D9241A, as discussed above. Moreover, the sensitivity of this approach is significantly higher than that based on the simple fall of AE parameters derived from the WD sensor. The increase in the R_1 parameter in the time interval from 8 min to 10 min is about 77 % and the R_2 parameter increases two times in the same time interval. The abrupt fall of the R_1 and R_2 ratios after the tool breakage is connected with considerable changes in the tool geometry, the corresponding stress and temperature distribution ahead of the cutting edge and the associated chip appearance. This new suggested data processing increases the sensitivity, not only considering the tool-failure prediction, but also considering the CTF detection itself.

The different information can be obtained from $AE_{strength}$. **Figure 19** shows that the abrupt increase of $AE_{strength}$ can be found only for the low-frequency sensor, whereas the $AE_{strength}$ extracted from the high-frequency WD sensor exhibits a remarkable drop. As was reported, the information from WD sensors is mainly correlated with the energy released during the segment formation and corresponds to the length of the cracked region in

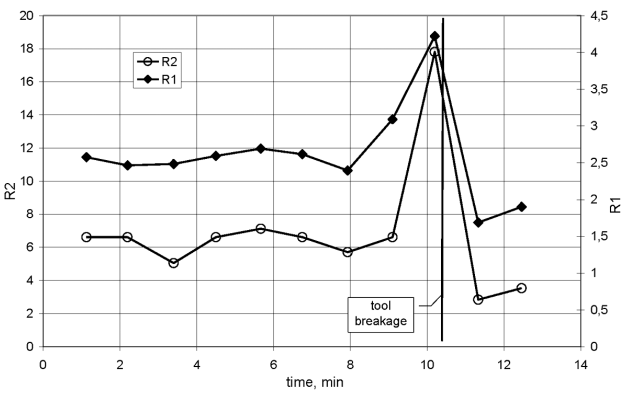

Figure 20: Influence of tool wear on the ratios R_1 and R_2
Slika 20: Vpliv obrabe orodja na razmerje R_1 in R_2

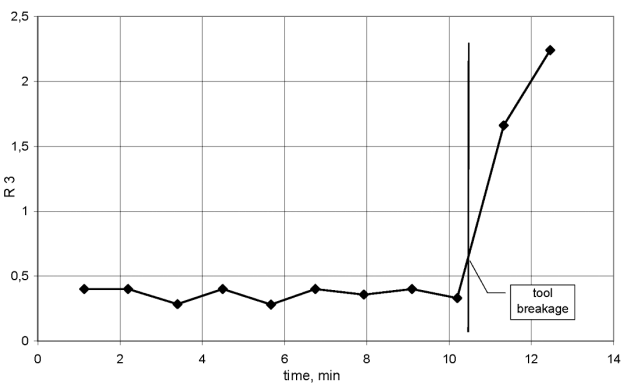

Figure 21: Influence of tool wear on the ratio R_3
Slika 21: Vpliv obrabe orodja na razmerje R_3

the shearing zone. Being so, the feature $AE_{strength}$ is a quantity more properly corresponding with the appearance of the obtained chips in the different phases of the tool wear (**Figures 6** and **7**) than those expressed in AE_{rms} and $AE_{absolute}$ energy. **Figure 7** shows that the cracked region is reduced after the CTF due to an alteration of the tool geometry (compared to the initial or normal phase of tool wear). The $AE_{strength}$ of the WD sensor also drops down after the CTF, whereas the AE_{rms} and $AE_{absolute}$ energy abruptly increases. A different appearance is also exhibited by the R_3 ratio (indicated by Equation (3) and illustrated in **Figure 21**. While nearly constant values of this ratio can be found in the initial and normal phases of tool wear, an abrupt increase due to the CTF failure corresponds with transformations in the processes ahead of the cutting edge (mainly a reduced cracking region and the corresponding decrease of the energy released during the brittle cracking):

$$R_1 = AE_{rms\ (D9241)}/AE_{rms\ (WD)} \quad (1)$$

$$R_2 = AE_{absolute\ energy\ (D9241)}/AE_{absolute\ energy\ (WD)} \quad (2)$$

$$R_3 = AE_{strength\ (D9241)}/AE_{strength\ (WD)} \quad (3)$$

4 CONCLUSIONS

AE techniques are very sensitive for monitoring the specific processes in the cutting zone. The formation of a segmented chip during hard turning is a very specific example of different processes in the cutting zone. This aspect indicates some conclusions connected with this experimental study.

- The application of two AE sensors with different frequency ranges makes it possible to detect the different processes in the cutting zone.
- While the low-frequency AE sensor 9241A allows the real dynamic character of chip segmentation to be detected, the high-frequency AE sensor WD is sensitive to the real intensity of the deformation processes in the different zones.
- Both sensors make it possible to detect tool breakage through the conventional parameters derived from the AE signals, and the AE signals reflect the transformation in the formation of the chip produced.
- The sensitivity of the tool-breakage prediction through the conventional parameters derived from the AE signals is poor.
- The ratios of AE features such as AE_{rms} and $AE_{absolute}$ energy between sensors change at the end of the normal phase of the tool wear. This transformation forms peaks that occur before the tool breakage, providing a warning of imminent tool failure.
- The ratio of $AE_{strength}$ between the sensors changes after the CTF. The $AE_{strength}$ itself more properly expresses the true intensity of the processes during chip separation than the AE_{rms} and $AE_{absolute}$ energy.
- The results of the experimental work presented in this paper were verified by many similar experiments carried out under different cutting conditions. A certain difference was found at low cutting depths, but the signals ratio also significantly increases the sensitivity for the detection of tool breakage and the prediction of tool failure.

Acknowledgement

This article was edited under the financial support of KEGA projects n. 005ŽU – 4/2014, 009ŽU – 4/2014.

5 REFERENCES

[1] H. K. Tönshoff, C. Arendt, R. B. Mor, Cutting of Hardened Steel, CIRP, 49 (**2000**), 547–564, doi:10.1016/S0007-8506(07)63455-6

[2] S. J. Heo, Environmentally conscious hard turning of cemented carbide materials on the basis of micro-cutting, J. of Mech. Sci. and Technol., 22 (**2008**), 1383–1390, doi:10.1007/s12206-008-0411-z

[3] M. Neslušan, Hard turning, Edis, Žilina 2010

[4] Y. Lee, D. A. Dornfeld, P. K. Wright, Open Architecture Based Framework in Integrated Precision Machining System, IMECE Anaheim, 1998

[5] M. Teti, K. Jemielniak, G. O. Donnell, D. Dornfeld, Advanced monitoring of machining operations, CIRP, 59 (**2010**), 717–739, doi:10.1016/j.cirp.2010.05.010

[6] M. C. Shaw, A. Vyas, The mechanism of chip formation with hard turning steel, CIRP, 47 (**1998**), 77–82, doi:10.1016/S0007-8506(07)62789-9

[7] K. Nakayama, M. Arai, T. Kanda, Machining characteristics of hardened steels, CIRP, 37 (**1988**), 89–92, doi:10.1016/S0007-8506(07)62789-9

[8] G. Poulachon, A. Moisan, Contribution to the study of the cutting mechanism during high speed machining of hardened steel, CIRP, 47 (**1998**), 73–76, doi:10.1016/S0007-8506(07)62788-7

[9] H. K. Tönshoff, M. Jung, S. Mannel, W. Rietz, Using acoustic emission signals for monitoring of production processes, Ultrasonics, 37 (**2000**), 681–686, doi:10.1016/S0041-624X(00)00026-3

[10] D. A. Dornfeld, Acoustic emission in monitoring and analysis in manufacturing, Proceedings of AE Monitoring, 14 (**1984**), 124–131

[11] D. A. Dornfeld, Manufacturing process monitoring and analysis using acoustic emission, Journal of Acoustic Emission, 4 (**1985**), 123–126

[12] I. Inasaki, Application of acoustic emission sensor for monitoring machining processes, Ultrasonics, 36 (**1998**), 273–281, doi:10.1016/S0041-24X(97)00052-8

[13] J. Barry, G. Byrne, D. Lennon, Observations on chip formation and acoustic emission in machining Ti-6Al-4V alloy, International Journal of Machine Tools and Manufacture, 41 (**2001**) 7, 1055–1070, doi:10.1016/S0890-6955(00)00096-1

[14] I. Marinescu, D. A. Axinte, A critical analysis of effectiveness of acoustic emission signals to detect tool and workpiece malfunctions in milling operations, International Journal of Machine Tool and Manufacture, 48 (**2008**), 1148–1160, doi:10.1016/j.ijmachtools.2008.01.011

[15] M. P. Gómez, A. M. Hey, J. E. Ruzzante, C. E. D´Attellis, Tool wear evaluation in drilling by acoustic emission, Physica Procedia, 3 (**2010**), 819–825, doi:10.1016/j.phpro.2010.01.105

[16] D. E. Lee, I. Hwang, C. M. O. Valente, J. F. G. Oliveira, D. A. Dornfeld, Precision manufacturing process monitoring with acoustic emission, International Journal of Machine Tool and Manufacture, 46 (**2006**), 176–188, doi:10.1016/j.ijmachtools.2005.04.001

[17] R. Babel, P. Koshy, M. Weiss, Acoustic emission spikes at workpiece edges in grinding: Origin and applications, International Journal of Machine Tool and Manufacture, 63 (**2013**), 96–101, doi:10.1016/j.ijmachtools.2012.08.004

[18] S. Min, J. Lidde, N. Raue, D. Dornfeld, Acoustic emission based tool contact detection for ultra-precision machining, CIRP, 60 (**2011**), 141–144, doi:10.1016/j.cirp.2011.03.079

[19] K. Jemielniak, O. Otman, Tool failure detection based on analysis of acoustic emission signals, Journal of Material Processing Technology, 76 (**1998**), 192–197, doi:10.1016/S0924-0136(97)00379-8

[20] X. Li, Z. Yuan, Tool wear monitoring with wavelet packet transform-fuzzy clustering method, Wear, 219 (**1998**), 145–154, doi:10.1016/S0043-1648(98)00165-3

[21] S. Dolinšek, J. Kopač, Acoustic emission signals for tool wear identification, Wear, 225–229 (**1999**), 295–303, doi:10.1016/S0043-1648(98)00363-9

[22] E. Govekar, J. Gradišek, I. Grabec, Analysis of acoustic emission signals and monitoring of machining processes, Ultrasonics, 38 (**2000**), 598–603, doi:10.1016/S0041-624X(99)00126-2

[23] M. Sekulič et al., Influence of material properties on the machinability in face milling, Mater. Tehnol., 46 (**2012**) 6, 601–606

[24] O. Topku, M. Übeyli, A. Acir, Effect of the martensite volume fraction on the machining of a dual – phase steel using a milling operation, Mater. Tehnol., 45 (**2011**) 2, 145–150

[25] K. Uehara, Identification of Chip Formation Mechanism through Acoustic Emission Measurements, CIRP, 33 (**1974**), 71–74, doi:10.1016/S0007-8506(07)61382-1

[26] Y. B. Guo, S. C. Ammula, Real-time acoustic emission monitoring for surface damage in hard machining, International Journal of Machine Tool and Manufacture, 45 (**2005**), 1622–1627, doi:10.1016/j.ijmachtools.2005.02.007

[27] J. Barry, G. Byrne, Chip Formation, Acoustic Emission and Surface White Layers in Hard Machining, CIRP, 51 (**2002**), 65–70, doi:10.1016/S0007-8506(07)61467-X

[28] D. A. Axinte, D. R. Natarajan, N. Z. Gindy, An approach to use an array of three acoustic emission sensors to locate uneven events in machining – Part 1: method and validation, International Journal of Machine Tool and Manufacture, 45 (**2005**), 1605–1613, doi:10.1016/j.ijmachtools.2005.02.005

[29] M. Šípek, M. Neslušan, M. Čilliková, Analysis of segmented chip when hard turning through acoustic emission, Manufacturing Technology, 14 (**2010**), 254–257

[30] M. Neslušan, I. Mrkvica, R. Čep, M. Čilliková, Influence of cutting speed on intensity of the plastic deformation during hard turning, Mater. Tehnol., 47 (**2013**) 6, 745–755

[31] B. Karpuschewski, K. Schmidt, J. Prilukova, J. Beňo, I. Maňková, N. T. Hieu, Influence of tool edge preparation on performance of ceramic tool inserts when hard turning, Journal of Materials Processing Technology, 213 (**2013**), 1978–1988, doi:10.1016/j.jmatprotec.2013.05.016

[32] J. Y. Wang, C. R. Liu, The effect of tool flank wear on the heat transfer, thermal damage and cutting mechanics in finishing hard turning, CIRP, 48 (**1999**), 53–56, doi:10.1016/S0007-8506(07)63130-8

UDK 666.3/.7:620.179.1:620.193.16
Original scientific article/Izvirni znanstveni članek

ISSN 1580-2949
MTAEC9, 49(3)365(2015)

EROSIVE WEAR RESISTANCE OF SILICON CARBIDE-CORDIERITE CERAMICS: INFLUENCE OF THE CORDIERITE CONTENT

ODPORNOST KERAMIKE SILICIJEV KARBID-KORDIERIT PROTI OBRABI PRI EROZIJI: VPLIV VSEBNOSTI KORDIERITA

Milica Pošarac-Marković[1], Djordje Veljović[2], Aleksandar Devečerski[1], Branko Matović[1], Tatjana Volkov-Husović[2]

[1]University of Belgrade, Vinca Institute of Nuclear Sciences, P.O. Box 522, 11001 Belgrade, Serbia
[2]University of Belgrade, Faculty of Technology and Metallurgy, Karnegijeva 4, POB 3503, Belgrade, Serbia
tatjana@tmf.bg.ac.rs

Prejem rokopisa – received: 2014-04-28; sprejem za objavo – accepted for publication: 2014-06-18

doi:10.17222/mit.2014.071

A cordierite/SiC composite was created in situ with reactive sintering at 1250 °C and 1300 °C. The cordierite precursor was made from commercially available spinel, alumina and quartz and was mixed with the comercial SiC powder to obtain composite materials during the sintering. It was found that cordierite particles bind efficiently with the SiC powder during sintering and that reactive sintering is an effective way to produce ceramics at a relativly low temperature.
The goal of this investigation was to check the possibilities of using the silicon carbide-cordierite composite as a material resistant to the erosive wear. The fluid dynamic system of the experimental methodology was used here to produce ultrasonic erosive wear. Two kinds of SiC/cordierite samples were investigated, KS 50 and KS 30, with different mass contents of cordierite (w = 50 % and w = 30 % of cordierite). The mass loss and the level of surface degradation were measured before and during the experiment. The level of surface degradation of the samples was monitored using the Image-Pro Plus program for the image analysis. It was found that after 150 min the mass loss was below 1.3 mg and the surface degradation was below 7 %. The obtained results indicated that both samples exhibited an excellent erosion resistance during the cavitation experiment.

Keywords: ceramic-matrix composites (CMCs), damage tolerance, non-destructive testing, cavitation-erosion diameter and area

Kompozit kordierit-SiC je bil izdelan in-situ z reakcijskim sintranjem pri 1250 °C in 1300 °C. Kordieritna predoblika, izdelana iz komercialno dostopnega špinela, aluminijevega oksida in kremena, je bila zmešana s prahom komercialnega SiC, da bi dobili s sintranjem kompozitni material. Ugotovljeno je, da delci kordierita učinkovito vežejo SiC-prah med sintranjem in da je reakcijsko sintranje učinkovita metoda za izdelavo keramike pri relativno nizki temperaturi.
Cilj te raziskave je preveriti možnost uporabe SiC-kordieritnega materiala, odpornega proti obrabi z erozijo. Za ultrazvočno erozijsko obrabo je bila uporabljena eksperimentalna metoda fluidnega dinamičnega sistema. Preiskovani sta bili dve vrsti vzorcev SiC-kordierit, KS 50 in KS 30, z različnima masnima vsebnostima kordierita (w = 50 % in w = 30 % kordierita). Masni delež obrabe površine je bil izmerjen pred preizkusom in po njem. Stopnja degradacije površine vzorcev je bila ugotovljena s programom za analizo slik Image Pro Plus. Ugotovljeno je bilo, da je bila izgube mase po 150 min manjša od 1,3 mg in degradacija površine manjša od 7 %. Dobljeni rezultati kažejo, da imata med preizkusom kavitacije oba vzorca odlično odpornost proti eroziji.

Ključne besede: kompozit s keramično osnovo (CMCs), toleranca poškodb, neporušne preiskave, premer in površina erozije pri kavitaciji

1 INTRODUCTION

Ceramic materials have been used for centuries as the materials with a very wide range of mechanical and thermal properties suitable for various applications. Today, their common industrial use is more related to the electronics for mechanical parts and biomedicine applications (hip prosthesis, dental implants). One of the main reasons for this is the improvement of the fracture toughness that allows a ceramic material to perform better when it is subjected to the operating conditions. Sometimes these operating conditions may involve rapid changes in the temperature, or a high-temperature application as well as the conditions that include cavitation erosion. This could be related to the technical ceramics, for example, the operations of bearings, injectors or valves. Cavitation, i.e., the appearance of vapor cavities inside an initially homogeneous liquid medium, occurs in very different situations. Hence, the study of the cavitation and cavitation-erosion mechanisms of technical ceramics is of importance to improve their performance in real applications.[1–4]

Metallic materials are the most common choice when cavitation-erosion resistance is required. Research results concerning the applications of different classes of materials, including ceramics and composite materials for a similar use, were published in the last decade.[1–10] Different types of ceramics based on silicon nitride and zirconia, as well as alumina-based ceramic materials were investigated in the conditions of cavitation erosion.[2,4–9] In numerous papers[1–12] related to the investigations of the erosion rate of these materials, attempts were made to

investigate the type of cracking as well as the influence of the grain sizes and the contents of different compounds and phases on the resistance of the materials to the erosive wear.

The goal of our investigation was to study the possibilities of using a silicon carbide/cordierite based ceramic material as a potential cavitation-resistant material.

2 MATERIALS

The properties of cordierite/silicon carbide based ceramics that enable a widespread use in high-temperature conditions are a particularly low coefficient of thermal expansion, a high thermal conductivity, an excellent thermal fire resistance and an excellent resistance to a thermal shock. Their target application is in the furnaces for the use at the temperatures of over 1000 °C. An addition of silicon carbide improves the physical and mechanical properties of refractory cordierite. The high thermal conductivity of silicon carbide reduces the thermal stresses within a cordierite ceramic body. A mixture of commercially available spinel ($MgAl_2O_4$), quartz (SiO_2) and alumina (Al_2O_3) corresponding to a cordierite stoichiometric composition was attrition milled using Al_2O_3 balls and ethyl alcohol as the media for four hours; henceforth, this mixture was labeled as KS. Mixture KS was used for preparing the cordierite/SiC composite ceramics with the mass ratio of 30 : 70 and 50 : 50, respectively. After the milling with the Al_2O_3 balls in DI water in a polyethylene bottle for 24 h, the samples were uniaxially pressed and sintered at 1300 °C and 1250 °C, for 3 h, and the ceramic composite samples were marked as KS 30 and KS 50, respectively. The typical values of the selected properties of the dense constituents used in the refractory materials investigated are listed in the previous papers.[13–15]

An XRD analysis of the KS 30 sample (**Figure 1**) shows a presence of three crystalline phases: SiC, cordierite and sapphirine and a presence of a certain amount of a glassy phase. In the case of sample KS 50, the phase analysis shows a presence of four crystalline phases: SiC, cordierite, sapphirine and enstatite. There is also a small amount of a glassy phase, which affects the formation of cordierite and sapphirine. One can conclude that an increase in the added amount of the mixture with a composition corresponding to stoichiometric cordierite improves the quantity and crystallization of cordierite.

The microstructures of samples KS 30 and KS 50 (**Figure 2**) were examined with scanning electron micro-

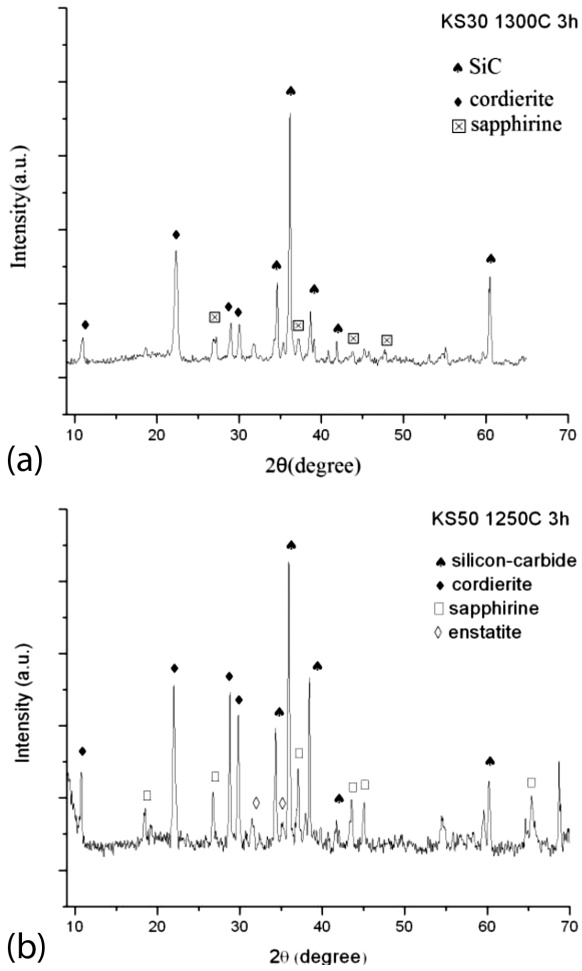

Figure 1: XRD of the: a) KS 30 and b) KS 50 samples
Slika 1: XRD-posnetka vzorcev: a) KS 30 in b) KS 50

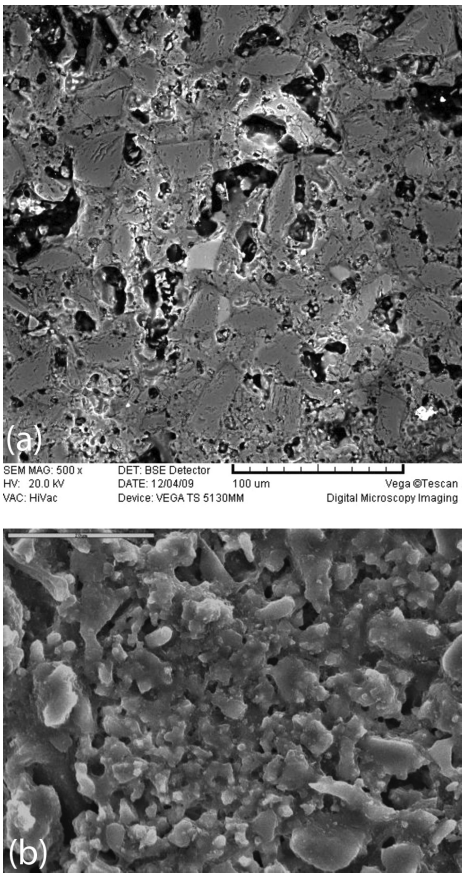

Figure 2: SEM of the: a) KS 30 and b) KS 50 samples
Slika 2: SEM-posnetka vzorcev: a) KS 30 in b) KS 50

scopy using a VEGA TS 5130 mm (TESCAN) device; the samples were coated with a layer of the Au-Pd mixture. A porous structure was observed, with the particles of different sizes and pronounced necks formed during the densification. The pores that are not spherical indicate the initial stages of sintering. The pores present have different sizes and shapes.

3 CAVITATION-EROSION TESTING

The experimental methodology used for the cavitation-erosion testing is explained in[7,10,16,17]. With respect to the used equipment, the diameter of the horn was 10 mm and the distance between the horn and a sample was 1 mm. The samples were discs with a diameter of 3 cm and a height of 1 cm.

4 RESULTS AND DISCUSSION

4.1 Mass loss and level of destruction during the testing

The mass losses of the test specimens were determined using the analytical balance with an accuracy of ± 0.1 mg. The measurements were performed after subjecting each test specimen to cavitation for 30 min. The duration of the tests was 150 min. The light microscopy technique was applied to analyze the effect of the erosion and to interpret the results of the cavitation tests (**Figure 3**).

The mass loss was below 1.3 mg, which is similar to metallic[15–25] and ceramic[5,6,24,25] materials. From **Figure 2** it can be seen that sample KS 30 exhibited a better resistance to erosive wear, as after 150 min the mass loss for KS 30 was 0.12 mg and for KS 50 it was 1.23 mg.

The next experiment consisted of the measurements of the degradation levels before and during the testing. In order to carry out an image analysis determining the level of destruction before and during the testing, the samples were photographed as shown in **Figure 4**.

The results of the image analysis of samples KS 50 and KS 30 are given in **Figure 5**.

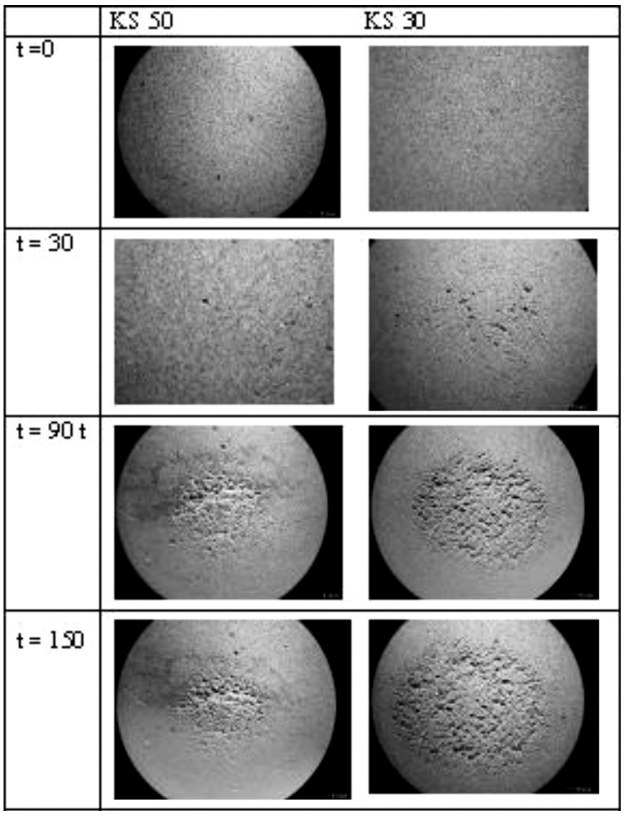

Figure 4: Photographs of the samples during the testing
Slika 4: Posnetki vzorcev med preizkusi

Based on the obtained results, similar conclusions regarding the level of degradation and the mass loss of the samples can be given. Samples KS 50 exhibited a better erosion resistance as their level of damage was 4.4 % compared to 6.9 % for the KS 30 samples. The differences in the sample behavior can be related to the crack nucleation and propagation during the cavitation testing.

As can be seen from **Figure 5**, samples KS 50 exhibited a stable increase in the level of degradation and similar rates of degradation for the entire time range. At

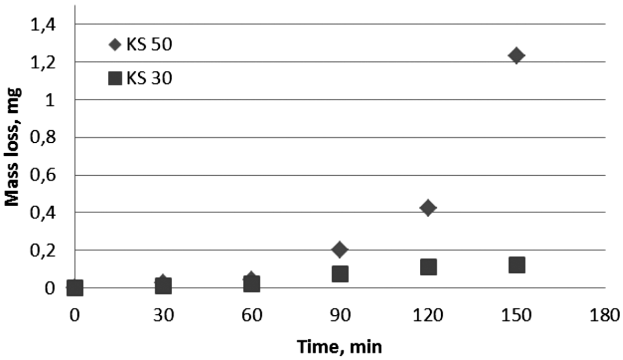

Figure 3: Mass loss during the experiment
Slika 3: Izguba mase med preizkusom

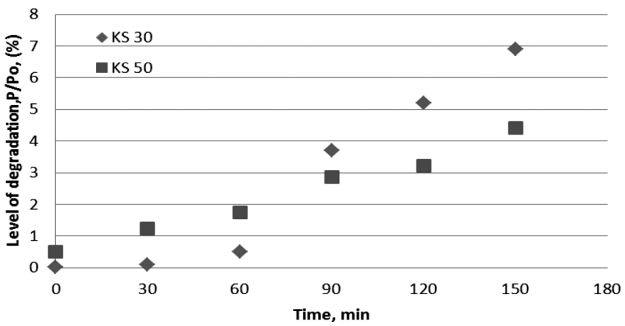

Figure 5: Level of destruction of the samples (P/P_o) versus the time of experiment (P is the damaged area after the testing and P_o is the undamaged area)
Slika 5: Nivo propada vzorcev (P/P_o) v odvisnosti od časa preizkusa, (P je poškodovano področje po preizkusu in P_o je nepoškodovano področje)

the end of the experiment, after 150 min, the level of degradation was below 5 %.

For the KS 30 samples, two regimes can be observed on **Figure 5**. The first regime is characterized by a slow increase in the level of destruction over the period from 0 min to 60 min. The second regime, after 60 min of the testing, is characterized by a more rapid change in the damage level. However, it has to be mentioned that the total level of degradation, after 150 min of the testing, did not exceed 8 %, which is an excellent result for the cavitation resistance.

From these results it can be concluded that samples KS 30 have a better resistance to crack nucleation and propagation up to the 60th minute of the experiment. After this critical time, the crack propagation is very rapid. The increased cordierite amount and decreased SiC amount influenced the crack nucleation and propagation, as the higher values of cordierite in samples KS 50 caused lower rates of crack propagation during the entire time (0–150 min) and the total degradation of the samples after 150 min of the testing was lower.

4.2 Erosion-ring diameter and erosion-ring area

The samples exposed to cavitation erosion (**Figure 3**) were also monitored in order to measure the diameters and the areas of the erosion-ring regions. These measurements were performed using the following steps:

Step 1: Making appropriate micrographs that include the erosion ring areas (**Figure 3**)

Step 2: Measuring the ring diameters: at this point two types of measurements were taken: diameters (d_1) and (d_2) of the cavitation-ring erosion measured with the Image-Pro Plus program. The effective diameter of each ring is calculated according to the following equation:

$$d = \frac{d_1 + d_2}{2} \tag{1}$$

Step 3: Calculating the effective area of the erosion ring using the values of the diameters measured in Step 2:

$$P_{av} = \frac{\pi d_1 d_2}{4} \tag{2}$$

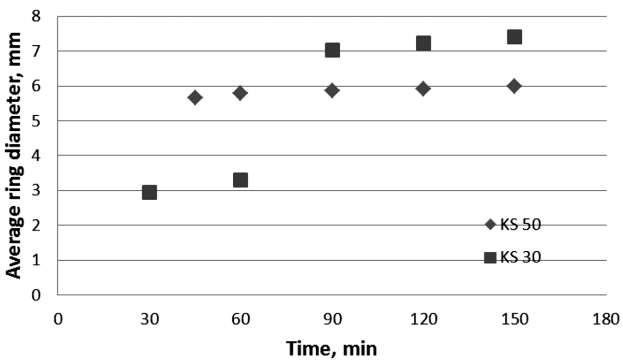

Figure 6: Average diameter of the erosion ring during the testing
Slika 6: Povprečni premer erozijskega kroga med preizkušanjem

Step 4: Using the Image-Pro Plus program to determine the average erosion-surface area of the ring, (P_{meas}).

4.3 Erosion-ring measuremets

The measurements of the average diameter of the erosion ring were made after (30, 45, 60, 90, 120 and 150) min.

Samples KS 50: The results presented in **Figure 6** show that the formation of an erosion ring can be observed after 45 min of the testing. The average erosion-ring diameter increased from 5.68 mm after 45 min to 6.03 mm after 150 min of the testing.

Samples KS 30: The errosion-ring formation of this sample was observed after 30 min. A rapid increase in the ring diameter was observed after 90 min, when the ring diameter increased from 3.29 mm after 60 min to 7.04 mm after 90 min of the testing. After 90 min the increase in the ring diameter was very slow so that after 150 min the ring diameter reached only 7.41 mm.

The results for the erosion-ring measuremet are in a strong correlation with the results for the level of destruction (**Figure 5**) supporting the conclusions about the influence of cordierite and SiC content on the level of degraration. The same conlusions are valid if the erosion-ring measurements are taken into account. With respect to the energy for crack nucleation, lower values are expected for the KS 30 samples where the formation of the erosion ring was observed after 30 min, while for the KS 50 samples it was formed after 45 min. This difference could be important for some specific applica-

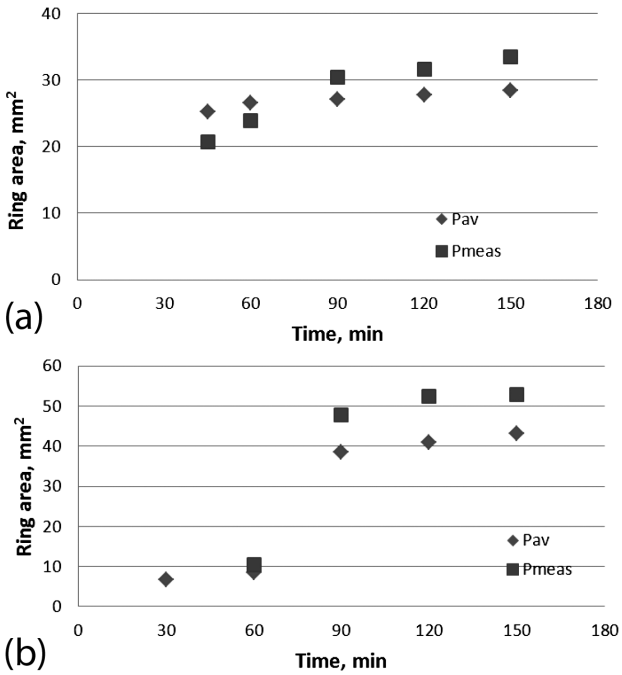

Figure 7: Average area of the erosion ring based on diameter measurements and area measurements: a) KS 50 and b) KS 30
Slika 7: Povprečna površina erozijskega kroga na podlagi meritev premera in površine: a) KS 50 in b) KS 30

tions where the specific resistance to either crack nucleation or crack propagation is requested.

4.4 Average erosion-surface area

According to the procedure described above, **Figure 7** shows the values obtained for the average erosion-surface areas based on monitoring the erosion-ring diameters.

Samples KS 50: The formation of the erosion ring was detected after 45 minutes and the average erosion-surface area was P_{meas} = 20.73 mm^2 and P_{av} = 25.23 mm^2. Both values for the erosion ring area were slowly increased, reaching the values of P_{av} = 28.35 mm^2 and P_{meas} = 33.42 mm^2 after 150 min of the testing. The results showed the differences caused by implementing the method for the erosion-ring-area determination (during the above steps) and these differences apply to the whole experiment.

Samples KS 30: As for the ring-diameter measurements, after 60 min of the testing the erosion ring was detected, with the erosion-surface area of P_{meas} = 10.56 mm^2 and P_{av} = 8.49 mm^2. After 90 min a rapid change in the erosion area was observed so that after 150 min of the testing the erosion-surface values raised to P_{av} = 43.76 mm^2 and P_{meas} = 52.81 mm^2. The differences in the values obtained with step 4 (P_{av}) and step 5 (P_{meas}) were increasing during the experiment.

Based on the obtained results it can be concluded that samples KS 30 are more sensitive to the formation of the erosion ring. Also, after 90 min of the testing there are rapid changes in the diameter and the surface of the erosion ring, but by the end of the testing (150 min) this increase is slowed down.

Samples KS 50 exhibited a better erosion resistance as the ring diameter and the average area of erosion were lower, and their increase was slower over the testing time.

The formation of the erosion ring for the KS 50 samples is visible after 30 min. This can be related to the influence of the crack nucleation caused by the erosion experiment.

5 CONCLUSION

Ceramic composite samples based on the SiC/cordierite ceramic material were synthesized in order to investigate the sample resistance to the erosive wear. Two samples with different mass contents of cordierite and SiC were used in this investigation: KS 50 (w = 50 % of cordierite) and KS 30 (w = 30 % of cordierite).

The results for the mass loss as well as for the level of degradation indicate a similar (or even better) erosion resistance compared to the metallic and low-alumina samples.

Both samples exhibited an excellent erosive resistance, but sample KS 50 exhibited the better resistance of the two as its mass loss was lower, as were the level of degradation, the erosion-ring diameter and the erosion area.

These experiments showed that composite ceramic materials based on SiC/cordierite can be used as erosion-resistant materials, used for new applications.

Also, an implementation of non-destructive testing such as an image analysis to determine the erosion-ring diameter and the erosion-ring area improved the reliability of predicting the sample behavior in the conditions of erosive wear.

Acknowledgement

This research was financed by the Ministry of Education, Science and Technological Development of Serbia as part of project III 45012.

6 REFERENCES

[1] W. J. Tomlinson, S. J. Matthews, Cavitation erosion of structural ceramics, Ceramics International, 20 (**1994**), 201–209, doi:10.1016/0272-8842(94)90040-X

[2] U. Litzow, K. H. Z. Gahr, J. Schneider, Cavitation erosion of advanced ceramics in water, International Journal of Materials Research: Zeitschrift für Metallkunde, 97 (**2006**), 1372–1377, doi:10.3139/146.101380

[3] D. Niebuhr, Cavitation erosion behavior of ceramics in aqueous solutions, Wear, 263 (**2007**), 295–300, doi:10.1016/j.wear.2006.12.040

[4] G. Garcia-Atance Fatjó, M. Hadfield, K. Tabeshfar, Pseudoplastic deformation pits on polished ceramics due to cavitation erosion, Ceramics International, 37 (**2011**), 1919–1927, doi:10.1016/j.ceramint.2011.03.043

[5] S. Martinovic, M. Dojcinovic, J. Majstorovic, A. Devecerski, B. Matovic, T. Volkov Husovic, Implementation of image analysis on thermal shock and cavitation resistance testing of refractory concrete, Journal of European Ceramic Society, 30 (**2010**), 3303–3309, doi:10.1016/j.jeurceramsoc.2010.07.041

[6] S. Martinovic, M. Vlahovic, M. Dojcinovic, T. Volkov-Husovic, J. Majstorovic, Thermomechanical properties and cavitation resistance of a high-alumina low-cement castable, International Journal of Applied Ceramic Technology, 8 (**2011**) 5, 1115–1124, doi:10.1111/j.1744-7402.2010.02545.x

[7] G. Garcia-Atance Fatjó, M. Hadfield, C. Vieillard, J. Sekulic, Early stage cavitation erosion within ceramics—an experimental investigation, Ceramics International, 35 (**2009**), 3301–3312, doi:10.1016/j.ceramint.2009.05.020

[8] M. H. Korkut, Y. Küçük, A. C. Karaoğlanli, A. Erdoğan,Y. Er, M. S. Gök, Effect of the abrasive grit size on the wear behavior of ceramic coatings during micro-abrasion test, Mater. Tehnol., 47 (**2013**) 6, 695–699

[9] J. Bažan, L. Socha, L. Martínek, P. Fila, M. Balcar, J. Chmelař, Wear of refractory materials for ceramic filters of different porosity in contact with hot metal, Mater. Tehnol., 45 (**2011**) 6, 603–608

[10] G. Garcıá-Atance Fatjó, A. Torres Pérez, M. Hadfield, Experimental study and analytical model of the cavitation ring region with small diameter ultrasonic horn, Ultrasonics Sonochemistry, 18 (**2011**), 73–79, doi:10.1016/j.ultsonch.2009.12.006

[11] F. G. Hammit, Cavitation and Multiphase Flow Phenomena, McGraw-Hill, New York 1980

[12] R. T. Knapp, J. W. Daily, F. G. Hammit, Cavitation, McGraw-Hill, New York 1970

[13] M. Posarac, M. Dimitrijevic, T. Volkov-Husovic, A. Devecerski, B. Matovic, Determination of thermal shock resistance of silicon carbide/cordierite composite material using nondestructive test methods, Journal of the European Ceramic Society, 28 (**2008**) 6, 1275–1278, doi:10.1016/j.jeurceramsoc.2007.09.038

[14] M. Dimitrijevic, M. Posarac, J. Majstorovic, T. Volkov-Husovic, B. Matovic, Behavior of silicon carbide/cordierite composite material after cyclic thermal shock, Ceramics International, 35 (**2009**) 3, 1077–1081, doi:10.1016/j.ceramint.2008.04.029

[15] M. Posarac-Markovic, Ph.D. Thesis, University of Belgrade, Faculty of Technology and Metallurgy (in Serbian)

[16] T. Okada, S. Hattori, M. Shimizu, A fundamental study of cavitation erosion using a magnesium oxide single crystal (intensity and distribution of bubble collapse impact loads), Wear, 186–187 (**1995**), 437–443, doi:10.1016/0043-1648(95)07162-8

[17] S. Hattori, H. Mori, T. Okada, J. Fluid Eng, Trans. ASME, 120 (**1998**), 179–185, doi:10.1115/1.2819644

[18] T. Okada, S. Hattori, Proc. of the Int. Symposium on Aerospace and Fluid Science, Sendai, Japan, 1993, 347

[19] K. Steller, Proc. of the 6th Int. Conf. on Erosion by Liquid and Solid Impact, Cambridge, UK, 1983, 121

[20] G. Bregliozzia, A. Di Schinob, S. I. U. Ahmeda, J. M. Kennyb, H. Haefkea, Wear, 258 (**2005**), 503–510, doi:10.1016/j.wear.2004.03.024

[21] W. J. Tomlinson, A. S. Bransden, Wear, 185 (**1995**), 59–65, doi:10.1016/0043-1648(94)06584-5

[22] C. J. Lin, J. L. He, Wear, 259 (**2005**), 154–159, doi:10.1016/j.wear.2005.02.099

[23] M. Dojcinovic, T. Volkov Husovic, Cavitation damage of the medium carbon steel: impelmentation of image anaysis, Materials Letters, 62 (**2008**), 953–956, doi:10.1016/j.matlet.2007.07.019

[24] S. Martinovic, M. Dojcinovic, J. Majstorovic, A. Devecerski, B. Matovic, T. Volkov Husovic, Implementation of image analysis on thermal shock and cavitation resistance testing of refractory concrete, Journal of European Ceramic Society, 30 (**2010**), 3303–3309, doi:10.1016/j.jeurceramsoc.2010.07.041

[25] S. Martinovic, M. Vlahovic, M. Dojcinovic, T. Volkov-Husovic, J. Majstorovic, Thermomechanical properties and cavitation resistance of a high-alumina low-cement castable, International Journal of Applied Ceramic Technology, 8 (**2011**) 5, 1115–1124, doi:10.1111/j.1744-7402.2010.02545.x

UDK 532.6
Original scientific article/Izvirni znanstveni članek

ISSN 1580-2949
MTAEC9, 49(3)371(2015)

INFLUENCE OF THE SUBSTRATE TEMPERATURE ON THE STRUCTURAL, OPTICAL AND THERMOELECTRIC PROPERTIES OF SPRAYED V_2O_5 THIN FILMS

VPLIV TEMPERATURE PODLAGE NA STRUKTURNE, OPTIČNE IN TERMOELEKTRIČNE LASTNOSTI NAPRŠENE TANKE PLASTI V_2O_5

Yelsani Vijayakumar[1], Katta Narasimha Reddy[1], Annasaheb Vitthal Moholkar[2], Musugu Venkata Ramana Reddy[1]

[1]Thin Films and Nanomaterials Research Laboratory, Department of Physics, Osmania University, 500007 Hyderabad, India
[2]Thin Film Nanomaterials Laboratory, Department of Physics, Shivaji University, Kolhapur, India
vijay.yelsani@gmail.com

Prejem rokopisa – received: 2014-05-13; sprejem za objavo – accepted for publication: 2014-07-11

doi:10.17222/mit.2014.079

Vanadium pentoxide (V_2O_5) thin films were deposited using the spray pyrolysis technique. An aqueous solution of ammonium vanadate with a 0.05 M concentration was used for depositing V_2O_5 thin films at three different substrate temperatures on glass substrates. The structural and optical characteristics of the V_2O_5 thin films were examined with X-ray diffraction (XRD) and double-beam UV-visible spectrophotometry. The X-ray diffraction study of the V_2O_5 thin films revealed a polycrystalline nature of the orthorhombic structure with the preferred orientation of (001). The crystallite size (d) was calculated from the (001) diffraction peak using the Debye-Scherrer formula. From the optical absorbance measurements, the optical band gap (E_g) was determined. A scanning electron microscope (SEM) was used to characterize the morphology of the films. Electrical measurements of the films indicated that the resistance decreases with an increase in the substrate temperature. From the thermoelectric measurements, the Seebeck coefficient was determined.

Keywords: V_2O_5 thin film, spray pyrolysis, optical band gap, activation energy, temperature coefficient of resistance, Seebeck coefficient

Tanka plast vanadijevega pentoksida (V_2O_5) je bila nanesena s tehniko piroliznega brizganja. Za nanos tanke plasti V_2O_5 na podlago iz stekla pri treh različnih temperaturah podlage je bila uporabljena koncentracija vodne raztopine amonijevega vanadata 0,05 M. Značilnosti strukture in optične značilnosti tanke plastiV_2O_5 so bile preiskovane z rentgensko difrakcijo in z dvožarkovno UV-vidno spektrofotometrijo. Rentgenska difrakcija tanke plasti V_2O_5 je odkrila polikristalno naravo ortorombične strukture s prednostno orientacijo (001). Velikost kristalitov (d) je bila izračunana iz difrakcijskega vrha (001) z Debye-Scherrerjevo formulo. Iz meritev optične absorbance je bila določena pasovna vrzel (E_g). Za karakterizacijo morfologije plasti je bil uporabljen vrstični elektronski mikroskop (SEM). Električne meritve tankih plasti so pokazale, da se upornost zmanjšuje z naraščanjem temperature podlage. Iz termoelektričnih meritev je bil določen Seebeckov koeficient.

Ključne besede: tanka plast V_2O_5, pirolizno brizganje, optična pasovna vrzel, aktivacijska energija, temperaturni koeficient upornosti, Seebeckov koeficient

1 INTRODUCTION

Vanadium oxide is of enormous research interest because of its multivalent nature. The VO_2, V_2O_3 and V_2O_5 multivalent oxides exhibit a lot of fascinating and novel properties. Among these vanadium pentoxide (V_2O_5) has been extensively studied and because of its highest oxidation state in the V – O system, a wide band gap, a better stability and its electrothermal effects it is useful for device applications. V_2O_5 is used in various devices, such as color filters, smart windows[1] and infrared detectors,[2] as well as gas sensing[3] and catalysis.[4]

Vanadium pentoxide thin films are prepared with different physical and chemical techniques, namely, thermal evaporation,[5] pulsed-laser deposition,[6] sputtering,[7] inorganic sol-gel method[8] and spray pyrolysis.[9] Being simple and less expensive, the spray-pyrolysis technique (SPT) is a better chemical technique, carried out at a lower cost, for the preparation of thin films with a larger area. In addition, it provides an easy way to dope any element in the ratio of a required proportion through the solution medium. This method is convenient for preparing pinhole-free, uniform thin films with the required thickness.[10] In the spray-pyrolysis technique, various deposition parameters like the compressed-air pressure, the spray rate, the substrate temperature, the distance between the nozzles and the substrate and the cooling rate after deposition also affect the physical, electrical and optical properties of thin films.[11] However, few efforts have been made to systematically investigate the effects of deposition parameters on the structural, electrical and optical properties of the vanadium oxide thin films deposited with SPT.[12]

In the present investigation, a synthesis of V_2O_5 made with the spray-pyrolysis technique was investigated at

low substrate temperatures, and the structural, optical and thermoelectric properties of the films are reported.

2 MATERIAL AND METHODS

Before depositing the V_2O_5 thin films, the glass substrates were cut into 2.25 cm × 2.25 cm pieces and subjected to cleaning and degreasing protocols. 0.05 M concentrated ammonium vanadate with deionized water was used as the starting material. The spray solution was introduced into the air stream by means of a syringe pump. In the spray system, compressed and purified air was used as the carrier gas with a 3 kg/cm^2 pressure and the solution spray rate was maintained at 3 mL/min. The distance between the spray nozzle and the substrate was fixed at 25 cm. The spray head moved in the horizontal plane due to a stepper motor to achieve a uniform deposition of the films on the heated substrates maintained at different temperatures, i.e., (250, 300 and 350) °C. The substrate temperature was controlled through a digital temperature controller with an accuracy of ±5 °C.

The crystal structures of the films were studied with XRD using a Philips Xpert diffractometer with Cu-$K\alpha$ radiation (the X-ray wavelength λ = 0.154 nm). Microphotography of the films was carried out using a scanning electron microscope. Optical parameters were calculated from the absorption spectra recorded against the wavelength using a Lab India UV-Visible 3000 spectrophotometer. The resistance of the films was measured with the two-point probe method using a Keithley electrometer (model no. 196) in the temperature range of 27–100 °C. The metallic contacts on the films were made of silver paint. Thermoelectric power [TEP] was measured using a home-built system with two copper blocks, one for the heat source and the other one for the heat sink to create a temperature gradient and produce the Seebeck voltage. The whole apparatus was kept in an enclosure to minimize the air-current disturbances. The temperature of the hot junction was raised slowly and the thermo e.m.f. was noted at regular intervals of 5 °C. The thermo e.m.f. was measured with a Keithley nanovoltmeter (model no.181).

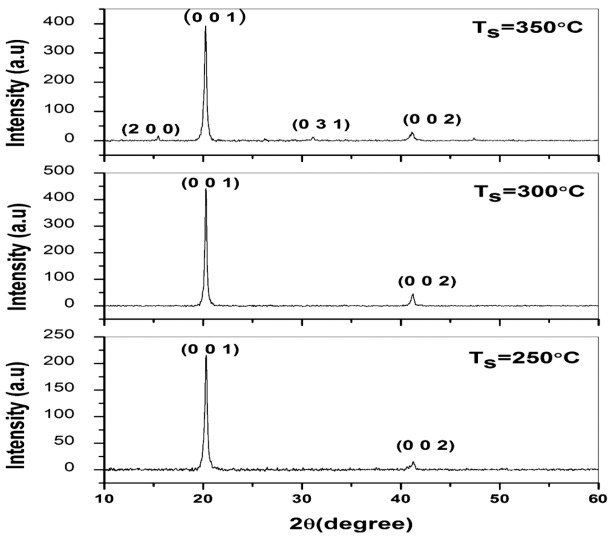

Figure 1: X-ray diffraction patterns of V_2O_5 films at different substrate temperatures

Slika 1: Posnetek rentgenske difrakcije tanke plasti V_2O_5 pri različnih temperaturah podlage

3 RESULTS AND DISCUSSION

3.1 Structural properties

The X-ray diffraction (XRD) patterns of V_2O_5 thin films at different substrate temperatures are shown in **Figure 1**. The peaks obtained in the XRD pattern match the peaks in JCPDS # 89-2482, corresponding to the orthorhombic V_2O_5 phase with the lattice-parameter values of a = 1.154 nm, b = 0.3571 nm and c = 0.4383 nm. The V_2O_5 phase formation starts on the films deposited at the substrate temperature of 250 °C with the (001) reflection and this reflection was more dominant with the film deposited at 300 °C. The XRD patterns suggest that the texture of a V_2O_5 thin film is oriented along the c-axis and, on a further increase in the substrate temperature, up to 350 °C, other reflections – (200), (301) – also appear. The orthorhombic V_2O_5 phase is in agreement with the earlier reports on the V_2O_5 thin films deposited with the spray pyrolysis and also with other methods.[13,14] The crystallite size of the films was estimated with the Debye-Scherrer formula for the (001) reflection:

$$d = \frac{0.94\lambda}{\beta \cos\theta} \tag{1}$$

where d is the crystallite size, λ is the X-ray wavelength (0.154 nm), β is the full-width half maximum and θ is the Bragg diffraction angle in degrees.

The variation in the crystallite size with the substrate temperature is summarized in **Table 1**. The results show that the crystallite size varies from 67 nm for the film deposited at 250 °C to 84 nm for the film deposited at 300 °C and it further changes to 74 nm for the film deposited at 350 °C. It can also be observed that the crystallite size increases with the substrate temperature varying from 250 °C to 300 °C. This could be associated with the coalescence process being favored in this temperature range, leading to an increase in the crystal-

Table 1: Variation in the crystallite size, optical band gap, activation energy and Seebeck coefficient with the substrate temperature

Tabela 1: Spreminjanje velikosti kristalitov, optične pasovne vrzeli in Seebeckovega koeficienta s temperaturo podlage

Substrate temperature	Crystallite size d/nm	Optical band gap E_g/eV	Activation energy E_a/eV	Seebeck coefficient S/(μV/K)
250 °C	67	2.34	0.15	–70
300 °C	84	2.29	0.13	–66
350 °C	74	2.21	0.12	–65

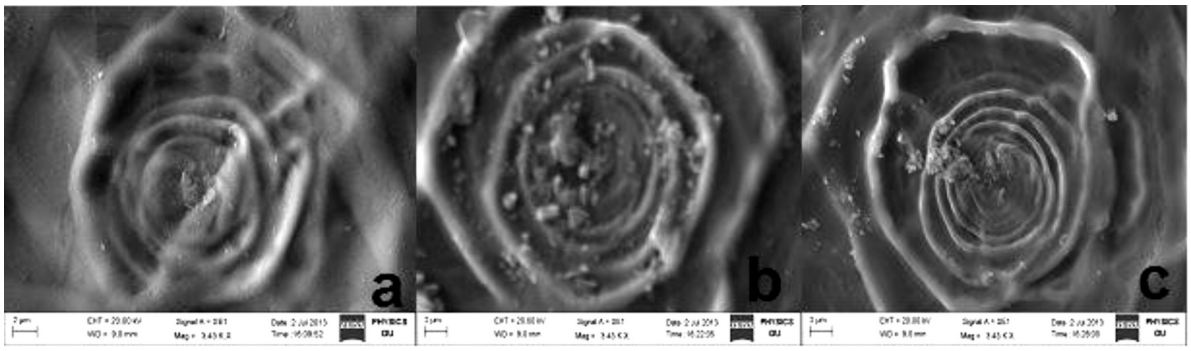

Figure 2: SEM images of V_2O_5 films at different substrate temperatures: a) 250 °C, b) 300 °C, c) 350 °C
Slika 2: SEM-posnetki tanke plasti V_2O_5 pri različnih temperaturah podlage: a) 250 °C, b) 300 °C, c) 350 °C

lite size. A further increase in the substrate temperature leads to a decrease in the crystallite size which may be due to the re-crystallization of the material.

The dislocation density (δ) is described as the length of dislocation lines per unit volume of the crystal. The dislocation density (δ) of the crystal gives information about the crystal structure. The dislocation density for the preferential orientation can be calculated using the formula below:[15]

$$\delta = \frac{1}{d^2} \tag{2}$$

where d is the crystallite size. The dislocation density obtained from Equation (2) for various crystallite sizes is found to be $15 \cdot 10^{-3}$ nm^{-2}, $12 \cdot 10^{-3}$ nm^{-2} and $13 \cdot 10^{-3}$ nm^{-2}. It can be concluded from the above results that the smaller the dislocation density the better is the crystallization of the film.

Figure 2 presents the SEM images of the films deposited at different substrate temperatures. Similar results were observed for MoO_3 thin films.[16]

It can be seen from the SEM images and analyses of the topographical profiles that the surfaces of the films grown at a substrate temperature of 300 °C clearly grew like a sponge-type structure with macropores.

3.2 Optical properties

The impact of the substrate temperature on the optical energy-gap (E_g) values was investigated with the optical-absorbance measurements. The absorbance spectra of the films deposited at different substrate temperatures are presented in **Figure 3**. By increasing the substrate temperature, the absorbance of the films was increased. The optical absorption coefficient α was estimated with the following relation:

$$\alpha = \frac{A}{t} \tag{3}$$

where t is the film thickness and A is the absorbance.

According to the interband absorption theory, the optical band gap (E_g) of the films was calculated using the following relation:

$$\alpha h\nu = B(h\nu - E_g)^m \tag{4}$$

where B is the probability parameter for the transition, E_g is the optical band gap of the material, $h\nu$ is the incident photon energy, and m is the transition coefficient.

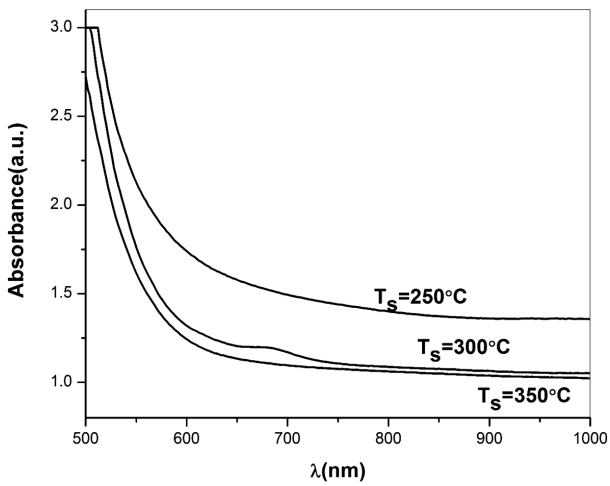

Figure 3: Absorbance versus wavelength at different substrate temperatures
Slika 3: Odvisnost absorbance od valovne dolžine pri različnih temperaturah podlage

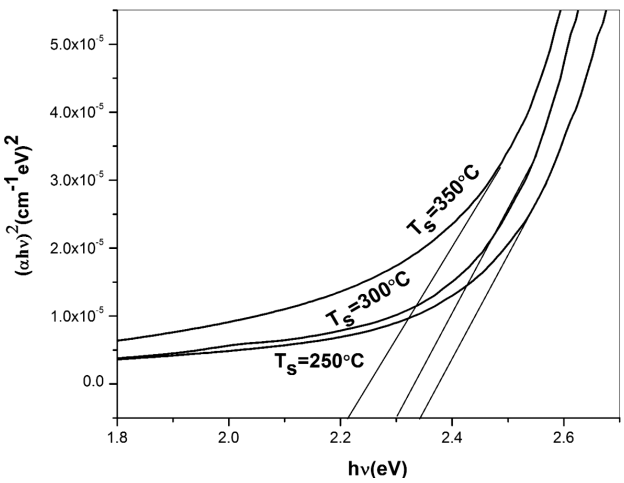

Figure 4: $(\alpha h\nu)^2$ versus $h\nu$ at different substrate temperatures
Slika 4: Odvisnost $(\alpha h\nu)^2$ od $h\nu$ pri različnih temperaturah podlage

The value of m was taken as 1/2 for direct transitions, 3/2 for direct forbidden transitions, 2 for indirect transitions and 3 for indirect forbidden transitions.[17]

The plotting of $(\alpha h\nu)^{1/m}$ versus the photon energy ($h\nu$) and extrapolating it to $(\alpha h\nu)^{1/m} = 0$ gives the value of E_g. **Figure 4** shows the plots of $(\alpha h\nu)^2$ versus $h\nu$ for the V_2O_5 films deposited at different substrate temperatures. The results obey the above equation with $m = 1/2$ indicating a direct transition. The calculated values of the optical band gap E_g were found to be (2.34, 2.29 and 2.21) eV for the films deposited at (250, 300 and 350) °C, respectively. These values for the V_2O_5 thin films investigated in the present study are consistent with the values reported in[14]. The decrease in the optical band gap is attributed to the microstructural changes caused by a high substrate temperature. At high temperatures the interatomic distance decreases, leading to a decrease in the localized states in the conduction and valance bands.

3.3 Thermoelectric properties

Figure 5 presents the room-temperature resistances of the films deposited at different substrate temperatures (T_s). It was found that the room-temperature surface resistance decreased from 180 kΩ to 50 kΩ as the substrate temperature increased from 250 °C to 350 °C. We maintain that the resistances are related to the microstructures of the films, which strongly depend on the substrate temperature. The film growth is directly related to the diffusion of atoms into the substrates:[18]

$$D = D_0 \exp\left(-\frac{E_d}{kT}\right) \quad (5)$$

Here D is the surface-atomic-diffusion coefficient, E_d is the activation energy (atom), k is the Boltzmann constant and T is the absolute temperature. In the film growth mechanism, it is evident that the resistance of the films is dependent on the substrate temperature which can be expressed with Equation (5) supported with **Figure 5**. At lower temperatures, the atoms may not have the sufficient energy for the atomic-jump process to overcome the potential energy of the nucleation sites of the substrate. At higher substrate temperatures, the mobility of atoms on the substrate surface is generally higher. As a result, the diffusion distance of atoms on the surface increases and the collision process initiates the nucleation for more atoms joined together, resulting in a decrease in the room-temperature resistance. To further investigate the electrical properties of the films, we measured the resistance and the temperature coefficient of resistance (*TCR*) of the films. The variation in the resistance with different substrate temperatures is plotted in **Figure 6**. These plots are in good agreement with the thermal-activation mechanism evaluated with the following relation:[19]

$$R = R_0 \exp\left(\frac{E_a}{kT}\right) \quad (6)$$

where R is the resistance, R_0 is the constant, E_a is the activation energy, k is the Boltzmann constant and T is the absolute temperature. The values of E_a derived according to the plots shown in **Figure 7**, using Equation (6) are (0.15, 0.13 and 0.12) eV. These results indicate that electrons need less activation energy to jump from a vanadium site to another one with an increased temperature as the substrate temperature increased. They also explain that in the case of a film grown at a higher substrate temperature, atoms are closely packed, there are fewer defects and, hence, the hopping energy related to the thermally assisted tunneling process decreases.[18] The temperature coefficient of resistance (*TCR*) can be calculated as:[20]

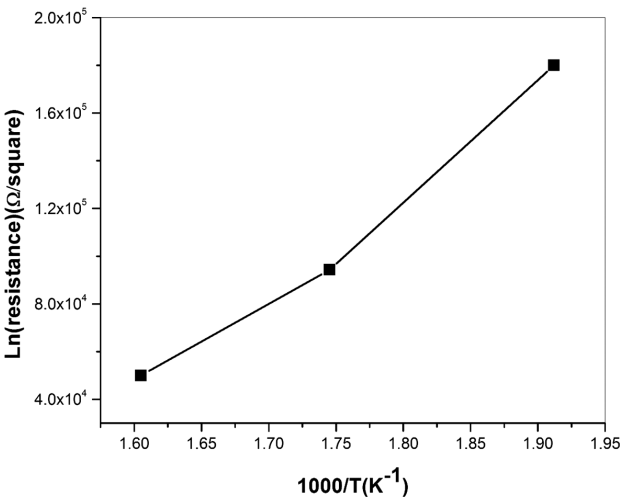

Figure 5: Resistance of V_2O_5 film versus the substrate temperature
Slika 5: Odvisnost upornosti tanke plasti V_2O_5 od temperature podlage

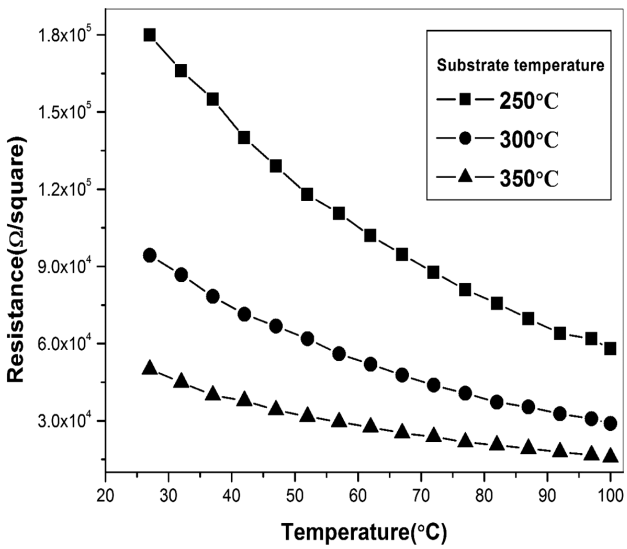

Figure 6: Resistance of V_2O_5 thin films as a function of the heating temperature
Slika 6: Upornost tanke plasti V_2O_5 kot funkcija temperature ogrevanja

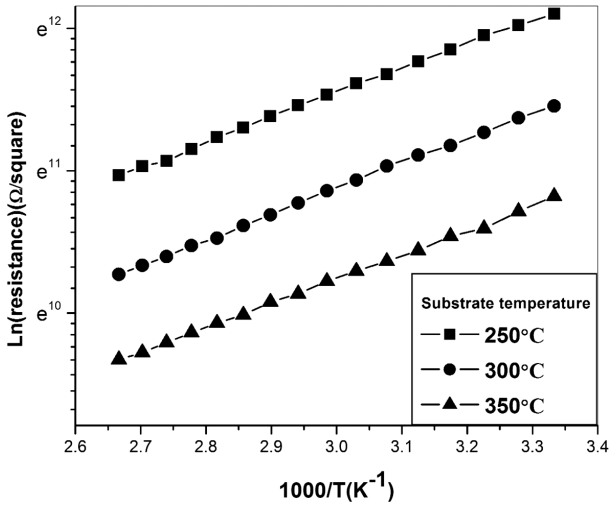

Figure 7: L_n (resistance) versus 1000/T
Slika 7: Odvisnost L_n (upornost) od 1000/T

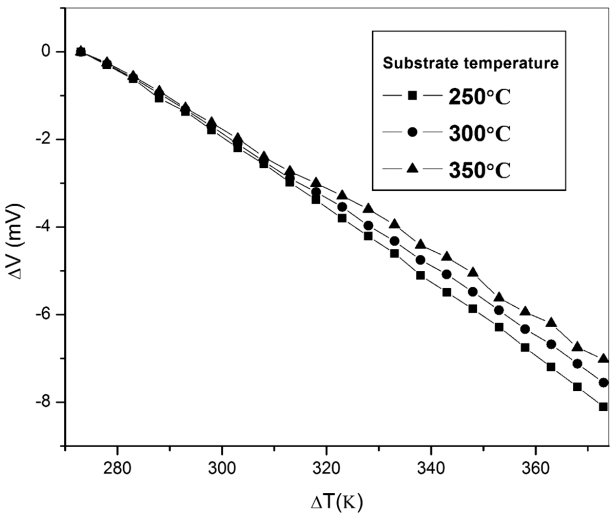

Figure 8: ΔV versus ΔT for different substrate temperatures
Slika 8: Odvisnost ΔV od ΔT pri različnih temperaturah podlage

$$TCR = \frac{\ln R}{\mathrm{d}T} \tag{7}$$

where R is the resistance and T is the absolute temperature.

The TCR values are (1.53, 1.59 and 1.50) · 10^{-2} K^{-1} for the substrate temperatures of (250, 300 and 350) °C, respectively. The increase in the TCR value up to 1.59 · 10^{-2} K^{-1} at the substrate temperature of 300 °C may be due to a more intense crystallization of the film at this temperature.

The Seebeck coefficient was determined by measuring the thermo e.m.f (ΔV) as a function of the temperature difference (ΔT). Typical data from the Seebeck measurements are shown in **Figure 8**, the thermo e.m.f. (ΔV) shows a linear dependence of ΔT. The negative value of the thermo e.m.f. was consistent with the n-type semiconductor behavior. The Seebeck coefficient (S) could be found from the slope of the graphs (**Figure 8**):[21]

$$S = \frac{\Delta V}{\Delta T} \tag{8}$$

The Seebeck-coefficient value increases as the substrate temperature T_s is increased to the maximum value of 65 μV/K at 350 °C. The enhancement of the Seebeck-coefficient value due to the increase in the substrate temperature leads to a decrease in the activation energy, which can be attributed to the improvement in the crystallinity compared to the low-substrate-temperature films. The thermoelectric properties of the V_2O_5 thin films produced are relatively suitable for the IR sensor applications.

4 CONCLUSIONS

V_2O_5 thin films were prepared, with spray pyrolysis, on glass substrates at different substrate temperatures. XRD patterns of the V_2O_5 thin films showed a crystalline orthorhombic structure with the preferential orientation of (001). The films deposited at a temperature of 300 °C are well textured and c-axis oriented with good crystalline properties. The optical band gaps of the films prepared at different temperatures are found to be (2.27, 2.25 and 2.16) eV. The electrical resistance decreased with an increase in the substrate temperature. The electrical resistance, TCR and the Seebeck coefficient of the V_2O_5 films were also strongly influenced by the substrate temperature.

Acknowledgment

One of the authors, Y. V. K., thanks the UGC, New Delhi, for providing the financial assistance in the form of RFSMS. M. V. R. R. thanks UGC-MRP F.41-907/2012(SR), New Delhi, and DST-PURSE, Osmania University, Hyderabad, for providing the financial assistance in the form of a project.

5 REFERENCES

[1] K. Nagase, Y. Shimizu, N. Miura, N. Yamazoe, Electrochromic properties of vanadium pentoxide thin films prepared by new wet process, Appl. Phys. Lett., 60 (**1992**) 7, 802, doi:10.1063/1.106523

[2] R. T. Rajendra Kumar, B. Karunagaran, D. Mangalaraj, S. K. Narayandass, P. Manoravi, M. Joseph et al., Room temperature deposited vanadium oxide thin films for uncooled infrared detectors, Mater. Res. Bull., 38 (**2003**) 7, 1235–1240, doi:10.1016/S0025-5408(03)00118-1

[3] D. Manno, A. Serra, M. DiGiulio, G. Micocci, A. Taurino, A. Tepore et al., Structural and electrical properties of sputtered vanadium oxide thin films for applications as gas sensing material, J. Appl. Phys., 81 (**1997**) 6, 2709–2714, doi:10.1063/1.363973

[4] M. Ponzi, C. Duschatzky, A. Carrascull, E. Ponzi, Obtaining benzaldehyde via promoted V2O5 catalysts, Appl. Catal. A, 169 (**1998**) 2, 373–379, doi:10.1016/S0926-860X(98)00026-X

[5] M. F. Al-Kuhaili, E. E. Khawaja, D. C. Ingram, S. M. A. Durrani, A study of thin films of V_2O_5 containing molybdenum from an evaporation boat, Thin Solid Films, 460 (**2004**) 1–2, 30–35, doi:10.1016/j.tsf.2004.01.076

[6] C. V. Ramana, B. S. Naidu, O. M. Hussain, R. Pinto, Low-temperature growth of vanadium pentoxide thin films produced by pulsed laser ablation, J. Phys. D: Appl. Phys., 34 (**2001**) 7, L35, doi:10.1088/0022-3727/34/7/101

[7] C. W. Zou, X. D. Yan, J. Han, R. Q. Chen, W. Gao, Microstructures and optical properties of β-V_2O_5 nanorods prepared by magnetron sputtering, J. Phys. D: Appl. Phys., 42 (**2009**) 14, 145402, doi:10.1088/0022-3727/42/14/145402

[8] Y. V. Kumar, M. V. R. Reddy, K. N. Reddy, Preparation and optical characterization of V_2O_5 thin films, International Conference on Nanoscience, Engineering and Technology (ICONSET), Chennai, India, 2011, 244–246, doi:10.1109/ICONSET.2011.6167931

[9] M. A. Kaid, Characterization of Electrochromic Vanadium Pentoxide Thin Films Prepared By Spray Pyrolysis, Egypt. J. Solids, 29 (**2006**) 2, 273–291

[10] P. S. Patil, Versatility of chemical spray pyrolysis technique, Materials Chemistry and Physics, 59 (**1999**) 3, 185–198, doi:10.1016/S0254-0584(99)00049-8

[11] P. S. Patil, Preparation and characterization of spray pyrolyzed nickel oxide (NiO) thin films, Appl. Surf. Sci., 199 (**2002**) 1–4, 211–221, doi:10.1016/S0169-4332(02)00839-5

[12] M. Mousavi, A. Kompany, N. Shahtahmasebi, M. M. Bagheri-Mohagheghi, Study of structural, electrical and optical properties of vanadium oxide condensed films deposited by spray pyrolysis technique, Adv. Manuf., 1 (**2013**) 4, 320–328, doi:10.1007/s40436-013-0045-y

[13] A. Kumar, P. Singh, N. Kulkarni, D. Kaur, Structural and optical studies of nanocrystalline V2O5 thin films, Thin Solid Films, 516 (**2008**) 6, 912–918, doi:10.1016/j.tsf.2007.04.165

[14] R. Irani, S. M. Rozati, S. Beke, Structural and optical properties of nanostructural V_2O_5 thin films deposited by spray pyrolysis technique: Effect of the substrate temperature, Materials Chemistry and Physics, 139 (**2013**) 2–3, 489–493, doi:10.1016/j.matchemphys.2013.01.046

[15] S. Aydogu, O. Sendil, M. B. Coban, The Optical and Structural Properties of ZnO Thin Films Deposited by the Spray Pyrolysis Technique, Chinese Journal of Physics, 50 (**2012**) 1, 89–100

[16] H. M. Martínez, J. Torres, L. D. López-Carreño, M. E. Rodríguez-García, The Effect of Substrate Temperature on the Optical Properties of MoO3 Nano-crystals Prepared Using Spray Pyrolysis, J. Supercond. Nov. Magn., 26 (**2013**) 7, 2485–2488, doi:10.1007/s10948-012-1692-0

[17] G. A. Khan, C. A. Hogarth, Optical absorption spectra of evaporated V_2O_5 and co-evaporated V2O5/B2O3 thin films, Journal of Materials Science, 26 (**1991**) 2, 412–416, doi:10.1007/BF00576535

[18] Z. Luo, Z. Wu, X. Xu, M. Du, T. Wang, Y. Jiang, Impact of substrate temperature on the microstructure, electrical and optical properties of sputtered nanoparticle V_2O_5 thin films,Vacuum, 85 (**2010**) 2, 145–150, doi:1016/j.vacuum.2010.05.001

[19] R. M. Öksüzoğlu, P. Bilgiç, M. Yıldırım, O. Deniz, Influence of post-annealing on electrical, structural and optical properties of vanadium oxide thin films, Optics and Laser Technology, 48 (**2013**), 102–109, doi:10.1016/j.optlastec.2012.10.001

[20] H. Wang, X. Yi, S. Chen, Low temperature fabrication of vanadium oxide films for uncooled bolometric detectors, Infrared Physics & Technology, 47 (**2006**) 3, 273–277, doi:10.1016/j.infrared.2005.04.001

[21] S. Iwanaga, M. Marciniak, R. B. Darling, F. S. Ohuchi, Thermopower and electrical conductivity of sodium-doped V2O5 thin films, J. Appl. Phys., 101 (**2007**), 123709, doi:10.1063/1.2739311

UDK 621.95:519.233.4:621.9.048
Original scientific article/Izvirni znanstveni članek

ISSN 1580-2949
MTAEC9, 49(3)377(2015)

DEEP MICRO-HOLE DRILLING FOR HADFIELD STEEL BY ELECTRO-DISCHARGE MACHINING (EDM)

VRTANJE GLOBOKIH MIKROLUKENJ V JEKLA HADFIELD Z METODO ELEKTRORAZREZA (EDM)

Volkan Yilmaz[1], Murat Sarıkaya[2], Hakan Dilipak[1]

[1]Manufacturing Department, Technology Faculty, Gazi University, 06500 Ankara, Turkey
[2]Department of Mechanical Engineering, Sinop University, 57030 Sinop, Turkey
msarikaya@sinop.edu.tr

Prejem rokopisa – received: 2014-06-23; sprejem za objavo – accepted for publication: 2014-09-05

doi:10.17222/mit.2014.091

In this study, a new system for drilling deep micro-holes was designed for Hadfield steel (which is difficult to process with classical methods) with the electro-discharge-machining method (EDM) and the system was experimentally examined. The tests were carried out at three different discharge currents (6, 12 and 24) A, three different electrode-tool rotational speeds (200, 400 and 600) r/min, three different dielectric spray pressures (40, 80 and 120) bar, a constant pulse duration (12 μs) and a constant pulse interval (3 μs). After the tests the effects of the processing parameters on the basic performance outputs (the material removal rate – *MRR*), the electrode wear rate (*EWR*) and the relative wear (*RW*)) were investigated. Additionally, an analysis of variance (ANOVA) was also applied to identify the most significant factor. Optimum operating parameters were determined using the desirability-function analysis through the response surface methodology (RSM). It was found that the most effective variable affecting the *MRR*, *EWR* and *RW* was the discharge current. The discharge current was found to be the most significant control factor influencing the performance of the machining process.

Keywords: deep micro-EDM, hole drilling, Hadfield steel, multi-response optimization, ANOVA

V tej študiji je bil postavljen nov sistem za vrtanje globokih mikrolukenj v jeklo Hadfield (ki se težko obdeluje z navadnimi metodami) z metodo elektroerozije (EDM) in bil tudi eksperimentalno preizkušen. Poskusi so bili izvedeni s tremi različnimi tokovi (6, 12 in 24) A, pri treh različnih hitrostih vrtenja orodja (200, 400 in 600) r/min, pri treh različnih dielektričnih tlakih razprševanja (40, 80 in 120) bar, pri konstantnem trajanju impulza (12 μs) in konstantnem intervalu impulza (3 μs). Preiskovani so bili učinki procesnih parametrov na zmogljivost (hitrost odvzema materiala (*MRR*), stopnja obrabe elektrode (*EWR*) in relativna obraba (*RW*)). Dodatno je bila uporabljena analiza variance (ANOVA) za ugotovitev najpomembnejšega faktorja. Optimalni obratovalni parametri so bili določeni z analizo funkcije odziva na metodologijo odziva površine (RSM). Ugotovljeno je bilo, da je razelektritveni tok najpomembnejši kontrolni faktor, ki vpliva na zmogljivost procesa obdelave.

Ključne besede: globoka mikro-EDM, vrtanje luknje, jeklo Hadfield, optimiranje multiodziva, ANOVA

1 INTRODUCTION

The diameters of the holes are becoming smaller with the developing micro-mechanical systems and the classical chip-removal methods are insufficient for obtaining micro-holes, so the researchers are focusing on new manufacturing methods. Among these methods, the most applicable and commercially used one is the processing using EDM. Easy processing of hard materials and complex geometries made this method one of the most preferred uncommon manufacturing methods.[1] The most important characteristic that must be exhibited by the workpieces to be processed by EDM is electrical conductivity. The characteristics such as the workpiece hardness and toughness that are effective in the processing with conventional manufacturing methods are not important with respect to EDM. On the other hand, a good processing performance depends on the thermal and electrical conductivities of a material.[2–4] Studies of EDM are generally concentrated on the performance outputs. In the studies based on the lower-duration, low-cost and high-quality expectations of the manufacturing industry, the improvement of *MRR*, *EWR*, *RW* and surface-roughness outputs is emphasized.[5–8] Besides these studies on the EDM system, rapid hole-drilling electro-discharge-machining machines were also developed to meet the new development expectations. This new EDM technique became a production technique that is often preferred in the aviation (cooling holes in plane turbine blades), automotive (fuel injection) and medical (dental and surgical implants) areas, used for medical materials, cutting-tool cooling channels and micro-hole drilling of hard, brittle and difficult-to-process materials.[9–12] In this method, small-sized processing residuals are removed from the processing area by means of a dielectric liquid sprayed at a desired pressure through a tube-type electrode of a small diameter, rotating at a specified speed. Holes with larger diameters than the one of the used electrode tool are easily produced. The most important advantage of the method is that holes can be drilled into any electrically conductive metal. Micro-EDM is an important method, especially for small pieces, micro-constituents and the production of micro-tools providing a good surface quality and high integrity. Besides, it is

Table 1: Chemical composition of the workpiece material in mass fractions, *w*/%
Tabela1: Kemijska sestava materiala obdelovanca v masnih deležih, *w*/%

C	Si	Mn	P	S	Cr	Mo	Ni	Al	Co	Cu	V	Fe
1.08	0.621	13.6	0.0152	0.0004	0.721	0.263	0.286	0.004	0.023	0.183	0.0003	Balance

maintained that micro-production technology can be developed with the micro-EDM.[13] In addition to the tube-like tools, the use of the tools that are not tube-like is also increasing and it is maintained that the holes obtained with the cylindrical tool with an orbital motion are more uniform than the ones made with the tool not having a rotational motion.[14] It was observed that *MRR* increased with the inverse polarity (tool '+',workpiece '–') causing the electrode wear as well.[15] It is known that vibration applications give favorable results with respect to the increased *MRR* and *MRR* increases during vibrational processes with the shortening of the process duration.[16,17]

When the studies in the literature are evaluated, it is seen that hole-drilling applications using the developing EDM method are used for the micro-hole drilling processes as an alternative method. The current studies relating to all the metals are developing in the direction of drilling deep holes with desired sizes and geometries using the above types of drilling units. In deep micro-hole drilling applications, the main expectations are to obtain a higher *MRR* and lower *EWR* and *RW* for a small diameter and a higher hole length. The aim of this study is to meet these expectations during the drilling of micro-holes into Hadfield steel, which is hard to process with the classical chip-removal methods due to deformation hardening; the effects of the discharge current, the electrode-tool rotational speed and the dielectric spray pressure on the basic performance outputs were investigated. Besides, in the literature, no study on deep micro-hole drilling of Hadfield steel with EDM was encountered.

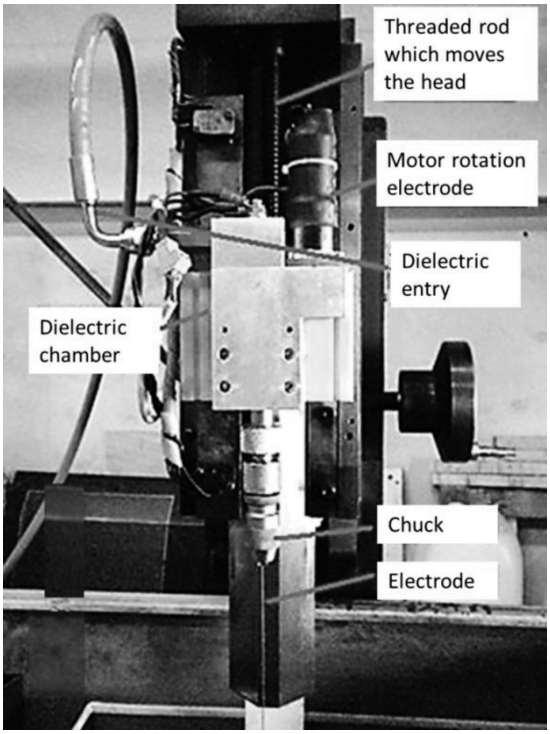

Figure 1: Pressure head
Slika 1: Tlačna glava

2 MATERIAL AND METHOD

2.1 Experimental material and equipment

As the test sample, Hadfield steel, which is hard to process with the classical chip-removal methods (because of deformation hardening) was used. Because of its unique properties such as hardness, wear resistance, strength and low thermal conductivity, this material has recently been commonly utilized in many engineering operations involving mining equipment, excavators, railways, pumping equipment, rolling-mill parts for steel factories and wear-resistant components of machining elements[18,19]. Test samples in the size of 10 mm × 20 mm × 200 mm were prepared. The chemical composition of Hadfield material is given in **Table 1**. In the tests, the FURKAN brand, "EEİ M50A" type EDM machine was used. A head was fixed to the moving head of the electro-erosion machine to rotate the electrode tool at different rotations and spray the process liquid (dielectric liquid) to the processing area at the desired pressure. The fixed head is seen in **Figure 1**. In the tests, brass electrodes with a length 400 mm, inside diameter 0.18 mm and outside diameter 0.8 mm were used as the electrode tool. A fixed electrode and the test samples are presented in **Figure 2**.

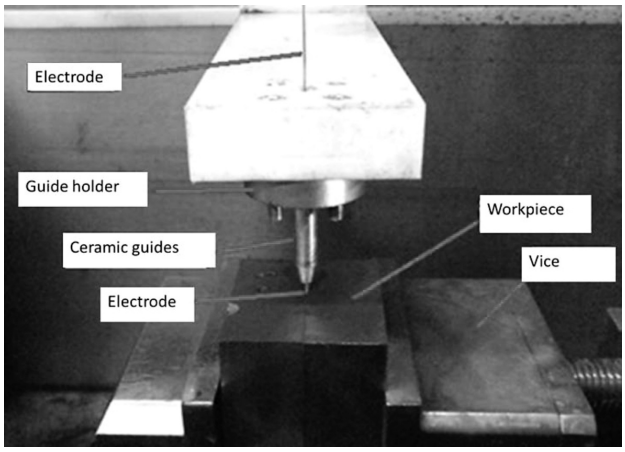

Figure 2: Fixing the electrode
Slika 2: Pritrditev elektrode

2.2 Experiments

In this study, tests were made using the EDM method at three different discharge currents (6, 12 and 24) A, three different electrode rotational speeds (200, 400 and 600) r/min, three different dielectric spray pressures (40, 80 and 120) bar, a constant pulse duration (12 µs) and a constant pulse interval (3 µs). A schematic view of the EEP unit designed for the tests is given in **Figure 3**. As seen in this figure, the pressure head is mounted on the moving part of the EDM machine at the *Z*-axis. Owing to the pressure head, the electrode had a rotational motion and the pressurized dielectric liquid had access to the processing area through the electrode. The rotational motion was given to the electrode by a D. A motor on the pressure head. Due to the power source added to the system, the rotational speed of the electrode was controlled and it reached the desired r/min values. In this system, the motion of the electrode at the vertical axis was provided by another D. A motor included in the EDM machine. Dielectric liquid reached the pressure head by means of a pressure pump. The dielectric liquid pressure was continuously controlled by a manometer mounted on the by-pass mechanism. The desired dielectric liquid pressure was achieved with a set screw. With a high-pressure resistant hose, dielectric liquid was pumped to the pressure head at the pressure of up to 200 bar. Dielectric liquid was pumped to the processing area, passing through the interior part (0.18 mm) of the electrode fixed to the pressure head by means of a mandrel. The processes were carried out in a separate tank mounted in the process chamber. The workpieces in the process tank were fixed with a clamp. The parallelism of the clamp and the process tank was controlled with an assay balance and it was verified that they were also parallel to the EDM machine base and perpendicular to the pressure head.

2.3 Determination of the EDM basic performance outputs (MRR, EWR and RW)

At the end of the tests, the *MRR*, *EWR* and *RW* values were calculated with the following formulas:

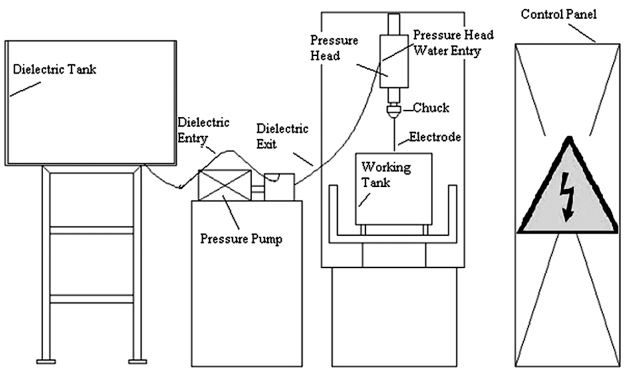

Figure 3: Schematic view of designed EEP test set-up
Slika 3: Shematski prikaz zasnovanega EEP-preizkuševališča

$$MRR = \frac{\text{Total workpiece wear volume (mm}^3\text{)}}{\text{Total working time (min)}} \quad (1)$$

$$EWR = \frac{\text{Total electrode wear volume (mm}^3\text{)}}{\text{Total working time (min)}} \quad (2)$$

$$RW = \frac{EWR}{MRR} \cdot 100 \quad (3)$$

MRR is material removal rate (mm^3/min), *EWR* is electrode wear rate (mm^3/min), *RW* is relative wear (%).

3 RESULTS AND DISCUSSION

The hole pictures obtained after the tests are given in **Figure 4** and the test results are in **Table 2**. The performance characteristics were specified as *MRR*/(mm^3/min), *EWR*/(mm^3/min) and *RW*/%. The results were expressed graphically in order to be easily discussed and compared.

Table 2: Experimental results
Tabela 2: Eksperimentalni rezultati

Test number	Discharge current (A)	Dielectric spray pressure (bar)	Electrode rotational speed (r/min)	Material removal rate *MRR*/(mm^3/min)	Electrode wear rate *EWR*/(mm^3/min)	Relative wear *RW*/%
1	6	40	200	1.452	0.473	32.595
2			400	1.654	0.457	27.622
3			600	1.801	0.419	23.282
4		80	200	1.433	0.519	36.217
5			400	1.707	0.540	31.664
6			600	1.808	0.561	31.043
7		120	200	2.017	0.613	30.41
8			400	2.291	0.622	27.163
9			600	2.173	0.616	28.344
10	12	40	200	5.228	2.678	51.221
11			400	4.932	2.417	49.015
12			600	5.301	2.715	51.221
13		80	200	5.614	2.875	51.221
14			400	6.524	3.182	48.782
15			600	6.769	4.098	60.534
16		120	200	5.875	3.283	55.878
17			400	7.218	3.309	45.845
18			600	7.126	3.921	55.031
19	24	40	200	8.815	10.567	119.88
20			400	9.950	11.501	115.59
21			600	9.474	9.722	102.62
22		80	200	10.527	10	94.989
23			400	14.385	10.960	76.197
24			600	12.632	9.625	76.197
25		120	200	11.475	7.898	68.835
26			400	14.982	9.842	65.694
27			600	16.452	8.325	50.6

3.1 Variation of the metal removal rate (MRR) with the processing parameters

MRR is expressed as the amount of the removed material (chip) per unit time (mm^3/min) and it is one of the most important output parameters in the EDM operations. In the EDM operations, obtaining high *MRR*-values is the main requirement and the studies are focusing on this issue. The variations in the *MRR*-values obtained in the tests with the processing parameters are graphically expressed in **Figures 5** and **6**.

When the variation of *MRR* with the discharge current (*I*) is examined in **Figure 5**, it is seen that the *MRR*-values increase with an increase in the *I*-values. Increasing the crater dimensions (occurring on the surface of the workpiece due to electrical discharges) with the direct proportional increase in the discharge energy is the general principle of the electro-erosion processing method. The reason for this is the evaporation of a large amount of the material (through fusion) per unit time from the workpiece surface due to the increasing discharge energy with the increase in the discharge current. Namely, with the increase in the discharge current each spark becomes more severe and each time these sparks pull off a greater area from the workpiece material. So, with the increasing discharge current (*I*) more material is fused and evaporated in a shorter time,

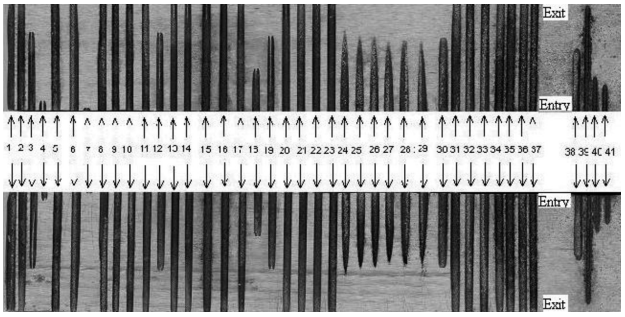

Figure 4: Hole pictures after the tests
Slika 4: Videz lukenj po preizkusih

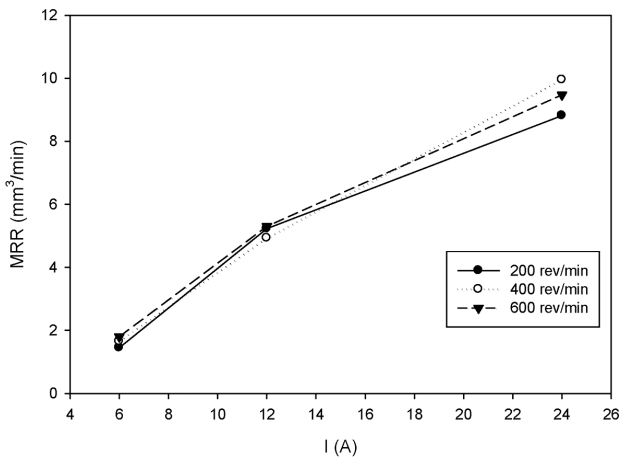

Figure 5: *MRR – I* variation
Slika 5: Diagram *MRR – I*

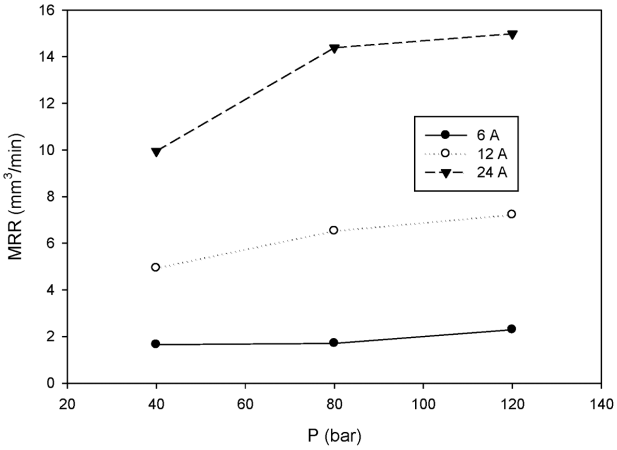

Figure 6: *MRR – P* variation
Slika 6: Diagram *MRR – P*

causing an increase in the *MRR*-values. In the tests, the *MRR*-values obtained in the interval of 1.4–2.3 mm^3/min with the 6 A discharge current, increased by approximately 200 %, to the 4.9–7.2 mm^3/min interval, with the 12 A discharge current, and by approximately 90 %, to the 8.8–16.4 mm^3/min interval, with the 24 A discharge current. When the general principle of the EDM system is taken to be the chip removing of high-energy sparks (occurring between the electrode and the workpiece) from the workpiece surface due to fusion and evaporation, the increase in the *MRR*-values with the increase in the discharge-current values is comparable with the results in[3–8]. When **Figures 5** and **6** are evaluated, it is seen that as the *I*-value is increased, keeping the electrode-tool rotational speed (*n*) constant, there is a gradual increase in the *MRR*-values. This shows that in all of the tests with the increasing discharge-current values the *MRR*-values increase without an exception. With the increasing electrode-tool rotational speed, the *MRR* performance values also increased. In the 6 A discharge-current tests at the 40 bar dielectric liquid spray pressure, with an increase in the electrode-tool rotational speed from 200 r/min to 400 r/min, the *MRR*-values increased by 14 %, and with an increase from 400 r/min to 600 r/min, *MRR* exhibited an increase of 9 %. This increase was 19 % and 6 % at the 80 bar dielectric liquid pressure. It is also valid for the other tests. The increase in the tool rotational speed provided a continuous and rapid flow of dielectric liquid to the processing area and, consequently, the formation of continuous sparks in the processing area made the processing more efficient and uninterrupted. The continuous spark discharge became the most important reason for the increase in the *MRR*-values. When the experimental values are considered the increase in the dielectric spray pressure, together with the rotational speed, makes a significant contribution to the effective washing of the processing area. In the 12 A discharge-current tests, at the 200 r/min electrode-tool rotational speed, with the increase in the dielectric liquid spray pressure from 40 bar to 80 bar, the *MRR*-values

increased by 8 %, and with an increase from 80 bar to 120 bar, *MRR* exhibited an increase of 5 %. The main reason for this is a faster motion of the fluid dielectric liquid in the area of the rotation of the tool. Due to this rapid motion, the dielectric liquid moves away from the side spaces between the electrode tool and the workpiece faster and the hole-drilling operation is carried out more effectively. When an evaluation of the *MRR*-values is made it can be found that the spray-type dielectric-application method is very effective. These results show parallelism with the studies in the literature. With respect to the spray-type dielectric-liquid applications, the reports in the literature state that higher *MRR*-values are obtained with the lateral-spray type, the reasons being a low temperature, a smaller amount of the processing-area contamination and a lower volume of gas in the processing space compared to the other methods.[15,16] With the spray-type washing used in the tests, an effective washing of the processed products can be carried out. This way a short-circuit formation of a continuous, clean dielectric liquid decreases and the sparks in the clean processing space affect the workpiece more effectively, increasing the *MRR*. Thus, for the higher *MRR*-values in the EDM operations, it was determined that the discharge current, the electrode-tool rotational speed and the dielectric spray pressure must be selected at high intervals.

3.2 Variation in the electrode-wear rate (EWR) with the processing parameters

Another important performance characteristic in the EDM applications is the *EWR*-value. The sparks created between the workpiece and the electrode in the EDM operations not only fuse the area and cause evaporation of the workpiece but they also cause evaporation of a certain area on the electrode tool. This loss of the electrode tool is expressed as *EWR* and in this study *EWR* was calculated as the decrease in the electrode volume per unit time (mm^3/min). *EWR* primarily depends on the thermal and electrical properties of the electrode material and then also on the processing parameters[7]. The relationships between the *EWR*-values and the discharge-current (*I*), electrode-tool-rotational-speed and dielectric-spray-pressure values are graphically shown in **Figures 7** and **8**.

When the variation in the *EWR* of the electrode tool (brass) (**Figure 7**) with the discharge current (*I*) is examined it is observed that the electrode-tool *EWR* increases with the increase in the *I*-value, keeping the tool rotational speed constant. It was also found that due to the increase in the *EWR* of the electrode tool more material is fused and evaporated, proportionally with the applied discharge energy. As seen from **Figure 4**, when the discharge current is 6 A, the *EWR*-values are in the interval of 0.4–0.6 mm^3/min and in the case of the 12 A discharge current the *EWR*-values increase by approximately 500 % and take place in the 2.4–4 mm^3/min interval. With the discharge current of 24 A, the *EWR*-values increase by approximately 300 % and rise to the 9.6–11.5 mm^3/min interval. According to these results, the increases in the discharge-current values caused very high increases in the brass-tool *EWR*-values. The reason for this is that the electrode has a fine structure and its inside space is empty. This fine structure heats up very rapidly by losing its electrical resistance with the increase in the tool discharge-current values. In the tests using 12 A and 24 A this was explicitly evident. During the processing these currents heated up the fine electrode material in a very short time and during the flowing of the sparks from the tool to the workpiece, big pieces were pulled off due to fusion, causing an increase in the *EWR*-values. From **Figures 7** and **8** it is seen that in the tests with the constant dielectric spray pressure and *I*-value, with an increase in the rotational speed the *EWR*-values had a tendency to increase. Since the increasing rotational speed provided a continuous, clean processing liquid in the processing area, more sparks occurred and an increased spark discharge increased the

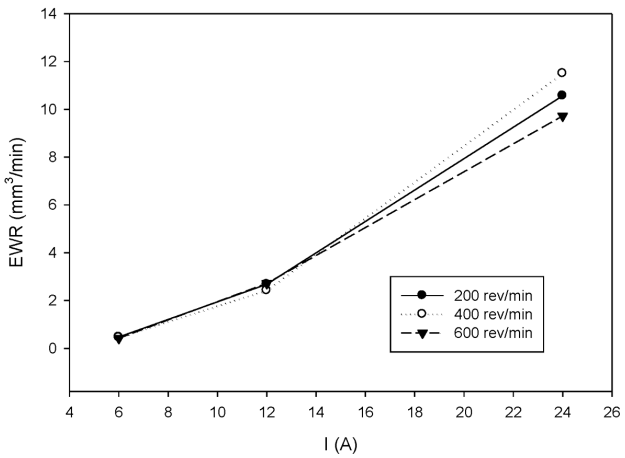

Figure 7: *EWR – I* variation
Slika 7: Diagram *EWR – I*

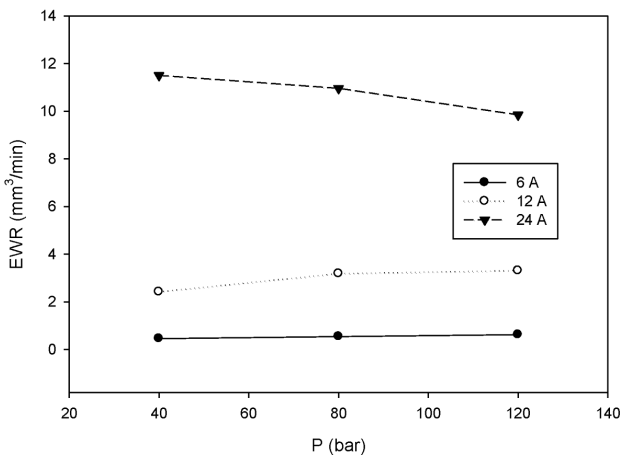

Figure 8: *EWR – P* variation
Slika 8: Diagram *EWR – P*

EWR.[3,7,10] Consequently, in the continuously cleaned processing area an effective and high amount of spark discharge caused more material to fuse and evaporate from the finely structured tool and, naturally, also caused the *EWR* to increase. This increase changes depending on the physical property of the electrode material, the discharge energy, the pulse duration, the dielectric spray characteristic and the type. When the relationship between the *EWR* and the dielectric spray pressure is examined in **Figure 8**, it is seen that the *EWR*-values increase with the increase in the dielectric spray pressure. With the increase in the dielectric spray pressure from 40 bar to 80 bar at the 6 A discharge current and 200 r/min electrode-tool rotational speed, the *EWR*-values increased by 9 %, and with the increase from 80 bar to 120 bar, the *EWR*-values increased by 20 %. The increases were 20 % and 15 % at the 400 r/min electrode-tool rotational speed and 37 % and 9 % at the 600 r/min electrode-tool rotational speed. The reason for the increase was found to be the rapid cleaning of the processing area with the increase in the dielectric spray pressure and the effective spark discharges. Besides, it is also known from the literature that the processed products are moved away from the processing area more effectively with the spraying of dielectric from the tool.[20–22] So, the decreases in *EWR* depending on the dielectric spray pressure relieve the processing area of effective spraying in electro-erosion drilling, clean the processing area more rapidly and, with a higher energy spark discharge, pull off a smaller amount of electrode material from the tube-like tool (from the point of separating the sparks).

3.3 Variation in the relative wear (RW) with the processing parameters

RW is a significant output parameter expressing the relationship between *EWR* and *MRR* during each process in the EDM operations. A graphical expression of the *RW*-values calculated with the data from the tests is given in **Figures 9** and **10**.

From **Figure 9**, it is seen that the increases in the *RW*-values also occurred, being parallel to the increase in the discharge current. The reason for this was a higher increase in the *EWR*-values with respect to the *MRR*-values at high discharge-current values. In the tests with the 6 A discharge current, the *RW*-values were in the interval of 23–33 % and in the tests with the 12 A discharge current the interval increased to 49–52 %. This shows that both *EWR*- and *MRR*-values increased by the same, small amount during the increase in the discharge-current value from 6 A to 12 A. The *RW*-values exhibited a significant increase with the 24 A discharge current compared to the results obtained with the 6 A and 12 A values and the *RW*-values increased to the 102–120 % interval. This was explained with the fact that the finely structured and empty electrode tool had a higher *EWR* with respect to the *MRR* at high discharge-current values. As an empty and finely structured electrode tool rapidly loses its electrical resistance at a high discharge current, it causes the *EWR*-values to increase. So, when *RW* is calculated with the (*EWR*/*MRR*) × 100 formula, these increases in the *EWR*-values that are higher than the *MRR*-values also cause an increase in the *RW*-values. In **Figure 9** it is seen that the *RW*-values have a tendency to increase with the rotational speed applied to the electrode tool. This was explained with the increase in the *EWR*-values caused by the increasing electrode rotational speed. In **Figure 10** it is observed that the *RW*-values decrease with the increase in the dielectric spray pressure. Processing residuals can be easily removed from the processing area owing to the spray-type washing applied in the tests (in line with the studies in the literature)[21–24] and for this reason the *MRR*-values increase in the clean processing area. So, increasing the *MRR*-values more than the *EWR*-values caused a decrease in the *RW*-values.

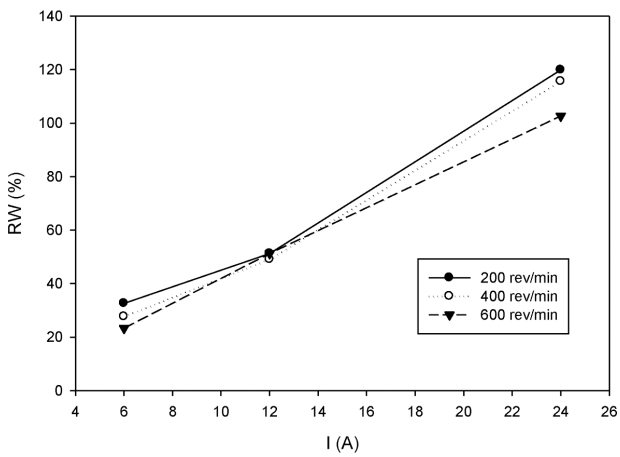

Figure 9: *RW – I* variation
Slika 9: Diagram *RW – I*

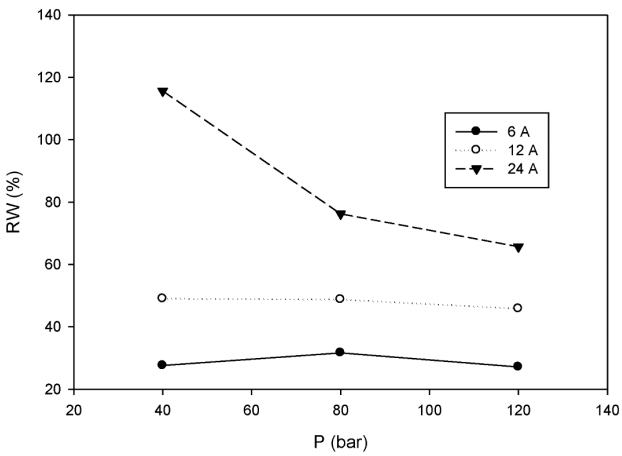

Figure 10: *RW – P* variation
Slika 10: Diagram *RW – P*

3.4 Analysis of variance (ANOVA)

Analysis of variance (also known as ANOVA) is a statistical method used to identify individual interactions of all the control factors in the experimental results. In the present work, ANOVA was used to determine the effects of the discharge current, the dielectric spray pressure and the electrode rotational speed on *MRR*, *EWR* and *RW*. ANOVA results for the responses are given in **Table 3**. The ANOVA analysis was performed at the 95 % confidence level and 5 % significance level. The *F*-values of the control factors indicated the significance of the control factors with the ANOVA analysis.[19,25–27] The percentage contribution of each parameter is shown in the last column of the ANOVA table. This column shows the influence rates of the control factors for the experimental results. In addition, ANOVA results are also summarized as a column chart in **Figure 11**. In **Table 3**, the percent contributions of the factors such as discharge current, dielectric spray pressure and electrode rotational speed to the *MRR* were determined as 88.1 %, 4.6 % and 1.7 %, respectively. Therefore, the most effective variable affecting the *MRR* was the discharge current (88.1 %). It was seen that the discharge current and dielectric spray pressure significantly affect the *MRR* at the reliability level of 95 % or the significance level of 5 %, because the *P*-values of these variables are lower than 0.05.[26] According to **Table 3**, the percent contributions of the input parameters to the *EWR* were found to be 96.9 %, 0.2 % and 0.2%, respectively, and the error was 2.7 %. It was determined that the most effective parameter with respect to the *EWR* is the discharge current. Moreover, among the input parameters, only the discharge current significantly affects the *EWR* at the reliability level of 95 % or the significance level of 5 %.

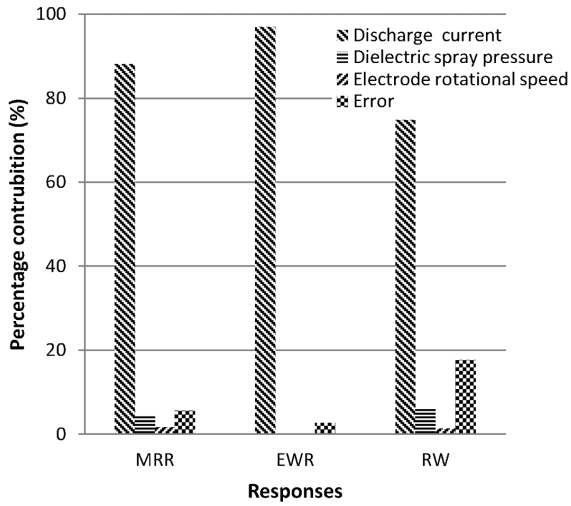

Figure 11: Histogram of the ANOVA results
Slika 11: Histogram rezultatov ANOVA

From **Table 3**, the effects of the control factors on the *RW* were obtained as 74.8 %, 6.2 % and 1.3 %, and the error amounted to 17.7 % of the contribution rate. The ANOVA table indicated that with respect to the *RW*, the most effective parameter is the discharge current.

3.5 Multi-response optimization of the EDM parameters based on RSM

Mono-response optimization is a common and popular method to solve the problems of optimization approaches. But the method cannot be used to determine the optimum combination of the machining parameters that simultaneously optimize the output parameters.[28] To overcome this problem in the present work, a multi-

Table 3: ANOVA results for means
Tabela 3: ANOVA povprečni rezultati

Variation of source	Degree of freedom (DF)	Sum of squares (SS)	Mean of squares (MS)	*F*-ratio	*P*-value	Contribution (%)
MRR						
Discharge current	2	478.516	239.258	156.96	0.000	88.1
Dielectric spray pressure	2	24.893	12.447	8.17	0.003	4.6
Electrode rotational speed	2	9.216	4.608	3.02	0.071	1.7
Error	20	30.487	1.524			5.6
Total	26	543.112				100
EWR						
Discharge current	2	412.892	206.446	358.86	0.000	96.9
Dielectric spray pressure	2	0.882	0.441	0.77	0.478	0.2
Electrode rotational speed	2	0.912	0.456	0.79	0.466	0.2
Error	20	11.506	0.575			2.7
Total	26	426.191				100
RW						
Discharge current	2	14205.4	7102.7	42.16	0.000	74.8
Dielectric spray pressure	2	1175.1	587.5	3.49	0.050	6.2
Electrode rotational speed	2	253.6	126.8	0.75	0.484	1.3
Error	20	3369.5	168.5			17.7
Total	26	19003.6				100

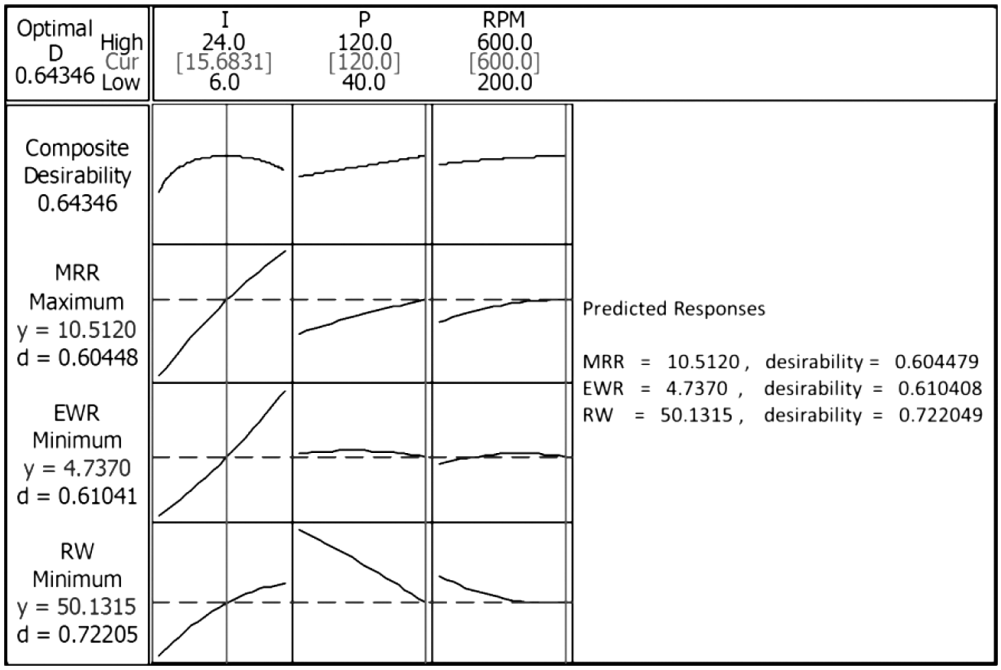

Figure 12: Plot of multi-response optimization
Slika 12: Prikaz multiodzivne optimizacije

Table 4: Best global solutions for multi-optimization
Tabela 4: Najboljše celotne rešitve multioptimizacije

Response	Goal	Global solution (Multi-optimization)			Lower	Target	Upper	Weight	Imp.	Predicted	Desira-bility
		I/A	*P*/bar	r/min							
MRR	Max.	15.6831	120	600	1.4332	16.4525	16.453	1	1	10.512	0.604479
EWR	Min.	15.6831	120	600	0.4194	0.4194	11.502	1	1	4.7370	0.610408
RW	Min.	15.6831	120	600	23.282	23.282	119.880	1	1	50.1315	0.722049
Composite desirability = 0.643461											

response optimization was performed to determine the objective values of three responses, i.e., *MRR*, *EWR*, and *RW* in deep micro-hole drilling of Hadfield steel with EDM. The multi-response optimization was employed through the Minitab 16.0 software based on the response surface methodology (RSM).[26] The graph of the multi-response optimization plotted in Minitab is shown in **Figure 12**. In this figure, each column of the plots shows the machining parameters, and the responses are shown by each row of the plots.

The objective value of each response, namely *y*, is displayed along with the desirability value range, namely *d*, which is between 0 and 1 as shown in the figure. If $d = 0$ or approaches to 0, then the output is clearly undesirable. If $d = 1$ or approaches to 1, then the output perfectly meets the target value. A higher value of desirability indicates a better optimization.[26] The highest desirability value is favored for the best solution of deep micro-EDM drilling. The goal, lower value, target value, upper value, mass, the importance of the factors and the best global solution were determined for the multi-response optimization as shown in **Table 4**. According to **Table 4** and **Figure 12**, the optimization values are found to be 10.512 mm^3/min, 4.737 mm^3/min and 50.1315 % for *MRR*, *EWR* and *RW*, respectively. Individual desirability values are 0.60448, 0.61041 and 0.72205. Moreover, the composite desirability value is 0.643461 for all the responses. The levels of the control parameters are found to be 15.6831 A for the discharge current, 120 bar for the dielectric spray pressure and 600 r/min for the electrode rotational speed for the multi-response optimization in deep micro-hole drilling of Hadfield steel by EDM.

4 CONCLUSION

In this study, using the EDM method, deep micro-hole drilling was carried out on Hadfield steel which is hard to process with classical chip-removing methods due to deformation hardening. The effects of the processing parameters of deep micro-hole drilling applications (discharge current, electrode tool rotational speed and dielectric spray pressure) on the processing performance outputs (*MRR, EWR, RW*) were examined experimentally. The results are given below.

- By means of the installed system, the holes with a diameter 0.8 mm and length 20 mm were drilled into

Hadfield steel. The most important parameter affecting the drilling durations was the discharge current. Increasing the electrode-tool rotational speed and dielectric spray pressure provided significant contributions to an easy drilling of the holes.

- When the *MRR* results were considered, a significant increase in the *MRR*-values was observed, related to the increase in the discharge-current values. The *MRR*-values had a tendency to increase with the increase in the electrode-tool rotational speed. Owing to the increasing dielectric spray pressure, the processing area always remained clean and the *MRR*-values increased accordingly.
- According to the *EWR* results, the *EWR*-values increased with the increase in the discharge current. The increase in the *EWR*-values was explained with a finely structured and empty electrode tool. The *EWR*-values increased with the increasing electrode-tool rotational speeds and decreased with the increasing dielectric spray pressure.
- When the *RW*-values were taken into consideration, the *RW*-values also increased depending on the increase in the discharge current. This was explained with the fact that the *EWR*-values increased more than the *MRR*-values because of the rise in the discharge current. The *RW*-values increased with the increase in the electrode-tool rotational speeds but decreased with the increasing dielectric spray pressure.
- From the results of ANOVA for all the responses, it was found that the most effective variable affecting the *MRR, EWR* and *RW* was the discharge current. Moreover, it was seen that the discharge current significantly affected the *MRR, EWR* and *RW* at the reliability level of 95 % or the significance level of 5 %.
- From the multi-response optimization results based on RSM, the optimum values were found to be 10.512 mm^3/min, 4.737 mm^3/min and 50.1315 % for *MRR, EWR* and *RW*. The levels of the control parameters for the optimum results were found to be 15.6831 A for the discharge current, 120 bar for the dielectric spray pressure and 600 r/min for the electrode rotational speed in deep micro-hole drilling of Hadfield steel with EDM.

5 REFERENCES

[1] V. Yilmaz, Experimental investigation of drillability of micro holes using electro discharge machining, Ph. D. Thesis, Gazi University Graduate School of Natural and Applied Sciences, Ankara, 2013

[2] P. C. Pandey, H. S. Shan, Modern machining processes, Tata McGraw-Hill Publishing Company Limited, New Delhi 1980, 84–114

[3] R. K. Springborn, Non-traditional machining processes, American Society of Tool and Manufacturing Engineers, USA 1967

[4] H. M. Chow, B. H. Yan, F. Y. Huang, J. C. Hung, Study of added powder in kerosene for the micro-slit machining of titanium alloy using electro-discharge machining, Journal of Materials Processing Technology, 101 (**2000**), 95–103, doi:10.1016/S0924-0136(99)00458-6

[5] Z. E. Ergün, C. Çoğun, Experimental investigation on workpiece surface characteristics in electric discharge machining (EDM), J. Fac. Eng. Arch. Gazi Univ., 21 (**2006**) 3, 427–441

[6] A. Özgedik, C. Çoğun, An Investigation on the effect of the applied machining tank vibrations on the machining performance in electrical discharge machining, Electronic Journal of Machine Technologies, 8 (**2011**) 3, 13–25

[7] A. Özgedik, C. Çoğun, Experimental investigation of the electrode front surface wear in electrical discharge machining, Engineer and Machinery, 521 (**2003**), 21–28

[8] C. Çoğun, B. Kocabaş, A. Özgedik, Experimental and theoretical investigation of workpiece surface profiles in electrical discharge machining (EDM), J. Fac. Eng. Arch. Gazi Univ., 19 (**2004**) 1, 97–106

[9] V. Yilmaz, H. Dilipak, Method of electro discharge machining (EDM) micro hole drilling system design, IV. UTIS 2013, Kuşadası, Turkey, 2013, 151–159

[10] F. N. Leao, Optimisation of EDM fast holedrilling through evaluation of dielectric and electrode materials, Proceedings of COBEM 2005, 18th International Congress of Mechanical Engineering, Ouro Preto, MG, 2005

[11] P. Kuppan, A. Rajadurai, S. Narayanan, Influence of EDM process parameters in deep hole drilling of Inconel 718, International Journal of Advanced Manufacturing Technology, 38 (**2008**) 1–2, 74–84, doi:10.1007/s00170-007-1084-y

[12] T. Asokan, S. S. Reddy, P. D. E. Costa, Electrical discharge drilling of titanium alloys for aerospace applications, Proceedings of 19th AIMTDR conference, IIT Madras, Chennai, 2000, 161–165

[13] D. T. Pham, S. S. Dimov, S. Bigot, A. Ivanov, K. Popov, Micro-EDM-recent developments and research issues, Journal of Materials Processing Technology, 149 (**2004**), 50–57, doi:10.1016/j.jmatprotec.2004.02.008

[14] E. Bamberg, S. Heamawatanachai, Orbital electrode actuation to improve efficiency of drilling micro-holes by micro-EDM, Journal of Materials Processing Technology, 209 (**2009**), 1826–1834, doi:10.1016/j.jmatprotec.2008.04.044

[15] B. H. Yan, C. C. Wang, The machining characteristics of Al_2O_3/6061Al composite using rotary electro-discharge machining with a tube electrode, Journal of Materials Processing Technology, 95 (**1999**) 1–3, 222–231, doi:10.1016/S0924-0136(99)00322-2

[16] W. Koenig, R. Weill, R. Wertheim, W. I. Jutzler, The flow fields in the working gap with electro-discharge-machining, Annals of the CIRP, 25 (**1977**) 1, 71–76

[17] O. Yılmaz, A. T. Bozdana, M. A. Okka, İ. H. Filiz, An intelligent and automated system for EDM hole drilling of super alloys, 5th International Conference on Responsive Manufacturing – Green Manufacturing, Ningbo, China, 2010

[18] D. Canadinc, H. Sehitoglu, H. J. Maier, Y. I. Chumlyakov, Strain hardening behavior of aluminum alloyed Hadfield steel single crystals, Acta Materialia, 53 (**2005**), 1831–1842, doi:10.1016/j.actamat.2004.12.033

[19] T. Kivak, Optimization of surface roughness and flank wear using the Taguchi method in milling of Hadfield steel with PVD and CVD coated inserts, Measurement, 50 (**2014**), 19–28, doi:10.1016/j.measurement.2013.12.017

[20] K. H. Ho, S. T. Newman, State of the art electrical discharge machining (EDM), International Journal of Machine Tools & Manufacture, 43 (**2003**), 1287–1300, doi:10.1016/S0890-6955(03)00162-7

[21] S. L. Chen, B. H. Yan, F. Y. Huang, Influence of kerosene and distilled water as dielectrics on the electric discharge machining characteristics of Ti-6Al-4V, Journal of Materials Processing Technology, 87 (**1999**) 1–3, 107–111, doi:10.1016/S0924-0136(98)00340-9

[22] N. Mohri, M. Suzuki, M. Furuya, N. Saito, Electrode wear process in electrical discharge machining, Annals of the CIRP, 44 (**1995**) 1, 165–168, doi:10.1016/S0007-8506(07)62298-7

[23] M. Znidarsic, M. Junkar, Deep Small Hole Drilling with EDM, Proceedings of 4th International Conference on Advanced Manufacturing Systems and Technology, Udine, 1996, 527–533

[24] H. S. Liu, B. H. Yan, C. L. Chen, F. Y. Huang, Application of micro-EDM combined with high-frequency dither grinding to improve micro-hole machining, International Journal of Machine Tools & Manufacture, 46 (**2006**), 80–87, doi:10.1016/j.ijmachtools.2005.03.017

[25] A. Kadirvel, P. Hariharan, Optimization of the die-sinking micro-EDM process for multiple performance characteristics using the Taguchi-based grey relational analysis, Mater. Tehnol., 48 (**2014**) 1, 27–32

[26] M. Sarikaya, A. Gullu, Taguchi design and response surface methodology based analysis of machining parameters in CNC turning under MQL, Journal of Cleaner Production, 65 (**2014**), 604–616, doi:10.1016/j.jclepro.2013.08.040

[27] M. Sarikaya, H. Dilipak, A. Gezgin, Optimization of the process parameters for surface roughness and tool life in face milling using the Taguchi analysis, Mater. Tehnol., 49 (**2015**) 1, 139–147

[28] M. Sarikaya, V. Yilmaz, H. Dilipak, Modeling and multi-response optimization of milling characteristics based on Taguchi and gray relational analysis, Proc IMechE Part B: J Engineering Manufacture, (**2015**), doi:10.1177/0954405414565136

UDK 532.6:669.058
Original scientific article/Izvirni znanstveni članek

ISSN 1580-2949
MTAEC9, 49(3)387(2015)

SURFACE ANALYSIS OF ELECTROCHROMIC Cu_xO FILMS IN THEIR COLORED AND BLEACHED STATES

POVRŠINSKA ANALIZA ELEKTROKROMIZNIH PLASTI Cu_xO V NJIHOVIH OBARVANIH IN OBELJENIH STANJIH

Mimoza M. Ristova[1,2], Milorad Milun[3], Biljana Pejova[4]

[1]Faculty of Natural Sciences and Mathematics, Institute of Physics, P.O. Box 162, Skopje, R. Macedonia
[2]Materials Science Division, Lawrence Berkeley National Laboratory, Berkeley, CA, USA
[3]Institute of Physics, Bijenicka Cesta 46, Zagreb, Croatia
[4]Faculty of Natural Sciences and Mathematics, Institute of Chemistry, P.O. Box 162, Skopje, R. Macedonia
mima.ristova@gmail.com

Prejem rokopisa – received: 2014-06-25; sprejem za objavo – accepted for publication: 2014-07-04

doi:10.17222/mit.2014.092

Cu_xO is known as an electrochromic material with a possible applicability for solar-light modulation. The reversible transition between the two different oxidation states, CuO and Cu_2O, is responsible for the visible-light switching ability. Cu_xO films in their as-prepared, colored and bleached states were subjected to a surface analysis in order to relate the bleaching/coloring effects to the quantified Cu-oxide transition. An XPS analysis on the Cu2p electrons of the as-prepared, bleached and colored films showed that the Cu-ion quantity reversibly turning from CuO to Cu_2O during the electrochromic cycling was about 3.4 %. An analysis of the XRD patterns of the film's three states confirmed that a small portion of the surface Cu-atoms probably participate in the coloration/bleaching process. Scanning electron microscopy (SEM) images revealed obvious changes in the surface morphology due to bleaching and coloration transitions, particularly in the grain size and porosity of the Cu_xO films. The surface morphology of the films was also studied with the atomic force microscopy (AFM). This technique allowed significant conclusions to be derived relating to the surface roughness as well as the compositional homogeneity of the films before and after electrochemical treatments. These results appeared to be complementary to those derived from the X-ray diffraction patterns. One may assume that the coloration centers are located at very few film's monolayers of the interface with the electrolyte.

Keywords: electrochromism, Cu_2O, CuO, XPS, XRD, SEM, AFM

Cu_xO je poznan kot elektrokromizni material z možnostjo uporabe za modulacijo sončne svetlobe. Reverzibilni prehod med dvema oksidacijskima stanjema, CuO in Cu_2O, vpliva na možnost preklapljanja vidne svetlobe. Tanke plasti Cu_xO v izhodnem, obarvanem ali obeljenem stanju so bile analizirane na površini, da bi ugotovili učinke barvanja/beljenja pri kvantificiranem prehodu Cu-oksidov. XPS-analiza z elektroni Cu2p pripravljene, obeljene in obarvane plasti je pokazala, da se okrog 3,4 % količine Cu-ionov med elektrokromizno obdelavo reverzibilno odmika od CuO proti Cu_2O. Analiza XRD-sledov treh stanj traku je potrdila, da verjetno majhen delež Cu-atomov sodeluje v postopku obarvanje/beljenje. Vrstična elektronska mikroskopija (SEM) je potrdila občutne spremembe v morfologiji površine zaradi prehodov obarvanja in obeljenja, posebno velikost zrn in poroznost plasti Cu_xO. Morfologija površine plasti je bila pregledana z mikroskopijo na atomsko silo (AFM). Ta tehnika omogoča pomembne sklepe glede površinske hrapavosti, kot tudi homogenosti sestave plasti pred elektrokemijsko obdelavo in po njej. Ti rezultati se ujemajo s tistimi, dobljenimi z XRD-posnetkov. Lahko sklepamo, da so centri obarvanja locirani v nekaj monoplasteh na stiku z elektrolitom.

Ključne besede: elektrokromizem, Cu_2O, CuO, XPS, XRD, SEM, AFM

1 INTRODUCTION

Electrochromic materials are known as modulators of the reflection/transmission of the incident illumination[1]. There are many applications of electrochromic films, one of the most important being the production of large-area electrochromic displays[2]. Rear-view mirrors with a variable reflectance, based on electrochromic oxide films, are commercially available for many kinds of vehicles[2]. The most attractive, very useful and environmental friendly applications of electrochromic materials are the so-called "smart windows"[3] that are able to automatically modulate the incoming solar illumination in the interior. Smart windows may also be alternatively powered by photovoltaic cells, thus, operating as energetically independent devices.

A copper (I) oxide (Cu_2O) thin film has been a subject of research in numerous studies, as a candidate for a solar cell application[4]. It is known that copper oxide thin films exhibit cathode electrochromism[5–8], i.e., they are transparent for visible light in their oxidized state and almost black in their reduced state.

Thin Cu_xO films can be deposited with different techniques: sputtering[8], electrochemical deposition[9,10], sol-gel-like dip technique[5,11], thermal oxidation[12], anode oxidation[13] or chemical-deposition method[14–17]. Chemically deposited Cu_xO films were the subject of our previous research[17] and are the topic of our present interest. Our former publication[18] showed some of the advantages and disadvantages of this electrochromic material for solar-light-modulation applications, implying the necessity for a more profound surface examination of their light-switching mechanism.

2 EXPERIMENTAL WORK

2.1 Electrochromic Cu_xO film preparation

Fluorine-doped tin oxide films on glass (FTO) with a sheet resistance of 10–20 Ω and transmittance for the visible light of about 80–85 %, products of Solar-Split, Croatia, were used as the substrates. Electrochromic Cu_xO films were deposited with the electroless-chemical-bath deposition method, described elsewhere[15–17]. The thickness of Cu_xO was estimated from the SEM image of the cross-section of the glass/film interface.

2.2 Surface analysis of the Cu_2O electrochromic films

The X-ray diffraction patterns of the Cu_xO films on the SnO_2 (FTO) substrates in their as-prepared, bleached and colored states were recorded with a Rigaku Ultima IV X-ray diffractometer, using Cu-$K\alpha$ radiation of 0.15418 nm. XRD scans were taken within an angular interval 2θ from 20 ° to 70 ° via a step method applying 0.02 ° steps (2θ) and a counting time of 0.6 s per scan. Scattered X-ray radiation was detected using a DteX detector. The XRD pattern of the FTO (SnO_2) substrate was recorded as well. In addition to the identification, the XRD patterns were also used for estimating the average crystal size with the Scherrer method.

The X-ray photoelectron spectroscopy (XPS) instrument consisted of a non-chromatized X-ray source with an Mg-Al dual anode. A hemispherical electrostatic electron analyzer VSW HA100 was employed under the following operating conditions: a fixed-analyzer-transition (FAT) mode of 50 eV and a resolution of 1.1 eV. The XPS spectra were taken from the Cu_xO electrochromic films deposited onto the conductive FTO surface, in their as-prepared, bleached and colored states. The Mg-$K\alpha$ XPS spectra were taken from the film surfaces with no previous Ar^+ ion-beam cleaning, taking into account that the electrochromic modifications possibly take place on the immediate surface of the interface with the electrolytes. The binding energy of the Cu2p electrons was subjected to an analysis. Taking into account that the Cu2p electron binding energy shifts due to the presence of various copper-oxygen compounds each of the compounds was quantified.

Scanning electron microscopy (SEM) was used for an estimation of the Cu_xO film thickness by taking the scans from the film/glass substrate cross-section profile. Surface SEM scans were taken from the surface of the Cu_xO/substrate as well as from the sole substrate. The SEM analyses of the scans taken from the Cu_xO/FTO samples in their as-prepared, bleached and colored states were used for depicting the variation in the crystal grain size and the porosity. A digitalized system of JEOL JSM-T220A SEM was used.

The surface morphology and phase composition of the investigated Cu_xO films, in their as-prepared, colored and bleached state, were studied with atomic force microscopy (AFM). The height, amplitude error and phase images were measured using a scanning probe Shimadzu microscope SPM 9600 operating in a dynamic and phase mode. The measurements were performed using silicon SPM probes with a resonance frequency of 320 kHz and a force constant of 42 N/m. Several different regions on the investigated sample surface were explored. The scan rate was 1 Hz or 2 Hz depending on the size of the scanned area (1 μm or 5 μm). The image resolution was 512 lines per each scan direction. The measured images were only flattened, without any further processing. The surface roughness was calculated using the SMP Manager data processing software.

3 RESULTS AND DISCUSSION

3.1 Film bleaching and coloration

Three Cu_xO films were deposited under equal conditions onto the FTO substrate. One of the films was kept in the as-prepared condition for further examination. The second film was brought into the bleached state as it was biased with +1 V against the FTO adjacent electrode in a 0.2 M KNO_3 solution for 10 seconds. The third film was fully colored upon biasing with –1 V against the FTO adjacent electrode in the 0.2 M KNO_3 solution for 10 s. The three films were subjected to a surface analysis, described in section 3.2. It is worth mentioning that the films retained their electrochromic colors for a long time (over one year) upon the completion of the surface analysis.

3.2 Surface analyses of the Cu_xO films (XRD, XPS, SEM and AFM)

The XRD patterns of the Cu_xO electrochromic films, deposited onto the FTO substrate in their as-prepared, bleached and colored state, are presented in **Figure 1**. The SnO_2 (FTO) substrate alone was also analyzed. The corresponding CPDS files for CuO, Cu_2O and SnO_2 are given in[19–21].

As can be seen from **Figure 1**, only three peaks were identified in addition to the one of the SnO_2 substrate. The analysis showed that all three detectable peaks, low in intensity, pertained to the Cu_2O cuprite phase. The small Cu_2O peak intensity and the absence of the identifiable peaks typical for the tenorite crystalline oxide state of copper (CuO) did not allow us to draw any conclusions about the electrochromic reversible switching between the two Cu-oxide states. Thus, one may speculate that the transition from the bleached to the colored state and its reverse process occur through the known transition of only a minor (sub-detectable) portion of the dominant oxide of Cu_2O into CuO.

The diffraction pattern of the as-prepared Cu_xO sample shows two diffraction peaks between the 2θ angles of 42 ° and 36 °, which are characteristic for copper (I) oxide. Following the fitting procedure, the angular position and the full width at half maximum (FWHM) of

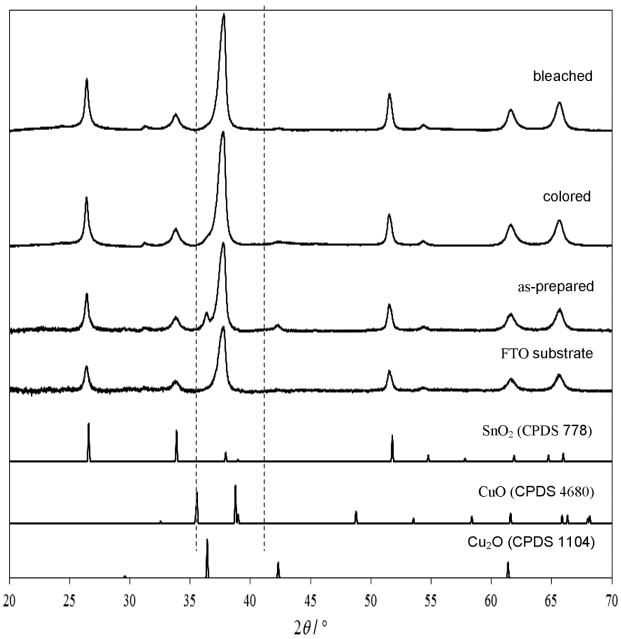

Figure 1: XRD patterns of the Cu_xO electrochromic films deposited onto the FTO substrate in their as-prepared, bleached and colored state. The pattern of the substrate and the corresponding CPDS files are given on the graph.

Slika 1: XRD-posnetki elektrokromiznih plasti, nanesenih na FTO-podlago v njihovem pripravljenem, obeljenem in obarvanem stanju. Na sliki so prikazani vzorec podlage in ustrezne CPDS-datoteke.

detectable diffraction peaks were found. The average crystal diameter was estimated to be about 24 nm using the Scherrer equation.

Figure 2 presents broad XPS spectra of the Cu_xO film in its as-prepared, bleached and colored states. The distinct peaks of the binding energy were found to originate from all the elements of the film compound, such as Cu (the 2p3/2 main peak centered at around 932 eV and a strong satellite centered at 943 eV), O (O1s) and C (C1s). The expected Auger peak of Cu $L_3M_{4.5}M_{4.5}$ is not sufficiently distinct on either of the three sample broad spectra). The three Cu2p3 spectra were corrected by fixing the C1s peak to 285 eV. Each of the corrected XPS Cu2p3 spectra was then deconvoluted into two Gaussian peaks corresponding to CuO, known to appear between 934.2 eV [22–24] and 935.2 eV [21], and to Cu_2O, known to appear between 932.3 eV and 933.8 eV [22–25]. Since the Cu^0 and Cu_2O Cu2p3 peaks can not be resolved with deconvolution (the binding energy shift between the two is only about 0.1 eV)[24], $Cu(OH)_2$ can not be clearly distinguished from CuO at 935.3 eV [22] due to their overlap. Disregarding the presence of the copper metal and hydroxide, we can assume that the entire Cu2p signal originates from the CuO and Cu_2O compounds. Each of the two Gaussian-peak areas (A1 and A2) of the Cu2p3/2 zero-leveled XPS spectra on **Figure 3** is proportional to

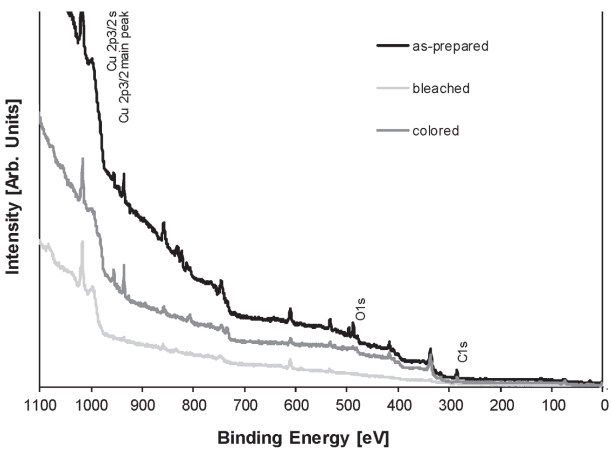

Figure 2: Broad XPS spectra of the Cu_xO film in its as-prepared, bleached and colored states

Slika 2: Širokopasovni XPS-spekter plasti Cu_xO v pripravljenem, obeljenem in obarvanem stanju

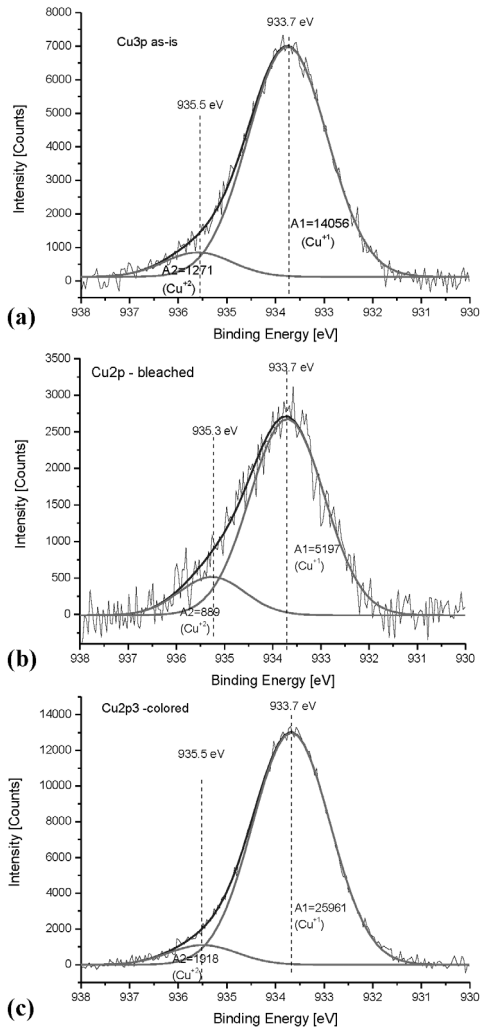

Figure 3: Deconvolution of the XPS spectra of Cu2p3 electrons on two Gaussian peaks: a) as-prepared, b) bleached and c) colored electrochromic Cu_xO film on FTO substrates. A1 and A2 are the corresponding peak areas.

Slika 3: Upadanje XPS-spektra elektronov Cu2p3 na dveh Gaussovih vrhovih: a) pripravljene, b) obeljene in c) obarvane elektrokromizne plasti Cu_xO na FTO-podlagi. A1 in A2 sta odgovarjajoči področji vrhov.

Table 1: Binding energies of Cu2p3/2 electrons, obtained from XPS spectra with deconvolution on two Gaussian peaks with areas A1 and A2. Reference values are given for comparison.
Tabela 1: Energije vezav elektronov Cu2p3/2, dobljenih iz XPS-spektra z dekonvolucijo v dva Gaussova vrhova A1 in A2. Za primerjavo so prikazane referenčne vrednosti.

	B. E. Cu2p in Cu^{+2} bonding (as in CuO) (eV)	B. E. Cu2p in Cu^{+1} bonding (as in Cu_2O) (eV)	ΔB. E. (eV)	Fraction of Cu^{+2} (as in CuO) of the total Cu atoms A2/(A1+A2) (%)	Fraction of Cu^{+1} (as in Cu_2O) of the total Cu atoms =A1/(A1+A2) (%)
XPS handbook[22]	933.6				
Literature –XPS native oxides[23]	934.2	932.5	1.7	22.1	77.9
T. Ghodselahi et al.[24]	934.5–935.2	932.3–933.8	1.4–2.2		
I. G. Casella et al.[25]		932.2–932.8			
As-prepared	935.5	933.7	1.8	9.8	90.2
Colored	935.5	933.7	1.8	6.8	93.2
Bleached	935.3	933.7	1.6	10.2	89.8

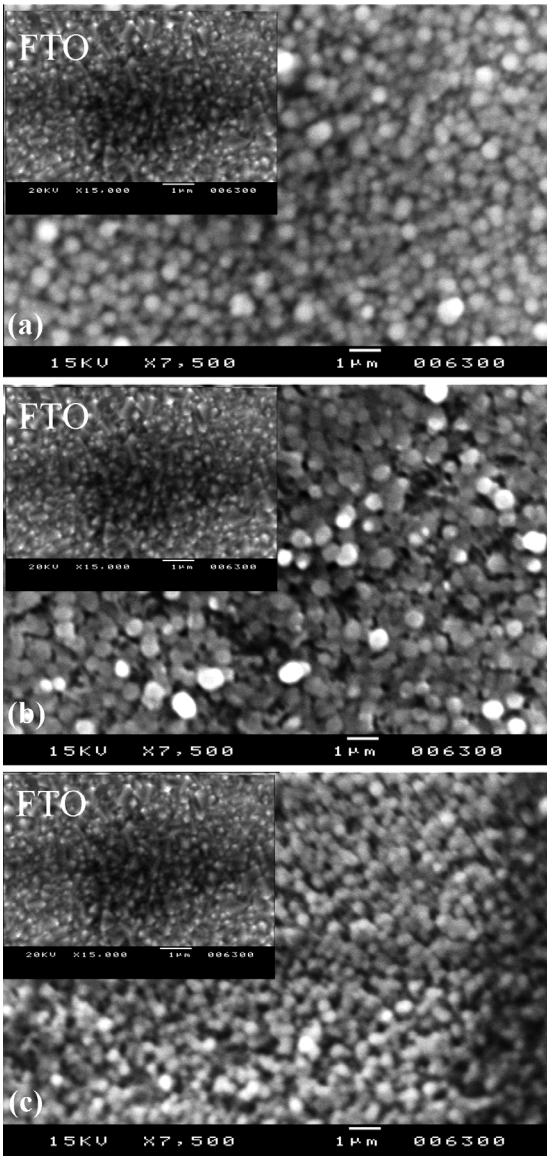

Figure 4: SEM micrographs taken of the surfaces of the: a) as-prepared, b) bleached and c) colored films on FTO substrates
Slika 4: SEM-posnetki površine plasti na FTO-podlagi: a) pripravljeno, b) obeljeno in c) obarvano

the signal yield from the Cu atoms bonded in either CuO or Cu_2O. Hence, the relative peak area of either A1 or A2 versus the total peak area (A1+A2) in percent can be considered a measure for the Cu^{+1} (as in CuO) and Cu^{+2} (as in Cu_2O) quantities in the film. A possible presence of the elemental copper and hydroxide was neglected because these are not active participants in the reversible electrochromic redox reactions.

The results for the Cu2p binding energies of the three states of the electrochromic Cu_xO film from **Figure 3** are

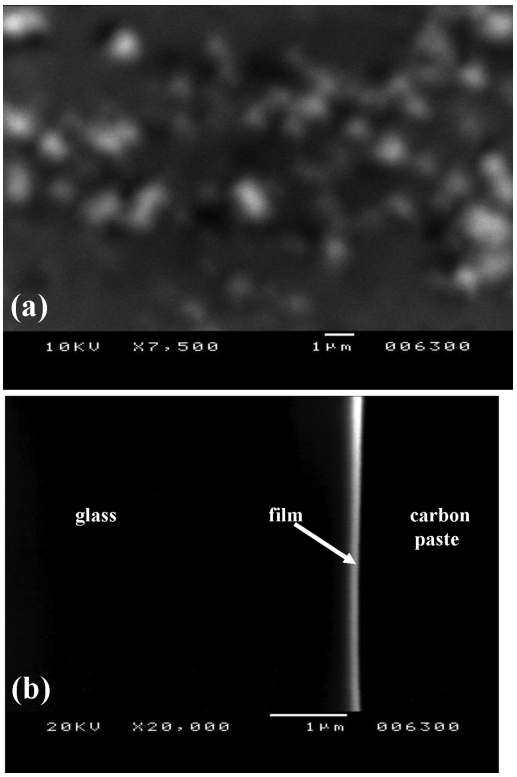

Figure 5: a) SEM of the Cu_xO film grown on an amorphous substrate (glass), b) SEM of the cross-section of the Cu_xO film on a glass interface. The estimated film thickness is about 250 nm.
Slika 5: a) SEM-posnetek Cu_xO filma, nastalega na amorfni podlagi (steklo), b) SEM-posnetek prereza plasti Cu_xO na steklu. Debelina plasti je okrog 250 nm.

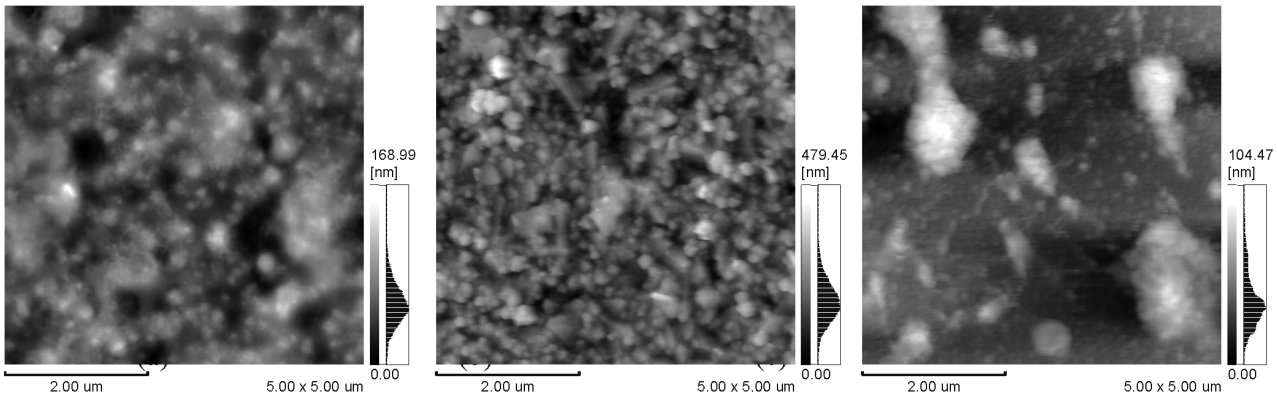

Figure 6: Two-dimensional surface images of: a) as-prepared, b) colored and c) bleached Cu_xO thin films
Slika 6: Dvodimenzionalni posnetek površine tanke plasti Cu_xO: a) pripravljeno, b) obarvano in c) obeljeno

summarized in **Table 1**. It is evident that the experimental values revealed somewhat greater binding energies (about 1.2 eV) than those reported for the bulk samples[23], but they are in good agreement with those reported for the films[24,25]. The results showed that the binding energies pertaining to the two Cu2p3/2 peaks retained the known difference of about 1.7 eV [23,24].

From **Table 1** it is clear that the as-prepared sample contained 90.2 % Cu^{+1} (bonded as in Cu_2O, the yellowish transparent oxide). From this point, it is evident that the amount of Cu^{+1} slightly increased in the bleached sample, up to 93.2 %, but decreased in the colored sample, to 89.8 %. By the same time, the amount of Cu^{+2} atoms (as in the CuO black-colored oxide) decreased in the bleached sample and increased in the colored sample, correspondingly. Hence, it can be assumed that the electrochromic switching occurs due to the transition of only about 3.4 % Cu atoms (93.2–89.8 %) from Cu^{+} to Cu^{+2} and vice versa. This result is in agreement with the XRD patterns, revealing no detectable peaks of the CuO phase due to their relatively small quantity compared to those of the Cu_2O phase. Furthermore, the characteristic O1s peaks of the XPS spectrum were practically useless for the CuO and Cu_2O quantification because the O1s peak at 530.6 eV [23] can be associated with both the CuO and Cu_2O phases, while the peak at 531.6 eV can only be associated with the electrochromic inactive $Cu(OH)_2$ compound.

If one takes into account the crystallography data for the unit cells of cuprite-Cu_2O and tenorite-CuO, one can make an estimation of the possible variations in the volume that may induce the strain in the Cu_xO structure and, hence, invoke film degradation due to repeatable cycling. Under the assumption that the Cu_xO electrochromic behavior relies on only 3.4 % of the Cu atoms, we can estimate the relative changes in the crystallite volume, in which about 3.4 % Cu atoms from tenorite (a monoclinic structure with a unit cell volume V_c (CuO) = $81.03 \cdot 10^{-3}$ nm^3 [19]) recrystallize into cuprite (a cubic structure with a unit cell volume V_c (Cu_2O) = $77.83 \cdot 10^{-3}$ nm^3 [20]). One can assume that the crystallites within the film undergo a negligible relative volume reduction during the coloration and a volume expansion during the bleaching. Hence, the limited cycling lifetime that was previously observed in these films[17,18] cannot be ascribed to the volume friction within the crystallites.

Figures 4a to **4c** present the SEM micrographs of the surfaces of the as-prepared, bleached and colored films on the FTO substrates, correspondingly. The micrograph on **Figure 4a** reveals round grains of the as-prepared film with a diameter of about 250 nm. The grain size of the bleached films on **Figure 4b** seems similar. However, the micrograph of the colored-sample surface from **Figure 4c** reveals notably smaller round crystal grains.

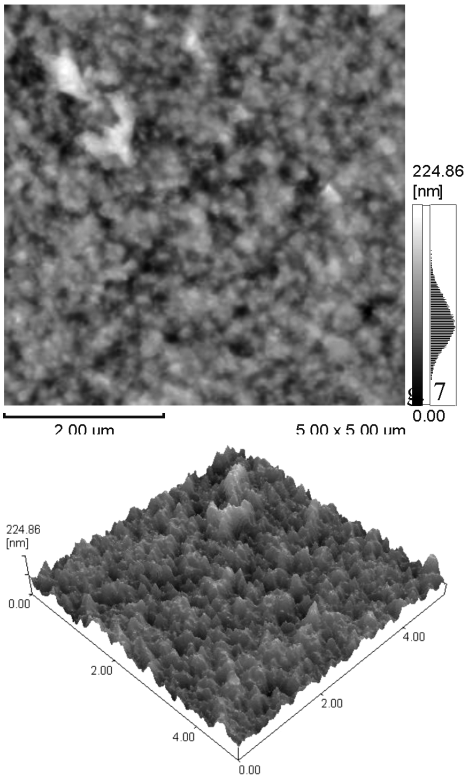

Figure 7: 2D and 3D surface images of FTO substrates
Slika 7: 2D- in 3D-posnetek površine FTO-podlage

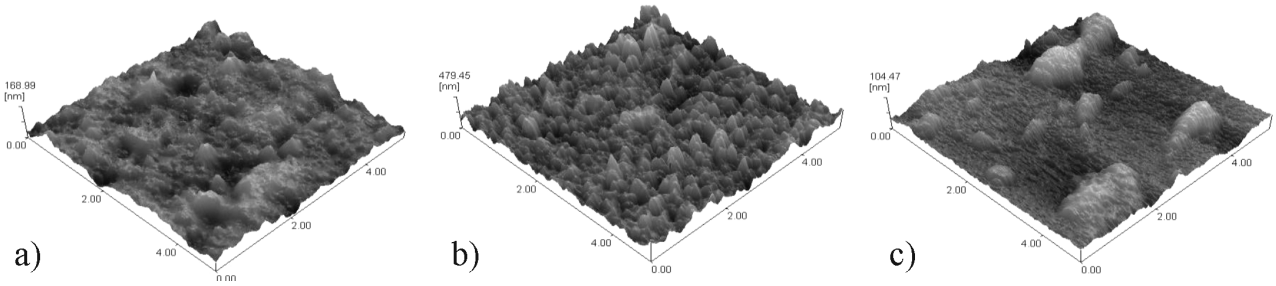

Figure 8: Three-dimensional surface images of Cu_xO thin films: a) as-prepared, b) colored and c) bleached
Slika 8: Tridimenzionalen posnetek površine tanke plasti Cu_xO: a) pripravljeno, b) obarvano in c) obeljeno

Furthermore, as a consequence of the grain shrinkage, the porosity of the colored film seems to have increased notably (an obviously larger empty space among the grains upon the coloration). In addition, **Figure 5** shows the SEMs of: (a) the Cu_xO films deposited onto the glass (amorphous) substrate and (b) a profile of about 250 nm Cu_xO film on the glass substrate (the interface cross-section). From **Figure 5a** it is obvious that the Cu_xO film grows irregularly and non-homogeneously on an amorphous substrate, such as glass. However, the SEMs on **Figure 4**, along with the XRD patterns, showed a mixed amorphous-crystalline growth on the crystalline substrate (FTO).

Two-dimensional AFM surface images of the as-prepared, bleached and colored Cu_xO thin films are presented in **Figure 6**. For a comparison, **Figure 7** includes 2D and 3D surface images of the FTO substrate. The scale of all the three images is 5 µm. As can be seen from **Figure 6**, there are significant differences between the surfaces of the as-prepared, bleached and colored samples. In addition, from **Figure 8** one can see that the electrochemical voltage cycling notably affects the surface roughness. In other words, the oxidation process (coloration), taking place on a sample surface, deteriorates the surface smoothness, increasing the root-mean-square roughness. On the other hand, the reduction process (bleaching) is followed by an improvement of the surface smoothness. Furthermore, the roughness parameter (R_q) derived from the AFM scans of the observed surfaces (an area of 5 µm × 5 µm) decreased from 480 nm for the colored to 108 nm for the bleached sample.

In order to compare the compositional homogeneity of the Cu_xO thin films in their as-prepared, colored and bleached state, their phase surface images are presented on **Figure 9**, correspondingly. Besides Cu_2O and CuO, some minor amounts of $Cu(OH)_2$ were found in all three samples. Furthermore, the results showed that the cuprite (Cu_2O) phase is the most abundant in the bleached state, which is in agreement with the XPS results of this study. Comparing the phase images of the as-prepared and colored states, it could be concluded that the amount of the tenorite (CuO) phase is comparable in both the as-prepared and colored states which is again in line with the XPS results.

4 CONCLUSION

The coloration process of the chemically deposited Cu_xO films can be considered as a reversible transfer of the film 3–4 % of the total 90 % Cu^{+1} into Cu^{+2}. The coloration can thus be attributed to a decrease of 3–4 %

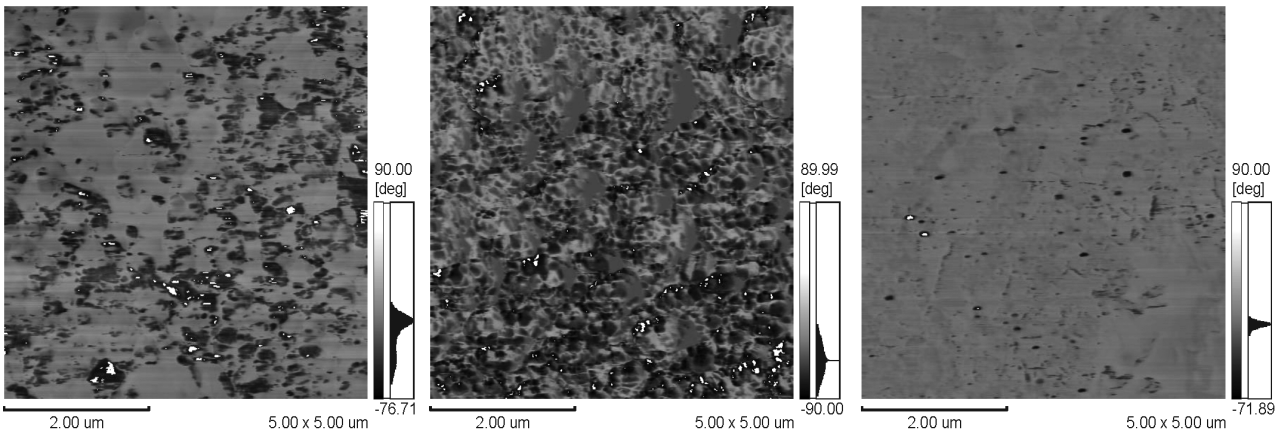

Figure 9: Phase surface images of Cu_xO thin films: a) as-prepared, b) colored and c) bleached. The scale is 5 µm in both directions and 90 nm in height.
Slika 9: Površinska slika faz v tanki plasti Cu_xO: a) pripravljeno, b) obarvano in c) obeljeno. Merilo je 5 µm v obeh smereh in 90 nm po višini.

of the interstitial oxygen, creating oxygen vacancies in the CuO film. From all the above findings, it appears that only 3–4 % of the copper atoms in the film surface represent the coloration centers that are driven to switch the transmittance between 30 % and 80 % [17,18]. The SEM micrographs showed that the grain size of the Cu_xO crystallites notably shrank upon the coloration of the film, whereas the porosity grew up. Significant changes in the surface morphology among the as-prepared and treated samples were also detected by AFM. While the oxidation process (the coloring) deteriorated the surface smoothness, the reduction (the bleaching) invoked the surface smoothening. The AFM phase imaging revealed the existence of three different phases in the as-deposited, colored and bleached films: Cu_2O, CuO and a minor amount of the hydroxide phase – $Cu(OH)_2$. In agreement with the XPS results, the amount of the dominant cuprite phase was found to be the highest for the bleached state, while the tenorite phase (CuO) appeared in comparable amounts in the as-prepared and the colored states. The limited quantity of the electrochromic active Cu-atoms within the thin Cu_xO films on the transparent conductive oxide (TCO) limits its performance in the white-light-transmittance modulation between 20 % and 80 %. If the Cu_xO films are sensitized as nanocrystals within a TCO matrix, it can be expected that a more efficient coloration can be achieved.

5 REFERENCES

[1] C. G. Granqvist, Handbook of Inorganic Electrochromic Materials, Elsevier, Amsterdam 1995

[2] J. I. Pankove, Display Devices, Springer, Berlin 1980

[3] C. M. Lampert, T. R Omstead, P. C. Yu, Sol. Energy Mater., 14 (**1986**), 161–174, doi:10.1016/0165-1633(86)90043-2

[4] A. E. Rakhshani, J. Appl. Phys., 62 (**1987**), 1528–1529, doi:10.1063/1.339619

[5] N. Ozer, F. Tepehan, Sol. Energy Mater. Sol. Cells, 30 (**1993**), 1–26, doi:10.1016/0927-0248(93)90027-Z

[6] H. Demiryont, US Patent No. 4830471, 16 May 1989

[7] F. I. Brown, S. C. Schulz, US Patent No. 5585959, 17 Dec. 1996

[8] T. J. Richardson, J. L. Slack, M. R. Rubin, Electrochim. Acta, 46 (**2001**), 2281–2284, doi:10.1016/S0013-4686(01)00397-8

[9] M. E. Abu-Zeid, A. E. Rakhshani, A. A. Al-Jassar, Y. A. Youssef, Phys. Stat. Solidi (A), 93 (**1986**), 613-620, doi:10.1002/pssa.2210930226

[10] V. Georgieva, M. Ristov, Sol. Energy Mater. Sol. Cells, 73 (**2002**), 67–73, doi:10.1016/S0927-0248(01)00112-X

[11] S. C. Ray, Sol. Energy Mater. Sol. Cells, 68 (**2001**), 307–312, doi:10.1016/S0927-0248(00)00364-0

[12] W. M. Sears, E. Fortin, Sol. Energy Mater., 10 (**1984**), 93–103, doi:10.1016/0165-1633(84)90011-X

[13] E. Fortin, D. Masson, Solid-State Electron., 25 (**1982**), 281–283, doi:10.1016/0038-1101(82)90136-8

[14] A. Roos, T. Chibuye, B. Karlsson, Sol. Energy Mater., 7 (**1983**), 453–465, doi:10.1016/0165-1633(83)90018-7

[15] M. Ristov, Gj. Sinadinovski, I. Grozdanov, Thin Solid Films, 123 (**1985**), 63–67, doi:10.1016/0040-6090(85)90041-0

[16] M. Ristova, J. Velevska, M. Ristov, Sol. Energy Mater. Sol. Cells, 71 (**2002**), 219–230, doi:10.1016/S0927-0248(01)00061-7

[17] R. Neskovska, M. Ristova, J. Velevska, M. Ristov, Thin Solid Films, 515 (**2007**), 4717–4721, doi:10.1016/j.tsf.2006.12.121

[18] M. Ristova, R. Neskovska, V. Mirceski, Sol. Energy Mater. Sol. Cells, 91 (**2007**) 14, 1361–1365, doi:10.1016/j.solmat.2007.05.018

[19] Powder Diffraction File No. 4680, CPDS International Center for Diffraction Data, Newtown Square, 2006

[20] Powder Diffraction File No. 1104, CPDS International Center for Diffraction Data, Newtown Square, 1985

[21] Powder Diffraction File No. 778, CPDS International Center for Diffraction Data, Newtown Square, 1975

[22] G. E. Muileenberg (Ed.), Handbook of X-ray photoelectron spectroscopy, Perkin – Elmer Corporation, 1979

[23] XPS Handbook of elements and native oxides, XPS International Incorporated, 1999

[24] T. Ghodselahi, M. A. Vesaghi, A. A. Shafiekhani, A. Baghizadeh, M. Lameii, Applied Surface Science, 255 (**2008**), 2730–2734, doi:10.1016/j.apsusc.2008.08.110

[25] I. G. Casella, M. Gatta, Journal of Electroanalytical Chemistry, 494 (**2000**), 12–20, doi:10.1016/S0022-0728(00)00375-2

UDK 621.77:536.7
Original scientific article/Izvirni znanstveni članek

ISSN 1580-2949
MTAEC9, 49(3)395(2015)

THERMODYNAMIC ANALYSIS OF THE PRECIPITATION OF CARBONITRIDES IN MICROALLOYED STEELS

TERMODINAMSKA ANALIZA IZLOČANJA KARBONITRIDOV V MIKROLEGIRANIH JEKLIH

Marek Opiela

Silesian University of Technology, Institute of Engineering Materials and Biomaterials, Konarskiego Street 18a, 44-100 Gliwice, Poland
marek.opiela@polsl.pl

Prejem rokopisa – received: 2014-07-01; sprejem za objavo – accepted for publication: 2014-07-08

doi:10.17222/mit.2014.096

The production of mass-products of microalloyed steels with a high strength requires a proper adjustment of the thermomechanical processing and the kinetics of the precipitation of the MX-type (M – microalloying element, X – metalloid) phases in austenite. The understanding of the effect of carbonitrides on the processes of hot-working and cooling from the finishing deformation temperature requires the knowledge of the mechanism of their formation and their stability in austenite. The research was carried out on newly manufactured Ti-V and Ti-Nb-V steels for forged machine parts with thermomechanical processing. The analysis of the precipitation of the carbonitrides with the stoichiometric compositions of $Ti_xV_{1-x}C_yN_{1-y}$ and $Ti_xNb_vV_{1-x-v}C_yN_{1-y}$ was based on the Hillert-Staffanson model improved by Adrian. The effect of the austenitizing temperature in the range from 900 °C to 1200 °C on the grain size of the original austenite was investigated to verify the results of the calculation. The result provides the basis for a suitable design of the manufacturing process of the thermomechanical treatment to obtain high-strength forged elements of microalloyed steels.

Keywords: microalloyed steels, MX-type phases, thermomechanical processing

Proizvodnja masovnih izdelkov iz mikrolegiranih jekel z visoko trdnostjo zahteva pravilno prilagoditev termomehanske predelave in kinetike izločanja faze MX (M – mikrolegirni element, X – metaloid) v avstenitu. Razumevanje vpliva karbonitridov na procese vroče predelave in ohlajanja iz temperature končne deformacije zahteva poznanje mehanizma njihovega nastanka in stabilnosti v avstenitu. Raziskava je bila izvršena na novo izdelanih jeklih za odkovke Ti-V in Ti-Nb-V po postopku termomehanske obdelave. Analiza izločanja karbonitridov s stehiometrično sestavo $Ti_xV_{1-x}C_yN_{1-y}$ in $Ti_xNb_vV_{1-x-v}C_yN_{1-y}$ temelji na Hillertovem in Staffansonovem modelu, ki ga je izboljšal Adrian. Preiskovan je bil vpliv temperature avstenitizacije v območju 900 °C do 1200 °C na prvotno velikost avstenitnih zrn, da bi preverili rezultate izračunov. Rezultati omogočajo pridobitev osnove za pravilno načrtovanje postopka izdelave s termomehansko obdelavo odkovkov z veliko trdnostjo iz mikrolegiranih jekel.

Ključne besede: mikrolegirana jekla, faze vrste MX, termomehanska obdelava

1 INTRODUCTION

The production of metallurgical products with high mechanical properties from microalloyed steels requires the conditions of plastic working to be adjusted to the kinetics of the dissolution (precipitation) of the MX type of micro-additions introduced into steel. The solubility of the MX phases, i.e., nitrides, carbides and carbonitrides of the alloying elements such as Ti, Nb, V, Zr or B in austenite is determined with the logarithm of the solubility product expressed with the equation:[1–5]

$$\lg [M] \cdot [X] = B - A/T \quad (1)$$

where $[M]$ and $[X]$ are the mass fractions of the metallic micro-addition and the metalloid dissolved in austenite at temperature T, respectively, A and B are the constants associated with the free enthalpy of the MX-phase formation. It should be noted that constants A and B depend on the method of determination; for this reason slightly different values for the same phase can be found in[6,7].

High technical usability belongs to the diagrams of different MX phases dissolved in austenite, determined for different steels on the basis of Equation (1) as well as to the computer programs calculating the chemical compositions and fractions of these phases as a function of temperature. The chemical composition of austenite ($[M]$, $[X]$) and the portion of the undissolved compound can be determined using the solubility product and the mass balance of the elements included in the reaction. A simplified thermodynamic model based on the laws of thermodynamic equilibrium, concerning the precipitation of the compound, is described with a system of equations:[8]

$$[M] \cdot [X] = k_{MX} \quad (2)$$

$$\mathrm{M} = [\mathrm{M}] + \frac{(\mathrm{M})}{(\mathrm{MX})} < \mathrm{MX} > \quad (3)$$

$$\mathrm{X} = [\mathrm{X}] + \frac{(\mathrm{M})}{(\mathrm{MX})} < \mathrm{MX} > \quad (4)$$

where $k_{MX} = [M] \cdot [X]$ indicates the solubility product of MX, M and X indicate the total concentrations of these elements in steel in mass fractions (w/%), the atomic mass of the elements, as the symbols in parentheses, ( ).

The solution of this system of equations is a quadratic function that allows us to calculate the amount of the interstitial element dissolved in austenite:

$$[X]^2+[X]\cdot\left[\frac{(X)}{(M)}\cdot M-X\right]-\frac{(X)}{(M)}k_{MX}=0 \quad (5)$$

By avoiding the negative solution and $\Delta > 0$, the equation has two solutions. However, in the case of $\Delta = 0$, the austenitizing temperature is higher than, or equal to, the temperature of the dissolution of the compound. The part of the interstitial element dissolved in austenite with $\Delta > 0$ is determined from the following equation:

$$[X]=\frac{X-\frac{(X)}{(M)}\cdot M+\sqrt{\left(\frac{(X)}{(M)}\cdot M-X\right)^2+4\frac{(X)}{(M)}\cdot k_{MX}}}{2} \quad (6)$$

The models of the precipitation processes in microalloyed steels, based on the laws of thermodynamic equilibrium, also include the formation of complex carbonitrides during hot working. The carbides and nitrides of the Nb, Ti and V micro-additions reveal mutual solubility and, as a result of this process, carbonitrides are formed, with the chemical composition and dissolution temperature dependent on the chemistry of the steel.[9] The precipitation of the complex carbonitrides with a MC_yN_{1-y} stoichiometric constitution is determined with a thermodynamic model based on the assumptions of the sublattice model created by Hillert and Staffanson[10], with the basic simplifying assumption that the metallic element M and the interstitial elements (C, N) in the steel form dilute solutions in austenite and that their activities meet Henry's law. The final form of the equations of this model describes the state of thermodynamic equilibrium in the Fe-M-C-N system:

$$\ln\left(\frac{yk_{MC}}{[M_a]\cdot[C_a]}\right)+(1-y)^2\frac{L^M_{CN}}{RT}=0 \quad (7)$$

$$\ln\left(\frac{(1-y)k_{MN}}{[M_a]\cdot[N_a]}\right)+y^2\frac{L^M_{CN}}{RT}=0 \quad (8)$$

where $[M_a]$, $[N_a]$ and $[C_a]$ indicate the atomic fractions of the metallic element [M] and interstitial elements [N] and [C] dissolved in austenite, k_{MN} and k_{MC} indicate the reaction equilibrium constants, L^M_{CN} is the interaction parameter of the M element affecting C-N, and the y and $(1 - y)$ solutions indicate the *MC* and *MN* moles, respectively. The system of Equations (7) and (8) contains four unknowns: $[M_a]$, $[N_a]$, $[C_a]$ and y. In the solutions based on the mass balance of carbonitrides, the following reactions are used:

$$M_a=\frac{f}{2}+(1-f)[M_a] \quad (9)$$

$$C_a=\frac{yf}{2}+(1-f)[C_a] \quad (10)$$

$$N_a=\frac{(1-y)f}{2}+(1-f)[N_a] \quad (11)$$

with the amount fraction of the MC_yN_{1-y} precipitations.

Complex $M'_xM''_{1-x}C_yN_{1-y}$ or $M'_xM''_vM'''_{1-x-v}C_yN_{1-y}$ type carbonitrides can be formed in microalloyed steels containing two or three micro-additions (M', M'', M''') at the same time. A thermodynamic model describing the state of thermodynamic equilibrium in steel containing up to three micro-additions and Al was elaborated by Adrian[11,12]. It can calculate the chemical composition of austenite and the concentration of carbonitride in a Fe-Nb-V-Ti-Al-C-N multicomponent system. The final form of the equations determining the thermodynamic equilibrium of the Fe-M'-M''-M'''Al-C-N system is as follows:[13]

$$y\ln\frac{xyk_{M'C}}{[M'_a]\cdot[C_a]}+(1-y)\ln\frac{x(1-y)k_{M'N}}{[M'_a]\cdot[N_a]}+ +y(1-y)\frac{L_{CN}}{RT}=0 \quad (12)$$

$$y\ln\frac{vyk_{M''C}}{[M''_a]\cdot[C_a]}+(1-y)\ln\frac{v(1-y)k_{M''N}}{[M''_a]\cdot[N_a]}+ +y(1-y)\frac{L_{CN}}{RT}=0 \quad (13)$$

$$y\ln\frac{(1-x-v)yk_{M'''C}}{[M'''_a]\cdot[C_a]}+(1-y)\ln\frac{(1-x-v)(1-y)k_{M'''N}}{[M'''_a]\cdot[N_a]}+ +y(1-y)\frac{L_{CN}}{RT}=0 \quad (14)$$

$$vy\ln\frac{x[M'''_a]k_{M'C}}{v[M_a]k_{M'C}}+(1-x-v)(1-y)\ln\frac{(1-x-v)[M'_a]k_{M'N}}{X[M'''_a]k_{M'N}} +(1-y)\ln\frac{x(1-y)k_{M'N}}{[M'_a]\cdot[N_a]}+y^2(1-y)\frac{L_{CN}}{RT}=0 \quad (15)$$

$$[Al_a]\cdot[N_a]=k_{AlN} \quad (16)$$

The system of equations consists of eleven unknowns describing the chemical compositions of $[M'_a]$, $[M''_a]$, $[M'''_a]$, $[Al_a]$, $[C_a]$, $[N_a]$ of austenite and (x, v, y) carbonitrides. The subsequent equations, describing the law of conservation of mass during the reaction of the carbonitride and nitride AlN formations are necessary for the solution:

$$M'_a=\frac{x}{2}f+(1-f-f_a)[M'_a] \quad (17)$$

$$M''_a=\frac{v}{2}f+(1-f-f_a)[M''_a] \quad (18)$$

$$M'''_a=\frac{z}{2}f+(1-f-f_a)[M'''_a] \quad (19)$$

$$C_a=\frac{y}{2}f+(1-f-f_a)[C_a] \quad (20)$$

$$N_a = \frac{1-y}{2} f + (1-f-f_a)[N_a] \quad (21)$$

$$Al_a = \frac{f_a}{2} f + (1-f-f_a)[Al_a] \quad (22)$$

where f is the amount fraction of carbonitride, f_a is the amount fraction of nitride AlN, k_{MX} is the product of the MX compound solubility converted into amount fractions (x_{MX}/%), the values in square brackets [ ] indicate the concentrations of the elements in the solution in amount fractions (%), the values in parentheses ( ) indicate the atomic mass of the elements and the values without any brackets indicate the total concentrations of the elements in steel in mount fractions (%).

The input data for the solution of the above system of equations are: the chemical composition of steel, the austenitizing temperature, the k_{MX} product of the solubility of simple carbides and nitrides, MX, the parameter of the impact of the M element on the C-N solution, L_{CN} = –4260 J/mol, and the R gas constant.

The presented model can be used for the solutions of the technological problems associated with the production of microalloyed steels, by designing and modifying chemical compositions. The calculation involves the following parameters: the chemical composition of austenite, the chemical composition and the fraction of carbonitrides and the dissolving temperature of carbonitrides.

2 EXPERIMENTAL PROCEDURE

The research was performed on newly manufactured microalloyed steels (**Table 1**). Steels with the weight of 100 kg were molten in a VSG-100 type laboratory vacuum-induction PVA TePla AG furnace. The steels were cast in argon, forming square ingots with the dimensions of 160/140 mm × 640 mm and hot worked to 32 mm × 160 mm flat bars, by open die forging in a high-speed hydraulic press, applying a force of 300 MN. The range of the forging temperature was 1200–900 °C.

The thermodynamic analysis of the equilibrium of the structural constituents in the stable austenite of the steels mainly focused on the analytic calculations of the austenite chemical composition, and the amounts and chemical compositions of the potential interstitial phases of carbides, nitrides or complex carbonitrides, performed as a function of the heating or cooling temperature. Also, the calculations based on the Hillert-Staffanson thermodynamic model developed by Adrian for the analysis of interstitial complex phases were conducted. For the calculation of the chemical composition of austenite and the concentration of carbonitride based on the chemistry of the analyzed microalloyed steels, CarbNit[11], the computer program operating in a Delphi environment was used.

To verify the performed analysis, the effect of the austenitizing temperature on the austenite grain size was investigated. The samples of 25 mm × 20 mm × 32 mm were austenitized at the temperatures of (900, 1000, 1100 and 1200) °C for 30 min and water-quenched. To reveal the grain boundaries, the samples were etched in a saturated water solution of picric acid with an addition of $CuCl_2$ at a temperature of 60 °C. The metallographic observations of the etched specimens were carried out using a Leica MEF 4A light microscope applying the magnifications of 200–800-times.

3 RESULTS AND DISCUSSION

The micro-additions of Nb, Ti and V in the investigated steels form carbides, nitrides or simple and complex carbonitrides, most often with a NaCl cubic lattice and complete intersolubility. These phases nucleated both heterogeneously, on the existing precipitates such as TiN and TiC created at an increased temperature, and in a homogeneous, independent way.

The concentration of Ti in the examined steel was selected to bond with all the nitrogen. For this reason, VN, NbN and AlN were not included in the thermodynamic analysis of the single interstitial phases. In addition, AlN does not dissolve in carbonitrides as it has a different, hexagonal lattice. The solubility of particular phases of the austenite of microalloyed steels is determined with the logarithmic dependence (Equation 1). The calculated solubility temperatures of the investigated phases, formed in the examined A and B microalloyed steels are listed in **Table 2** with respect to the solubility products of the TiN, TiC and VC type phases precipitated in steel A and also of NbC in steel B. The maxi-

Table 2: Summary of the solubility temperatures of individual interstitial phases
Tabela 2: Pregled temperature topnosti posameznih intersticijskih faz

No.	Type of MX phase	Constants in Equation (1)		Solubility temperature, °C	
		A	*B*	Steel A	Steel B
1.	TiN	15490	5.19	1350	1331
2.	TiC	10745	5.33	1188	1167
3.	NbC	7900	3.42	–	1137
4.	VC	9500	6.72	734	776

Table 1: Chemical compositions of the investigated steels in mass fractions, *w*/%
Tabela 1: Kemijska sestava preiskovanih jekel v masnih deležih, *w*/%

Steel	Mass fractions, *w*/%												
	C	Mn	Si	P	S	Cr	Ni	Mo	Nb	Ti	V	B	Al
A	0.31	1.45	0.30	0.006	0.004	0.26	0.11	0.22	–	0.033	0.008	0.003	0.040
B	0.28	1.41	0.29	0.008	0.004	0.26	0.11	0.22	0.027	0.028	0.019	0.003	0.025

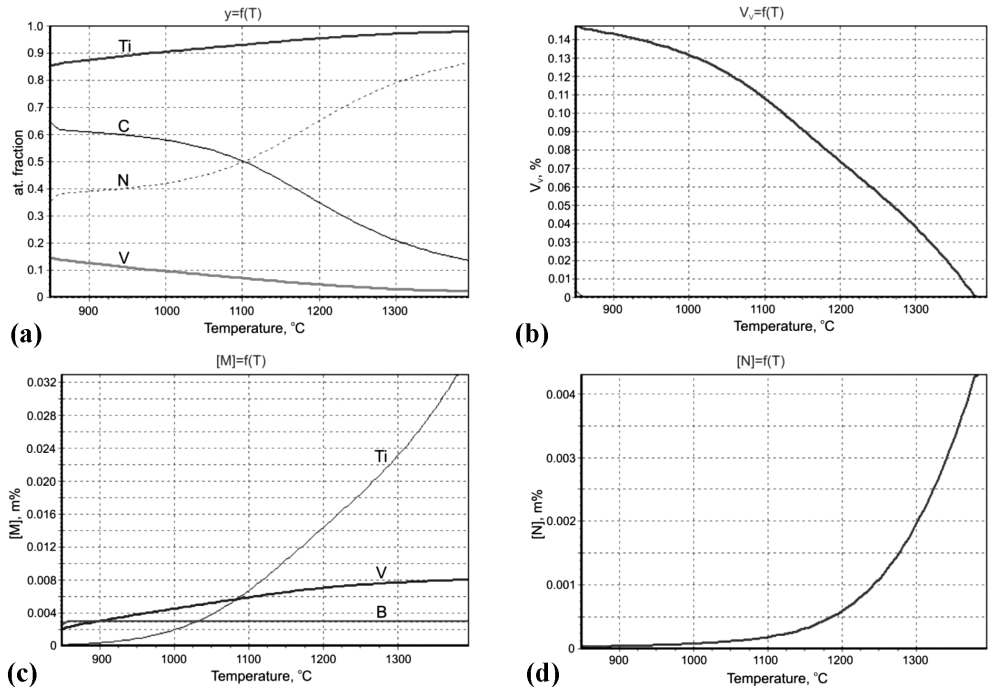

Figure 1: Calculation results for: a) $Ti_xV_{1-x}C_yN_{1-y}$ carbonitride, $y = f(T)$, b) volume fraction of (Ti, V)(C, N) carbonitride and BN, $V_V = f(T)$, c, d) elements dissolved in austenite: $[M] = f(T)$ and $[N] = f(T)$; steel A

Slika 1: Rezultati izračunov: a) $Ti_xV_{1-x}C_yN_{1-y}$ karbonitrid, $y = f(T)$, b) volumenski delež (Ti, V)(C, N) karbonitrida in BN, $V_V = f(T)$, c, d) elementi, raztopljeni v avstenitu: $[M] = f(T)$ in $[N] = f(T)$; jeklo A

mum solubility temperatures of the TiN type interstitial phases in the γ base were 1350 °C and 1331 °C for the A and B steels, respectively. Thus, it is assumed that a high austenitizing temperature – close to 1200 °C – does not cause a significant grain growth of the austenite through the undissolved TiN fraction and the high heating and forging temperatures increase the durability of forging tools.

The NbC carbide in the austenite of the B steel with the maximum solubility temperature of 1137 °C contributes essentially to the steel strengthening through a grain refinement and precipitation hardening with a simultaneous decrease in the ductile-to-brittle-transition temperature. In turn, the VC carbide is completely dissolved in the austenite of the examined steels in the range of hot-working temperature.

Due to the mutual solubility of the interstitial phases, a complex $Ti_xV_{1-x}C_yN_{1-y}$ carbonitride can form in steel A with the micro-additions of Ti and V, under the conditions of thermodynamic equilibrium, and a $Ti_xNb_vV_{1-x-v}C_yN_{1-y}$ complex carbonitride forms in the B steel with the micro-additions of Ti, Nb and V (**Table 3**). The calculation results of the chemical composition of the austenite of the examined microalloyed steels, namely, the determination of the temperature dependence of the amounts of the metallic element $[M] = f(T)$ and non-metallic element $[N] = f(T)$, as well as the assumed chemical constitution of the $Ti_xV_{1-x}C_yN_{1-y}$ and $Ti_xNb_vV_{1-x-v}C_yN_{1-y}$ type complex carbonitrides as $y = f(T)$ with the defined volume fractions of the analyzed $V_V = f(T)$ phases are depicted in **Figures 1** and **2**.

Table 3: Calculated stoichiometric thermodynamic-equilibrium compositions of complex carbonitrides in the investigated steels

Tabela 3: Izračunane stehiometrične termodinamsko ravnotežne sestave kompleksnih karbonitridov v preiskovanih jeklih

No.	Temperature °C	Type of carbonitrides	
		Steel A	Steel B
1	850	$Ti_{0.854}V_{0.146}C_{0.645}N_{0.355}$	$Ti_{0.600}Nb_{0.292}V_{0.108}C_{0.748}N_{0.252}$
2	900	$Ti_{0.874}V_{0.126}C_{0.610}N_{0.390}$	$Ti_{0.646}Nb_{0.301}V_{0.053}C_{0.697}N_{0.303}$
3	950	$Ti_{0.890}V_{0.110}C_{0.598}N_{0.402}$	$Ti_{0.668}Nb_{0.308}V_{0.024}C_{0.680}N_{0.320}$
4	1000	$Ti_{0.904}V_{0.096}C_{0.580}N_{0.420}$	$Ti_{0.681}Nb_{0.300}V_{0.019}C_{0.662}N_{0.338}$
5	1050	$Ti_{0.917}V_{0.083}C_{0.550}N_{0.450}$	$Ti_{0.705}Nb_{0.282}V_{0.013}C_{0.628}N_{0.372}$
6	1100	$Ti_{0.930}V_{0.070}C_{0.502}N_{0.498}$	$Ti_{0.736}Nb_{0.258}V_{0.006}C_{0.578}N_{0.422}$
7	1150	$Ti_{0.942}V_{0.058}C_{0.432}N_{0.568}$	$Ti_{0.786}Nb_{0.214}C_{0.481}N_{0.519}$
8	1200	$Ti_{0.954}V_{0.046}C_{0.349}N_{0.651}$	$Ti_{0.851}Nb_{0.149}C_{0.350}N_{0.650}$
9	1250	$Ti_{0.963}V_{0.037}C_{0.272}N_{0.728}$	$Ti_{0.897}Nb_{0.103}C_{0.244}N_{0.756}$
10	1300	$Ti_{0.970}V_{0.030}C_{0.210}N_{0.790}$	$Ti_{0.915}Nb_{0.085}C_{0.180}N_{0.820}$
11	1350	$Ti_{0.975}V_{0.025}C_{0.165}N_{0.835}$	$Ti_{0.923}Nb_{0.077}C_{0.146}N_{0.854}$

The analysis of thermodynamic equilibrium leads to the conclusion that the volume fraction $V_v(T)$ of $Ti_{0.978}V_{0.022}C_{0.146}N_{0.854}$ increases with a decrease in the temperature to approximately amount fraction 0.15 % at 850 °C in steel A, cooled from 1378 °C (**Figure 1**). The

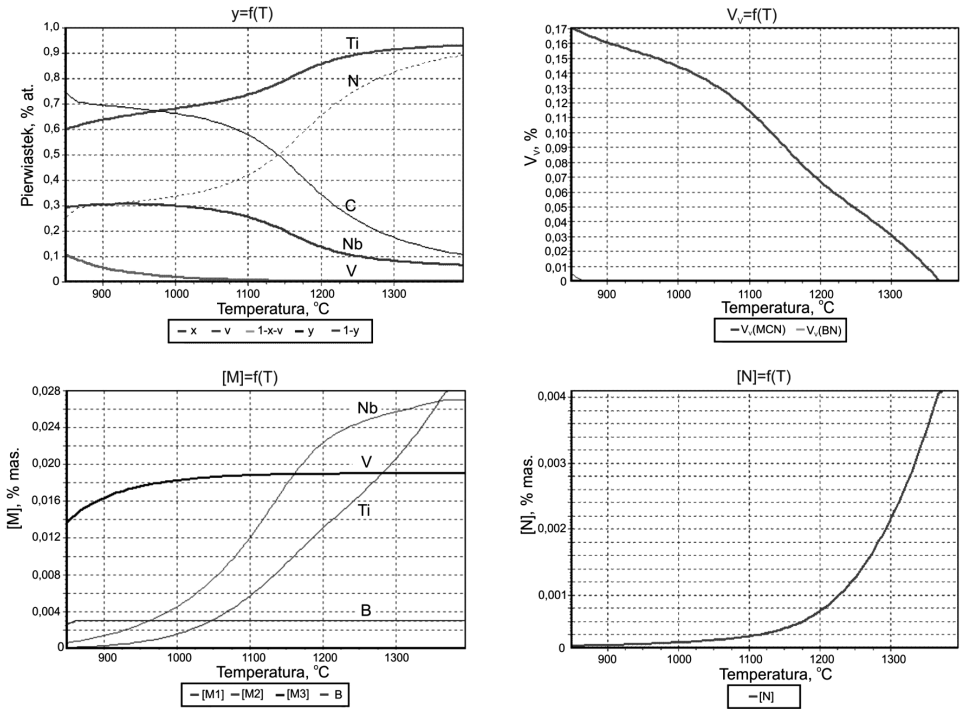

Figure 2: Calculation results of the chemical compositions of: a) $Ti_xNb_vV_{1-x-v}C_yN_{1-y}$ carbonitride, $y = f(T)$, b) volume fraction of (Ti, Nb, V)(C, N) carbonitride and BN, $V_V = f(T)$, c, d) elements dissolved in austenite: $[M] = f(T)$ and $[N] = f(T)$; steel B

Slika 2: Rezultati izračunov kemijske sestave: a) $Ti_xNb_vV_{1-x-v}C_yN_{1-y}$ karbonitrid, $y = f(T)$, b) volumenski delež (Ti, Nb, V)(C, N) karbonitrida in BN, $V_V = f(T)$, c, d) elementi, raztopljeni v avstenitu: $[M] = f(T)$ in $[N] = f(T)$; jeklo B

amount of V in the carbonitride increases from amount fractions 0.02 % to 0.15 % cooled from 1378 °C to 850 °C. In the temperature range from 1378 °C to 856 °C, the amount of carbon in the carbonitride increases from amount fractions 0.14 % to 0.65 %, while in the same temperature range the amount of nitrogen decreases from amount fractions 0.85 % to 0.36 %. At 1100 °C, the amounts of C and N are similar, being 0.502 % and 0.498 %, respectively. The calculated stoichiometric compositions, in the conditions of thermodynamic equilibrium, for the analyzed (Ti, V)(C, N) carbonitrides are listed in **Table 3**.

The thermodynamic-equilibrium solubility temperature of $Ti_{0.928}Nb_{0.072}C_{0.140}N_{0.860}$ in steel B is 1361 °C (**Figure 2**). The thermodynamic analysis of the precipitation of the investigated carbonitrides allows us to state that its volume fraction in austenite $V_V = f(T)$ increased up to about amount fraction 0.14 % due to a decrease in the temperature to 850 °C. The decrease in the temperature from 1300 °C to 1100 °C causes a relative decrease in the Ti concentration and an increase in the Nb concentration. By further lowering the temperature to 850 °C a mild decrease in the Ti amount and a slight increase in the Nb amount occur; an increase in the V amount fraction to 0.11 % in the analyzed carbonitride occurs in the temperature range from 1100 °C to 850 °C. By analyzing the amounts of the interstitial elements in the investigated carbonitride, it was found that the carbon concentration at 1361 °C is 0.14 % and it increases up to 0.75 % at 850 °C. In the examined temperature range the

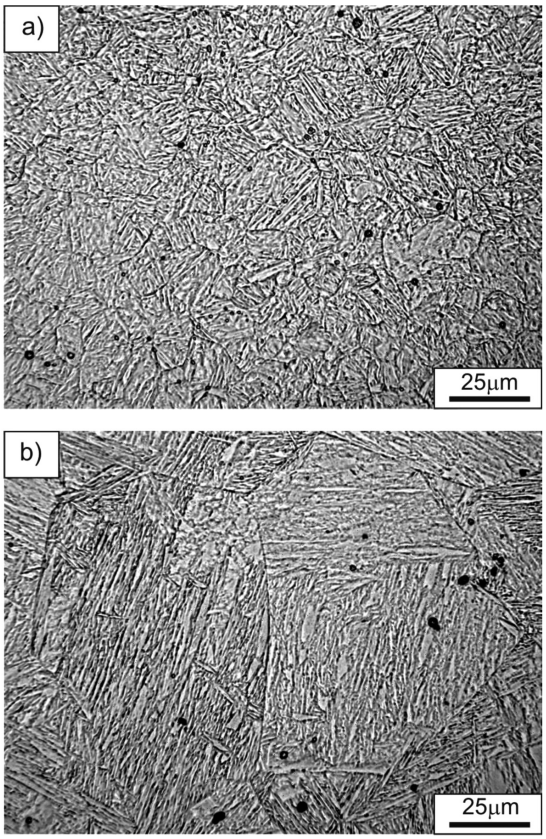

Figure 3: Austenite grains and MX particles in steel A; austenitizing temperatures of: a) 900 °C and b) 1200 °C

Slika 3: Avstenitna zrna in MX-delci v jeklu A; temperatura avstenitizacije: a) 900 °C in b) 1200 °C

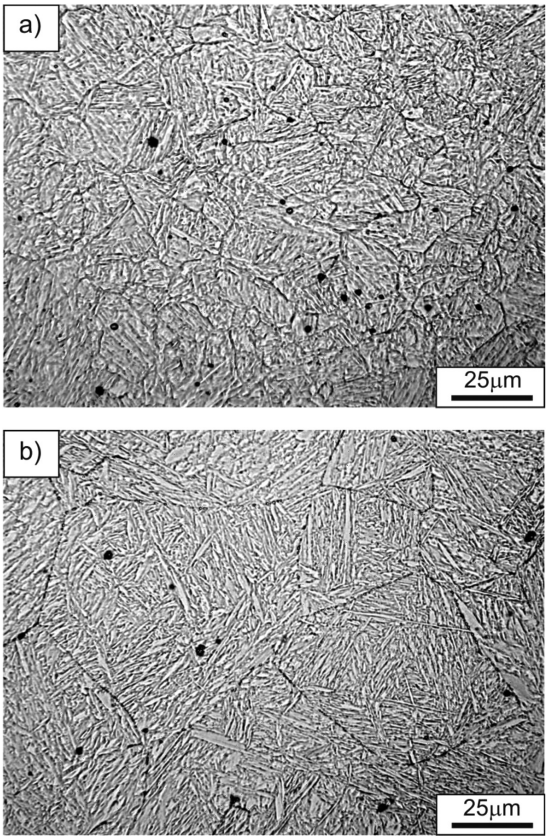

Figure 4: Austenite grains and MX particles in steel B; austenitizing temperatures of: a) 900 °C and b) 1200 °C
Slika 4: Avstenitna zrna in MX delci v jeklu B; temperatura avstenitizacije: a) 900 °C in b) 1200 °C

changes in the nitrogen amount are opposite to the changes in the amount of carbon.

The effect of the temperature from 900 °C to 1200 °C on the austenite grain size was investigated to verify the results of the calculation of the precipitation of MX particles. Austenite grains and particles are presented in **Figures 3** and **4**, while **Figure 5** shows the effect of the temperature on the average size of the austenite grains at a given temperature. The size of the austenite grains at 900 °C to 1000 °C is very small, from 11 μm to 18 μm in the Ti-V steel and 8 μm to 12 μm in the Ti-Nb-V steel. This fine-grained microstructure is a result of the presence of significant fractions of the (Ti, V)(C, N) particles and complex (Ti, Nb, V)(C, N) carbonitrides (respectively for the A and B steels) that effectively inhibit the growth of the austenite grains. An increase in the temperature causes a gradual growth in the austenite grains, more distinct for the Nb-free steel (**Figure 5**). The average diameters of the austenite grains after austenitizing the steels at the temperature of 1200 °C are 66 μm and 62 μm for the A and B steel, respectively. These values are several times lower compared to the C-Mn steels, where a typical austenite grain size at 1200 °C is reported to be from 200 μm to 300 μm.[1,4] The observed grain sizes of the austenite for the investigated steels are

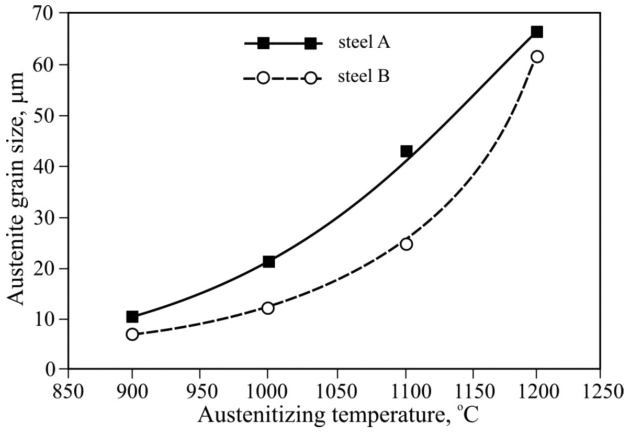

Figure 5: Influence of the austenitizing temperature on the austenite grain size
Slika 5: Vpliv temperature avstenitizacije na velikost avstenitnih zrn

also similar to those reported for the other Ti-V or Ti-Nb steels.[4,14–17]

The austenite grain growth in steel A is mainly controlled with the (Ti, V)(C, N) particles generally precipitating above 1200 °C. The curve in **Figure 5** for the Nb steel is characteristic for microalloyed steels and the grain growth can be combined with the precipitation process of complex carbonitrides. Due to the gradual dissolution of the Nb-rich MX-type phases, the austenite grain size increases gradually with the increasing austenitizing temperature and the growth is much faster above 1100 °C. At 1200 °C the fractions of the particles in both steels are comparable, consisting only of the Ti-rich MX-type phases that lead to similar austenite grain sizes.

4 CONCLUSIONS

The simplified-thermodynamic-model analysis of the precipitation of the MX-type phases in both steels found the highest thermal stability in the austenite of TiN. The TiN precipitation starts at around 1350 °C. The TiC precipitation occurs in the temperature range from 1150 °C to 1200 °C. It was shown in[1,4,14,17,18] that the MX-type phases show mutual solubility. Hence, the austenite grain growth in steel A should be controlled with complex (Ti, V)(C, N) carbonitrides. More complex carbonitrides are found in the Ti-Nb steel and the grain growth in steel B is controlled with the precipitation of the (Ti, Nb, V)(C, N) particles.

The analysis of the precipitation of the MX-type phases in austenite allows us to select a proper forging temperature range, which should correspond to the temperature range of the precipitation of these phases. High mechanical properties of forged parts can be achieved with an appropriate selection of the forging conditions, i.e., the temperature of charge heating and the plastic deformation range since the distribution of the strain and strain rate during the production of die forgings with a

complex shape is difficult to adjust. Forge heating should not lead to a total dissolution of the interstitial elements in the solid solution because it causes a grain growth. Hence, the A and B steels may be heated up to the forging temperature of 1200 °C, without an excessive growth of the austenite grains.

The investigation of the influence of the austenitizing temperature on the austenite grain size confirms the correctness of the precipitation analysis of the MX phases in the investigated steels. The steels have a fine-grained austenite over the whole investigated austenitizing temperature range. In both steels the austenite grain size grows with the increasing temperature and it is several times lower in comparison to the C-Mn steels. A faster grain growth is observed for the Ti-V steel. In the Nb steel, the grain growth is delayed due to Ti and Nb combined microalloying, resulting in a slower dissolution of the complex (Ti, Nb, V)(C, N) particles.

The performed analysis of the precipitation process of the MX-type phases provides the basis for a suitable design of the thermomechanical processing of microalloyed steels for high-strength forged machine parts.

5 REFERENCES

[1] T. Gladman, The physical metallurgy of microalloyed steels, 1st ed., The University Press, Cambridge 1997

[2] J. Adamczyk, Journal of Achievements in Materials and Manufacturing, 20 (**2007**), 399–402

[3] M. Opiela, A. Grajcar, Arch. Civ. Mech. Eng., 12 (**2012**), 327–333, doi:10.1016/j.acme.2012.06.003

[4] R. Kuziak, T. Bold, Y. Cheng, J. Mater. Proc. Tech., 53 (**1995**), 255–262, doi:10.1016/0924-0136(95)01986-L

[5] J. Adamczyk, E. Kalinowska-Ozgowicz, W. Ozgowicz, R. Wusatowski, J. Mater. Proc. Tech., 53 (**1995**), 23–32, doi:10.1016/0924-0136(95)01958-H

[6] H. Adrian, Proc. of the Inter. Conf. Microalloying '95, Iron and Steel Soc., Pittsburgh, 1995, 285–305

[7] E. J. Palmiere, Proc. of the Inter. Conf. Microalloying '95, Iron and Steel Soc., Pittsburgh, 1995, 307–320

[8] D. A. Skobir, M. Godec, M. Balcar, M. Jenko, Mater. Tehnol., 44 (**2010**) 6, 343–347

[9] A. Grajcar, S. Lesz, Mater. Sci. Forum, 706–709 (**2012**), 2124–2129, doi:10.4028/www.scientific.net/MSF.706-709.2124

[10] M. Hillert, L. I. Staffanson, Acta Chem. Scand., 24 (**1970**), 3618–3636, doi:10.3891/acta.chem.scand.24-3618

[11] H. Adrian, Scientific Editions of University of Mining and Metallurgy, Kraków, 1995

[12] H. Adrian, Mater. Sci. Technol., 8 (**1992**), 406–415

[13] M. Opiela, Journal of Achievements in Materials and Manufacturing, 47 (**2011**), 7–18

[14] D. K. Matlock, G. Krauss, J. G. Speer, J. Mater. Proc. Tech., 117 (**2001**), 324–328, doi:10.1016/S0924-0136(01)00792-0

[15] M. MacKenzie, A. J. Craven, C. J. Collins, Scri. Mater., 54 (**2006**), 1–5, doi:10.1016/j.scriptamat.2005.09.018

[16] P. S. Bandyopadhyay, S. K. Ghosh, S. Kundu, S. Chatterjee, Metall. Mater. Trans. A, 42 (**2011**), 2742–2752, doi:10.1007/s11661-011-0711-2

[17] A. Nowotnik, T. Siwecki, J. Microsc., 237 (**2008**), 258–262, doi:10.1111/j.1365-2818.2009.03238.x

[18] M. Opiela, A. Grajcar, Arch. Civ. Mech. Eng., 12 (**2012**), 427–435, doi:10.1016/j.acme.2012.06.013

UDK 620.1:539.42
Original scientific article/Izvirni znanstveni članek

ISSN 1580-2949
MTAEC9, 49(3)403(2015)

EXPERIMENTAL INVESTIGATION OF THE CRACK-INITIATION MOMENT OF CHARPY SPECIMENS UNDER IMPACT LOADING

EKSPERIMENTALNA PREISKAVA TRENUTKA INICIACIJE RAZPOKE PRI UDARNI OBREMENITVI CHARPYJEVIH VZORCEV

Valeriy Kharchenko, Evgeniy Kondryakov, Alexandr Panasenko

Institute for Problems of Strength, National Academy of Sciences, Tymiryazevska str. 2, Kyiv, Ukraine
alaenonn@ya.ru

Prejem rokopisa – received: 2014-07-09; sprejem za objavo – accepted for publication: 2014-09-05

doi:10.17222/mit.2014.103

A new experimental method for the investigation of crack initiation and propagation was developed. Strain gauges on a specimen surface made it possible to obtain surface-deformation data. These data were compared with the force-time curve obtained using a vertical instrumented impact tester. An analysis of the results of this comparison enabled us to determine the moment of crack initiation on the force-time curve. Investigations of crack propagation were conducted in two orthogonal directions.

Keywords: Charpy specimens, crack, moment of crack initiation, specific zones of fracture

Razvita je bila nova eksperimentalna metoda za preiskavo iniciacije in rasti razpoke. Merilni lističi na površini vzorca omogočajo pridobivanje podatkov o deformaciji površine. Ti podatki so bili primerjani s krivuljo sila – čas, dobljeno iz instrumentirane vertikalne udarne naprave. Analiza rezultatov te primerjave omogoča določitev trenutka iniciacije razpoke na krivulji sila – čas. Preiskave rasti razpoke so bile izvršene v dveh ortogonalnih smereh.

Ključne besede: Charpyjevi vzorci, razpoka, trenutek iniciacije razpoke, posebna področja na prelomu

1 INTRODUCTION

At present, impact bending tests are one of the simplest and cheapest methods to determine the material properties that describe its tendency to brittle fracture. The simplicity and efficiency of this method, a relative ease of calibration and adjustment of the equipment allow this test method to be used in many areas of science and technology and industrial sectors, particularly, in the programs aimed to identify and predict the properties of reactor-vessel materials based on surveillance-specimen tests.[1–3] Obtaining load diagrams for the contact between a specimen and a striker under impact loading with the use of strain gauges and modern recording systems implemented in a vertical instrumented drop-weight impact-testing machine, as well as a further comparison of the data-analysis results with the results of fractographic investigations, make it possible to get more important information about the crack-propagation mechanisms in Charpy specimens.[4,5]

2 MATERIALS

The present paper describes the results of an investigation of the moment of crack initiation and the features of crack propagation in Charpy V-notch specimens in the course of impact-bending testing on a vertical instrumented drop-weight impact-testing machine. The scheme, the methods and the test procedures are described in detail.[6]

Standard Charpy V-notch specimens were used. The specimen material is hot-rolled sheet of steel 45, with a microstructure of a ferrite-pearlite mixture (**Figure 1**). The mean diameter of ferrite grains is 35 μm, and the mean diameter of pearlite grains is 54 μm.

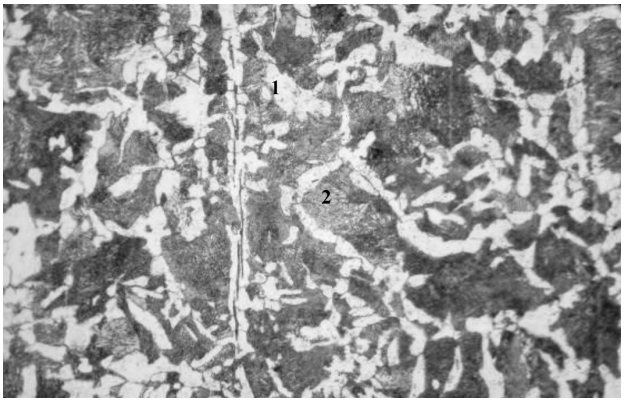

Figure 1: Microstructure of a specimen of steel 45, 500-times, 1 – ferrite; 2 – pearlite

Slika 1: Mikrostruktura vzorca jekla 45, povečava 500-kratna, 1 – ferit; 2 – perlit

3 METHODS AND EXPERIMENTAL WORK

To investigate the moment of crack initiation and the features of its propagation, two directions of the crack propagation were chosen – the direction of the rolling plane and the one perpendicular to it.

Specimens were produced according to the State Standard of Ukraine GOST-9454-78. The dimensions of the specimens are 55 cm × 10 cm × 10 cm. The notch parameters are: the notch depth 2 mm, the convergence angle 45 °, the curvature radius near the notch tip 0.25 mm. The specimens were produced from a metal sheet with collinear directions of the principal axis of a specimen and the direction of the metal-sheet rolling plane. The plane of crack propagation was perpendicular to the direction of the rolling plane. Specimens with two different orientations of the crack-propagation direction were produced (**Figure 2**). The specimen marked with "T" has a notch orientation (and direction of crack propagation) perpendicular to the rolling plane. The specimen marked with "S" has a notch orientation (and direction of crack propagation) parallel to the rolling plane.

The crack propagation during the fracture of the Charpy specimens under impact bending has some specific features.[7,8] With instrumented impact tests, diagrams of the impact contact force with the specimen force time $P(t)$ are obtained and their analysis enables us to describe every stage of the crack propagation in detail. A comparison of the diagram specific zones with the specific zones of the fracture makes it possible to calculate the specific energy for the crack propagation in a given zone and relate the energy to the fracture mechanism.[5,9]

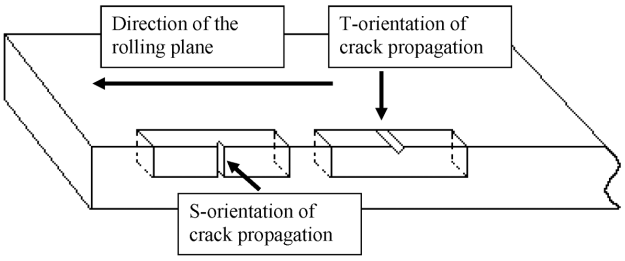

Figure 2: Scheme of the produced specimens with two different notch orientations (marked as S and T) relative to the direction of the rolling plane

Slika 2: Shematski prikaz izdelave vzorcev z dvema orientacijama razpoke (oznaka S in T) glede na smer ravnine valjanja

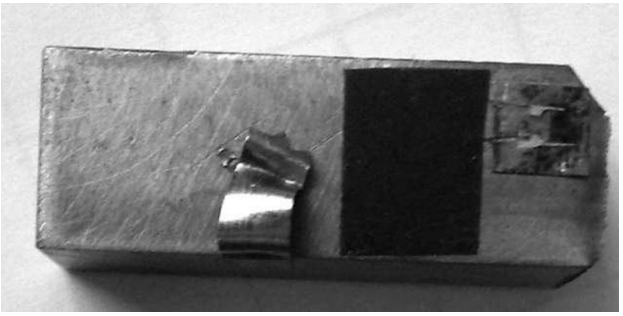

Figure 3: Half of the specimen with a strain gauge

Slika 3: Polovica vzorca z merilnim lističem

To determine the moment of crack initiation (brittle or ductile) in the $P(t)$ diagram, additional gauges for measuring lateral deformation were used. The gauges were located on the specimen surface near the V-notch concentrator along the assumed crack-propagation front (**Figure 3**). The signal recording the channels for the gauge and the $P(t)$ diagram were synchronized in time. The discretization of the signal in time was 2e-7 s (the sampling frequency was $5 \cdot 10^6$ Hz). The temperature on the specimen surface during the testing was measured with a chromel/alumel thermocouple.

Fractographic investigations of the specimen fracture at the macro-level were performed using an Axiotech-Vario microscope, while the micro-zones of the specimen fracture were studied using a SEM-100U microscope.

4 RESULTS AND DISCUSSION

The height of the blade fall for the tested group varied from 0.05 m to 0.5 m. A height (h) of 0.1 m was used for a ductile/brittle crack initiation inside a specimen without an expansion on the lateral surface of the specimen. A height of 0.05 m was used for a shear-lip formation on the lateral surface without a crack initiation inside the specimen. A height of 0.5 m was used for the final rupture of the specimens with a brittle crack initiation followed by ductile crack growing.

All the experimental data with the parameters of the specimens and the test conditions are shown in **Table 1**.

Figures 4 and **5** show the diagrams of the gauge signal and $P(t)$ and **Figures 6** and **7** show the enlarged zones (in time) in the vicinity of the diagram maximum values for specimens ShK7-1 (T = 25.8 °C, h = 1 m, the concentrator orientation is S) and ShK7-2 (T = 35 °C, h = 1 m, the concentrator orientation is S). The maximum

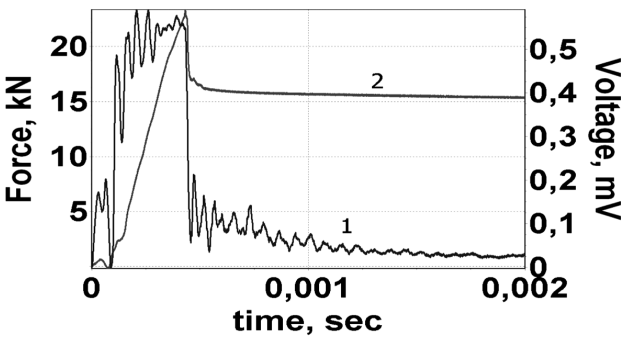

Figure 4: Specimen ShK7-1, h = 50 cm: 1 – diagram of the striker contact with the specimen, 2 – diagram of the gauge signal

Slika 4: Vzorec ShK7-1, h = 50 cm: 1 – diagram stika kladiva z vzorcem, 2 – diagram signala iz merilnega lističa

Table 1: Experimental data and test conditions
Tabela 1: Eksperimentalni podatki in razmere pri preizkušanju

Specimen	Notch orientation	Temperature, °C	Height of the blade fall, *h*/m	Impact velocity, m/s	Experimental result
ShK7-1	S	25.8	0.5	3.13	Rupture with a brittle crack initiation
ShK7-2	S	35	0.5	3.13	Rupture with a brittle crack initiation
ShK7-3	T	26.6	0.05	0.99	No crack initiation, a shear-lip formation
ShK7-3	T	26.6	0.1	1.4	Brittle-crack initiation in the center without an expansion on the lateral surface of the specimen
ShK7-3	T	26.6	0.5	3.13	Final rupture after an initiated brittle crack
ShK7-4	T	23	0.1	1.4	Ductile-crack initiation and shear-lip formation
ShK7-4	T	23	0.5	3.13	Final rupture after an initiated ductile crack

force is situated close to the beginning of drastic force reduction.

The diagrams for specimen ShK7-2 have similar shapes (**Figure 5**). The results of the specimen testing at various temperatures revealed that the maximum value of the gauge diagram has a tendency to shift mainly to the left, with an increase in the temperature, in the direction of the maximum value of the $P(t)$ diagram.

The fractographic analysis revealed several typical zones on the fracture surfaces: a stable crack-growth area, an unstable crack-jump area, a rupture area and a shear-lip area. **Figure 8** presents a macro-fracture of specimen ShK7-1. An analysis of the physical interpretation of the strain-gauge diagram suggests that the essential feature of the fracture of these specimens is the form of a stable crack-growth area, which is of an elongated triangle or trapezoid with the maximum length (in the direction of the main crack propagation) in the central section of the specimen and with the minimum length (frequently close to zero) at the fracture edges, i.e., close to the lateral surfaces of the specimen (the shear-lip zone).

Thus, a crack initiation is most likely to occur in the middle of a specimen with the subsequent extension to the surface, which relates to the formation of lateral necking (shear lips).

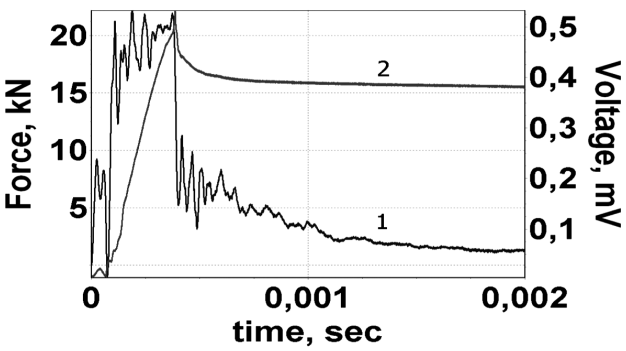

Figure 5: Specimen ShK7-2, *h* = 50 cm: 1 – diagram of the striker contact with the specimen, 2 – diagram of the gauge signal
Slika 5: Vzorec ShK7-2, *h* = 50 cm: 1 – diagram stika kladiva z vzorcem, 2 – diagram signala iz merilnega lističa

To confirm the given assumption, additional strain tests on the Charpy specimens with and without a crack initiation were conducted. In the light of this fact it is obvious that the strain gauge responds to the strain of a specimen surface during the brittle-crack propagation (an unstable crack-jump area). It is improbable that the gauge will register an initiation of a crack of a stable growth considering its current shape and dimensions.

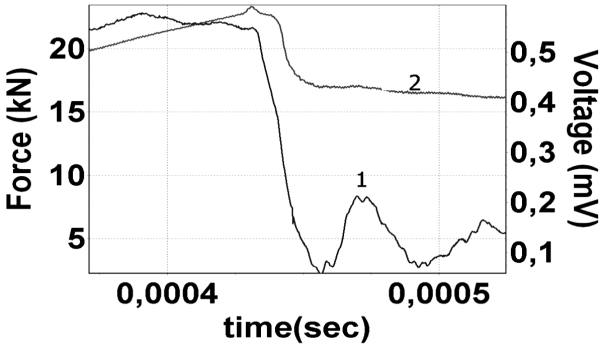

Figure 6: Specimen ShK7-1, *h* = 50 cm. An enlarged section: 1 – diagram of the striker contact with the specimen, 2 – diagram of the gauge signal.
Slika 6: Vzorec ShK7-1, *h* = 50 cm. Povečano področje: 1 – diagram stika kladiva z vzorcem, 2 – diagram signala iz merilnega lističa.

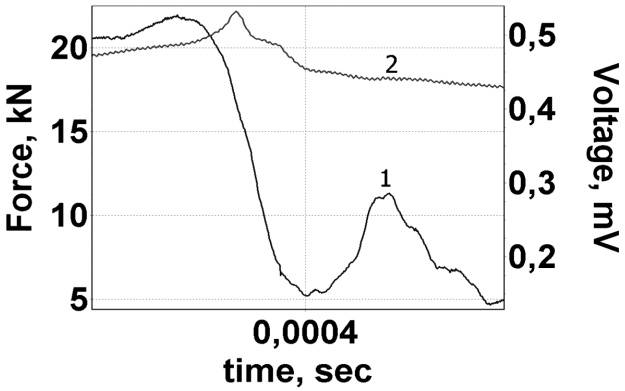

Figure 7: Specimen ShK7-2, *h* = 50 cm. An enlarged section of the diagrams: 1 – diagram of the striker contact with the specimen, 2 – diagram of the gauge signal.
Slika 7: Vzorec ShK7-2, *h* = 50 cm. Povečano področje: 1 – diagram stika kladiva z vzorcem, 2 – diagram signala iz merilnega lističa.

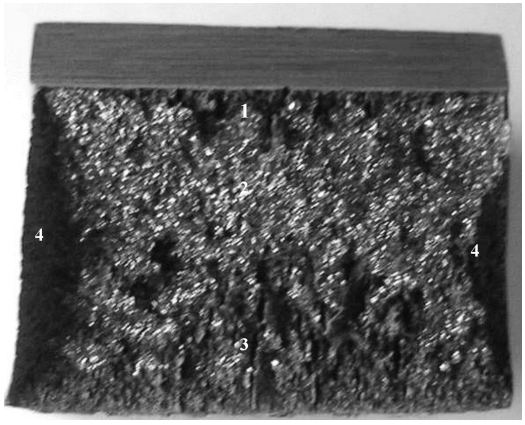

Figure 8: Fractograph of a macro-fracture of a Charpy specimen: 1 – stable crack-growth area, 2 – unstable crack-jump area, 3 – rupture area, 4 – shear lips

Slika 8: Makroposnetek preloma Charpy vzorca: 1 – področje stabilne rasti razpoke, 2 – nestabilno področje skoka razpoke, 3 – prelom pri upogibu, 4 – strižne ustnice

Using these considerations one can explain the fact that the maximum value in the gauge diagram does not coincide with the maximum value in the contact diagram, as it is shifted to the right in time with respect to the contact diagram.

The values for the striker velocity at the moment of its contact with a specimen, at which the specimen underwent deformation without a crack initiation, were determined by varying the values of the height (h) of the blade fall.

Figure 9 shows the diagrams of the strain gauge and $P(t)$ for specimen ShK7-3 (T = 26.6 °C, the concentrator orientation is T) at the impact velocity of 1 m/s. At this impact velocity no crack initiation is observed (during a visual inspection using optical methods both on the surfaces and inside the concentrator). Moreover, the gauge registered the strain on the specimen surface (a shear-lip initiation).

It should be mentioned that the maximum value of the gauge signal was significantly lower (0.32 mV) compared with the maximum value of the gauge signal at the crack initiation (0.55 mV).

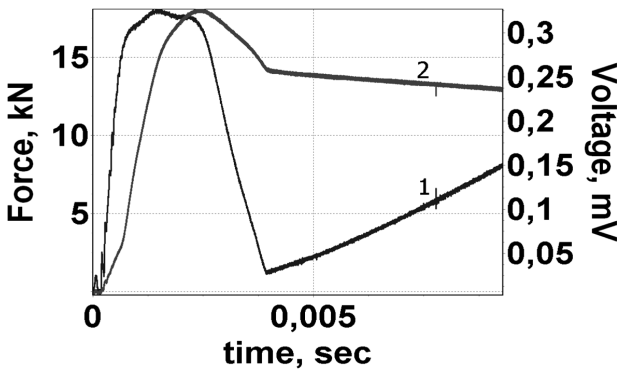

Figure 9: Specimen ShK7-3, h = 5 cm: 1 – diagram of the striker contact with the specimen, 2 – diagram of the gauge signal

Slika 9: Vzorec ShK7-3, h = 5 cm: 1 – diagram stika kladiva z vzorcem, 2 – diagram signala iz merilnega lističa

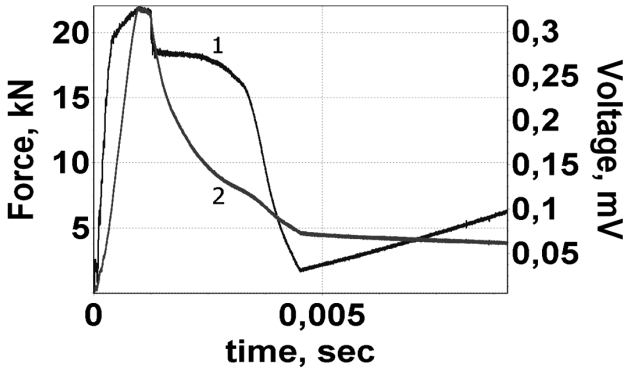

Figure 10: Specimen ShK7-3, h = 10 cm: 1 – diagram of the striker contact with the specimen, 2 – diagram of the gauge signal

Slika 10: Vzorec ShK7-3, h = 10 cm: 1 – diagram stika kladiva z vzorcem, 2 – diagram signala iz merilnega lističa

At the impact velocity of 1.4 m/s (**Figures 10** and **11**) a crack initiated in the central section of specimen ShK7-3 (**Figure 12**). It is obvious that the crack nucleates in the central section of the specimen (the

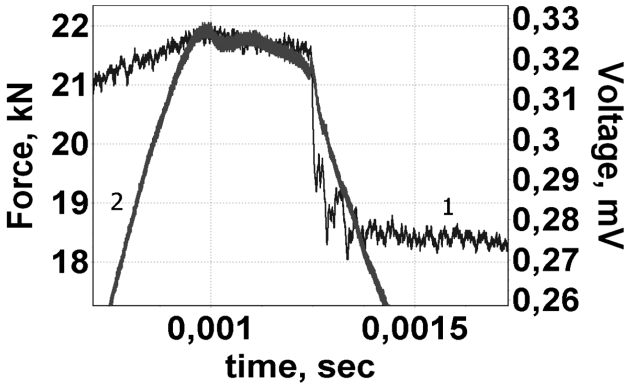

Figure 11: Specimen ShK7-3, h = 10 cm. An enlarged section of the diagrams: 1 – diagram of the striker contact with the specimen, 2 – diagram of the gauge signal.

Slika 11: Vzorec ShK7-3, h = 10 cm. Povečano področje: 1 – diagram stika kladiva z vzorcem, 2 – diagram signala iz merilnega lističa.

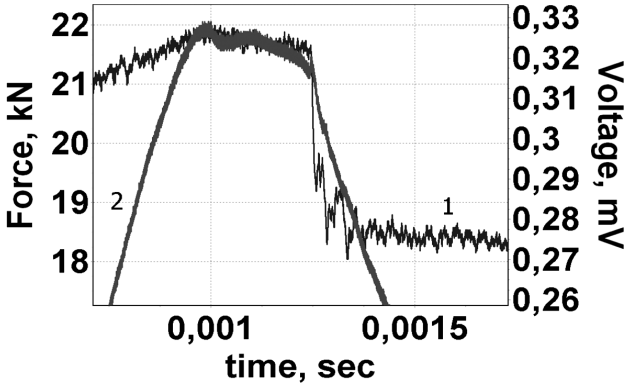

Figure 12: Specimen ShK7-3 (initiated crack), h = 10 cm

Slika 12: Vzorec ShK7-3 (začetna razpoka), h = 10 cm

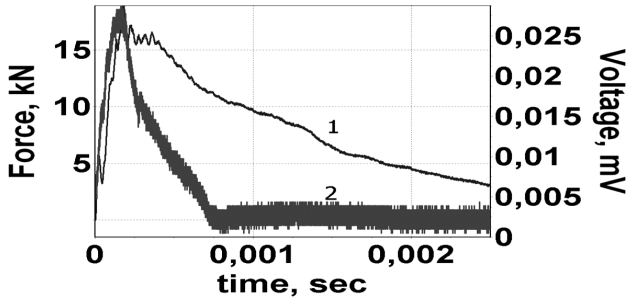

Figure 13: Specimen ShK7-3, h = 50 cm: 1 – diagram of the striker contact with the specimen, 2 – diagram of the gauge signal

Slika 13: Vzorec ShK7-3, h = 50 cm: 1 – diagram stika kladiva z vzorcem, 2 – diagram signala iz merilnega lističa

crack opening has the maximum value – of approximately 1 mm in the center).

In specimens ShK7-3 and ShK7-4, at the impact velocity of 1.4 m/s, the initiated cracks did not extend to the lateral surfaces of the specimens (**Figure 12**). The $P(t)$ diagram clearly shows the region of an abrupt decrease in the force at the moment of brittle-crack initiation and propagation in the central section of the specimen.

Then, the specimen was fractured at the impact velocity of 3 m/s. **Figure 13** provides a diagram of the fracture. Like in the $P(t)$ diagram there is a lack of the area of deformation/crack initiation; the initial section has the form of a straight line (elastic deformation) with its fluctuations. This is related to the presence of the crack initiated in specimen ShK7-3.

A large area of a stable crack growth and an area of an unstable crack jump (brittle fracture) formed at the impact velocity of 1.4 m/s are shown on **Figure 14**.

Figure 15 shows the diagram of the gauge signal and the $P(t)$ diagram for specimen ShK7-4. The crack initiation was similar to the one in specimen ShK7-3 after the impact with the velocity of 1.4 m/s. The crack

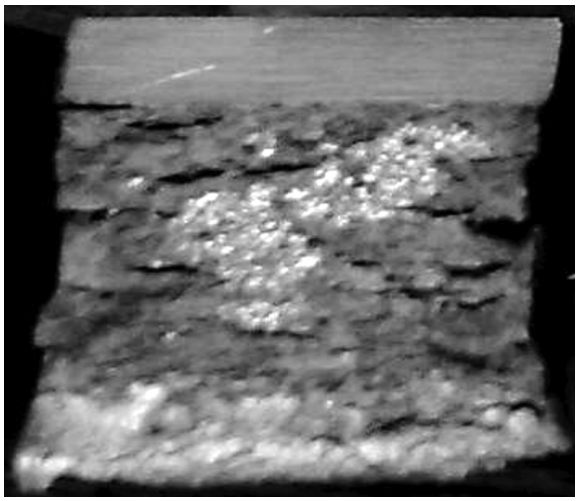

Figure 14: Specimen ShK7-3 (fracture)

Slika 14: Vzorec ShK7-3 (prelom)

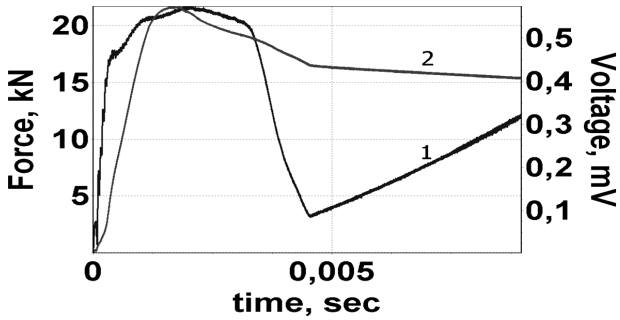

Figure 15: Specimen ShK7-4, h = 10 cm: 1 – diagram of the striker contact with the specimen, 2 – diagram of the gauge signal

Slika 15: Vzorec ShK7-4, h = 10 cm: 1 – diagram stika kladiva z vzorcem, 2 – diagram signala iz merilnega lističa

initiated inside the specimen and it demonstrated its maximum opening in the specimen central section, but did not extend to the lateral surfaces of the specimen (**Figure 16**). The gauge-signal diagram has its maximum value shifted to the left, relative to the maximum value in the $P(t)$ diagram.

In this case the gauge measuring the strain on the specimen surface did not register the initiation of a stable

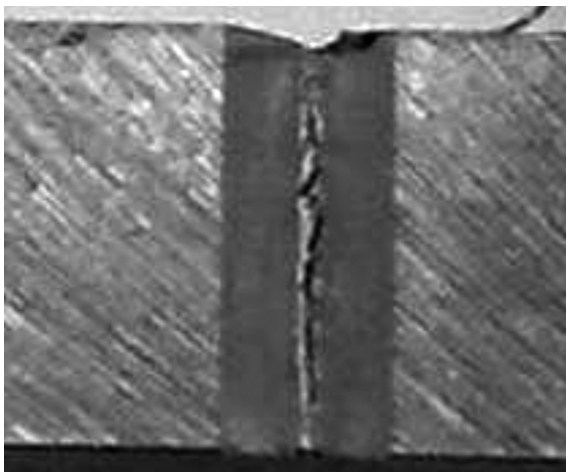

Figure 16: Crack nucleation, specimen ShK7-4, h = 10 cm

Slika 16: Nukleacija razpoke, vzorec ShK7-4, h = 10 cm

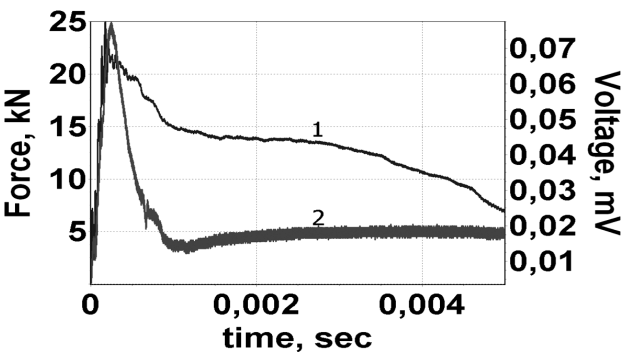

Figure 17: Specimen ShK7-4, h = 50 cm: 1 – diagram of the striker contact with the specimen, 2 – diagram of the gauge signal

Slika 17: Vzorec ShK7-4, h = 50 cm: 1 – diagram stika kladiva z vzorcem, 2 – diagram signala iz merilnega lističa

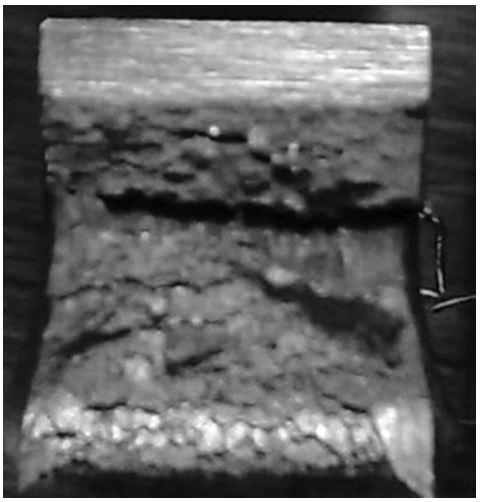

Figure 18: Fracture of specimen ShK7-4
Slika 18: Prelom vzorca ShK7-4

ductile crack inside the specimen. The crack did not extend to the specimen lateral surfaces.

The $P(t)$ diagram does not include the area of an abrupt force decrease, which implies the propagation of an unstable brittle crack in the specimen.

Specimen ShK7-4 was fractured at the impact velocity of 3 m/cm. The $P(t)$ diagram for specimen ShK7-4 (**Figure 17**) is similar to the diagram for specimen ShK7-3 (**Figure 13**).

The deformation/crack initiation site is not observed and the force increases linearly with the time in the initial part of the diagram. The maximum value in the gauge-signal diagram is more to the left compared with the one for specimen ShK7-3. The signal level is very low (0.028 mV), which evidences a significant deformation of the gauge tracks after the impact with the velocity of 1.4 m/s. At the fracture there is no unstable (brittle) crack-jump site (**Figure 18**); however, the gauge registered the moment of a ductile crack extension to the specimen lateral surface as demonstrated by its diagram.

The conducted investigations showed that the used procedure for the determination of the crack-initiation moment exhibits a number of drawbacks associated primarily with the formation of lateral necking. To obtain more accurate results, specimens with deep side grooves should be used to eliminate the influence of the specimen lateral-surface deformation.

5 CONCLUSIONS

The investigations of the moment of crack initiation in Charpy V-notch specimens were performed. The procedure of recording the crack initiation during the impact-bending testing using a vertical instrumented impact tester was developed and tested. A comparison of the gauge diagrams with the striker-contact diagrams made it possible to determine the moment of crack initiation in the contact diagram. The comparison of the gauge/deformation diagrams with the results of the fractographic investigations enabled us to find the relation between the moment of crack initiation in the striker contact diagram and the specimen with specific fracture zones.

It was determined that a crack in a Charpy specimen formed during the impact-bending testing is initiated in the specimen central section. The applicability of the given procedure for recording both a brittle-crack initiation in the specimen central section and a propagation of a ductile crack to the specimen lateral surface was shown.

There are large differences between the material properties of the specimens with the T-orientation and S-orientation. This difference can be revealed during an impact-loading test. The shapes of the diagrams of the specimens with different orientations of the notch are significantly different.

6 REFERENCES

[1] PNAE-G-007-86 Norms based on the strength of equipment and pipelines of nuclear power plants, Energoatomizdat, Moscow 1989

[2] VERLIFE - Unified Procedure for Lifetime Assessment of Components and Piping in WWER NPPs, European Commission under the Euratom Research and Training Programme on Nuclear Energy, Version 8, 2008, 275 p

[3] RD EO 1.1.2.09.0789-2009 – Method of determining fracture toughness according to test results witness samples underlying strength and life of WWER - 1000 NPPs, Energoatomizdat, Moscow 2009

[4] Standard ISO EN DIN 14 556 Instrumented Impact Test, Deuth Verlag, Berlin 2000

[5] R. Chaouadi, A. Fabry, On the utilization of the instrumented Charpy impact test for characterization the flow and fracture behavior of reactor vessel steels, European Structural Integrity Society, 30 (**2002**), 103–117, doi:10.1016/S1566-1369(02)80011-5

[6] V. Kharchenko, E. Kondryakov, V. Babutskii, V. Zhmaka, An instrumented testing machine for impact tests: basic elements, operation analysis, Reliability and Life of Machines and Structures, 27 (**2006**), 121–130

[7] V. Kharchenko, E. Kondryakov, A. Panasenko, Crack propagation peculiarities in steels at Charpy and disc-shaped specimens tests, Questions of nuclear science and technology, 84 (**2013**) 2, 31–38

[8] L. Botvina, Fracture, Kinetics, Mechanisms, General Laws, Nauka, Moscow 2008 (in Russian)

[9] V. Goritskii, Thermal embrittleness of steel, Metalurizdat., Moscow 2007

UDK 544.23:537.622
Original scientific article/Izvirni znanstveni članek

ISSN 1580-2949
MTAEC9, 49(3)409(2015)

STRUCTURAL, THERMAL AND MAGNETIC PROPERTIES OF Fe-Co-Ni-B-Si-Nb BULK AMORPHOUS ALLOY

STRUKTURNE, TERMIČNE IN MAGNETNE LASTNOSTI MASIVNE AMORFNE ZLITINE Fe-Co-Ni-B-Si-Nb

Sabina Lesz[1], Marcin Nabiałek[2], Ryszard Nowosielski[1]

[1]Silesian University of Technology, Institute of Engineering Materials and Biomaterials, Konarskiego Street 18a, 44-100 Gliwice, Poland
[2]Institute of Physics, Czestochowa University of Technology, Av. Armii Krajowej 19, 42-200 Czestochowa, Poland
sabina.lesz@polsl.pl

Prejem rokopisa – received: 2014-07-15; sprejem za objavo – accepted for publication: 2014-09-05

doi:10.17222/mit.2014.108

In the present paper the structure, thermal stability and magnetic properties of the $Fe_{43}Co_{22}Ni_7B_{19}Si_5Nb_4$ bulk amorphous alloy were investigated. The investigated alloy was cast as rods with three different diameters. The thermal stability associated with the glass transition temperature (T_g), crystallization temperature (T_x) and supercooled-liquid region ($\Delta T_x = T_x - T_g$) was examined with differential scanning calorimetry (DSC). The Curie temperature of the investigated glassy rods was determined from the results obtained with the DSC method. The magnetic properties and microstructure of the rods were examined with the vibrating-sample magnetometer (VSM) and X-ray diffraction (XRD) methods, respectively. The crystallization temperature (T_x) and the glass transition temperature (T_g) as well as the parameter of $\Delta T_x = T_x - T_g$ as the criterion of the glass-forming ability (GFA) of the investigated alloy were determined. The investigated alloys have good soft-magnetic properties.

Keywords: bulk amorphous alloy, structure, thermal and magnetic properties

Predstavljena je preiskava strukture, toplotne stabilnosti in magnetnih lastnosti masivne amorfne zlitine $Fe_{43}Co_{22}Ni_7B_{19}Si_5Nb_4$. Preiskovana zlitina je bila ulita kot palice s tremi različnimi premeri. Toplotna stabilnost, povezana s prehodom v steklasto stanje (T_g), temperaturo kristalizacije (T_x) in s podhlajenim področjem taline ($\Delta T_x = T_x - T_g$), je bila preiskovana z diferenčno vrstično kalorimetrijo (DSC). Curiejeva temperatura preiskovanih steklastih palic je bila določena iz rezultatov, dobljenih pri DSC-metodi. Magnetne lastnosti in mikrostruktura palic so bile preiskane z magnetometrom z vibrirajočimi vzorci (VSM) in z metodo rentgenske difrakcije (XRD). Določeni so bili temperatura kristalizacije (T_x) in temperatura prehoda v steklasto stanje (T_g) ter tudi parameter $\Delta T_x = T_x - T_g$ kot merilo sposobnosti tvorbe steklastega stanja (GFA) preiskovanih zlitin. Preiskovane zlitine imajo dobre mehkomagnetne lastnosti.

Ključne besede: masivna amorfna zlitina, struktura, termične in magnetne lastnosti

1 INTRODUCTION

A large number of studies on the development of soft-magnetic metallic glasses have been carried out over the last 20 years. It is well recognized that the low glass-forming ability (GFA) of Fe-based alloys has limited the potential of using them as engineering materials. For this reason extensive efforts have been carried out to improve the GFA of metallic materials and the understanding of the mechanism of the effects of various factors on the formation, crystallization, thermal stability and property of bulk metallic glass (BMG). Bulk metallic glasses (BMGs) represent a new class of amorphous metallic alloys. BMGs are valuable materials for environmental applications (e.g., solar cells, hydrogen production, the systems for retention and purification of dangerous pollutants, the nuclear industry, etc.) and for industrial applications in different areas (e.g., aerospace, automotive, electronics, computer, telecommunication areas, etc.).[1–12]

These multi-component metallic alloys can be obtained at low cooling rates of 1 K/s to 100 K/s, which allow an increase in the time (from milliseconds to minutes) before the crystallization, enabling a greater critical casting thickness (> 1 cm) by conventional moulding.[1,2,4–7]

Among BMGs, the Fe-based BMGs are more attractive for application since they do not exhibit only good properties, such as excellent soft-magnetic properties, a high strength and a good corrosion resistance, but are also cheaper in comparison to the other BMGs.[1–10]

For the preparation of a Fe-based BMG, $Fe_{80}B_{20}$ is often used as the starting alloy. Later the Nb metal with a high melting temperature is added. The additions of small amounts of Nb to (Fe,Co,Ni)-(B,Si) alloys are effective for the increase in the GFA through the increase in the stability of the supercooled liquid against crystallization.[3] A temperature interval of the supercooled-liquid region ΔT_x has been suggested to evaluate the glass-forming ability (GFA) of bulk amorphous alloys. An addition of amount fraction of Nb 4 % was found to be very effective in improving the GFA of Fe- and Co-based glassy alloys.[7]

As BMGs can be produced by adding four and five elements to the basic ternary alloys, small amounts of the elements such Ni, Co and Si were added. A partial substitution of Fe with the other magnetic elements, Ni or

Co, may significantly enhance the GFA and soft-magnetic properties of the Fe-based glass-forming alloys. The metalloid elements of Si and B play a crucial role in the formation of BMGs. They also affect the GFA, the thermal stability, the crystallization and the properties of BMGs. These materials have a strong affinity with the conventional BMG base elements such Fe and rare-earth elements, i.e., they have a large, negative heat of mixing with these base elements. The metalloid elements result in crystallization, degrading the GFA of the BMGs, but, on the other hand, due to a small atomic size of the Si and B atoms, a proper addition can tighten the alloy structure, stabilizing the alloy against crystallization.[3]

The Fe-Co based glassy alloys exhibit good soft-magnetic properties, i.e., a high saturation magnetization (0.8–1.3 T) and a low coercivity (1–2.5 A/m).[3] Magnetic properties of these alloys are dependent on the Ni and Fe contents. A decrease in the coercivity (H_c) with the increasing Co content was found to originate in the reduction of saturation magnetostriction.[3] Coercivity H_c is proportional to the ratio of saturation magnetostriction (λ_s) to saturation magnetization (J_s), i.e.:[8]

$$H_c \approx \Delta V \cdot \sqrt{\rho d \frac{\lambda_s}{J_s}} \quad (1)$$

and the slope is related to the volume (ΔV) and density (ρd) of internal defects in the glassy structure.[8]

Due to their unique properties, the Fe-Co based glassy alloys have been commercialized in the following application fields: precision-mould material, precision-imprint material, precision-sensor material, precision-machinery material, surface-coating material, cutting-tool material, shot penning material, fuel-cell separator material and so forth.[1,2,9,10]

In the present paper the structural, thermal and magnetic properties of a Fe-Co-Ni-B-Si-Nb bulk amorphous alloy with a selected chemical composition was investigated.

2 EXPERIMENTAL PROCEDURE

Investigations were carried out on amorphous rods with a composition of $[(Fe_{0.6}Co_{0.3}Ni_{0.1})_{0.75}B_{0.2}Si_{0.05}]_{96}Nb_4$. Fe-based master-alloy ingots with a composition of $[(Fe_{0.6}Co_{0.3}Ni_{0.1})_{0.75}B_{0.2}Si_{0.05}]_{96}Nb_4$ were prepared by induction melting of pure Fe, Co, Ni, Nb and pure B and Si crystals in an argon atmosphere. The $Fe_{43}Co_{22}Ni_7B_{19}Si_5Nb_4$ alloy composition represents the nominal atomic percentages. The master alloy was melted in a quartz crucible using an induction coil. Rods with (1.5, 2.5 and 3) mm diameters were prepared with the pressure copper-mould casting method.[11]

The microstructure of the rods was examined with the X-ray diffraction (XRD) method. The X-ray method was performed using a Seifert-FPM XRD 7 diffractometer with filtered Co-$K\alpha$ radiation.

The thermal stability associated with the glass transition temperature (T_g), crystallization temperature (T_x) and supercooled-liquid region ($\Delta T_x = T_x - T_g$) was examined with differential scanning calorimetry (DSC) at a heating rate of 0.1 K/s. The Curie temperature of the investigated glassy rods was determined from the results obtained with the DSC method.

High-field magnetization curves were measured with a vibrating-sample magnetometer (VSM) in a magnetic field up to 2 T. The magnetizing field was parallel to the sample length to minimize the demagnetization effect. The magnetization curves were analyzed using the least-squares method.

3 RESULTS AND DISCUSSION

It was found from the obtained results of the structural studies performed with X-ray diffraction that the diffraction patterns of the surface rods with (1.5, 2.5 and 3.0) mm diameters of the $Fe_{43}Co_{22}Ni_7B_{19}Si_5Nb_4$ alloy consist of a broad-angle peak, indicating the existence of an amorphous phase (**Figure 1**).

The DSC curves determined on the $Fe_{43}Co_{22}Ni_7B_{19}Si_5Nb_4$ rods with the diameters of (1.5, 2.5 and 3) mm in the as-cast state for the studied alloy are shown in **Figures 2** to **4**, and summarized in **Table 1**. **Table 1** also gives information about the thermal properties of the studied amorphous-alloy rods. The onset crystallization temperatures T_x for the glassy rod samples with the diameters of (1.5, 2.5 and 3) mm are slightly different and equal to (828, 827 and 826) K (**Figures 2** to **4**), respectively. It is seen that T_x decreases from 828 K to 826 K with an increase in the diameter of the rods. On the basis of an analysis of DSC curves the glass transition temperature T_g and supercooled-liquid region

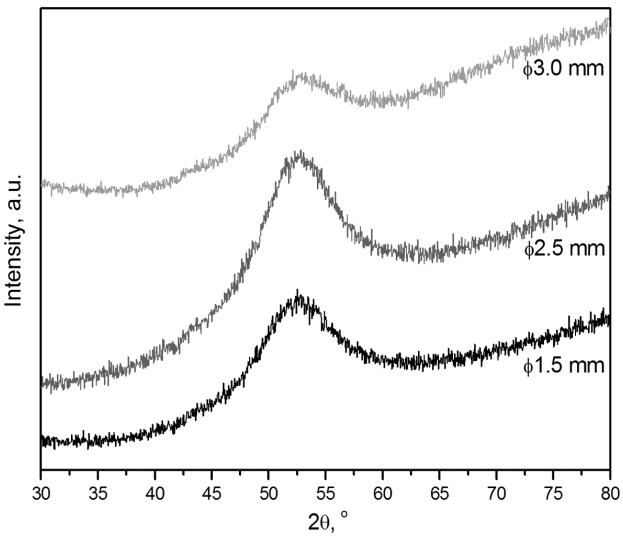

Figure 1: X-ray diffraction patterns of the bulk amorphous $Fe_{43}Co_{22}Ni_7B_{19}Si_5Nb_4$ rods

Slika 1: Rentgenogrami masivnih amorfnih palic $Fe_{43}Co_{22}Ni_7B_{19}Si_5Nb_4$

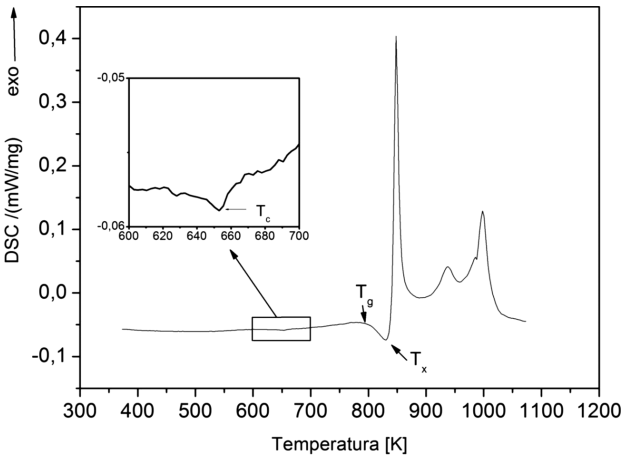

Figure 2: DSC curve of the $Fe_{43}Co_{22}Ni_7B_{19}Si_5Nb_4$ glassy-alloy rod with a diameter of 1.5 mm

Slika 2: DSC-krivulja palice premera 1,5 mm iz steklaste zlitine $Fe_{43}Co_{22}Ni_7B_{19}Si_5Nb_4$

$\Delta T_x = T_x - T_g$ for the glassy rod samples with the diameters of 1.5 mm to 3 mm are determined, too. The value of the supercooled-liquid region is an experimental parameter that determines the glass-forming ability of the tested alloy. The glass transition temperature T_g and supercooled-liquid region ΔT_x for the glassy rod samples with the diameters of (1.5, 2.5 and 3) mm are: T_g = 794 K, ΔT_x = 34 K (**Figure 2**), T_g = 790 K, ΔT_x = 37 K (**Figure 3**), T_g = 797 K, ΔT_x = 29 K (**Figure 4**), respectively. The value of the Curie temperature T_C for the $Fe_{43}Co_{22}Ni_7B_{19}Si_5Nb_4$ rods with the diameters of (1.5, 2.5 and 3.0) mm is (652, 650 and 655) K, respectively. Similar values of T_g and T_C were obtained in[1,9], where the results are T_g = 813 K and T_C = 643 K for the $[(Fe_{0.6}Co_{0.3}Ni_{0.1})_{0.75}B_{0.2}Si_{0.05}]_{96}Nb_4$ alloy in the form of a rod with a diameter of 4 mm.

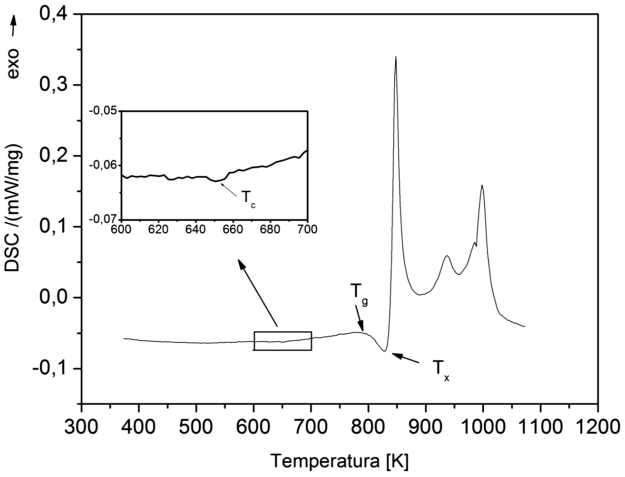

Figure 3: DSC curve of the $Fe_{43}Co_{22}Ni_7B_{19}Si_5Nb_4$ glassy-alloy rod with a diameter of 2.5 mm

Slika 3: DSC-krivulja palice premera 2,5 mm iz steklaste zlitine $Fe_{43}Co_{22}Ni_7B_{19}Si_5Nb_4$

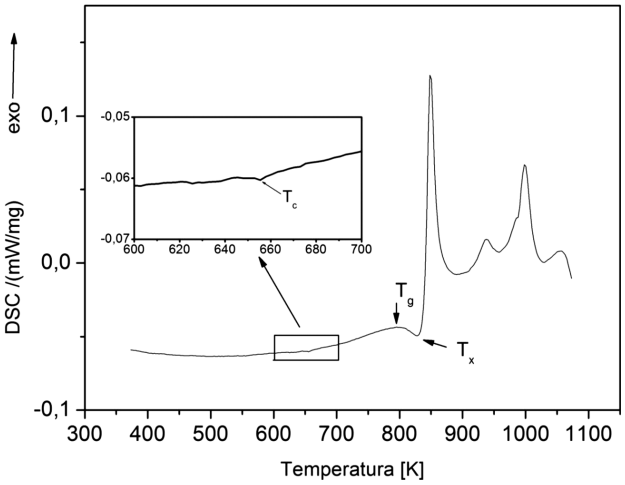

Figure 4: DSC curve of the $Fe_{43}Co_{22}Ni_7B_{19}Si_5Nb_4$ glassy-alloy rod with a diameter of 3.0 mm

Slika 4: DSC-krivulja palice premera 3,0 mm iz steklaste zlitine $Fe_{43}Co_{22}Ni_7B_{19}Si_5Nb_4$

Table 1: Thermal (T_g – the glass transition temperature, T_x – the crystallization temperature, ΔT_x – the temperature interval of the supercooled-liquid region) and magnetic (T_C – the Curie temperature, M_s – the saturation induction) properties of the bulk glassy $Fe_{43}Co_{22}Ni_7B_{19}Si_5Nb_4$ rods with the diameters of (1.5, 2.5 and 3.0) mm

Tabela 1: Termične (T_g – temperatura prehoda v steklasto stanje, T_x – temperatura kristalizacije, ΔT_x – temperaturni interval področja superpodhlajene taline) in magnetne (T_C – Curiejeva temperatura, M_s – nasičenje indukcije) lastnosti masivnih steklastih palic $Fe_{43}Co_{22}Ni_7B_{19}Si_5Nb_4$ s premeri (1,5, 2,5 in 3,0) mm

Diameter	Thermal properties			Magnetic properties	
Φ/mm	T_g/K	T_x/K	ΔT_x/K = T_x-T_g	T_C/K	M_s/T
1.5	794	828	34	652	1.07
2.5	790	827	37	650	1.22
3.0	797	826	29	655	1.18

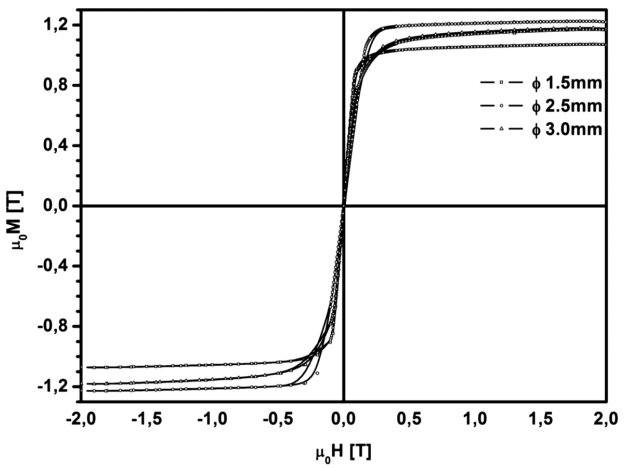

Figure 5: Magnetic hysteresis loops of the bulk amorphous $Fe_{43}Co_{22}Ni_7B_{19}Si_5Nb_4$ rods

Slika 5: Magnetne histerezne zanke masivnih steklastih palic $Fe_{43}Co_{22}Ni_7B_{19}Si_5Nb_4$

The saturation induction (M_s) of the studied glassy rods is (1.07, 1.22 and 1.18) T for the samples with the diameters of (1.5, 2.5 and 3) mm, respectively (**Figure 5**).

The obtained magnetic properties allow us to classify the studied bulk amorphous alloy in the as-cast state as a soft-magnetic material. These excellent magnetic properties lead us to believe that the Fe-based amorphous alloy could be used as a new engineering and functional material intended for the parts of inductive components.

4 CONCLUSIONS

Bulk metallic glass rods with the diameters of (1.5, 2.5 and 3) mm and a composition of $Fe_{43}Co_{22}Ni_7B_{19}Si_5Nb_4$ were made by pressure copper-mould casting. The glassy rods show good soft-magnetic properties and thermal stability.

A high magnetization of 1.07 T to 1.22 T of the $Fe_{43}Co_{22}Ni_7B_{19}Si_5Nb_4$ rods leads us to believe that the Fe-based bulk glassy alloy with a Ni addition will be used as a new engineering material for the parts of micro-motors, force sensors and other applications. Moreover, force sensors based on the newly developed amorphous alloys may operate in a high-temperature range. The temperature of the operation of such a sensor is limited mainly by the Curie temperature and the value of T_C for the $Fe_{43}Co_{22}Ni_7B_{19}Si_5Nb_4$ alloy is in the range from 650 K to 655 K.

5 REFERENCES

[1] A. Inoue, B. L. Shen, C. T. Chan, Fe- and Co-based bulk glassy alloys with ultrahigh strength of over 4000 MPa, Intermetallics, 14 (**2006**), 936–944, doi:10.1016/j.intermet.2006.01.038

[2] A. Inoue, B. Shen, A. Takeuchi, Properties and applications of bulk glassy alloys in late transition metal-based systems, Materials Science and Engineering, A 441 (**2006**), 18–25, doi:10.1016/j.msea.2006.02.416

[3] W. H. Wang, Roles of minor additions in formation and properties of bulk metallic glasses, Progress in Materials Science, 52 (**2007**), 540–596, doi:10.1016/j.pmatsci.2006.07.003

[4] A. Inoue, Stabilization of metallic supercooled liquid and bulk amorphous alloys, Acta Materialia, 48 (**2000**), 279–306, doi:10.1016/s1359-6454(99)00300-6

[5] B. Shen, A. Inoue, C. Chang, Superhigh strength and good soft-magnetic properties of (Fe,Co)–B–Si–Nb bulk glassy alloys with high glass-forming ability, Applied Physics Letters, 85 (**2004**) 21, 4911–4913, doi:10.1063/1.1827349

[6] K. F. Yao, C. Q. Zhang, Fe-based bulk metallic glass with high plasticity, Applied Physics Letters, 90 (**2007**), 061901, doi:10.1063/1.2437722

[7] C. Chang, B. Shen, A. Inoue, FeNi-based bulk glassy alloys with superhigh mechanical strength and excellent soft magnetic properties, Applied Physics Letters, 89 (**2006**) 5, 051912, doi:10.1063/1.2266702

[8] T. Bitoh, A. Makino, A. Inoue, Origin of Low Coercivity of Fe-(Al, Ga)-(P, C, B, Si, Ge) Bulk Glassy Alloys, Materials Transactions, 44 (**2003**) 10, 2020–2024

[9] B. Shen, C. Chang, A. Inoue, Formation, ductile deformation behavior and soft-magnetic properties of (Fe,Co,Ni)–B–Si–Nb bulk glassy alloys, Intermetallics, 15 (**2007**), 9–16, doi:10.1016/j.intermet.2005.11.037

[10] S. Lesz, R. Babilas, M. Nabialek, M. Szota, M. Dospial, R. Nowosielski, The characterization of structure, thermal stability and magnetic properties of Fe–Co–B–Si–Nb bulk amorphous and nanocrystalline alloys, Journal of Alloys and Compounds, 509 (**2011**), 197–201, doi:10.1016/j.jallcom.2010.12.146

[11] R. Nowosielski, R. Babilas, G. Dercz, L. Pajak, Structure of Fe-based metallic glass after crystallization process, Solid State Phenomena, 163 (**2010**), 165–168, doi:10.4028/www.scientific.net/SSP.163.165

[12] L. A. Dobrzański, A. Drygala, Influence of Laser Processing on Polycrystalline Silicon Surface, Materials Science Forum, 706–709 (**2012**), 829–834, doi:10.4028/www.scientific.net/MSF.706-709.829

UDK 532.64:541.183
Original scientific article/Izvirni znanstveni članek

ISSN 1580-2949
MTAEC9, 49(3)413(2015)

THE NANO-WETTING ASPECT AT THE LIQUID-METAL/SiC INTERFACE

VIDIK NANOOMAKANJA NA STIKU STALJENA KOVINA-SiC

Marija Mihailović[1], Karlo Raić[2], Aleksandra Patarić[1], Tatjana Volkov - Husović[2]

[1]Institute for Technology of Nuclear and other Mineral Raw Materials, Franchet d'Esperey St. 86, 11000 Belgrade, Serbia
[2]Faculty of Technology and Metallurgy, University of Belgrade, Karnegijeva 4, 11000 Belgrade, Serbia
m.mihailovic@itnms.ac.rs

Prejem rokopisa – received: 2014-07-18; sprejem za objavo – accepted for publication: 2014-07-31

doi:10.17222/mit.2014.111

The wetting process on the nano-scale, as an initial and essential step in liquid metal/ceramic joining, is discussed here. Thanks to recent breakthroughs in experimental techniques with nanometre resolution, questions posed several decades ago are being looked at again. Despite recorded facts on acting mechanisms, the published results are very diverse due to the variety of materials and their structures, as well as experimental conditions, so the modeling is inevitable for process development and to overcome the multi-scale influencing parameters issues. A nano-scale wetting model have been proposed and tested on results obtained in a liquid-metal/SiC system that was published in the literature.

Keywords: wetting, modelling, nano-scale, metal/ceramic interface

Razložen je postopek omakanja na nanonivoju kot začetni in bistveni del pri spajanju staljena kovina-keramika. Zaradi sedanjih, prelomnih eksperimentalnih tehnik do nanometrske resolucije se ponovno pojavljajo vprašanja, stara več desetletij. Kljub dejstvom glede delujočih mehanizmov so objavljeni rezultati zelo različni zaradi različnosti materialov in njihovih struktur, kot tudi eksperimentalnih razmer. Zato je neizogibno modeliranje razvoja procesov, da se preseže številne večdimenzijske vplivne parametre. Na podlagi literaturnih podatkov iz sistema staljena kovina-SiC je bil predložen in preizkušen model omakanja na nanonivoju.

Ključne besede: omakanje, modeliranje, nanopodročje, stik kovina-keramika

1 INTRODUCTION

Although such different materials in terms of heat and electrical conductivity, as well as hardness, ductility, wear or corrosion resistance, metals and ceramics have integrated the advantages of their differences in many modern applications when operating together. Wetting as the initial and inevitable phenomenon of the liquid metal to ceramic joining process have been investigated, both experimentally and theoretically for more than three decades.[1–5] In the most recent decade, experimental techniques enabled an insight into wetting phenomena at high resolution, i.e., at the nanoscale.[6] Nevertheless, modeling is still a required method for wetting-process prediction. Despite, or simply because of modern experimental techniques, any investigation of metal/ceramic wetting mechanisms acting on the micro and nano levels is still demanding, both experimentally and theoretically.[5,7,8] These mechanisms are important for understanding metal/ceramics interfacial bonding and further process development.[3] The trend in several fields of science today is miniaturization and developing towards the nano-scale, both for the sake of sensitive processes and for lowering the costs; whereas for metal/ceramic systems the intention is the miniaturization of electronic devices.[8,9] This pushed SiC to the center of investigations again. Besides superconductivity, it has a very low coefficient of thermal expansion and an absence of phase transformations at operating temperatures, enabling the observed crystal structure to be stable. Together with new technical developments, new theoretical concepts are also required.

There are several theories used to describe interface bonding in the two adjacent components, i.e., liquid metal and solid ceramic, materials that are diverse due to the different types of atomic bonding.[5] One of the first theories was confined to reactive wetting, known as the 'reaction product control' theory, claimed that the interface reactions take control over the wetting mechanism at the interface,[1,10] while the opposite theory claimed that chemical reactions are not crucial for controlling the wetting phenomenon, but the capillary effects and adsorption of metals onto the ceramic substrate, with triple line ridging[11,12]. During years of research, theories were supported by experimental data, some statements were reconsidered,[13,14] and plenty of influential parameters were investigated. For the sake of plenty of investigated metal/ceramic systems and different approaches, there were variations in the experimental work, as well as in the suggested theoretical models. For the comprehensive modeling, both the physical and chemical approaches should be taken into account, as well as the mechanisms acting at the nano scale.

2 A NANO-SCALE MECHANISM – THE FRACTIONAL SURFACE APPROCAH

The macroscopically measured contact angle, θ, defined by Young's equation (1), is usually interpreted as the bonding quality of the metal/ceramic interface, but this criteria is valid only up to the micron scale. The atomic structure of the liquid metal and of the substrate becomes important on the nano-scale, and nano-wetting properties have an important influence on the macroscopic wetting behavior of liquids on solid surfaces.[4,6,8]

The wetting properties of the liquid metal/ceramic interface are strongly affected by the composition of the solid and liquid components, the roughness and other irregularities on the macro level, or grain-boundary grooves and lattice pits at the micro-scale, the surface pattern of the ceramic substrate, and either the reactive or non-reactive wetting, by the mechanisms occurring at the nano scale, including thermal influences.[4–7,15–17]

Although the geometrically structured substrates were a matter of interest for years[18] at macro and micro scale, they can be investigated in a new light, since the recent development of experimental techniques at the nano level, as well as of accompanied theories.[4,6,19]

It is shown that a change in the type of liquid metal/substrate interface, in the same system (Ni-Si/C system with a formed reaction layer of SiC and hence an interface change), leads to a remarkable change in the wetting: from contact angles much higher than 90 ° to contact angles in the range 20–40 °.[20] This refers to the macroscopically measured contact angle θ.

There is a wide range of reported measured contact angles for the pure liquid metals in a contact with SiC, for different temperatures, in a literature review.[3] A dramatic change in the contact-angle values for the majority of reactive metals is normally used in metal/ceramic brazing is registered, even reflecting in a wetting-non-wetting transition for the same metal with the temperature change. The situation is more complicated when the liquid metal is in fact an alloy.

Recent *in-situ* experiments at the nano level brought into connection the high traveling angle of the molten metal over the SiC basal plane with a high interfacial energy between the molten metal (Ti) and the SiC.[6] So, the nano-level analysis can also start from the interfacial energies relation in the Young's equation (1):

$$\cos\theta = \frac{\gamma_{SA} - \gamma_{LS}}{\gamma_{LA}} \quad (1)$$

where γ_{SA}, γ_{LS} and γ_{LA} are solid-air (i.e., the corresponding atmosphere), liquid-solid and liquid-air interfacial energies, respectively. Combining this with the Cassie and Baxter relationship for rough surfaces,[18] modified with two coefficients concerning the surface area, one can see that the net energy in the system is expressed according to Equation (2):

$$E_N = f_2\gamma_{LA} - f_1\gamma_{LA}\cos\theta = \gamma_{LA}(f_2 - f_1\cos\theta) \quad (2)$$

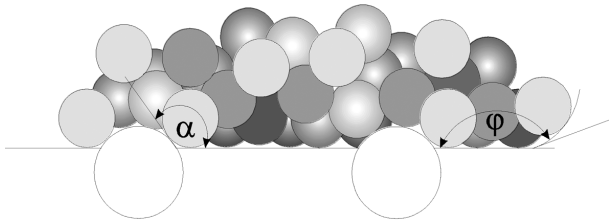

Figure 1: The liquid-metal atoms in contact with the ceramic-substrate atoms
Slika 1: Atomi staljene kovine v stiku z atomi keramike v podlagi

where f_1 is the total area of the solid-liquid interface and f_2 is the total area of the liquid-air interface (fractional surface factors).

Using the energy Equation (2), the cosine of the apparent contact angle, θ_A, for the geometrically structured surface, can be expressed as:

$$\cos\theta_A = -\frac{E_N}{\gamma_{LA}} = f_1\cos\alpha - f_2 \quad (3)$$

The atomistic arrangement of atoms in a liquid metal is not entirely random. During melting the crystal structures are being broken down, and the average packing density becomes smaller than in the solid state. The interatomic forces keep trying to establish the original arrangement, at the same time being disturbed by the thermal motion of the atoms. So, the melt is much more like the crystal than the completely random state of a gas. **Figure 1** shows the liquid metal atoms in contact with the ceramic substrate atoms, with the apparent contact angle φ and advancing contact angle between the liquid metal atoms and the ceramic substrate (α). Several authors[21] found that in the liquid Cu/SiC system, the liquid Cu spreads over the hexagonal crystal structure of β-SiC, maintaining a hexagonal shape. Since SiC has over 250 crystalline forms, it is necessary to develop a model taking into account the crystal lattice and the planes' orientation.

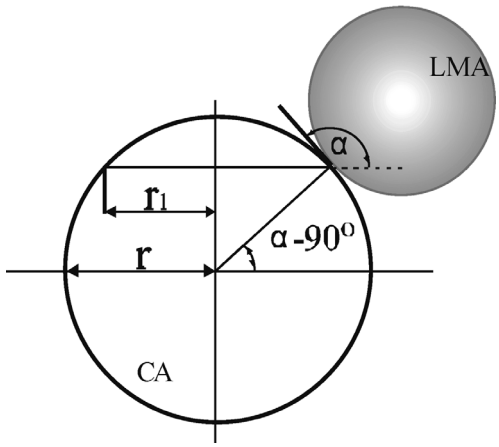

Figure 2: Angles describing the position of liquid metal atoms (LMA) in contact with the ceramic substrate atoms (CA)
Slika 2: Koti, ki opisujejo položaj atomov v staljeni kovini (LMA) v stiku z atomi iz keramike v podlagi (CA)

At the atomistic level, the new dimensions of f_1 and f_2 can be introduced. Areas f_1 and f_2 can be derived from the value of the angle α, the contact angle between the atoms of the metal and the ceramic, as denoted in **Figure 2**, and the atom packing density s in the plane of the crystal lattice along which the contact with the liquid metal is established.

If the reciprocal atom packing density is denoted with s, and expressed through the atomic radius in the plane along which the wetting process occurs in a monocrystal, then the total plane area (P) will be:

$$P = s \cdot \pi\ r^2 \tag{4}$$

P_1 is the ceramic atom surface area in contact with the metal atoms:

$$P_1 = 2\pi r^2 \cdot [1 - \sin(\alpha - 90°)] \tag{5}$$

while P_2 is the area of the liquid metal at the metal/ceramic interface, which is not in contact with the crystal lattice atoms:

$$P_2 = P - \pi r_1^2 \tag{6}$$

The contact point of the liquid metal atoms in contact with the solid substrate atoms is at the distance r_1, shown in **Figure 2**. According to **Figure 2**, it can be written:

$$r_1 = r \cdot \cos(\alpha - 90°) \tag{7}$$

and hence the f_1 and f_2 are:

$$f_1 = \frac{P_1}{P} = \frac{2 \cdot [1 - \sin(\alpha - 90°)]}{s} \tag{8}$$

$$f_2 = \frac{P_2}{P} = \frac{s - \cos^2(\alpha - 90°)}{s} = 1 - \frac{1}{s}\cos^2(\alpha - 90°) \tag{9}$$

Similar to our calculations, there is an expression for the apparent contact-angle cosine on a super-hydrophobic surface, Equation (10).[22] With the same Cassie-Baxter approach, it is postulated that the measured contact angle is a sum calculated for n surfaces:

$$\cos\theta_A = \frac{1}{\gamma_{LA}} \sum_{n=1}^{N} f_n (\gamma_{n,SA} - \gamma_{n,LS}) \quad \text{where} \quad \sum_{n=1}^{N} f_n = 1 \tag{10}$$

where γ_{SA}, γ_{LS} and γ_{LA} are the interfacial energies, as described previously, and f_n is the fractional coverage of the nth chemical species.

There is a coincidence in the wetting approaches at the nano level, although contradictory processes have been observed: the wetting and super-non-wetting. It has been observed that both wetting processes can be enhanced, i.e., modified by introducing the geometrically structured surface approach.

3 RESULTS AND DISCUSSION

Knowing the f_1 and f_2 factors in their new, nano-scale meaning, the apparent contact angle on a nano-structured surface can be calculated according to Equation (3), for contact angles larger than 90 ° (the non-wetting case). For the wetting case, angles smaller than 90 °, this equation is modified by using supplementary angles to the apparent contact angles, due to the different substrate (CA) and the position of the liquid metal atoms (LMAs), and hence the different geometry. So, Equation (3), according to **Figures 2** and **3**, becomes (11):

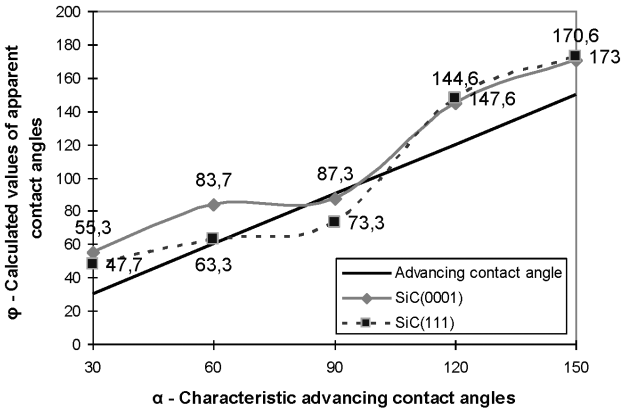

Figure 3: Comparison between calculated values of apparent contact angles φ and the characteristic advancing contact angles α for different orientations of the substrate planes

Slika 3: Primerjave med izračunanimi vrednostmi navideznih kotov stika φ in značilnih napredujočih kotov kontakta α pri različnih orientacijah ravnin podlage

$$\cos\varphi = f_1 \cos(180° - \alpha) - f_2 \tag{11}$$

Most researchers deal with the α-SiC(0001) and β-SiC(111) crystallographic planes, so this calculation is based on the determined atomic packing factors for these types of crystal lattice, although there are more than 250 different polytypes of SiC.[23,24] The obtained results are summarized in **Figure 3**.

The influence of the substrate planes' orientation on the calculated values of the apparent contact angles is clear in **Figure 3**. A deviation from the straight line, representing the characteristic advancing contact angles, differs more between the two different SiC planes for the wetting case, i.e., for angles smaller than 90 °, in comparison to the non-wetting case, where the lines are almost overlapped. It is clear that the minimum discrepancy between the advancing and the apparent calculated contact angle is around 90 °, i.e., where the transition wetting–non-wetting occurs. Besides, the trend is somewhat similar, but shifted, for both the α-SiC(0001) and β-SiC(111) crystallographic planes. This is due to the similarity in the configuration between those two crystallographic planes, already reported by others.[3]

It must be emphasized that this consideration is restricted to the non-reactive wetting case. During the formation of the new reaction product at interface, the distortion of the substrate lattice at the interface is inevitable, so other specific lattice factor calculations would have to be performed.

4 CONCLUSIONS

The wetting effect on the nano-scale depends on the structure of the crystal lattice and the planes' orientation according to the proposed model tested with measured apparent contact angles.

This is an aspect of possible liquid-metal/ceramic interface phenomena and this approach should contribute to a better understanding of the complex interface wetting behavior and should help in predicting the wetting modification on the nano-scale. But there is still the need for further investigations and modeling of the wetting at the liquid metal/ceramic interface, since quite different mechanisms take place at the nano level, compared to the well-established theories based on macroscopic contact-angle measurements.

Acknowledgement

The authors wish to acknowledge the financial support from the Ministry of Education, Science and Technological Development of the Republic of Serbia through the projects TR 34002 and P-172005.

5 REFERENCES

[1] B. Drevet, K. Landry, P. Vikner, N. Eustathopoulos, Scripta Materialia, 35 (**1996**) 11, 1265–1270, doi:10.1016/1359-6462(96)00305-3

[2] P. Wynblatt, Acta Mater., 48 (**2000**), 4439–4447, doi:10.1016/S1359-6454(00)00230-5

[3] G. W. Liu, M. L. Muolo, F. Valenza, A. Passerone, Ceramics International, 36 (**2010**), 1177–1188, doi:10.1007/s10853-009-3858-0

[4] T. Hofmann, M. Tasinkevych, A. Checco, E. Dobisz, S. Dietrich, B. M. Ocko, Physical Review Letters, 104 (**2010**) 10, 106102, doi:10.1103/PhysRevLett.104.106102

[5] M. W. Finnis, J. Phys.: Condens. Matter., 8 (**1996**) 32, 5811–5836, doi:10.1088/0953-8984/8/32/003

[6] S. I. Tanaka, C. Iwamoto, Materials Science and Engineering A, 495 (**2008**), 168–173, doi:10.1016/j.msea.2007.11.096

[7] K. T. Raic, Ceramics International, 26 (**2000**) 1, 19–24, doi:10.1016/S0272-8842(99)00013-9

[8] S. Dietrich, M. N. Popescu, M. Rauscher, J. Phys.: Condens. Matter., 17 (**2005**) 9, S577–S593, doi:10.1088/0953-8984/17/9/017

[9] S. Stopic, R. Rudolf, J. Bogovic, P. Majerič, M. Čolić, S. Tomić, M. Jenko, B. Friedrich, Mater. Tehnol., 47 (**2013**) 5, 577–583

[10] C. Rado, B. Drevet, N. Eustathopoulos, Acta Mater., 48 (**2000**), 4483–4491, doi:10.1016/S1359-6454(00)00235-4

[11] E. Saiz, R. M. Cannon, A. P. Tomsia, Acta Mater., 48 (**2000**), 4449–4462, doi:10.1016/S1359-6454(00)00231-7

[12] E. Saiz, A. P. Tomsia, R. M. Cannon, Scripta Mater., 44 (**2001**), 159–164, doi:10.1016/S1359-6462(00)00549-2

[13] N. Eustathopoulos, Curr. Opin. Solid State Mater. Sci., 9 (**2005**), 152–160, doi:10.1016/j.cossms.2006.04.004

[14] E. Saiz, A. P. Tomsia, Curr. Opin. Solid State Mater. Sci., 9 (**2005**), 167–173, doi:10.1016/j.cossms.2006.04.005

[15] M. Mihailović, T. Volkov-Husović, K. Raić, Adv. Sci. Tec., 45 (**2006**), 1526–1531, doi:10.4028/www.scientific.net/AST.45

[16] M. Tasinkevyich, S. Dietrich, Eur. Phys. J. E, 23 (**2007**), 117–128, doi:10.1140/epje/i2007-10184-5

[17] K. T. Raić, R. Rudolf, A. Todorović, D. Stamenković, I. Anžel, Mater. Tehnol., 44 (**2010**) 2, 59–66

[18] A. B. D. Cassie, S. Baxter, Trans. Faraday. Soc., 40 (**1944**), 546–551, doi:10.1039/TF9444000546

[19] K. T. Raic, Adv. Sci. Tec., 32 (**2003**), 725–733

[20] V. Bougiouri, R. Voytovych, O. Dezellus, N. Eustathopoulos, J. Mater. Sci., 42 (**2007**), 2016–2023, doi:10.1007/s10853-006-1483-8

[21] K. Nogi, Y. Hirata, T. Matsumoto. H. Fuji, Journal of Physics: Conference Series, 165 (**2009**) 1, 012073, doi:10.1088/1742-6596/165/1/012073

[22] A. H. F. Wu, K. Nakanishi, K. L. Cho, R. Lamb, Biointerphases, 8 (**2013**) 5, 1–10, doi:10.1186/1559-4106-8-5

[23] M. E. Levinshtein, S. L. Rumyantsev, M. S. Shur, Properties of Advanced Semiconductor Materials, John Wiley & Sons, 2001

[24] A. Gasse, G. Chaumat, C. Rado, N. Eustathopoulos, J. Mat. Sci. Let., 15 (**1996**) 18, 1630–1632, doi:10.1007/BF00278110

UDK 691:620.1
Original scientific article/Izvirni znanstveni članek

ISSN 1580-2949
MTAEC9, 49(3)417(2015)

THE EFFECT OF A SUPERPLASTICIZER ADMIXTURE ON THE MECHANICAL FRACTURE PARAMETERS OF CONCRETE

VPLIV DODATKA SUPERPLASTIFIKATORJA NA PARAMETRE MEHANSKEGA ZLOMA BETONA

Hana Šimonová, Ivana Havlíková, Petr Daněk, Zbyněk Keršner, Tomáš Vymazal

Brno University of Technology, Faculty of Civil Engineering, Veveří 331/95, 602 00 Brno, Czech Republic
simonova.h@fce.vutbr.cz

Prejem rokopisa – received: 2014-07-23; sprejem za objavo – accepted for publication: 2014-09-03

doi:10.17222/mit.2014.114

This paper focuses on the mechanical fracture parameters obtained from records of three-point bending tests on concrete specimens with a central edge notch. The tests were conducted on four sets of specimens made of different materials. The concrete of the specimens was different in the dosage of Portland cement CEM I 42.5 R (305 kg/m^3 or 355 kg/m^3) and superplasticizer (none or 0.25 % of the mass of the cement). The consistency class of fresh concrete determined using a slump test and a flow-table test was the same for all the mixtures. Three specimens in each set were tested after aging for 28 d. Increasing the dosage of cement and superplasticizer admixture influences the mechanical fracture properties of the concrete in both positive and negative ways. It follows that it is proper to monitor not only the effect of the superplasticizer admixture on the compressive strength values, but also focused attention on the fracture parameter values. The resistance to stable and unstable crack propagation, which is evidently connected with the durability of material, was quantified using a double-*K* fracture model.

Keywords: concrete, mechanical fracture parameters, superplasticizer, fracture test, double-*K* model

V tem članku se avtorji osredinjajo na parametre mehanskega zloma, ugotovljene pri tritočkovnem upogibnem preizkusu vzorcev iz betona s sredinsko zarezo na robu. Preizkusi so bili izvršeni na štirih serijah vzorcev z razliko v materialu. Beton vzorcev se je razlikoval v dodanem Portland cementu CEM I 42,5 R (305 kg/m^3 ali 355 kg/m^3) in superplastifikatorju (z masnim deležem 0,25 % cementa ali brez njega). Razred konsistence svežega betona, določen s preizkusom posedanja in preizkusom tečenja na mizi, je bil enak za vse mešanice. Iz vsake serije so bili preizkušeni trije vzorci, stari 28 d. Naraščanje dodatka cementa in superplastifikatorja je vplivalo na lastnosti pri mehanskem lomljenju betona v pozitivno in negativno smer. Iz tega izhaja, da je bilo treba nadzirati ne samo vpliv dodatka superplastifikatorja na tlačno trdnost, temveč tudi nameniti pozornost vrednostim parametrov pri prelomu. Odpornost proti stabilnem in nestabilnem napredovanju razpoke, ki je nedvoumno povezano z zdržljivostjo materiala, je bila ocenjena količinsko z uporabo dvojnega *K*-modela preloma.

Ključne besede: beton, parametri mehanskega preloma, superplastifikator, preizkus preloma, dvojni *K*-model

1 INTRODUCTION

The project of the Grant Agency of the Czech Republic "Assessment and Prediction of the Concrete Cover Layers Durability" deals with the study of problems of concrete cover layers' durability and contributes to the development of knowledge in the field of durability assessment and evaluation. The project is aimed especially at the determination of the transport characteristics of the concrete cover layers using the water- and gas-permeability methods. These so-called "durability parameters" are completed, especially with the fracture parameters (e.g., fracture toughness and fracture energy) and the basic physical and mechanical properties of fresh and hardened concrete[1].

The quality of the surface layer is significantly related to the permeability of the material, which defines its transport properties, and the thermal and electrical conductivity. The permeability of the concrete with the dense aggregate depends mainly on the porosity of the cement stone structure and is affected, besides other things, by cracks with a width greater than 10^{-4} m, resulting from the hardening of the concrete. Cracks (or microcracks) may combine together during the external loading of the concrete structure and create cracks, causing a significant reduction of durability or even serious failure of the structure. The connection of durability and content of the microcracks in the concrete is therefore obvious. The content of microcracks, and their resistance to stable and unstable propagation can be quantified by a number of fracture parameters.

In this paper the authors are focused on the mechanical fracture parameters obtained from records of three-point bending tests on concrete specimens with a central edge notch. The tests were conducted on four sets of specimens made of different materials. The concrete of the specimens was different in terms of the dosage of Portland cement CEM I 42.5 R and superplasticizer.

The resistance to stable and unstable crack propagation was quantified using the double-*K* fracture model[2]. Using this double-*K* model it is possible to determine the critical crack-tip opening and the fracture toughness of the investigated concrete, and quantify – as indicated model name – two different levels of crack pro-

pagation: initiation, which corresponds to the beginning of the stable crack growth and the level of unstable crack propagation.

The results obtained using the double-*K* model are completed by values of the compressive strength, the modulus of elasticity, the effective fracture toughness and the specific fracture energy.

2 EXPERIMENTAL PART

2.1 Material

The tests were conducted on four sets of specimens differing in terms of the material. The Portland cement CEM I 42.5 R was used as the binder. The aggregate consisted of three grain size fractions (0–4, 4–8 and 8–16) mm. The superplasticizer Sika ViscoCrete 4035 was used in two mixtures in the amount of 0.25 % of the weight of the cement. **Table 1** introduces the details regarding the theoretical concrete mixtures' composition and their designation. **Table 2** introduces the real concrete mixtures' composition. **Table 3** introduces the properties of the fresh concrete, which were determined according Czech Standards[3–6] in the laboratory at the concrete-mixing plant, when all four mixtures were prepared. The consistency class of the fresh concrete determined using the slump test and the flow-table test was the same for all the mixtures (**Table 3**).

Table 1: Theoretical composition of the mixtures
Tabela 1: Teoretična sestava mešanic

Component	Mixture			
	0/1	1/1	0/2	1/2
CEM I 42.5 R (kg)	305	305	355	355
Sand 0–4 (kg)	929	951	886	923
Aggregate 4–8 (kg)	182	186	182	186
Aggregate 8–16 (kg)	690	706	690	706
Water (kg)	200	185	209	180
Superplasticizer (kg)	0	0.76	0	0.89

Table 2: Real composition of the mixtures
Tabela 2: Realna sestava mešanic

Component	Mixture			
	0/1	1/1	0/2	1/2
CEM I 42.5 R (kg)	309	303	358	359
Sand 0–4 (kg)	927	952	892	921
Aggregate 4–8 (kg)	182	190	175	190
Aggregate 8–16 (kg)	698	707	695	712
Water (kg)	202	149	192	170
Superplasticizer (kg)	0	0.73	0	0.93

Table 3: Properties of fresh concrete
Tabela 3: Lastnosti svežega betona

Property	Mixture			
	0/1	1/1	0/2	1/2
Density (kg/m^3)	2315	2275	2315	2300
Slump test (mm)	60	60	60	50
class	S2	S2	S2	S2
Flow test (mm)	410	360	385	350
class	F2	F2	F2	F2
Air content (%)	2.7	3.6	2.5	2.8

2.2 Testing procedure

Beam specimens (of nominal dimensions 100 mm × 100 mm × 400 mm) with a central edge notch were subjected to three-point bending fracture tests (**Figure 1**). The notches were made before testing with a diamond blade saw. The notch depth was approximately equal to 1/3 of the depth of the specimen. The span length was equal to 300 mm. Three specimens from each set were tested after aging for 28 d. The fracture tests were carried out using a Heckert FPZ 100/1 testing machine (**Figure 2**) with the load range of 0–10 kN.

Load versus deflection diagrams (*P* – *d*-diagrams) and load versus crack mouth opening diagrams (*P* – *CMOD*-diagrams) were recorded using induction sensors and an extensometer (crack-opening displacement transducer) connected in a HBM SPIDER 8 device during the fracture experiments.

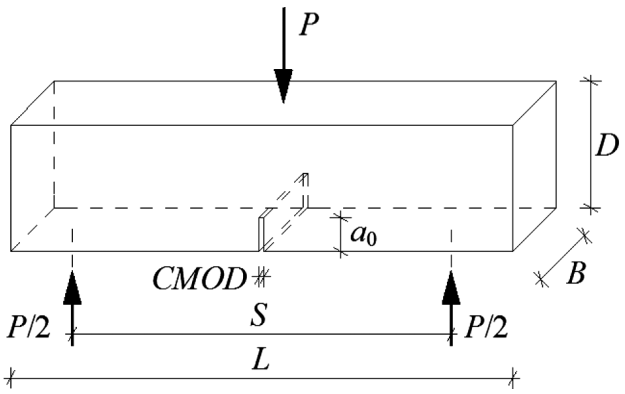

Figure 1: Three-point bending fracture test geometry
Slika 1: Geometrija vzorca za tritočkovni upogibni preizkus

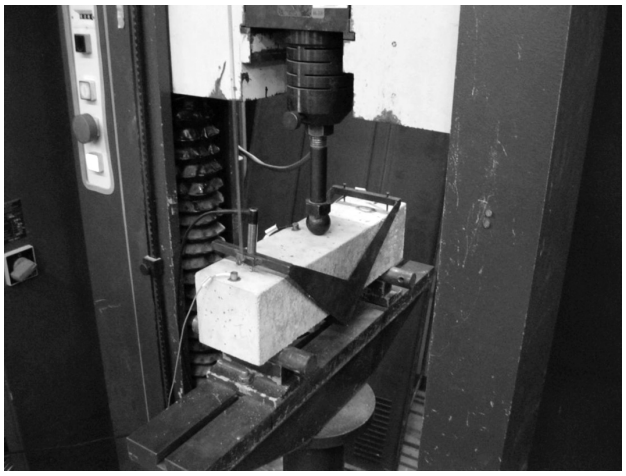

Figure 2: Fracture-test configuration in testing machine
Slika 2: Priprava preizkusa preloma na preizkusni napravi

Cubes with edge lengths of 150 mm were used for the determination of the compressive strength values. The compressive tests were carried out using a FORM+TEST ALPHA 3-3000 testing machine with the load range 0–3000 kN. The compressive strength tests were performed according to the Czech standard ČSN EN 12 390-3[7]; the loading rate was 0.6 MPa/s.

2.3 Methods

The modulus of elasticity values were obtained from the first (almost) linear part of the corrected P – d-diagrams. The effective fracture toughness was determined using the Effective Crack Model[8], which combines linear elastic fracture mechanics and the crack-length approach. Estimations of the fracture energy values according to the RILEM method were calculated using a "work of fracture" value[9]. Note that, especially in the case of the plain concrete specimens, a stability loss during the displacement-controlled loading can occur due to the low rigidity of the loading set-up. This stability loss appears as a jump in the measured parameters. A procedure was developed to recognise this problem and correct it in the case of fracture tests conducted on concrete specimens[10].

The measured P – $CMOD$-diagrams were used to determine the fracture parameters of the double-K model. Two levels of crack propagation were quantified: the initiation of stable crack growth and the level of unstable crack propagation.

The unstable fracture toughness K_{Ic}^{un} was numerically determined first, followed by the cohesive fracture toughness K_{Ic}^{c}. When both of these values are known, the following formula can be used to calculate the initiation fracture toughness K_{Ic}^{ini}:

$$K_{Ic}^{ini} = K_{Ic}^{un} - K_{Ic}^{c} \tag{1}$$

Details regarding the calculation of both the unstable and cohesive fracture toughness can be found, e.g., in the following articles[11,12].

Finally, in accordance with Equation (2) the value of the load P_{ini} is determined. This value can be defined as the load level at the beginning of stable-crack propagation from an initial crack/notch and can be obtained using the expression[1]:

$$P_{ini} = \frac{4WK_{Ic}^{ini}}{SF_1(\alpha_0)\sqrt{a_0}} \tag{2}$$

where $W = 1/6\ BD^2$ is the section modulus, B is the specimen width, D is the specimen depth, S is the load span, a_0 is the initial notch length according to **Figure 1** and $F_1(\alpha_0)$ is the geometry function given by the following equation:

$$F_1(\alpha_0) = \frac{1.99 - \alpha_0(1-\alpha_0)(2.15 - 3.93\alpha_0 + 2.7\alpha_0^2)}{(1+2\alpha_0)(1-\alpha_0)^{3/2}} \tag{3}$$

where α_0 is the ratio a_0/D.

3 RESULTS

The arithmetic mean and the standard deviation values of the selected parameters are introduced in following figures: compressive strength f_c (**Figure 3**), elasticity modulus E_c (**Figure 4**), specific fracture energy G_F (**Figure 5**), effective fracture toughness K_{Ice} (**Figure 6**), initiation level of the stress intensity factor K_{Ic}^{ini} (**Figure 7**), ratio K_{Ic}^{ini}/K_{Ic}^{un} (**Figure 8**), i.e., the ratio of the initiation fracture toughness to unstable fracture toughness, and the ratio P_{ini}/P_{max} (**Figure 9**), i.e., the ratio between the force at the beginning of stable-crack propagation from an initial stress concentrator and the maximum force corresponding to the peak of the P – $CMOD$-diagram.

The relative mean values of these properties are introduced in **Table 4** – the 100 % value for each material parameter represents the values of this parameter for the concrete with same amount of cement without superplasticizer.

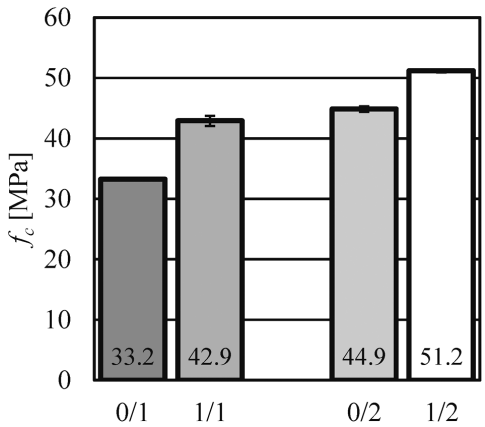

Figure 3: Comparison of the compressive strength values f_c of the concrete sets

Slika 3: Primerjava vrednosti tlačne trdnosti f_c za skupine betonov

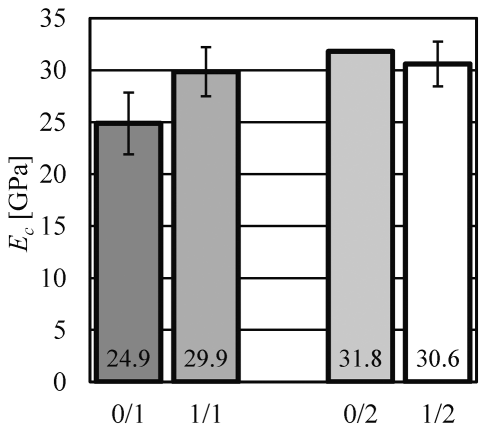

Figure 4: Comparison of the modulus elasticity values E_c of the concrete sets

Slika 4: Primerjava vrednosti modula elastičnosti E_c za skupine betonov

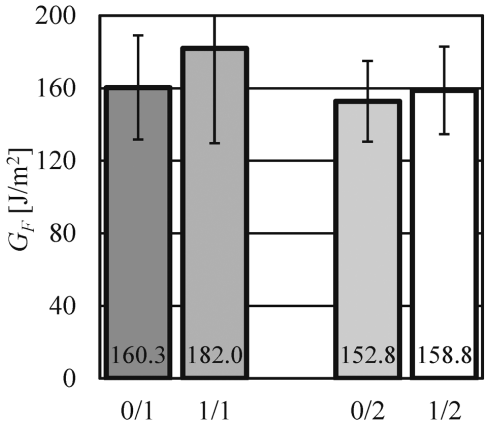

Figure 5: Comparison of the specific fracture energy G_F of the concrete sets

Slika 5: Primerjava specifične prelomne energije G_F za skupine betonov

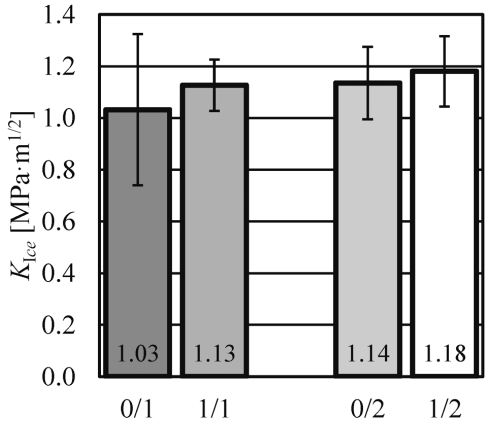

Figure 6: Comparison of the effective fracture toughness K_{Ice} of the concrete sets

Slika 6: Primerjava efektivne lomne žilavosti K_{Ice} za skupine betonov

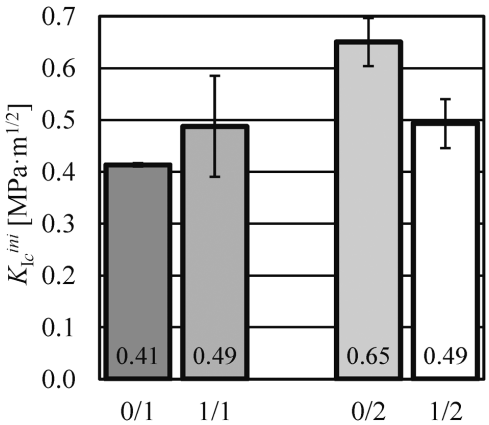

Figure 7: Comparison of the initiation level of stress intensity factor K_{Ic}^{ini} of the concrete sets

Slika 7: Primerjava iniciacijskega nivoja napetostnega intenzitetnega faktorja K_{Ic}^{ini} za skupine betonov

The concrete with the superplasticizer admixture achieved higher compressive strength values for both dosages of cement – concrete 1/1 had about 30 % higher value of compressive strength than concrete 0/1 without

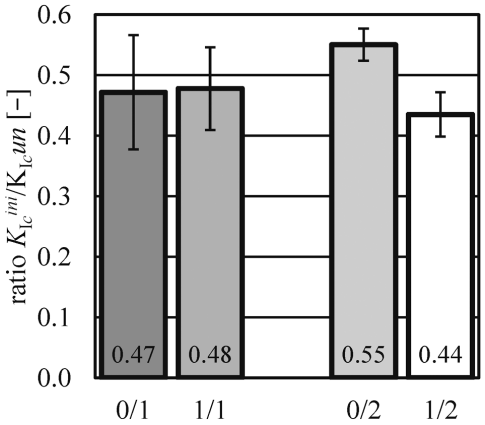

Figure 8: Comparison of the ratio K_{Ic}^{ini}/K_{Ic}^{un} of the concrete sets

Slika 8: Primerjava razmerij K_{Ic}^{ini}/K_{Ic}^{un} za skupine betonov

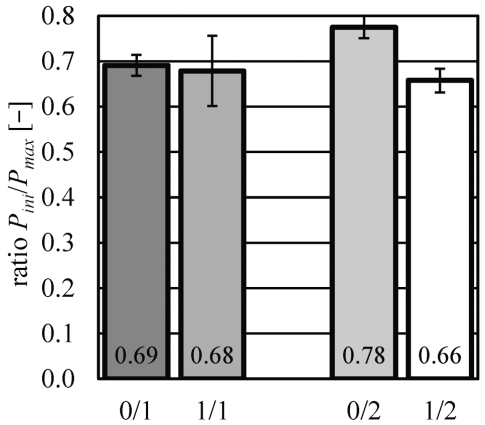

Figure 9: Comparison of the ratio P_{ini}/P_{max} of the concrete sets

Slika 9: Primerjava razmerja P_{ini}/P_{max} za skupine betonov

Table 4: The relative mean values of selected parameters of concrete sets in %

Tabela 4: Relativne glavne vrednosti izbranih parametrov vrst betona v %

Parameter	Concrete			
	0/1	1/1	0/2	1/2
f_c/MPa	100	129.1	100	114.0
E_c/GPa	100	120.1	100	96.2
G_F/J/m^2	100	113.5	100	103.9
K_{Ice}/(MPa m$^{1/2}$)	100	109.1	100	104.0
K_{Ic}^{ini}/(MPa m$^{1/2}$)	100	117.9	100	75.8
K_{Ic}^{ini}/K_{Ic}^{un}	100	101.3	100	79.0
P_{ini}/P_{max}	100	98.2	100	84.9

superplasticizer, and the concrete 1/2 was about 15 % higher than concrete 0/2.

The values of the modulus of elasticity also increased with a superplasticizer admixture in the case of a lower dosage of cement – concrete 1/1 achieved an about 20 % higher value of this parameter than the concrete 0/1. On the other hand, the modulus of elasticity values decreased in the case of concrete 1/2 in comparison with the concrete 0/2 by about 4 % – but the variability is higher in the case of concrete 1/2, so we could say that the superplasticizer admixture had no effect on the elasti-

city modulus value in the case of a higher dosage of cement.

The fracture energy quantifies the brittleness/toughness of the material through the evaluation of the whole $P - d$-diagram. This parameter value increased with the superplasticizer admixture in both cases of cement dosage. In addition, these values decreased with an increase of the cement dosage in both cases of concrete, with or without the superplasticizer. The variability of the results is relatively high.

The effective fracture toughness takes into consideration the brittleness/toughness of the materials through the encompassing nonlinearity of the $P - d$-diagram before reaching the peak load. This parameter value has probably slightly increased with the superplasticizer admixture in both cases of the cement dosage, but the variability of the results is quite high – concrete 1/1 had an about 10 % higher value than the concrete 0/1 without the superplasticizer, and the concrete 1/2 had an about 5 % higher value than concrete 0/2.

The initiation fracture-toughness value increased with the superplasticizer admixture in the case of the lower dosage of cement – concrete 1/1 achieved an about 20 % higher value for this parameter than concrete 0/1. On the other hand, this parameter decreased in the case of concrete 1/2 in comparison with concrete 0/2 by about 25 %.

The relative value of the stress-intensity factor for the the initiation of stable crack growth from the initial notch quantifies the initiation brittleness/toughness of the material corresponding to the loss of linearity of the $P - CMOD$-diagram before reaching the peak load. This parameter value did not change with the superplasticizer admixture presence for a lower dosage of cement. On the other hand, this parameter decreased in the case of concrete 1/2 in comparison with concrete 0/2 by about 20 %. Similar results were achieved for the ratio between the force at the beginning of the stable-crack propagation from an initial stress concentrator and the maximum force corresponding to the peak of the $P - CMOD$-diagram.

4 CONCLUSIONS

The authors focused their attention on the mechanical fracture parameters determined via the evaluation of the records of the experiments performed on four sets of concrete specimens with the stress concentrator. The concrete used in each set differed in terms of the dosage of Portland cement and superplasticizer. Increasing the dosage of cement and superplasticizer admixture influences the mechanical fracture properties of the concrete in both positive and negative ways. It follows that it is proper to monitor not only the effect of superplasticizer admixture on the compressive strength values[13,14], but also focus attention on the fracture parameter values. Particularly in the case of a higher dosage of cement the superplasticizer admixture presence had a negative effect on the values of the fracture parameters that quantify the resistance to stable and unstable crack propagation.

Acknowledgement

This research was carried out with the financial support of the Czech Science Foundation, project GA CR 13-18870S and the European Union's "Operational Programme Research and Development for Innovations", No. CZ.1.05/2.1.00/03.0097 as an activity of the regional Centre AdMaS "Advanced Materials, Structures and Technologies".

5 REFERENCES

[1] A. M. Nevile, Properties of Concrete, Pearson Education Limited, Harlow 2011, 846

[2] S. Kumar, S. V. Barai, Concrete Fracture Models and Applications, Springer, Berlin 2011, 406

[3] ČSN EN 12350-2 Testing fresh concrete – Part 2: Slump-test, Czech Standards Institute, 2009. (This standard is the Czech version of the European Standard EN 12350 -2: 2009)

[4] ČSN EN 12350-5 Testing fresh concrete – Part 5: Flow table test, Czech Standards Institute, 2009, (This standard is the Czech version of the European Standard EN 12350 -5: 2009)

[5] ČSN EN 12350-6 Testing fresh concrete – Part 6: Density, Czech Standards Institute, 2009 (This standard is the Czech version of the European Standard EN 12350 -6: 2009)

[6] ČSN EN 12350-6 Testing fresh concrete – Part 7: Air content – Pressure methods, Czech Standards Institute, 2009, (This standard is the Czech version of the European Standard EN 12350-7: 2009)

[7] ČSN EN 12390-3 Testing hardened concrete – Part 3: Compressive strength of test specimens, Czech Standards Institute, 2009, (This standard is the Czech version of the European Standard EN 12390-3: 2009)

[8] B. L. Karihaloo, Fracture Mechanics and Structural Concrete, Longman Scientific & Technical, New York 1995, 346

[9] RILEM TC-50 FMC (Recommendation): Determination of the fracture energy of mortar and concrete by means of three-point bend test on notched beams, Materials & Structures, 18 (**1985**), 285–290

[10] P. Frantík, J. Průša, Z. Keršner, J. Macur, About stability loss during displacement-controlled loading, Proc. of Inter. Conf. on Fibre Concrete 2007, Prague, 2007

[11] S. Xu, H. W. Reinhardt, Z. Wu, Y. Zhao, Otto-Graf-Journal, 14 (**2003**), 131–157

[12] X. Zhang, S. Xu, Engineering Fracture Mechanics, 78 (**2011**), 2115–2138, doi:10.1016/j.engfracmech.2011.03.014

[13] M. Mittal, S. Basu, A. Sofi, International Journal of Civil Engineering, 2 (**2013**) 4, 61–66

[14] S. M. A. El-Gamal, F. M. Al-Nowaiserb, A. O. Al-Baityb, Journal of Advanced Research, 3 (**2012**) 2, 119–124, doi:10.1016/j.jare.2011.05.008

UDK 544.022.51:669.017.13:621.762
Original scientific article/Izvirni znanstveni članek

ISSN 1580-2949
MTAEC9, 49(3)423(2015)

PROPERTIES AND STRUCTURE OF Cu-Ti-Zr-Ni AMORPHOUS POWDERS PREPARED BY MECHANICAL ALLOYING

LASTNOSTI IN STRUKTURA AMORFNIH PRAHOV Cu-Ti-Zr-Ni, PRIPRAVLJENIH Z MEHANSKIM LEGIRANJEM

Aleksandra Guwer, Ryszard Nowosielski, Anna Lebuda

Silesian University of Technology, Faculty of Mechanical Engineering, Institute of Engineering Materials and Biomaterials, Konarskiego Street 18A, 44-100 Gliwice, Poland
aleksandra.guwer@polsl.pl

Prejem rokopisa – received: 2014-07-26; sprejem za objavo – accepted for publication: 2014-09-02

doi:10.17222/mit.2014.119

The method of fabrication, an investigation and a comparison of the structure, size and shape of grains of a quaternary Cu-Ti-Zr-Ni alloy were investigated. Cu-based amorphous alloys have a high strength, ductility, fracture toughness, fatigue strength and excellent corrosion resistance in solutions such as H_2SO_4, NaOH, NaCl and HNO_3. Samples of powders were prepared by mechanical alloying in a high-energy ball mill SPEX 8000. To obtain the amorphous structure of the $Cu_{47}Ti_{34}Zr_{11}Ni_8$ powder, various milling times were used. Finally, four samples for testing were obtained with pure Cu, Ti, Ni, Zr (99.99 %). The structure of the $Cu_{47}Ti_{34}Zr_{11}Ni_8$ powders was examined by X-ray diffraction (XRD) after 7 h, 8 h, 9 h and 10 h of milling time. The chemical composition, particle size and shape of the prepared powders were investigated by scanning electron microscopy (SEM). The microhardness was measured by using a Vickers hardness-testing machine with automatic track measurement. The fully amorphous powders were obtained after 10 h of milling. The prolonged time of milling resulted in an increased particle size and a changed shape of the powders. The highest microhardness was obtained for the amorphous samples.
In further work the studied amorphous powders will be consolidated using spark-plasma sintering, which is an innovative method for the production of amorphous alloys.

Keywords: mechanical alloying, Cu-based amorphous alloys, SEM, XRD, microhardness

Preiskovan je bil način izdelave, preiskava in primerjava strukture, velikosti in oblike zrn kvaternerne zlitine Cu-Ti-Zr-Ni. Amorfne zlitine na osnovi Cu imajo visoko trdnost, duktilnost, lomno žilavost, odpornost proti utrujanju in odlično odpornost proti koroziji v raztopinah H_2SO_4, NaOH, NaCl in HNO_3. Vzorci prahov so bili pripravljeni z mehanskim legiranjem v visokoenergijskem krogličnem mlinu SPEX 8000. Za zagotovitev amorfne strukture prahu $Cu_{47}Ti_{34}Zr_{11}Ni_8$ so bili uporabljeni različni časi mletja. Iz čistega Cu, Ti, Ni, Zr (99,99 %) so bili izdelani štirje preizkušanci. Struktura prahov $Cu_{47}Ti_{34}Zr_{11}Ni_8$ je bila pregledana z rentgensko difrakcijo (XRD) po 7 h, 8 h, 9 h in 10 h mletja. Kemijska sestava, velikost in oblika delcev pripravljenih prahov je bila preiskana z vrstičnim elektronskim mikroskopom (SEM). Mikrotrdota je bila izmerjena z avtomatsko napravo za merjenje trdote po Vickersu. Popolnoma amorfni prahovi so bili dobljeni po 10 h mletja. Pri podaljšanju časa mletja je narasla velikost in spremenila se je oblika delcev prahov. Najvišjo mikrotrdoto so imeli amorfni vzorci.
V nadaljevanju dela bodo preiskovani amorfni prahovi, sintrani z uporabo iskrilnega plazemskega sintranja, ki je inovativna metoda za izdelavo amorfnih zlitin.

Ključne besede: mehansko legiranje, amorfne zlitine na osnovi Cu, SEM, XRD, mikrotrdota

1 INTRODUCTION

Bulk amorphous metallic alloys exhibit many superior properties compared to crystalline alloys. Lately, it has been noted that rods and ribbons of Cu-based alloys demonstrate a high tensile strength, fatigue strength, fracture strength, ductility, relatively low cost of products, a good glass-forming ability and excellent corrosion resistance in solutions such as H_2SO_4, NaOH, NaCl and HNO_3 [1–5].

The most frequently encountered methods for the preparation of amorphous materials are casting methods. An alternative process to prepare amorphous alloys is mechanical alloying combined with the method of spark-plasma sintering. Using this production method Cu-based amorphous alloys were produced by, e.g., Kim et al.[6] and Chu et al.[7]

Mechanical alloying (MA) is defined as a high-energy milling process during which the particles are subjected to multiple cold welding, cracking and re-welding. With rapid cold deformation the specimen's temperature is increased because of the transformation of the mechanical work into heat. The MA process allows the alloying of elements that are difficult or impossible to combine by conventional casting methods. The products of MA are advanced materials, including equilibrium, non-equilibrium (amorphous, quasicrystals, nanocrystalline) and composite materials. The final material properties depend on the MA process parameters (kind of mill, size and amount of grinding media, temperature and atmosphere of milling, ratio of grinding media mass to powder mass, etc.)[8,9].

In this paper we report on the fabrication and an investigation of $Cu_{47}Ti_{34}Zr_{11}Ni_8$ alloy powder prepared by mechanical alloying. The purpose of the present work was to obtain amorphous powders that could be sintered in the future.

2 EXPERIMENTAL

2.1 Materials

Four samples with the composition $Cu_{47}Ti_{34}Zr_{11}Ni_8$ were prepared using elemental powders of copper, titanium, zirconium and nickel (99.99 % purity, < 325 mesh). Each sample was prepared with 8 g of properly weighed powders. The masses and melting points[10] of the individual elements (Cu, Ti, Zr, Ni) are shown in **Table 1**. The powder composition was weighed on an analytical high-precision balance AS/X.

Table 1: Characteristics of used elements (Cu, Ti, Zr, Ni)
Tabela 1: Značilnosti uporabljenih elementov (Cu, Ti, Zr, Ni)

Powder	x/%	m(8 g)/g	T_m/°C
Copper	47	3.9252	1085 [10]
Titanium	34	2.1389	1670 [10]
Zirconium	11	1.3187	1854 [10]
Nickel	8	0.6170	1453 [10]

x/% – amount fraction
x/% – množinski delež

2.2 Research methodology

Four different milling times were applied: (7, 8, 9, 10) h. The process of mechanical alloying was interrupted every 30 min for 30 min to lower the temperature of the crucible and the powders. Cr steel balls of 13 mm diameter were used and the ball-to-powder weight ratio was 5 : 1. The powder mixture and the Cr steel balls were placed in an austenitic crucible in an argon atmosphere inside a glove bag, as shown in **Figure 1**.

Figure 1: Schematic illustration of the cylindrical steel vessel placed in the holder inside the SPEX 8000 mill
Slika 1: Shematski prikaz cilindrične jeklene posode, postavljene v mlin SPEX 8000

A high-energy ball mill SPEX 8000 CertiPrep Mixer/Mill "shaker" type was used, which generated vibrations of the balls and the powder inside the container[11,12].

An X-ray diffractometer X'Pert Pro Panalytical and radiation (λ Co-$K\alpha$) of 0.178897 nm were used to study the structure of the obtained powders. The data of the diffraction lines were recorded using the "step-scanning" method in the 2θ range from 30 ° to 70 ° and with a 0.013 ° step. The time of the step was 40 s and the scanning speed was 0.084 ° s^{-1}.

The particles size and shape of the $Cu_{47}Ti_{34}Zr_{11}Ni_8$ powders were assessed using the microscope SEM SUPRA 25 ZEISS with a magnification up to 500-times

The chemical compositions of the samples were measured with energy-dispersive X-ray spectroscopy (EDS) with an EDS analyzer as part of the SEM. The values of the characteristic radiation energy allow a qualitative analysis in the test sample, and the intensity (peaks height) allows for a quantitative analysis.

The microhardnesses of the particles were measured by the Vickers tester with automatic track measurement using image analysis FUTURETECH FM-ARS 9000. The microhardness measurements were made under a load of 0.97 N. In each of the prepared samples, seven particles were tested.

3 RESULTS AND DISCUSSION

3.1 XRD analysis

Figure 2 demonstrates the XRD patterns of the $Cu_{47}Ti_{34}Zr_{11}Ni_8$ powders after different milling times (7 h, 8 h, 9 h, 10 h). After 7 h of mechanical alloying there is no significant change in the position of the diffraction peaks and the slightly diminished intensity of those peaks is observed. After 8 h and 9 h of processing the broadening and intensity reduction of the crystalline diffraction lines were observed and a maximum broad diffuse diffraction started to form, and after 10 h of milling the samples were amorphous. The diffraction pattern shows a single broad diffraction halo with the 2θ range of 43–54 ° from the amorphous phase without simple peaks (**Figure 2d**).

The same alloy was tested by Shengzhong et al.[13] The team of researchers used different process parameters for a QM-1SP planetary high-energy ball miller and pure elemental powders, i.e., 99.9 %. The process of mechanical alloying was interrupted every hour for 30 min. They obtained an amorphous phase after 8 h, 9 h, 10 h and 12.5 h of milling time.

The amorphous structure of the $Cu_{50}Ti_{50}$ powders was obtained after 8 h of mechanical alloying by using identical parameters to those indicated in this article[14].

3.2 Microstructure

Figure 3 shows the powders after: a) 7 h, b) 8 h, c) 9 h, d) 10 h of milling time. The initial size of the powders

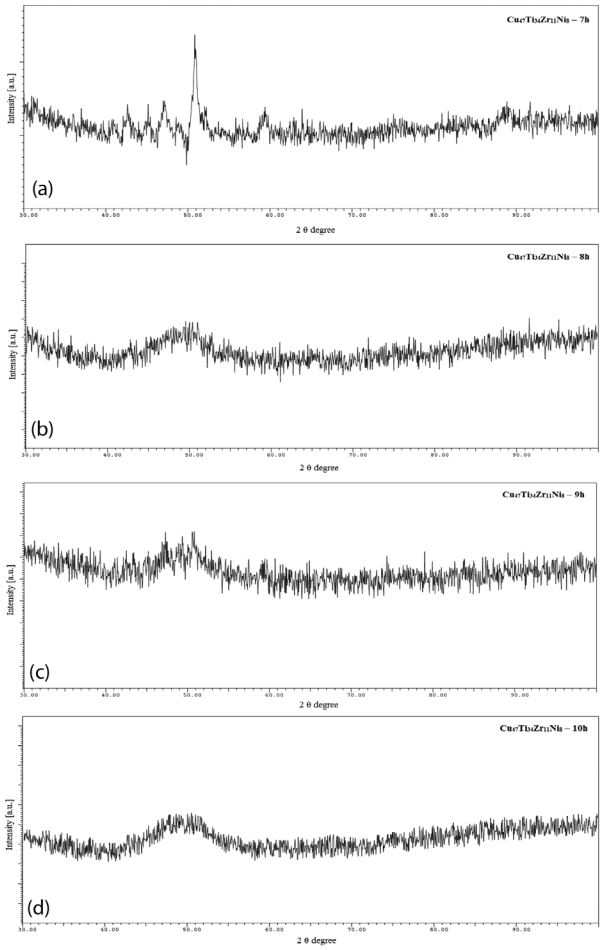

Figure 2: X-ray diffraction pattern of $Cu_{47}Ti_{34}Zr_{11}Ni_8$ powders after: a) 7 h, b) 8 h, c) 9 h, d) 10 h of mechanical alloying

Slika 2: Posnetek rentgenske difrakcije prahov $Cu_{47}Ti_{34}Zr_{11}Ni_8$ po: a) 7 h, b) 8 h, c) 9 h, d) 10 h mehanskega legiranja

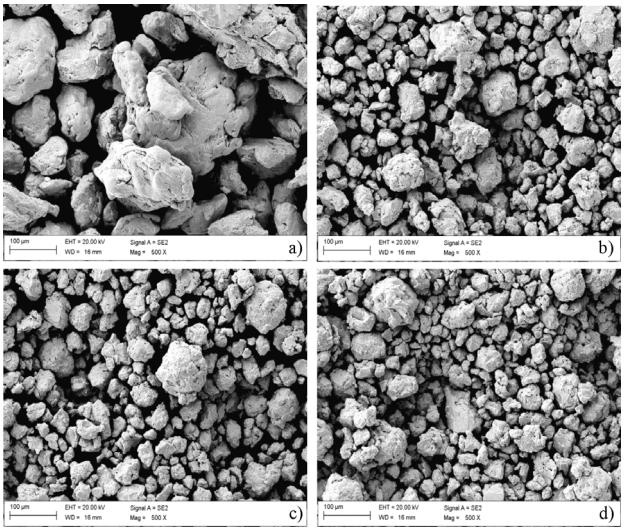

Figure 3: Shape and size of $Cu_{47}Ti_{34}Zr_{11}Ni_8$ powder after: a) 7 h, b) 8 h, c) 9 h, d) 10 h of mechanical alloying, (SEM, magnifications 500-times)

Slika 3: Oblika in velikost prahu $Cu_{47}Ti_{34}Zr_{11}Ni_8$ po: a) 7 h, b) 8 h, c) 9 h, d) 10 h mehanskega legiranja, (SEM, povečava 500-kratna)

was about 44 μm. As a result of the mechanical synthesis the powders changed their size and shape. The largest particles were found after 7 h of milling time (238 μm × 143 μm). During this milling time, the particles were stuck to large agglomerates, then after 8 h of milling time the particles disintegrated, because after 8 h of milling the particles were crushed to a smaller average of 47 μm × 25 μm. By using longer milling times (9 h, 10 h), the particles size was increased and their shape became more homogeneous and spherical. However, their size was below that after 7 h of milling time. The average size of the particles after the milling time is listed in **Table 2**.

Table 2: Average particle size (μm) of the MA powders

Tabela 2: Povprečna velikost delcev (μm) MA-prahov

Time of mechanical alloying (h)	7	8	9	10
Average particle size (μm)	238 × 143	47 × 25	63 × 41	87 × 62

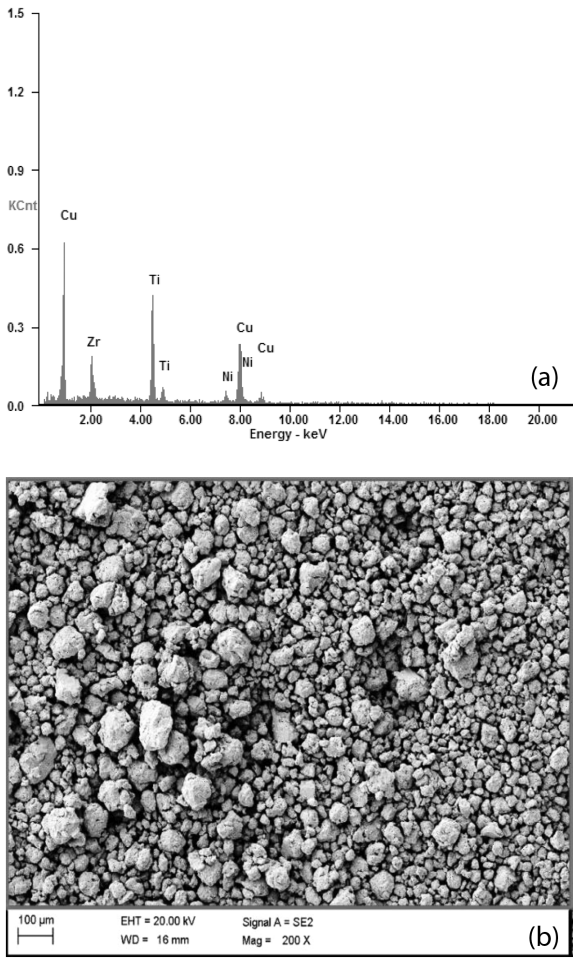

Figure 4: a) EDS spectrum with marked EDS X-ray lines and b) SEM micrographs of $Cu_{47}Ti_{34}Zr_{11}Ni_8$ powders after 10 h of mechanical alloying with 30 min interruption

Slika 4: a) EDS-spekter z označenimi EDS rentgenskimi linijami in b) SEM-posnetek prahov $Cu_{47}Ti_{34}Zr_{11}Ni_8$ po 10 h mehanskega legiranja s prekinitvijo 30 min

Figure 4 depicts the XRD spectrum and the analyzed area of the $Cu_{47}Ti_{34}Zr_{11}Ni_8$ powder after 10 h of milling. Energy-dispersive X-ray analysis (EDS) shows the X-ray lines of copper, titanium, zirconium and nickel elements in the sample. The amount of Cu, Zr, Ni and Ti depends on the time of milling. **Table 3** presents the detailed results of the chemical analysis for every sample. The particles contain the basic components (Ti, Cu, Zr and Ni). The initial atomic percentage of Cu equals 47 %, for Ti it is 34 %, for Zr it is 11 % and for Ni it is 8 %. The results indicate that the obtained powder particles after the alloying process have a very similar atomic composition compared to the initial weighed composition. The chemical composition of the milled powders confirms the existence of the metals identified from the XRD spectra.

Table 3: Chemical composition of the powders surface
Tabela 3: Kemijska analiza površine prahov

Milling Time (h)	Element	*x*/%
0	Cu	47
	Ti	34
	Zr	11
	Ni	8
7	Cu	50.61
	Ti	32.89
	Zr	09.23
	Ni	07.27
8	Cu	49.58
	Ti	33.02
	Zr	9.82
	Ni	7.58
9	Cu	48.73
	Ti	33.43
	Zr	10.02
	Ni	7.82
10	Cu	51.50
	Ti	30.94
	Zr	08.98
	Ni	08.57

3.3 Microhardness

The microhardness was measured on pressed powders with ten indentations for each sample and are shown in **Figure 5**. The deduced average microhardness after milling times (7 h, 8 h, 9 h, 10 h) is shown in **Table 4**. The highest average microhardness was obtained for the powders after 10 h of milling time (553 HV), i.e., for the powders with the fully amorphous structure. The average microhardness increases with the milling time. The difference between the lowest 334 HV, after 7 h of milling, and the highest (518 HV), after 10 h of milling, was 184 HV. This indicates the great heterogeneity of the obtained particles. The average microhardness of the amorphous powder $Cu_{47}Ti_{34}Zr_{11}Ni_8$ (553 HV) is higher than that of the amorphous powders $Cu_{50}Ti_{50}$ (542 HV).[14]

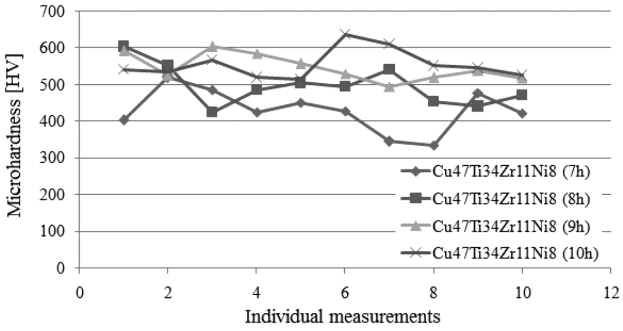

Figure 5: Powders microhardness after different milling times
Slika 5: Mikrotrdote prahov po različnih časih mletja

4 CONCLUSIONS

The result of the tests and the examination of the $Cu_{47}Ti_{34}Zr_{11}Ni_8$ powders lead to the following conclusions:

- It is possible to obtain an amorphous structure for a four-component alloy $Cu_{47}Ti_{34}Zr_{11}Ni_8$ by using mechanical synthesis in a SPEX 8000 mill.
- An amorphous structure was obtained for the 10 h milling-time sample.
- The largest particles are obtained after 7 h milling and the smallest after 8 h milling. The largest shape and the best size regularity were obtained for the amorphous powders.
- The presence of the initial elements Cu, Ti, Zr, Ni in the milled particles was confirmed. The content of elements in the milled powders corresponds to the initial weighed composition.
- The average microhardness value increases with the milling time and the highest hardness is achieved in the amorphous sample (553 HV).

Acknowledgments

The work was partially supported by the National Science Centre under research Project No.: 2012/07/N/ST8/03437.

Table 4: Average microhardness after different mechanical-alloying times
Tabela 4: Spreminjanje povprečne mikrotrdote pri različnem trajanju mehanskega legiranja

Samples	$Cu_{47}Ti_{34}Zr_{11}Ni_8$ (7 h)	$Cu_{47}Ti_{34}Zr_{11}Ni_8$ (8 h)	$Cu_{47}Ti_{34}Zr_{11}Ni_8$ (9 h)	$Cu_{47}Ti_{34}Zr_{11}Ni_8$ (10 h)
The average microhardness (HV)	428	496	545	553

5 REFERENCES

[1] P. Lee, C. Yao, J. Chen, L. Wang. R. Jeng, Y. Lin, Preparation and thermal stability of mechanically alloyed Cu–Zr–Ti–Y amorphous powders, Materials Science and Engineering A, 375–377 (**2004**), 829–833, doi:10.1016/j.msea.2003.10.107

[2] C. Suryanarayana, A. Inoue, Bulk Metallic Glasses, CRC Press, Boca Raton, London, New York 2011, 313–322

[3] H. Kim, K. Sumiyama, K. Suzuki, Formation and thermal stability of nanocrystalline Cu-Ti-Ni prepared by mechanical alloying, Journal of Alloys and Compounds, 239 (**1996**), 88–93, doi:10.1016/0925-8388(96)02274-8

[4] C. Hu, H. Wu, Formation of Cu–Zr–Ti amorphous powders with Band Si additions by mechanical alloying technique, Journal of Alloys and Compounds, 434–435 (**2007**), 390–393, doi:10.1016/j.jallcom.2006.08.219

[5] A. Inoue, B. Shen, A. Takeuchi, Fabrication, properties and applications of bulk glassy alloys in late transition metal-based systems, Materials Science and Engineering A, 441 (**2006**), 18–25, doi:10.1016/j.msea.2006.02.416

[6] C. K. Kim, H. S. Lee, S. Y. Shin, J. C. Lee, D. H. Kim, S. Lee, Microstructure and mechanical properties of Cu – based bulk amorphous alloy billets fabricated by spark plasma sintering, Materials Science and Engineering A, 406 (**2005**), 293–299, doi:10.1016/j.msea.2005.06.043

[7] Z. H. Chu, H. Kato, G. Q. Xie, G. Y. Yuan, W. J. Ding, A. Inoue, Consolidation and mechanical properties of $Cu_{46}Zr_{42}Al_7Y_5$ metallic glass by spark plasma sintering, Journal of Non-Crystalline Solids, 358 (**2012**), 1263–1267, doi:10.1016/j.jnoncrysol.2012.02.027

[8] C. Suryanarayana, Recent developments in mechanical alloying, Reviews on Advanced Materials Science, 18 (**2008**), 203–211

[9] M. Adamiak, Mechanical alloying for fabrication of aluminium matrix composite powders with Ti-Al intermetallics reinforcement, Journal of Achievements in Materials and Manufacturing Engineering, 31 (**2008**), 191–196

[10] The Engineering ToolBox /cited 2014-07-10/. Available from World Wide Web: http://www.engineeringtoolbox.com/melting-temperature-metals-d_860.html

[11] R. Nowosielski, R. Babilas, G. Dercz, L. Pajak, J. Wrona, Structure and properties of barium ferrite powders prepared by milling and annealing, Journal of Achievements in Materials and Manufacturing Engineering, 22 (**2007**), 45–48

[12] R. Nowosielski, R. Babilas, G. Dercz, L. Pająk, Microstructure of composite material with powders of barium ferrite, Journal of Achievements in Materials and Manufacturing Engineering, 17 (**2006**), 117–120

[13] K. Shengzhong, F. Liu, D. Yutian, X. Guangji, Synthesis and magnetic properties of Cu-based amorphous alloys made by mechanical alloying, Intermetallics, 12 (**2004**), 1115–1118, doi:10.1016/j.intermet.2004.04.007

[14] A. Guwer, R. Nowosielski, A. Borowski, R. Babilas, Fabrication of copper-titanium powders prepared by mechanical alloying, Indian Journal of Engineering & Materials Sciences, 21 (**2014**), 265–271

UDK 621.793:539.92:539.375.6
Original scientific article/Izvirni znanstveni članek

ISSN 1580-2949
MTAEC9, 49(3)429(2015)

INTERACTION OF Cr_2N AND Cr_2N/Ag THIN FILMS WITH CuZn-BRASS COUNTERPART DURING BALL-ON-DISC TESTING

INTERAKCIJA Cr_2N IN Cr_2N/Ag TANKIH PLASTI V PARU S CuZn-MEDENINO MED PREIZKUSOM KROGLA NA DISK

Pavel Bílek, Peter Jurči, Petra Dulová, Mária Hudáková, Jana Ptačinová, Matej Pašák

Institute of Materials Science, Faculty of Materials Science and Technology in Trnava, Slovak University of Technology in Bratislava, Paulínská 16, 917 24 Trnava, Slovak Republic
pavel-bilek@email.cz

Prejem rokopisa – received: 2014-07-28; sprejem za objavo – accepted for publication: 2014-09-04

doi:10.17222/mit.2014.121

Cr_2N- and Cr_2N/Ag-nanocomposite thin films were deposited on a substrate made of Cr-V ledeburitic tool steel Vanadis 6 by reactive magnetron sputtering, at a deposition temperature of 500 °C, using pure Cr and Ag targets, in a composite, low-pressure N_2/Ar atmosphere. The additions of silver to the Cr_2N/Ag coatings were w = (3, 7, 11 and 15) %. Tribological testing using a ball-on-disc apparatus was realized at ambient temperature and, for the Cr_2N with the additions of mass fractions of Ag 7 % and 11 %, at the elevated temperatures of (300, 400 and 500) °C, respectively. Balls made of binary CuZn-brass (55 % Cu, 45 % Zn) were used as the counterparts. The wear tracks after the ball-on-disc testing and the worn balls were analyzed with scanning electron microscopy (SEM) and a microanalysis (EDX), and the wear rates were calculated. The adhesive wear was derived from a quantitative-point metallographic analysis. The obtained results infer that a considerable material transfer from the counterpart onto the surface of the coatings takes place during dry sliding. The material transfer (and the adhesive wear of the counterpart) is mainly due to the low shear strength of the brass used. Two main trends were observed. The first one shows that the adhesive material transfer decreases with the increasing silver content when tested at ambient temperature. The second trend indicates that the use of a higher testing temperature leads to a higher adhesive wear of the counterpart.

Keywords: Cr_2N/Ag-nanocomposite PVD coatings, ball-on-disc, adhesion, friction coefficient, wear rate

Cr_2N- in Cr_2N/Ag-nanokompozitne tanke plasti so bile nanesene na podlago iz Cr-V ledeburitnega orodnega jekla Vanadis 6 z reaktivnim nanašanjem z magnetronom pri temperaturi nanašanja 500 °C z uporabo tarč iz čistega Cr in Ag v kompozit v nizkotlačni atmosferi N_2/Ar. Dodatki srebra v nanose Cr_2N/Ag so bili w = (3, 7, 11 in 15) %. Tribološki preizkusi z uporabo naprave krogla na disk so bili izvršeni pri sobni temperaturi in pri Cr_2N tudi z masnim deležem dodatka 7 % in 11 % Ag pri povišanih temperaturah (300, 400 in 500) °C. Krogle, izdelane iz binarne CuZn-medenine (55 % Cu, 45 % Zn), so bile izbrane kot par. Sledovi obrabe po preizkusu krogla na disk in obrabljene krogle so bili analizirani z vrstično elektronsko mikroskopijo (SEM) in mikroanalizo (EDX), izračunane pa so bile tudi hitrosti obrabe. Adhezivna obraba je bila prikazana s kvantitativno točkasto metalografsko analizo. Dobljeni rezultati kažejo, da se med suhim drsenjem pojavi občuten prenos materiala iz krogle na površino nanosa. Prenos materiala (in adhezijska obraba krogle) je nastal večinoma zaradi majhne strižne trdnosti medenine. Opaženi sta bili dve glavni usmeritvi. Prva je bila, da se pri preizkušanju pri sobni temperaturi adhezivni prenos materiala zmanjšuje z naraščajočo vsebnostjo srebra. Druga pa, da uporaba višje temperature pri preizkusu povzroči večjo adhezivno obrabo krogle.

Ključne besede: Cr_2N/Ag-nanokompozitni PVD-nanosi, krogla na disk, adhezija, koeficient trenja, hitrost obrabe

1 INTRODUCTION

Hard ceramic coatings like CrN and TiN have been used for the last three decades due to their high hardness and chemical stability, high oxidation resistance and low wear rate[1,2]. They have gained great scientific interest and industrial popularity due to these properties in copper machining[3], alumina die casting and forming, and wood processing[4]. However, the friction coefficient of most transition-metal nitride coatings is fairly high (0.6–0.8) and the tribological effectiveness, especially at elevated temperatures, is insufficient[5,6]. Therefore, a lot of effort has been made in recent years to decrease the friction coefficient at room as well as elevated temperatures. Multi-functional coatings combining soft lubricating phases within a hard wear-resistance matrix offer good properties[7,8]. These coatings generally include one or more nanocrystalline phases in a functional matrix to provide improved mechanical and tribological properties and/or corrosion resistance. Some coatings are designed to be adaptive, that is, their properties follow the changes in the operating conditions. An example of an adaptive coating is a hard wear-resistance matrix with an incorporation of soft metals like Cu, Ag or Au. This method can improve the lubricating in specific tribological conditions[9]. Chromium nitrides combined with noble metals are relatively easy to co-deposit by reactive magnetron sputtering and they form nanocomposite structures due to a lack of miscibility between the matrix and the lubricant[10,11].

Silver is most commonly used as an addition to the TM-nitride thin films. It exhibits a stable chemical behaviour over a wide temperature range as well as in a variety of aggressive environments. Ag is capable to mi-

grate to a free surface to form Ag particles providing lubrication above 300 °C and, thereby, distinctively reducing the friction coefficient[12].

Our recent investigations of the magnetron-sputtered Cr_2N-films with w = (3, 7, 11 and 15) % of silver amounts, deposited on the Cr-V ledeburitic steel Vanadis 6, can be summarized as follows[13–17]: the incorporation of silver in the Cr_2N matrix led to an improvement in the tribological properties at elevated temperatures, especially at 400 °C and 500 °C. Nevertheless, the addition of 15 % of Ag made the film too soft and sensitive to the wear, which resulted in a worsening of the tribological performance. On the other hand, the films with w = (7 and 11) % of Ag additions seem to be very promising.

In this paper, the tribological performance against a CuZn-brass counterpart of the nanocomposite coatings consisting of a hard Cr_2N matrix co-deposited with different Ag additions is investigated. The films were deposited onto the Cr-V ledeburitic steel Vanadis 6 using the magnetron-sputter technique.

2 EXPERIMENTAL WORK

The substrate material was the PM ledeburitic tool steel Vanadis 6 with mass fractions 2.1 % C, 1.0 % Si, 0.4 % Mn, 6.8 % Cr, 1.5 % Mo, 5.4 % V and Fe as the balance element.

The samples used for the investigation and the conditions for depositing Cr_2N- and Cr_2N/Ag- coatings were reported elsewhere[11]. In the case of the Cr_2N coatings, during the deposition, the power was 2.9 kW per cathode (both Cr). For the production of the Ag-containing coatings, the power of the Cr cathode was kept at 5.8 kW, while the power of the Ag cathode was varied (0.10, 0.21, 0.34 and 0.45) kW in order to prepare the films with different Ag concentrations (3, 7, 11 and 15) %.

The tribological properties of the coatings were measured using a CSM ball-on-disc tribometer at room temperature and, for the coatings with 7 % and 11 % of Ag, also at the elevated temperatures up to 500 °C. The balls of 6 mm in diameter, made from CuZn-brass (55 % Cu, 45 % Zn), were used for the tests. No external lubricant was added during the measurements. The normal load used for the investigation was 1 N and the total sliding distance for each measurement was 100 m. The volume losses V of the worn balls were calculated on the basis of the sketch shown on **Figure 1** using the following formula:

$$V = ((\pi \cdot h) \cdot (3\rho^2+h^2))/6 \quad (1)$$

where R is the ball radius, h and ρ are the height and the radius of the worn spherical segment of the ball. Relating the volume loss to the normal load and sliding distance, the wear rates W were calculated.

After the testing, the wear tracks and the worn balls were examined with a scanning electron microscope (SEM) JEOL JSM-7600F and an energy dispersive X-ray analysis (EDX).

The adhesive wear was derived from the quantitative-point metallographic analysis carried out on the SEM micrographs of the tracks after the ball-on-disc testing.

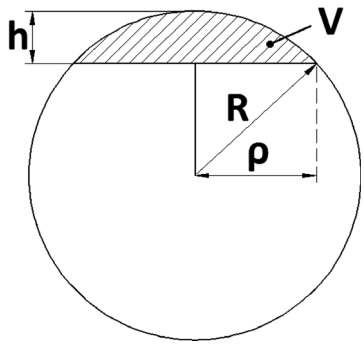

Figure 1: Sketch of a worn ball for the volume-loss calculation
Slika 1: Skica prikaza obrabe krogle za računanje volumenske izgube

3 RESULTS AND DISCUSSIONS

Figure 2 shows a detail of the track after the ball-on-disc test of the Cr_2N/11Ag coating tested at room temperature against the CuZn-brass counterpart. The surface of the coating did not show any indications of damage. On the other hand, thanks to the corresponding EDX maps, a considerable material transfer from the counterpart to the surface of the coating was detected; it was mainly due to the low shear strength of the brass used.

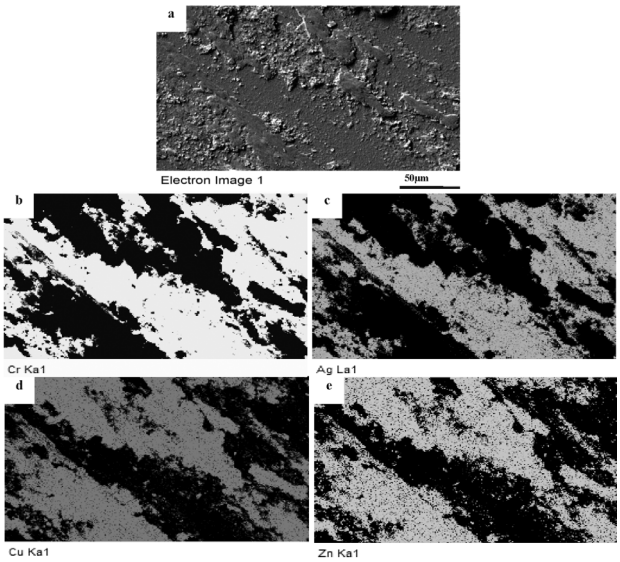

Figure 2: Transferred material of the CuZn-brass counterpart to the surface of the Cr_2N/11Ag coating after the ball-on-disc test at room temperature: a) overview, b) EDX of chromium, c) EDX of silver, d) EDX of copper, e) EDX of zinc

Slika 2: Prenesen material CuZn-medenine iz krogle na površino Cr_2N/11Ag-nanosa po preizkusu krogla na disk; preizkušeno pri sobni temperaturi: a) videz, b) EDX-kroma, c) EDX-srebra, d) EDX-bakra, e) EDX cinka

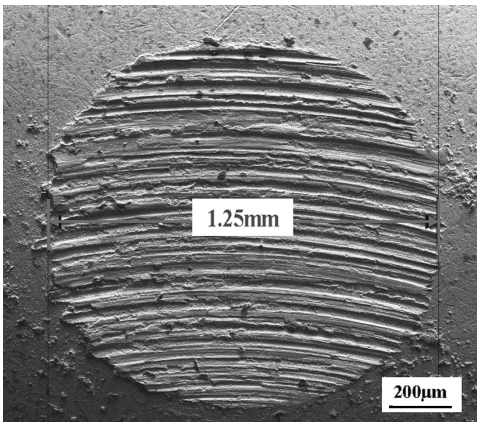

Figure 3: Worn CuZn-brass ball after the ball-on-disc test of the Cr_2N/11Ag coating at room temperature

Slika 3: Obrabljena krogla iz CuZn-medenine po preizkusu krogla na disku na Cr_2N/11Ag-nanosu, preizkušano pri sobni temperaturi

Figure 3 depicts the worn CuZn-brass ball after the ball-on-disc test of the Cr_2N/11Ag coating at room temperature. The parallel grooves oriented along the sliding direction are well visible and the diameter of the worn spherical segment is easily measurable. The surfaces of the worn balls were investigated with an EDX analysis to confirm the presence of silver. However, no signal of silver was obtained and one could assume that the silver content on the surface was too low to be detected with the EDX analysis.

The mean value of the friction coefficient examined at room temperature decreased with the increasing silver content in the Cr_2N matrix until 7 % (**Figure 4**). However, the influence of a higher silver content was not as positive for the friction coefficient as for the coating with 7 % Ag. The wear rates of the balls decreased by about 50 % for the coatings with the silver addition in comparison with the pure Cr_2N, and in the case of the coating with 15 % of Ag the decrease was about 75 % (**Figure 4**). These results were expected since silver can act as a solid lubricant, facilitating the sliding of the balls[12]. In our previous works[11,17] silver particles were well visible on the surface of the coatings after the deposition. On the other hand, the experiments carried out at the elevated temperature showed the opposite tendency. An increase in the testing temperature led to a slight increase in the mean value of the friction coefficient (**Figure 5**). As reported in the previous works[16,17], a decrease in the friction coefficient was observed with the increasing testing temperature, but there an alumina counterpart was used. In the case of the CuZn-brass counterpart the mechanism of the wear was different and a softening of the CuZn-brass alloy also took place at high temperatures.

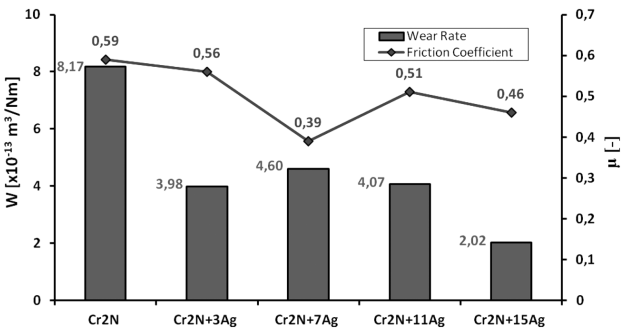

Figure 4: Wear rates W and friction coefficient μ of Cr_2N and Cr_2N/Ag coatings tested at room temperature

Slika 4: Hitrost obrabe W in koeficient trenja μ pri Cr_2N- in Cr_2N/Ag-prevlekah, preizkušanih pri sobni temperaturi

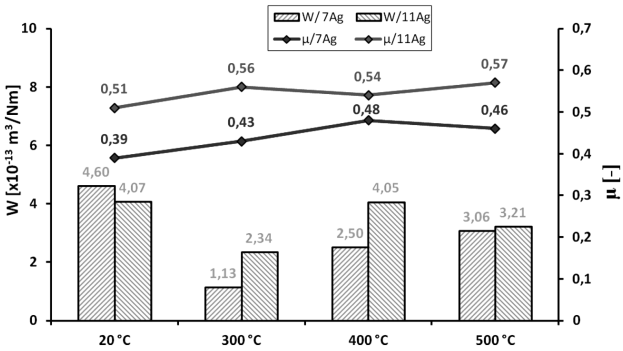

Figure 5: Wear rates W and friction coefficient μ of Cr_2N + 7Ag* and Cr_2N + 11Ag coatings tested at room and elevated temperatures, *previous result[16]

Slika 5: Hitrost obrabe W in koeficient trenja μ pri Cr_2N + 7Ag* in Cr_2N + 11Ag-nanosih, preizkušanih pri sobni in povišanih temperaturah, *predhodni rezultati[16]

Nevertheless, the wear rates of the CuZn-brass balls during the tribological testing of the coatings with mass fractions 7 % and 11 % of Ag at elevated temperatures were lower in comparison with the measurement at room temperature (**Figure 5**). The minimum values for both coatings were found at the temperature of 300 °C.

Figure 6 depicts the dependence of the friction coefficient on the sliding distance for the Cr_2N + 11Ag coating tested at ambient and elevated temperatures. All the measurements show a considerable instability. The friction coefficient is oscillating around the mean value in the range of 0.2. This can be explained with the cre-

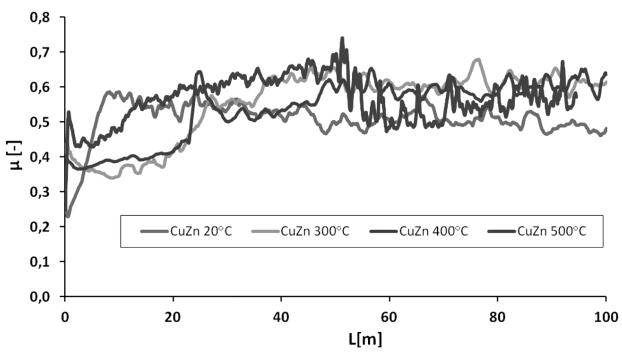

Figure 6: Dependence of friction coefficient μ on sliding distance L of the Cr_2N + 11Ag coating tested at different temperatures against the CuZn-brass counterpart

Slika 6: Odvisnost koeficienta trenja μ od dolžine drsenja L pri Cr_2N + 11Ag-nanosu, preizkušanem pri različnih temperaturah, v paru z CuZn-medeninasto kroglo

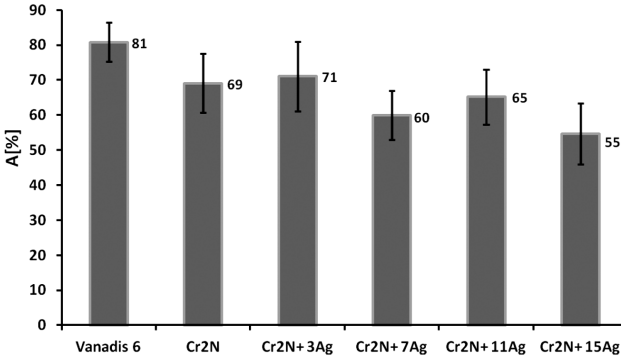

Figure 7: Area *A* of adhesion interactions between CuZn-brass and uncoated steel Vanadis 6, Cr_2N and Cr_2N/Ag coatings during ball-on-disc testing, at room temperature

Slika 7: Področje *A* adhezijske interakcije med CuZn-medenino in neprekritim jeklom Vanadis 6 ter Cr_2N- in Cr_2N/Ag-nanosi med preizkusom krogla na disk pri sobni temperaturi

ation of adhesion joins between the surface of the coating and the ball during the sliding and their subsequent release, accompanied with the oscillating of the friction coefficient.

A quantitative-point metallographic analysis was used to describe the adhesion interaction during the ball-on-disc testing. **Figure 7** shows the results of the testing at room temperature for the uncoated steel Vanadis 6, the pure Cr_2N and Cr_2N/Ag coatings. The highest adhesion wear was found for the uncoated substrate, where the area of adhesion interaction was A = (81 ± 5) %. For the coated substrate it is clearly evident that the adhesion wear decreases with the increasing silver content; the minimum A = (55 ± 8) % was found for the Cr_2N coating with the highest silver addition of 15 %. One can assume that the incorporation of silver into the Cr_2N matrix improves the wear of the CuZn-brass ball front view and also the area of adhesion interaction at room temperature.

On the other hand, the material transfer is more remarkable in the conditions of higher testing temperatures (**Figure 8**). Both coatings, Cr_2N with mass fractions of Ag w = (7 and 11) %, showed the same tendency, although the coating with 11 % of Ag exhibited a slower increase in the adhesion wear with the increasing testing temperature than the coating with 7 % of Ag. Most likely, the higher adhesion interaction at higher temperatures is caused by the softening of the CuZn-brass material, when the atoms of the ball material easily create the adhesion joins.

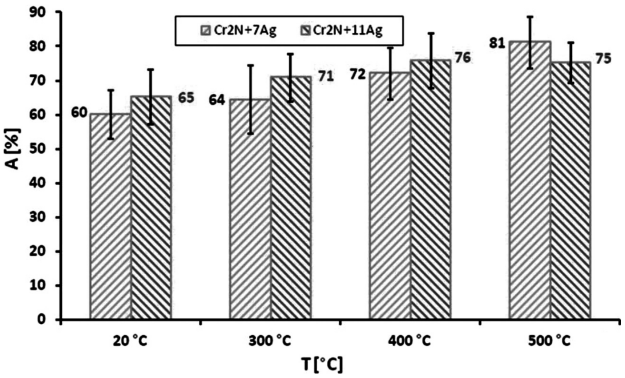

Figure 8: Area *A* of adhesion interactions between CuZn-brass and Cr_2N coatings with mass fractions of Ag 7 % and 11 % during the ball-on-disc testing at different temperatures

Slika 8: Področje *A* adhezijske interakcije med CuZn-medenino in Cr_2N-nanosi z masnim deležem Ag 7 % in 11 % med preizkusi krogla na disk pri različnih temperaturah

4 CONCLUSIONS

The friction and wear characteristics of the Cr_2N and Cr_2N/Ag coatings prepared with the magnetron-sputter-deposition method were investigated at room temperature and elevated temperatures during a ball-on-disc testing against a CuZn-brass counterpart. The results can be summarized as follows:

- During the tribological testing, a considerable material transfer from the CuZn-brass counterpart to the surfaces of all the tested coatings was observed.
- For the Cr_2N/Ag coatings, a lower friction coefficient and also lower wear rates of the balls were found during the testing at room temperature in comparison with the pure Cr_2N. This phenomenon is attributed to the silver incorporated into the Cr_2N matrix.
- Higher testing temperatures led to a slight increase in the friction coefficient. On the other hand, the wear rates of the balls were further decreasing, with the minimum values at 300 °C.
- During the testing at room temperature, the highest material transfer was found for the uncoated steel Vanadis 6. The adhesion wear was lower when the Cr_2N coating was tested. The decrease is more remarkable with the increasing silver content incorporated into the Cr_2N matrix.
- Higher testing temperatures led to increased adhesion interaction of both Cr_2N coatings, with mass fractions of Ag 7 % and 11 %.

Acknowledgements

This publication is the result of implementing the project: CE for development and application of advanced diagnostic methods in processing of metallic and non-metallic materials, ITMS: 26220120048, supported by the Research & Development Operational Programme funded by the ERDF. This research was supported by grant project VEGA 1/1035/12.

5 REFERENCES

[1] S. K. Pradhan, C. Nouveau, A. Vasin, M. A. Djouadi, Surface and Coatings Technology, 200 (**2005**), 141–145, doi:10.1016/j.surfcoat.2005.02.038

[2] P. Panjan, B. Navinšek, A. Cvelbar, A. Zalar, I. Milošev, Thin Solid Films, 281–282 (**1996**), 298-301, doi:10.1016/0040-6090(96)08663-4

[3] A. Kondo, T. Oogami, K. Sato, Y. Tanaka, Surface and Coatings Technology, 177–178 (**2004**), 238–244, doi:10.1016/j.surfcoat.2003.09.039

[4] R. Gahlin, M. Bronmark, P. Hedenqvist, S. Hogmark, G. Hakansson, Surface and Coatings Technology, 76–77 (**1995**), 174–180, doi:10.1016/0257-8972(95)02597-9

[5] T. Polcar, T. Kubart, R. Novak, L. Kopecky, P. Siroky, Surface and Coatings Technology, 193 (**2005**), 192–199, doi:10.1016/j.surfcoat.2004.07.098

[6] M. Brizuela, A. Garcia-Luis, I. Braceras, J. I. Onate, J. C. Sanchez-Lopez, D. Martinez-Martinez, C. Lopez-Cartes, A. Fernandez, Surface and Coatings Technology, 200 (**2005**), 192–197, doi:10.1016/j.surfcoat.2005.02.105

[7] S. M. Aouadi, B. Luster, P. Kohli, C. Muratore, A. A. Voevodin, Surface and Coatings Technology, 204 (**2009**), 962–968, doi:10.1016/j.surfcoat.2009.04.010

[8] C. Muratore, J. J. Hu, A. A. Voevodin, Thin Solid Films, 515 (**2007**), 3638–3643, doi:10.1016/j.tsf.2006.09.051

[9] H. C. Barshilia, M. S. Prakash, A. Jain, K. S. Rajam, Vacuum, 77 (**2005**), 169–179, doi:10.1016/j.vacuum.2004.08.020

[10] C. P. Mulligan, T. A. Blanchet, D. Gall, Wear, 269 (**2010**), 125–131, doi:10.1016/j.wear.2010.03.015

[11] P. Bílek, P. Jurči, M. Hudáková, M. Pašák, M. Kusý, J. Bohovičová, Applied Surface Science, 307 (**2014**), 13–19, doi:10.1016/j.apsusc.2014.03.044

[12] C. P. Mulligan, P. A. Papi, D. Gall, Thin Solid Films, 520 (**2012**), 6774–6779, doi:10.1016/j.tsf.2012.06.082

[13] P. Jurči, J. Bohovičová, M. Hudáková, P. Bílek, Mater. Tehnol., 48 (**2014**) 2, 159–170

[14] P. Jurči, I. Dlouhý, Applied Surface Science, 257 (**2011**), 10581–10589, doi:10.1016/j.apsusc.2011.07.054

[15] P. Jurči, S. Krum, Materials Engineering, 19 (**2012**), 64–70

[16] P. Bílek, P. Jurči, M. Hudáková, L. Čaplovič, M. Novák, Mater. Tehnol., 48 (**2014**) 5, 669-673

[17] P. Bílek, P. Jurči, M. Hudáková, L. Čaplovič, M. Novák, Wear, (**2015**), doi:10.1016/j.wear.2015.03.019

UDK 543.428.2:544.171.7
Original scientific article/Izvirni znanstveni članek

ISSN 1580-2949
MTAEC9, 49(3)435(2015)

USING SIMULATED SPECTRA TO TEST THE EFFICIENCY OF SPECTRAL PROCESSING SOFTWARE IN REDUCING THE NOISE IN AUGER ELECTRON SPECTRA

UPORABA SIMULIRANEGA SPEKTRA ZA PREIZKUS UČINKOVITOSTI PROGRAMSKE OPREME PREDELAVE SPEKTRA PRI ZMANJŠANJU ŠUMA SPEKTRA AUGERJEVIH ELEKTRONOV

Besnik Poniku[1,2], Igor Belič[1], Monika Jenko[1]

[1]Institute of Metals and Technology, Lepi pot 11, 1000 Ljubljana, Slovenia
[2]Jožef Stefan International Postgraduate School, Jamova 39, 1000 Ljubljana, Slovenia
besnik.poniku@imt.si

Prejem rokopisa – received: 2015-01-04; sprejem za objavo – accepted for publication: 2015-01-21

doi:10.17222/mit.2015.013

When attempting to automate Auger spectra analyses it becomes necessary to have a deeper knowledge of the constituent elements of the spectra. In order to obtain a reliable analysis, the unavoidable spectral noise must be reduced, thus giving a clearer view to the spectral peaks and the spectral background. Therefore, the necessary step is to analyze the spectral noise and to find a way to evaluate the noise-reduction algorithms. A method in which simulated Auger electron spectra are used for testing the efficiency of noise-reduction routines has been proposed. The performance of noise-reduction procedures on measured spectra cannot be evaluated since the intrinsic noiseless spectra is never available for reference; therefore, the spectra were simulated and the noise-reduction routines were used on the simulated spectra. After the processing, the simulated noiseless spectrum is subtracted from the complete spectrum, leaving the remaining noise for further analysis and a comparison with the exactly known simulated noise. For each spectrum data point the noise ratios are calculated by dividing the remaining noise levels by the initial noise. When plotting the noise ratios for each respective processing route, it was found that most of the noise ratios lie in the interval –1 to +1, indicating an improvement in regard to the initial noise. Such a plot of the noise ratios offers a convenient way for assessing the efficiency of the noise-reduction routine at a glance.

Keywords: Auger electron spectroscopy, spectra simulator, spectral noise, noise reduction

Avtomatizacija postopka analize Augerjevih spektrov zahteva dobro poznanje posameznih sestavnih elementov spektra. Zanesljivost avtomatske analize je v prvi vrsti odvisna od tega, v kolikšni meri nam uspe zmanjšati spektru primešan šum, ki sicer zamegli tako spektralne vrhove kot tudi spektralno ozadje. Zato moramo najprej analizirati lastnosti šuma, primešanega spektrom, in poiskati načine za ovrednotenje delovanja orodij, ki šum zmanjšujejo. V članku predlagamo uporabo simulatorja Augerjevih spektrov, ker sicer pri izmerjenih spektrih nikoli ne poznamo oblike primešanega šuma in torej nimamo osnove za dobro ovrednotenje delovanja uporabljenih orodij. Po uporabi orodja za zmanjševanje šuma, ki deluje na simuliranem spektru, odstranimo natančno poznano spektralno ozadje in spektralne vrhove. Tako dobimo preostali šum, ki ga primerjamo z znanim začetnim šumom. V vsaki točki spektra so izračunana razmerja med začetnim in končnim šumom. Razmerja so nato prikazana v grafu in v veliki večini spektralnih točk ležijo v intervalu –1, 1. Tako dobimo vizualno predstavitev delovanja orodij za zmanjševanje šuma, ki omogoča hitro oceno učinkovitosti preizkušanega orodja.

Ključne besede: Augerjeva elektronska spektroskopija, simulator spektra, spektralni šum, zmanjševanje šuma

1 INTRODUCTION

Auger electron spectroscopy is a technique often used for the elemental characterization of the surface of conductive samples.[1–8] Apart from a high surface sensitivity,[9] due to the fact that the primary electron beam can be focused down to approximately 10 nm in diameter,[10] analyses with very good spatial resolution can also be performed. This fact makes it possible to analyze features on a nanometer scale on the surface through this technique.

To interpret the measured spectra the measured data have to be manipulated by software for signal processing. This manipulation inevitably leaves its mark on the results obtained.[11]

Smoothing is one of the methods that are used for the purpose of reducing the noise in Auger electron spectra.[12] Very little can be said about the efficiency of such procedures in reducing the noise when applying them in measured spectra, because noise in both the input and the output spectra is at unknown levels. The aim of this work is to show a simple way in which the performance of the noise-reduction techniques can be assessed using simulated spectra. Using simulated spectra to assess the efficiency of noise-reduction routines is very appropriate. This comes about due to the fact that the values for the different components of the simulated AE spectra (including the noise) are known before processing, and thus any change due to the processing route may be found and then compared to the initial preprocessed values.

2 EXPERIMENT

The construction of the simulator for gathering the simulated spectra used for this assessment is described in detail in[11]. For the construction of this simulator a number of measured AE spectra obtained from spring-steel samples were closely inspected. The neural network was used to model the primary background by selecting a number of representative points for the background and including them in the training data set for the neural network. After carefully observing the behavior of the background in the measured spectra an equation was derived, which then would be used for generating various primary backgrounds that would resemble those observed in the measured spectra. After removing the primary background defined in this way the peak base and the peaks remained. The peak base was also modeled in the same way using the neural network, and the removal of the defined peak base left only the characteristic peaks. The peak base and the peaks of various elements were saved in the database. Combining the generated primary backgrounds, on the one hand, and the peak base and characteristic peaks from the database, on the other, produced the simulated spectrum. The generated noise that was then added to such a spectrum was also made to resemble the noise observed in measured spectra. It is important to note that while the components of the simulated spectra such as the background and noise are made to resemble those of the measured spectra, their exact values are simulated and therefore known and stored in the computer (**Figure 1**).

Through the modeling of the background, which was performed using the neural network, we have found that the AE spectra consist of three main components: the primary background, the peak base, and the peaks (**Figure 2**).

From the set of standard AE spectra that were obtained using COMPRO10, a freely available online spectral database, the peak base and the peaks of elements such as Al, C, Co, Cu, Fe, Au, Ni, O, Si, Ag, Ti, and V

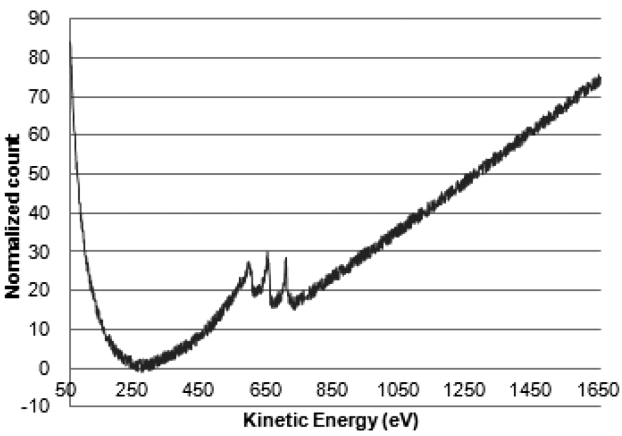

Figure 1: Simulated Auger electron spectrum
Slika 1: Simuliran spekter Augerjeve elektronske spektroskopije

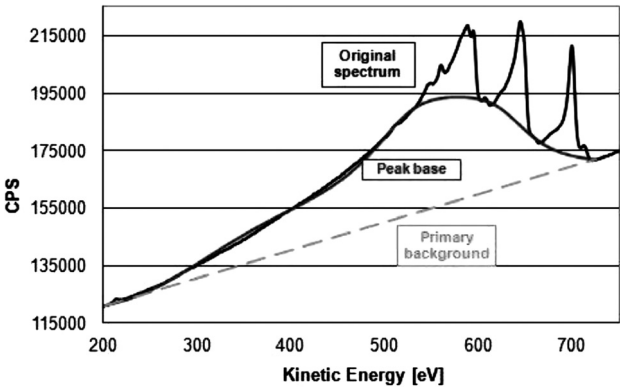

Figure 2: The AE spectra constituent elements: the primary background, the peaks base, and the peaks
Slika 2: Sestavni elementi AE-spektra: primarno ozadje, podlaga spektralnih vrhov in spektralni vrhovi

were extracted (as shown in **Figure 3** for the case of iron) and were stored separately.

The AE spectra simulator combines the extracted peak base and the peaks from various standard elements, and it combines them with the randomly defined primary background (**Figure 4**) to form the complete simulated spectrum without the noise.

At the end of the simulation process the random noise is added and also stored separately for further use. We have ensured that the properties of the simulated noise resemble the properties of the noise in the measured AE spectra.

Other AE spectra simulators can be used for this purpose as well. One such simulator is SESSA (Simulation of Electron Spectra for Surface Analysis). SESSA is

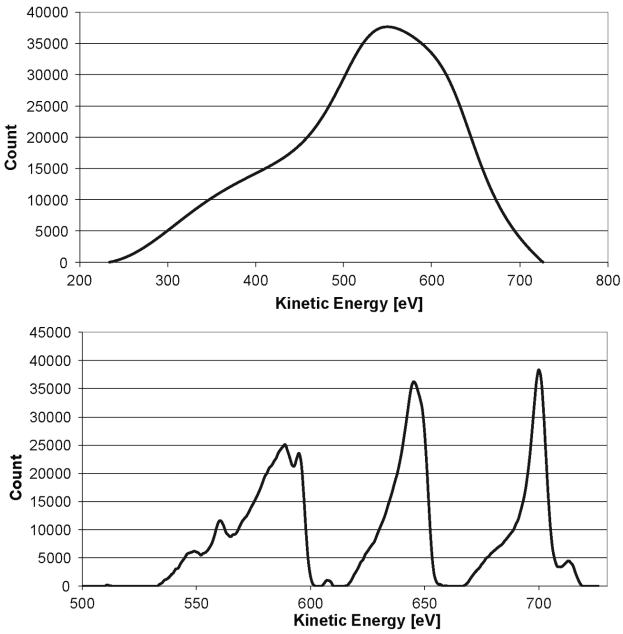

Figure 3: a) The AE spectra peak base and b) spectral peaks
Slika 3: a) Podlaga spektralnih vrhov in b) spektralni vrhovi AE-spektra

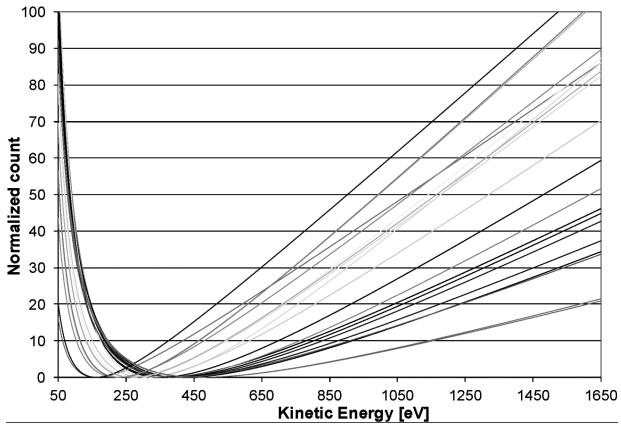

Figure 4: The randomly defined primary backgrounds
Slika 4: Naključno določena primarna ozadja

intended for facilitating the quantitative interpretation of electron spectra (Auger and XPS spectra), and therefore a lot of attention is paid to the detailed physical phenomena related to the excitation and emission of the Auger electron or photoelectron. The database of SESSA contains the data of many physical parameters needed in quantitative electron spectroscopy (AES and XPS).[13] The simulations needed for the purpose discussed in this paper do not require such detailed simulations. The key factor here is that the spectra resemble the real measured ones, and that the values of the different components of the spectra are known before the processing starts. This fact is of utmost importance for the comparison of values of any of the spectral components before and after the processing.

As mentioned in the introduction, smoothing is often used for reducing the noise in Auger electron spectra. For spectra measured with a energy step size 1 eV a 5-point averaging window is recommended.[14] Since most of the measured spectra that were used when building the simulator were of energy step size 1 eV, the same averaging window was used for processing the spectrum

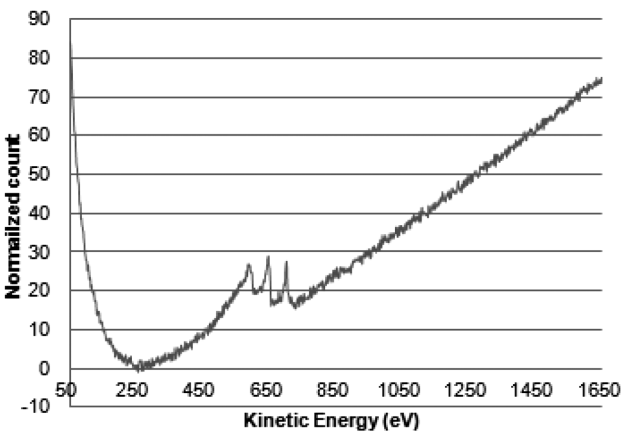

Figure 5: Processed spectrum from **Figure 1** using a 5-point window smoothing in CasaXPS
Slika 5: AE-spekter s **slike 1** po uporabljenem glajenju z oknom širine 5 točk (program CasaXPS)

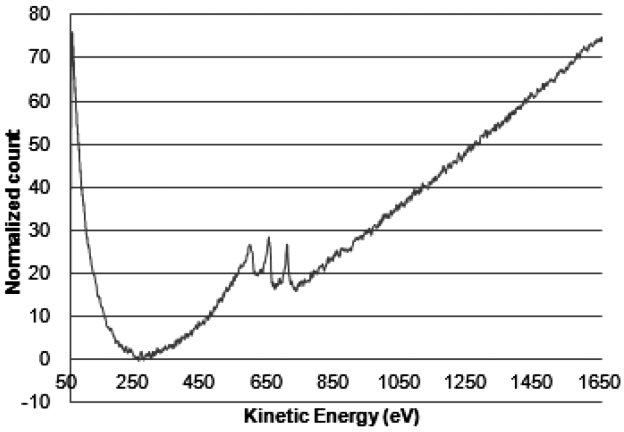

Figure 6: Processed spectrum from **Figure 1** using a notch filter in Audacity
Slika 6: AE-spekter s **slike 1** po uporabi ozkopasovnega filtra (program Audacity)

shown in **Figure 1**. The processing was performed using CasaXPS. The resulting spectrum is given in **Figure 5**.

The same simulated spectrum (**Figure 1**) was processed by applying a notch filter. The threshold frequency was selected arbitrarily for this case, just for a comparison. This procedure was completed using Audacity, where this procedure is used to reduce the noise in sound files. The resulting spectrum is given in **Figure 6**.

3 RESULTS AND DISCUSSION

After applying the smoothing procedures to the simulated spectrum, the noiseless simulated signal ($S_{\text{noiseless}}$) was subtracted from the processed spectrum ($S_{\text{processed}}$), thus obtaining the remaining noise after processing ($N_{\text{remaining}}$):

$$N_{\text{remaining}} = S_{\text{processed}} - S_{\text{noiseless}} \quad (1)$$

Such a procedure was used for obtaining the values of the remaining noise for each data point. These values were then compared to the initial simulated noise, N_{initial}, which is the random noise added to the simulated spectrum, thus obtaining the noise ratios that serve as a measure of the efficiency of the processing software in reducing the noise and bringing the signal closer to the noiseless one:

$$N_{\text{ratio}} = N_{\text{remaining}} / N_{\text{initial}} \quad (2)$$

Figure 7 illustrates the concept behind the use of the noise ratios for this kind of evaluation of the efficiency in noise reduction.

As may be inferred from **Figure 7**, when manipulating the signal for reducing the noise the obtained signal will have a new value with a different deviation from the target point, the noiseless signal. This new difference from the noiseless signal, the remaining noise, will be smaller than, equal to, or greater than that of the initial noise. Thus, for one specific data point a noise ratio of

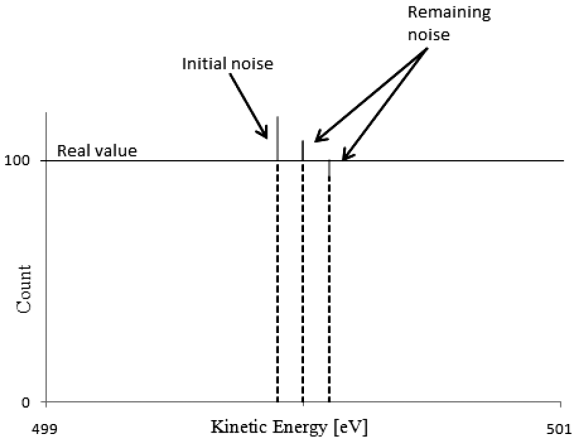

Figure 7: Concept of noise ratios as a measure of the efficiency in noise reduction

Slika 7: Koncept razmerja šumov kot merilo učinkovitosti zmanjševanja šuma

less than one means that the processing was successful in reducing the noise, a noise ratio of one means that the noise level is kept the same, and a noise ratio of more than one means that the noise level is actually increased due to the processing of the spectrum. A graphical plot of the noise ratios would serve as a quick assessment at a glance with respect to the success of the noise-reduction routine, as will be shown later on.

By using Equation (1), first the values for the remaining noise were found for each data point, and then by dividing at the respective data points according to Equation (2), the noise ratios were found and recorded in the data sheet, as shown in **Table 1** for the spectrum processed in CasaXPS, and in **Table 2** for the spectrum processed in Audacity.

By plotting the obtained noise ratios for each data point according to Equation (2), the graph obtained will give, at a glance, an indication of the improvement with regards to the noise. **Figure 8** shows such graphs for the two processing routes discussed in this paper.

Table 1: Data sheet with the noise ratios from the 5-point smoothed Auger spectrum

Tabela 1: Razmerja amplitud šumov pri glajenju spektra s 5-točkovnim povprečenjem

	A	B	C	D	E	F	G	H	I
1	Kinetic Energy	Fe Peaks	Simulated Background	Noiseles AE spectrum	Initial Noise	Complete AE spectrum	5 Point Smoothed	Remaining Noise (G-D)	Noise Ratios (H/E)
2	50	0	85.521594	85.52159	-1.29378	84.22782	84.3649	-1.1566939	0.89404339
3	51	0	83.178313	83.17831	0.421041	83.59935	83.225	0.04668741	0.11088572
4	52	0	80.927765	80.92777	-0.41938	80.50839	80.5747	-0.3530651	0.84188131
5	53	0	78.764702	78.7647	-0.88762	77.87708	78.6823	-0.0824024	0.09283547
6	54	0	76.684264	76.68426	1.545949	78.23021	77.389	0.70473584	0.45585978
7	55	0	74.681944	74.68194	0.384103	75.06605	75.3379	0.65595638	1.70776009
8	56	0	72.753556	72.75356	-0.69507	72.05849	72.2577	-0.4958559	0.71339476
9	57	0	70.89521	70.89521	-0.83461	70.0606	69.9403	-0.9549098	1.14414195
10	58	0	69.103282	69.10328	-1.16494	67.93834	67.9807	-1.1225824	0.96364053
1595	1643	0	74.301336	74.30134	-1.60146	72.69988	74.4497	0.14836413	-0.09264303
1596	1644	0	74.366858	74.36686	1.49713	75.86399	74.1172	-0.249658	-0.16675773
1597	1645	0	74.432383	74.43238	-1.13928	73.29311	74.7135	0.28111716	-0.24675032
1598	1646	0	74.49791	74.49791	0.11125	74.60916	73.6919	-0.8060105	-7.24505201
1599	1647	0	74.563441	74.56344	-1.35235	73.21109	73.6805	-0.8829409	0.65289337
1600	1648	0	74.628974	74.62897	-1.08518	73.5438	73.7001	-0.928874	0.85596404
1601	1649	0	74.69451	74.69451	0.224889	74.9194	74.6885	-0.0060099	-0.02672388
1602	1650	0	74.760049	74.76005	0.410064	75.17011	75.2536	0.49355147	1.20359684

Table 2: Data sheet with the noise ratios from the AE spectrum processed using a notch filter

Tabela 2: Razmerja amplitud šumov pri filtriranju spektra z ozkopasovnim filtrom

	A	B	C	D	E	F	G	H	I
1	Kinetic Energy	Fe Peaks	Simulated Background	Noiseles AE spectrum	Initial Noise	Complete AE spectrum	Audacity Smoothed	Remaining Noise (G-D)	Noise Ratios (H/E)
2	50	0	85.5215939	85.52159	-1.294	84.22782	19.85671	-65.664886	50.7543595
3	51	0	83.1783126	83.17831	0.421	83.59935	45.33394	-37.844375	-89.882924
4	52	0	80.9277651	80.92777	-0.419	80.50839	64.56315	-16.364618	39.0213159
5	53	0	78.7647024	78.7647	-0.888	77.87708	68.37446	-10.390246	11.7057686
6	54	0	76.6842642	76.68426	1.5459	78.23021	75.32746	-1.3568018	-0.8776499
7	55	0	74.6819436	74.68194	0.3841	75.06605	73.34811	-1.3338349	-3.4725938
8	56	0	72.7535559	72.75356	-0.695	72.05849	75.92464	3.1710817	-4.5622793
9	57	0	70.8952098	70.89521	-0.835	70.0606	71.43866	0.5434543	-0.6511494
10	58	0	69.1032824	69.10328	-1.165	67.93834	72.58164	3.4783531	-2.9858672
11	59	0	67.3743966	67.3744	-1.086	66.28791	68.05102	0.6766247	-0.622762
12	60	0	65.7054003	65.7054	-0.177	65.52819	69.1224	3.4169989	-19.281932
1596	1646	0	74.4979105	74.49791	0.1112	74.60916	74.49698	-0.0009344	-0.0083989
1599	1647	0	74.5634409	74.56344	-1.352	73.21109	73.67407	-0.8893705	0.6576478
1600	1648	0	74.628974	74.62897	-1.085	73.5438	74.11458	-0.5143922	0.47401608
1601	1649	0	74.6945099	74.69451	0.2249	74.9194	73.63111	-1.0633957	-4.7285443
1602	1650	0	74.7600485	74.76005	0.4101	75.17011	74.74124	-0.0188118	-0.0458752

As can be seen in **Figures 8a** and **8b**, in both cases most of the points representing the noise ratios occupy the region between –1 and 1, while some of the peaks lie outside these boundaries. If the ratio of the remaining noise to the initial noise is less than 1, this indicates that the new signal after processing is actually closer to the real signal than the one before processing, thus indicating an improvement with respect to the noise. The noise ratios whose values lie outside the [–1,1] interval

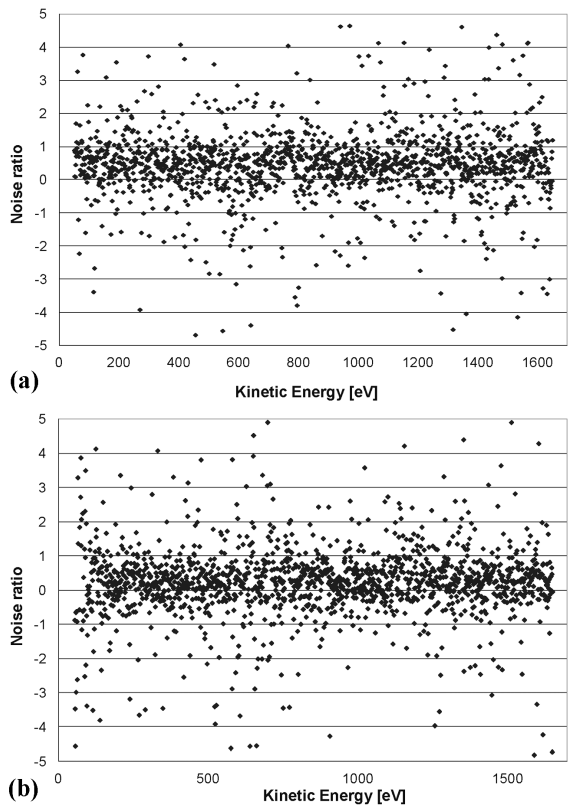

Figure 8: Noise ratios from: a) the 5-point smoothed spectrum and b) the spectrum smoothed using a notch filter

Slika 8: Razmerja amplitud šumov pri: a) filtriranju spektra s 5-točkovnim povprečenjem in b) pri filtriranju spektra z ozkopasovnim filtrom

indicate that for those specific data points the processing has actually worsened the situation with respect to the noise. Plotting these noise ratios for all the data points in the spectrum offers a convenient way to see at a glance whether there is an improvement in terms of the noise or not, as well as for comparing different processing techniques for this purpose. Again, the usefulness of the simulated spectra must be stressed in this regard, because no such comparison can be made if the values for the noise are not known at the beginning, as it is in the case of the measured spectra.

4 CONCLUSIONS

Simulated spectra have been used to assess the performance of two noise-reduction techniques. A simple idea of using the noise ratios as a measure of the efficiency of the noise-reduction routines was presented. By applying this idea on a simulated spectrum, which was processed using two different procedures, the values for the noise ratios at each data point were found for the respective procedures. Plotting the noise ratios provided a convenient way to assess, at a glance, the efficiency of the processing route in reducing the noise. The noise ratios for the majority of the data points lie in the [–1,1] interval, indicating an improvement with respect to the noise.

The only way in which the values of the noise ratios can be obtained is if the values of the noise and the noiseless signal are known before and after the processing. Such a condition can be fulfilled if simulated spectra are used in the assessment stage, as shown in this paper.

5 REFERENCES

[1] D. R. Baer et al., Challenges in Applying Surface Analysis Methods to Nanoparticles and Nanostructured Materials, Journal of Surface Analysis, 12 (**2005**) 2, 101–108

[2] D. R. Baer et al., Characterization challenges for nanomaterials, Surface and Interface Analysis, 40 (**2008**), 529–537, doi:10.1002/sia.2726

[3] D. R. Baer, D. J. Gaspar, P. Nachimuthu, S. D. Techane, D. G. Castner, Application of Surface Chemical Analysis Tools for Characterization of Nanoparticles, Analytical and Bioanalytical Chemistry, 396 (**2010**) 3, 983–1002, doi:10.1007/s00216-009-3360-1

[4] A. S. Karakoti et al., Preparation and characterization challenges to understanding environmental and biological impacts of ceria nanoparticles, Surface and Interface Analysis, 44 (**2012**), 882–889, doi:10.1002/sia.5006

[5] D. R. Baer, Application of surface analysis methods to nanomaterials: summary of ISO/TC 201 technical report: ISO 14187:2011 – surface chemical analysis – characterization of nanomaterials, Surface and Interface Analysis 44 (**2012**), 1305–1308, doi:10.1002/sia.4938

[6] M. P. Seah, Summary of ISO/TC 201 Standard: XXIII, ISO 24236:2005 – Surface chemical analysis – Auger electron spectroscopy – Repeatability and constancy of intensity scale, Surface and Interface Analysis 39 (**2007**), 86–88, doi:10.1002/sia.2493

[7] M. P. Seah, Summary of ISO/TC 201 Standard XI. ISO 17974: 2002 – Surface chemical analysis – High-resolution Auger electron spectrometers – Calibration of energy scales for elemental and chemical-state analysis, Surface and Interface Analysis, 35 (**2003**), 327–328, doi:10.1002/sia.1529

[8] M. P. Seah, Summary of ISO/TC 201 Standard XII. ISO 17973:2002 – Surface chemical analysis – Medium – resolution Auger electron spectrometers – Calibration of energy scales for elemental analysis, Surface and Interface Analysis, 35 (**2003**), 329–330, doi:10.1002/sia.1530

[9] N/A. Auger Electron Spectroscopy (AES): What is AES? http://www.phi.com/techniques/aes.html (accessed November 2014). Physical Electronics, Inc. Chanhassen, MN, 2006 – 2014.

[10] VG Scientific, Microlab 310 – F: Operators Manual, VG Scientific, East Sussex, 1997

[11] B. Poniku, I. Belič, M. Jenko, The Auger spectra recognition and modeling: Modeling Auger spectra for effective background removal and noise reduction, Lambert Academic Publishing, Saarbrücken 2011, doi:10.13140/2.1.3620.7045

[12] I. S. Gilmore, M. P. Seah, Savitzky and Golay differentiation in AES, Applied Surface Science, 93 (**1996**) 3, 273–280, doi:10.1016/0169-4332(95)00345-2

[13] W. S. M. Werner, W. Smekal, C. J. Powell, NIST Database for the Simulation of Electron Spectra for Surface Analysis (SESSA) – User's Guide, Version 1.3, National Institute of Standards and Technology, Maryland, 2011

[14] N. Fairley, CasaXPS Manual 2.3.15: Introduction to XPS and AES, Casa Software Ltd., Devon, 2009

UDK 669.14:621.78.015
Professional article/Strokovni članek

ISSN 1580-2949
MTAEC9, 49(3)441(2015)

SURFACE BEHAVIOR OF AISI 4140 MODIFIED WITH THE PULSED-PLASMA TECHNIQUE

LASTNOSTI POVRŠINE AISI 4140, SPREMENJENE S TEHNIKO PULZIRAJOČE PLAZME

Yıldız Yaralı Özbek, Mehmet Durman

Sakarya University, Engineering Faculty, Department of Metallurgical and Metarials Engineering, Esentepe Campus, 54187 Sakarya, Turkey
yyarali@sakarya.edu.tr

Prejem rokopisa – received: 2013-10-02; sprejem za objavo – accepted for publication: 2014-07-17

doi:10.17222/mit.2013.219

In this study, the microstructure and surface properties of a low-alloy steel (AISI 4140) treated with pulsed plasma were investigated. Three different plasma-gun nozzle distances of (60, 70 and 80) mm and one battery capacity were chosen for a surface modification. The modified surface layers were examined using a light microscope and X-ray analyses were carried out for all the samples. The X-ray diffraction confirmed a development of new phases after the surface treatment. The samples were subjected to micro-hardness measurements and it was found that the hardness values of the modified surfaces were four times higher than those of the untreated samples. The samples were immersed into liquid nitrogen and then broken in a Charpy machine. The fractured surfaces were exposed to SEM and EDS analyses. At the end of the study, thin grains originating from the consumable electrode were detected. After the pulsed-plasma treatment, new structures were obtained.

Keywords: pulsed plasma, fracture, consumable electrode, modification

V tej študiji so bile preiskovane mikrostruktura in lastnosti površine malolegiranega jekla (AISI 4140) po obdelavi s pulzirajočo plazmo. Za spremembo površine so bile izbrane tri različne razdalje plazemske šobe od površine: 60 mm, 70 mm in 80 mm, in kapaciteta ene baterije. Spremenjene površinske plasti so bile preiskovane s svetlobnim mikroskopom in izvršene so bile rentgenske analize. Rentgenska difrakcija je potrdila nastanek novih faz po obdelavi površine. Na vzorcih so bile izvršene meritve mikrotrdote in ugotovljeno je bilo, da je trdota spremenjene površine štirikrat večja od tiste pri neobdelanih vzorcih. Le-ti so bili potopljeni v tekoči dušik in nato prelomljeni na napravi Charpy. Površina preloma je bila analizirana s SEM in EDS. Odkrita so bila drobna zrna, ki izvirajo iz elektrode. Po obdelavi s pulzirajočo plazmo je nastala nova mikrostruktura.

Ključne besede: pulzirajoča plazma, prelom, porabljiva elektroda, sprememba

1 INTRODUCTION

High-intensity pulse or plasma irradiation has recently gained a growing interest as a potential tool in surface engineering. As in the cases of a laser or electron beam, ions from a pulsed beam rapidly heat the surface of the irradiated material. The surface remains at a high temperature (up to the melting point or higher) for a period in the nanosecond to microsecond range, and then rapidly cools through conduction into the bulk at the rates of the order of 10^7–10^{10} K/s. Obviously, the details of the heat evolution in a substrate depend on its thermal properties and dimensions as well as on the beam parameters. Heat-induced processes result in several non-equilibrium phenomena such as the mixing of metallic overlayers on various (even hardly miscible) substrates, the formation of metastable crystalline alloys and so on. Besides purely thermal effects, ion or plasma beams are used as well. It is also possible, under appropriate conditions, to modify the surface properties of solids via thermal effects in conjunction with the mass transport.[1–3]

The pulsed-plasma process is used to improve the surface properties of the workpieces of tool steels.[1–6] The pulsed-plasma system has high rates of heating and cooling. These lead to the formation of a nano/microcrystalline structure, a high dislocation density and a growth of the concentration of the alloying elements and, thus, an intensification of the diffusion mechanisms.[3–5]

In general, a modified surface consists of a compound layer (the white layer) that is a few micrometers deep. In the diffusion zone the nitrogen atoms can be interstitially dissolved or precipitated as iron nitrides, tungsten and/or tungsten alloys from the consumable electrode used. As a result, metastable states may appear in the surface layers, which are the origin of the improved physical, chemical and mechanical properties unattainable with the conventional surface-treatment techniques.[5]

The process parameters have significant effects in determining the final structure and mechanical properties of the surfaces. Among these parameters the controlling gas diffusion through the nozzle distance and the number of pulses, and the plasma composition are the most important ones. A proper combination of these parameters would provide the best surface properties and set out the duration of the process time as an important economic factor.[1] The pulsed plasma is the most advantageous one; its process time is very short (1 min), it is more economical and it can produce superior mechanical properties.

The aim of this study is to improve the material performance and functional properties of the surface of a commonly used steel without long and expensive heat-treatment operations. AISI 4140 was used in this study. The AISI 4140 steel is the most common type of steel dealt with in the studies discussing different methods. Different parameters of pulsed plasma were tried on the samples.

2 EXPERIMENTAL PROCEDURE

The standard, medium-carbon, low-alloy AISI 4140 steel was used in the study and the chemical composition of the steel is given in **Table 1**. The samples were exposed to the pulsed-plasma-modification technique. A schematic illustration of the pulsed-plasma technique used for the modification of the samples is shown in **Figure 1**. The parameters of pulsed plasma are given in **Table 2**.

Table 1: Chemical composition of the AISI 4140 steel used in the study in mass fractions, *w*/%

Tabela 1: Kemijska sestava jekla AISI 4140, uporabljenega za preizkuse v masnih deležih, *w*/%

AISI 4140	C	Si	Mn	P	S	Cr	Mo
w/%	0.40	0.30	0.70	0.035	0.035	0.98	0.27

Table 2: Parameters of the pulsed-plasma process

Tabela 2: Parametri postopka pulzirajoče plazme

No.	Nozzle distance mm	Number of pulses	Battery capacity, μF	Consumable electrode, W
1	70	15	800	Tungsten
2	70	10	800	Tungsten
3	70	5	800	Tungsten
4	80	15	800	Tungsten
5	80	10	800	Tungsten
6	80	5	800	Tungsten
7	60	15	800	Tungsten
8	60	10	800	Tungsten
9	60	5	800	Tungsten

The specimens used in the pulsed-plasma experiments were cut from the center of the modified surfaces with a cutting machine (Discotom-6) and then put in Bakelite. After that, they were grinded with the emery paper and polished. The samples were studied with a light microscope using different magnifications. The hardness values of the specimens were measured with a Future-Tech test apparatus for 15 s under a load 5 g. The phase compositions of the modified surfaces were investigated with X-ray diffractometry (XRD) using a Rigaku diffractometer employing monochromatic Cu-$K\alpha$ radiation. After the pulsed-plasma process, the notched specimens were immersed into liquid nitrogen for two minutes and then they were cracked with a Charpy test machine from the notched regions. The fractured regions were analyses with a scanning electron microscope JEOL 6600 (SEM) and an energy dispersive spectrometer (EDS).

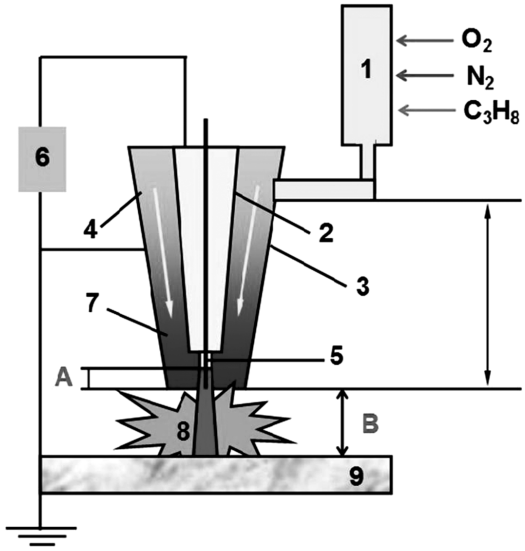

Figure 1: Schematic presentation of the pulsed-plasma modification system: 1-detonation chamber, 2-central electrode, anode, 3-conical electrode, cathode, 4-interelectrode gap, 5-consumable electrode, 6-power supply, 7-gap between the electrodes, 8-pulsed plasma forming, 9-work surface

Slika 1: Shematski prikaz sistema s pulzirajočo plazmo: 1-detonacijska komora, 2-centralna elektroda anoda, 3-konična elektroda katoda, 4-vrzel med elektrodama, 5-porabljiva elektroda, 6-izvir energije, 7-vrzel med elektrodama, 8-nastanek pulzirajoče plazme, 9-delovna površina

3 RESULTS AND DISCUSSION

In **Figure 2**, a light microstructure of Sample 4 is shown. It was obvious from the microstructural examination that the modified layer and the substrate could be easily seen due to the light contrast. A white layer was formed on the surface layer.

A homogeneous and ordered layer was obtained by increasing the pulse number as seen in the light

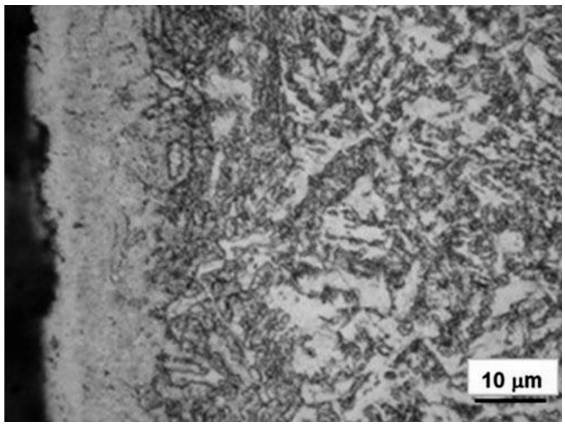

Figure 2: Microphotograph of the cross-section of Sample 4 modified with pulsed plasma

Slika 2: Mikrostruktura prereza vzorca 4, obdelanega s pulzirajočo plazmo

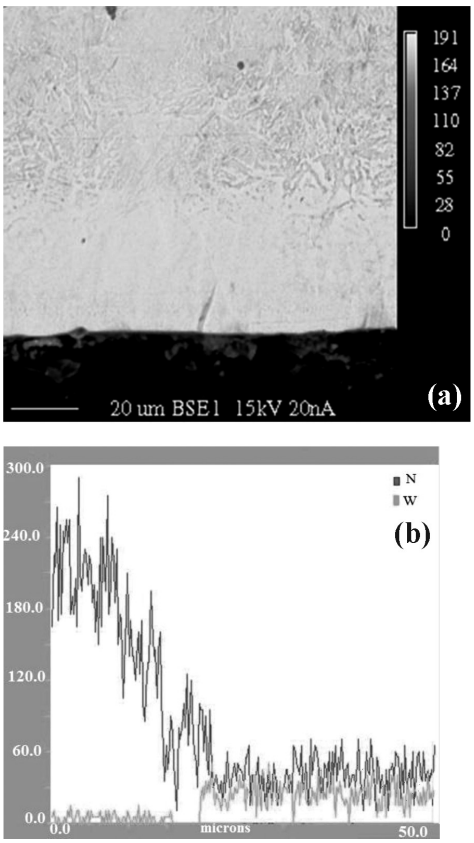

Figure 3: EPMA results for the modified layer of Sample 12
Slika 3: Rezultati EPMA spremenjene plasti vzorca 12

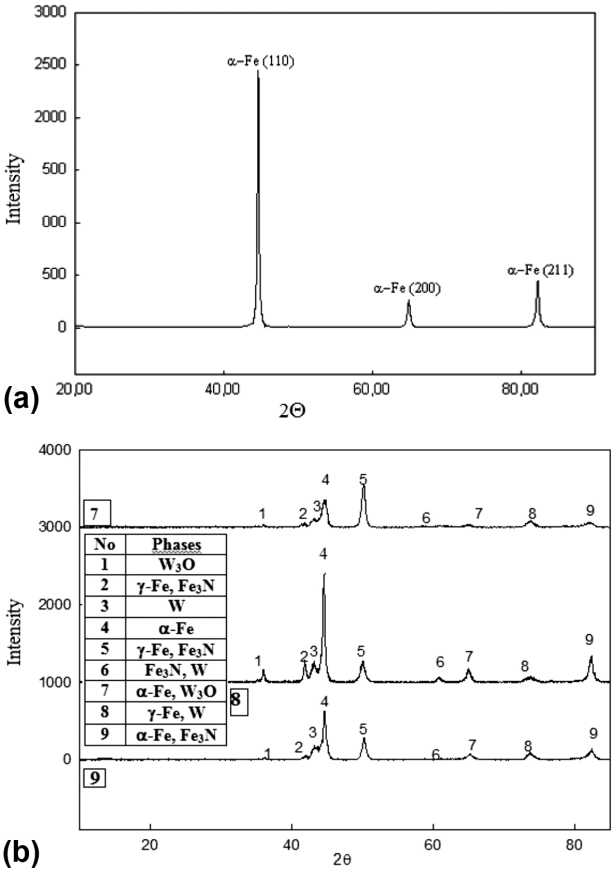

Figure 4: XRD analysis of: a) un-treated AISI 4140 steel, b) Sample 7, Sample 8 and Sample 9
Slika 4: Rentgenogram: a) neobdelano AISI 4140 jeklo, b) vzorec 7, vzorec 8 in vzorec 9

photographs. When the pulse number was increased, the thickness of the modified layer increased as due to the increased pulse number the process time and the amount of ionized gases were increased.[6,7]

Rapid heating and solidification induced a heavy plastic deformation, which caused a formation of dislocation cells due to one pulse bombardment. After the multi-pulse bombardments, both austenite and carbide types of the nanostructure particles were formed from the supersaturated solution.

The pulsed-plasma system affected the grain size of the modified layer.[4] The grain structure of the outer surface of the modified layer was very fine and dense. The previous studies showed that the thermal stability, mechanical and tribological properties and the corrosion behavior of the materials are greatly influenced by the grain size.[2,8,9]

Figure 3 shows the EPMA results for the modified layer. The amounts of nitrogen and tungsten changed from the surface to the inner space. Firstly, the nitrogen was increased, then it was decreased and after that point the amount of tungsten was increased. These phases were very important for the surface properties.[8]

The XRD results for the sample groups are given in **Figure 4**. The figure clearly shows that the pulsed-plasma treatment changed the diffraction profiles of the samples. The results of the X-ray analysis indicate that the new phases (such as γ-Fe, W and carbides) are formed on the steel surface after the plasma processing. Tungsten oxide was also determined from the analysis, due to the tungsten consumable electrode used during the pulsed-plasma treatment.[10]

While there was only the α-Fe phase in the untreated AISI 4140 steel (**Figure 4a**), Fe_3N, γ-Fe and tungsten were observed in the modified layer after the treatment (**Figure 4b**). As seen in **Figure 4b**, the pulse number is the only difference between the three specimens. The increased number of pulses leads to the growth of some existing phases, such as γ'-Fe, and the formation of new phases since the increasing pulse number also increases the pulsed-plasma-treatment time. This results in an increased amount of the ionized products doped into the surface. In addition, crystalline phases can be formed more easily with the increasing treatment time.[6,7]

Sample 7, having the highest pulse number, has the largest peak spacing (increased FWHM values). The increasing FWHM values of these phases cause a decrease in the grain size in accordance with the Scherer equation.[8] Besides, a high cooling rate results in a small size of the precipitates, making them hard to be found with XRD.[8,9]

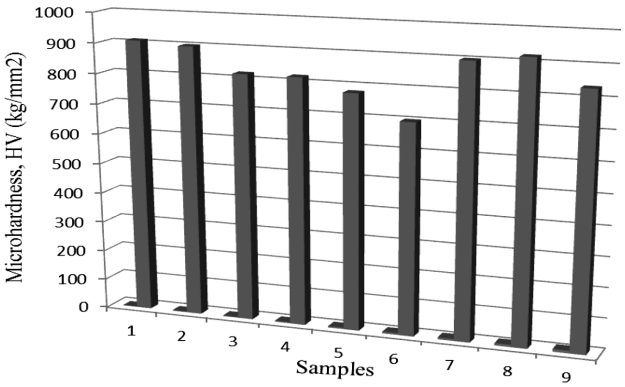

Figure 5: Microhardness values of the samples
Slika 5: Mikrotrdota vzorcev

A comparison of the X-ray analysis results for the sample surfaces processed with different numbers of pulses showed a profound effect on the creation of new phases in the surface structure, hence, enhancing the surface properties.[10,11]

Figure 5 shows the results of the microhardness measurements for all the samples. The figure clearly illustrates that the pulsed-plasma treatment has a profound effect on increasing the microhardness values of the AISI 4140 steel, depending on the treatment parameters used. The new phases and the structure transformations improved the surface mechanical characteristics.

It was also found that there were some tungsten, nitride and austenite phases on the surfaces of the modified samples. The amount of these strong phases precipitated in the matrix phase was one of the reasons leading to an increase in the hardness values of the treated samples.[4,12–14]

Prior to the pulsed-plasma treatment, the initial hardness value of the specimens was recorded as 180 HV and later its value was increased up to 700–950 HV. The hardness value measured for Sample 1 (15 pulses) was 910 HV; for Sample 2 (10 pulses) it was 900 HV and for Sample 3 (5 pulses) it was 820 HV. The number of pulses affected the hardness values. An increase in the pulse number, or the intensity of the energy density absorbed by the surface, leads to the growth of the microhardness value.[2,4,9]

In the experiments, the maximum value of the surface microhardness was achieved for the samples treated with the maximum number of pulses. However, in these treatment regimes, a partial melting of the surface layer was observed, being due to the high temperatures caused by the frequently repeated pulses.

The structural defects, or disorder trappings, are easily formed at the high solidification rate induced by pulsed plasma, increasing the material hardness, known as the established point-defect strengthening models.[13]

Another reason for the increase in the hardness values of the samples was the decreased grain size due to

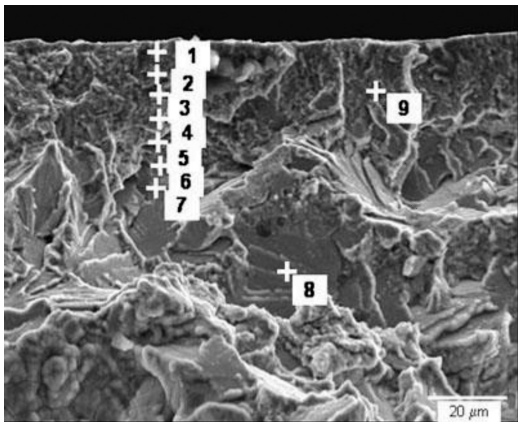

No.	1	2	3	4	5	6	7	8	9
W *w*/%	2.610	3.200	1.198	2.067	1.154	1.190	2.091	1.889	1.190

Figure 6: EDS analyses of the fracture surface of Sample 3
Slika 6: EDS-analize na površini preloma vzorca 3

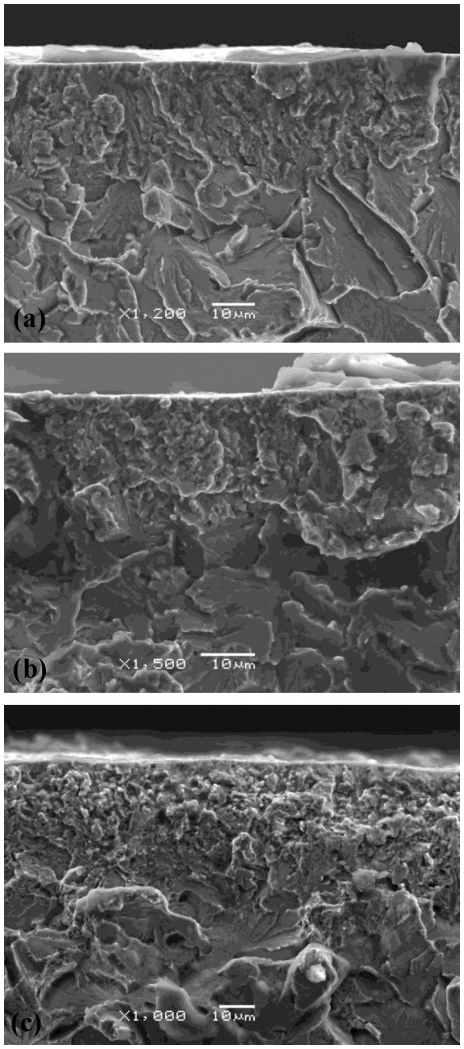

Figure 7: SEM micrographs of fracture surfaces: a) Sample 5, b) Sample 6, c) Sample 7
Slika 7: SEM-posnetki površine preloma: a) vzorec 5, b) vzorec 6, c) vzorec 7

the increased cooling rate within the cycles of pulses. In the present experiment, the samples subjected to a high number of pulses during the pulsed-plasma treatment exhibit a low grain size and a high amount of the phase.[11,13]

The EDS analyses of the modified layer of Sample 3 are given in **Figure 6**. The modified layer and the resultant structure were easily detected and clearly seen in the fractured regions of the specimens. The EDS analysis was performed and the tungsten element was observed. In addition to this, the consumable-electrode tungsten amount in the matrix phase was calculated on the basis of the EDS analysis. Since there is no tungsten ingredient in the base metal, the existence of the tungsten from the electrode after the analysis indicates that the pulsed-plasma treatment was performed successfully.

The process parameters affect the structure and thickness of the modified layer (**Figures 7a** to **7c**). From the SEM micrographs, it is observed that the fracture mechanism was brittle as characterized by the cleavage facets in the bulk material.[10,11] Different fracture mechanisms occurred on the modified layer and the substrate. A fine-grained structure observed in the modified zone where a ductile fracture occurred is an indication of a hard structure. But ultra-fine intermetallic compounds were found in the matrix of this zone.[4,14]

4 CONCLUSION

In the light of the results of the experimental studies carried out on the surfaces of AISI 4140 steels modified with the pulsed-plasma technique, the findings given below were obtained:

1) The pulsed-plasma technique is used for a surface modification. Due to this technique, the thickness of a modified layer increases with the increasing pulse number, and the resultant structure becomes homogeneous.

2) In addition, a decrease in the grain size is observed as a result of fast heating and cooling of the modified layer. The grains outside of the modified zone are larger than the ones in the inside regions.

3) The phase and structure transformations occurred during the modification of the surfaces. The γ-Fe, Fe_3N and W compounds were determined with the XRD studies.

4) The new phases and structure transformations improved the surface mechanical characteristics. The hardness values increased four times.

5) A ductile fracture occurred on the modified layer. A cleavage fracture was seen on the substrate.

5 REFERENCES

[1] K. M. Zhang, J. X. Zou, B. Bolle, T. Grosdidier, Vacuum, 87 (**2013**), 60–68, doi:10.1016/j.vacuum.2012.03.061

[2] N. Y. Tyurin, O. V. Kolisnichenko, N. G. Tsygankov, The Paton Welding Journal, (**2004**), 38–43

[3] C. Kwietniewski, W. Fontana, C. Moraes, A. S. Rocha, T. Hirsch, A. Reguly, Surface and Coatings Technology, 179 (**2004**) 1, 27–32, doi:10.1016/S0257-8972(03)00795-3

[4] Q. F. Guan, H. Zou, G. T. Zou, A. M. Wu, S. Z. Hao, J. X. Zou, Y. Qin, C. Dong, Q. Y. Zhang, Surface & Coatings Technology, 196 (**2005**) 1–3, 145–149, doi:10.1016/j.surfcoat.2004.08.104

[5] J. L. Fan, T. Liu, H. C. Cheng, D. L. Wang, Journal of Materials Processing Technology, 208 (**2008**) 1–3, 463–469, doi:10.1016/j.jmatprotec.2008.01.010

[6] Y. Y. Özbek, M. Durman, H. Akbulut, Tribology Transactions, 52 (**2009**) 2, 213–222, doi**:**10.1080/10402000802369721

[7] V. V. Uglov, V. M. Anishchik, N. N. Cherenda, Y. V. Sveshnikov, V. M. Astashynski, E. A. Kostyukevich, A. M. Kuzmitski, V. V. Askerko, Surface & Coatings Technology, 202 (**2008**) 11, 2439–2442, doi:10.1016/j.surfcoat.2007.08.045

[8] Y. Yarali, M. Durman, H. Akbulut, Key Engineering Materials, 264–268 (**2004**), 561–564, doi:10.4028/www.scientific.net/KEM.264-268.561

[9] Z. Zhou, J. Linke, G. Pintsuk, J. Du, S. Song, C. Ge, Journal of Nuclear Materials, 386–388 (**2009**), 733–735, doi:10.1016/j.jnucmat.2008.12.306

[10] A. Buranawong, N. Witit-anun, S. Chaiyakun, A. Pokaipisit, P. Limsuwan, Thin Solid Films, 519 (**2011**) 15, 4963–4968, doi:10.1016/j.tsf.2011.01.062

[11] Y. Hao, B. Gao, G. F. Tu, S. W. Li, C. Dong, Z. G. Zhang, Nuclear Instruments and Methods in Physics Research B, 269 (**2011**) 13, 1499–1505, doi:10.1016/j.nimb.2011.04.010

[12] Y. Y. Özbek, H. Akbulut, A. Ozel, M. Durman, Surface Modification of M2 Steel by Pulsed Plasma Technique, ICAMM, 2010, 46–50

[13] J. X. Zou, T. Grosdidier, K. M. Zhang, C. Dong, Applied Surface Science, 255 (**2009**) 9, 4758–4764, doi:10.1016/j.apsusc.2008.10.123

[14] X. Cheng, S. Hu, W. Song, X. Xiong, Applied Surface Science, 286 (**2013**), 334–343, doi:10.1016/j.apsusc.2013.09.083

UDK 666.3/.7:621.762.5
Professional article/Strokovni članek

ISSN 1580-2949
MTAEC9, 49(3)447(2015)

PREPARATION AND DIELECTRIC PROPERTIES OF THERMO-VAPOROUS $BaTiO_3$ CERAMICS

PRIPRAVA IN DIELEKTRIČNE LASTNOSTI TERMO-PARNO POROZNE KERAMIKE $BaTiO_3$

Anastasia Kholodkova[1], Marina Danchevskaya[1], Nellya Popova[2], Liana Pavlyukova[2], Alexandr Fionov[3]

[1]Chemistry Department, Moscow State University, GSP-1, Leninskie Gory 1-3, 119991 Moscow, Russia
[2]D. Mendeleev University of Chemical Technology of Russia, Geroev Panfilovtsev 20, 125047 Moscow, Russia
[3]Kotel'nikov Institute of Radio Engineering and Electronics of RAS, Mokhovaya 11-7, 125009 Moscow, Russia
anastasia.kholodkova@gmail.com

Prejem rokopisa – received: 2013-11-10; sprejem za objavo – accepted for publication: 2014-07-17

doi:10.17222/mit.2013.276

A crystalline $BaTiO_3$ powder was synthesized at 350 °C for 0–20 h from TiO_2 (> 99 % purity) and BaO (> 98 % purity) with water vapour acting as the reaction media. According to the XRD and SEM results, the $BaTiO_3$ synthesized for 3 h proved to be the most adequate raw material for ferroelectric ceramics among the obtained samples as long as it consisted of pure crystalline sphere-shaped $BaTiO_3$ particles with the average size of 156 nm. Pellets were pressed at (100, 150 and 200) MPa and sintered at 1300 °C for 1 h. The influence of the compacting pressure on the dielectric characteristics of $BaTiO_3$ ceramics was studied by monitoring the permittivity and loss-tangent values of the pellets at 20 Hz–2 MHz.

Keywords: barium titanate, thermo-vaporous synthesis, microstructure, dielectric ceramics

Kristalni prah $BaTiO_3$ je bil sintetiziran pri 350 °C od 0 do 20 h iz TiO_2 (čistost: > 99 %) in BaO (čistost: > 98 %) z vodno paro kot reakcijski medij. Iz rentgenogramov in SEM-posnetkov izhaja, da je $BaTiO_3$, sintetiziran 3 h, najprimernejša surovina med vsemi vzorci za feroelektrično keramiko, dokler sestoji iz čistih kristalnih okroglih delcev $BaTiO_3$ s povprečno velikostjo 156 nm. Peleti so bili stiskani pri (100, 150 in 200) MPa in sintrani 1 h pri temperaturi 1300 °C. Vpliv tlaka pri stiskanju na dielektrične lastnosti keramike $BaTiO_3$ je bil preiskovana s spremljanjem permitivnosti in velikosti izgube tg δ peletov pri 20 Hz–2 MHz.

Ključne besede: barijev titanat, termo-parno porozna sinteza, mikrostruktura, dielektrična keramika

1 INTRODUCTION

Since the 1940s barium titanate, $BaTiO_3$, has been known for its extremely high values of ferroelectric characteristics which make it widely used in the production of multilayer ceramic capacitors (MLCCs), resistors with a positive temperature coefficient of resistivity (PTCR), temperature/humidity/gas sensors, piezoelectric transducers and actuators, ultrasonic and electro-optic devices, IR-detectors, etc.[1–4] Generally, the $BaTiO_3$ powder is obtained as the raw material for the bulk-ceramic manufacturing, as well as thin-film and composite-material production.[4] For this purpose a homogeneous, well-dispersed pure $BaTiO_3$ powder, consisting of spherical particles up to 200 nm in size, is required.[1,5,6] Various synthesis routes for the as-characterized powder have been developed over several decades. In addition to the conventional solid-state method, the techniques such as pyrolysis (Pechini, citrate processes), dispersion (catecholate synthesis, spray pyrolysis, sol-gel), precipitation (oxalate, hydrothermal and solvothermal synthesis) are widely used for the fine-crystalline $BaTiO_3$ processing.[1,7–14] But, as some of them are multistage and require the use of auxiliary substances, mostly in the solid state, hydrothermal and oxalate techniques are industrially suitable. The development of a simple and low-cost method for the industrial $BaTiO_3$ production remains to be a pending problem.

In the present work water vapour at 350 °C was used as the medium for a $BaTiO_3$ synthesis from simple oxides. A similar technique combined with the treatment in supercritical water fluid was previously successfully used for the production of $MgAl_2O_4$, $ZnAl_2O_4$, $Y_3Al_5O_{12}$, $BaFe_{12}O_{19}$, $LiNbO_3$[15,16] and also $BaTiO_3$.[17,18] As ceramic manufacturing is one of the main application areas for the $BaTiO_3$ powder, steps were taken to develop this technique for obtaining the $BaTiO_3$ with the thermo-vaporous process. We prepared ceramic samples in the same conditions, but varied the compressing pressure and studied the phase content, the microstructure and dielectric properties of the pellets in order to determine the most appropriate value of the pressure for the ceramic-manufacturing route.

2 EXPERIMENTAL WORK

The synthesis of $BaTiO_3$ was performed in laboratory stainless-steel autoclaves using BaO (> 98 % purity) and TiO_2 (> 99 % purity) as the starting reagents. As BaO

interacts with CO_2 in the air, forming $BaCO_3$, in order to avoid a lack of Ba^{2+} ions in the reaction mixture, an amount fraction of excess of BaO 5 % was used. After a thorough mixing by means of grinding in an agate mortar with a pestle, the reagents were placed into a special container inside the autoclave, separated from the distilled water. Hermetically closed autoclaves were heated up to 350 °C (the water-vapour pressure of 16 MPa), kept at this temperature for (0, 0.5, 1, 2, 3, 4, 5, 20) h and then cooled so that the water vapour condensed at the bottom of the autoclaves separated from the product. The product was first washed with acetic acid solution to avoid a $BaCO_3$ contamination and then with distilled water.

To produce a ceramic powder, the sample synthesized for 3 h (named BT-3h) was mixed with 1 % PVA and uniaxially pressed into pellets at (100, 150 and 200) MPa at room temperature. The pellets were sintered at 1300 °C for 1 h.

The phase contents of the powders and ceramics were identified with an X-ray diffraction analysis (STOE STADI P) using the Cu-$K\alpha$ radiation in a range of $20° \leq 2\theta \leq 80°$. The crystallite size was calculated with the Scherrer equation. The morphologies of the powder and ceramic samples were studied with scanning electron microscopy (JSM-6390 LA). The dielectric permittivity and loss tangent of the pellets were calculated from the capacity and the conductivity, respectively, of the plane condenser, in which each pellet was used as a dielectric layer. Dielectric characteristics were obtained with a precision LCR meter Agilent E4980a with a frequency range of 20 Hz–2 MHz.

3 RESULTS AND DISCUSSION

During the thermo-vaporous $BaTiO_3$ synthesis, H_2O molecules from the vapour became incorporated into the TiO_2 structure due to the dissociative absorption manifested in the breaking of the Ti-O bonds and the creation of the Ti-OH bonds. In these conditions the TiO_2 structure becomes more flexible, interacting with the Ba^{2+} ions and reorganising into $BaTiO_3$. The XRD analysis of the powders prepared at 350 °C in the water-vapour atmosphere over the periods of 0–20 h showed that the powders consisted of crystalline $BaTiO_3$ (**Figure 1**). The formation of $BaTiO_3$ from TiO_2 and $Ba(OH)_2$ occurred already during the heating, thus, the sample synthesized for 0 h contained only crystalline $BaTiO_3$. The interaction of the newly formed $BaTiO_3$ phase with water vapour led to an elimination of lattice defects and to a perfection of the crystalline structure. **Figure 2** shows the $BaTiO_3$ crystallite-size dependence on the duration of the thermo-vaporous synthesis, calculated from the Scherrer equation. The crystallite size of the samples synthesized for 0–4 h fluctuates in a range of 35–45 nm, while, in the case of a longer synthesis, the crystallite

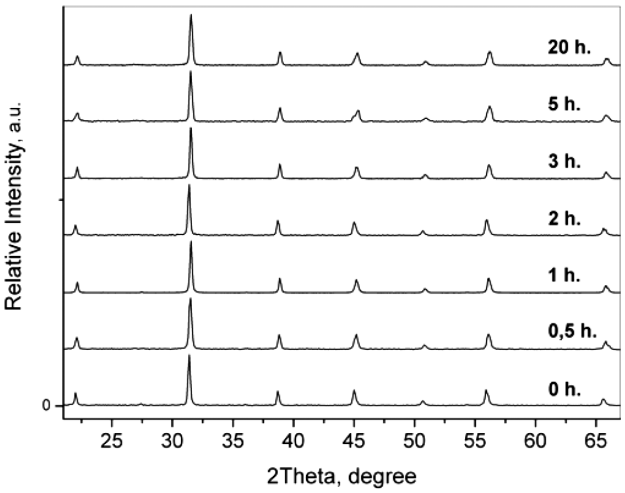

Figure 1: XRD patterns of the $BaTiO_3$ powders synthesized in water vapour at 350 °C and 16 MPa for 0–20 h

Slika 1: Rentgenogram prahov $BaTiO_3$ sintetiziranih od 0 do 20 ur, v vodni pari pri 350 °C in 16 MPa

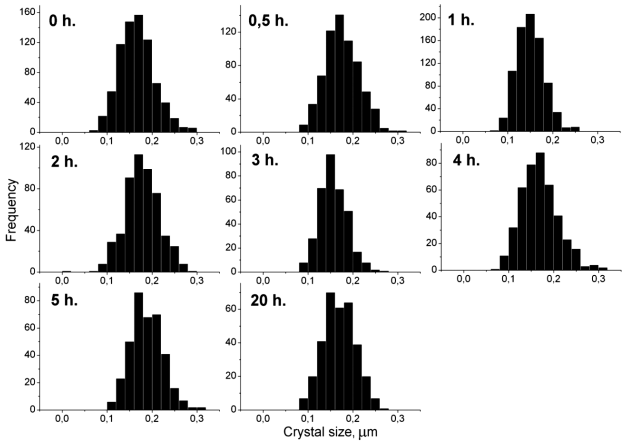

Figure 2: Crystal-size distributions of $BaTiO_3$ synthesized in water vapour at 350 °C and 16 MPa for 0–20 h

Slika 2: Razporeditev velikosti kristalov $BaTiO_3$, sintetiziranih od 0 do 20 ur, v vodni pari pri 350 °C in 16 MPa

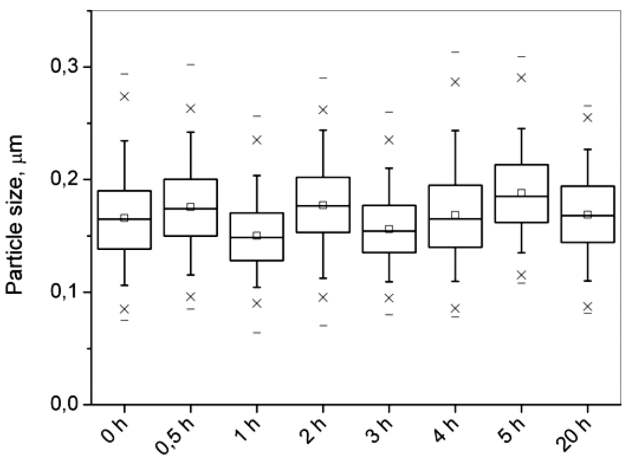

Figure 3: Box charts of the crystal-size distribution of $BaTiO_3$ synthesized in water vapour at 350 °C and 16 MPa for 0–20 h

Slika 3: Škatlasti diagram razporeditve velikosti kristalnih zrn $BaTiO_3$, sintetiziranih od 0 do 20 ur, v vodni pari pri 350 °C in 16

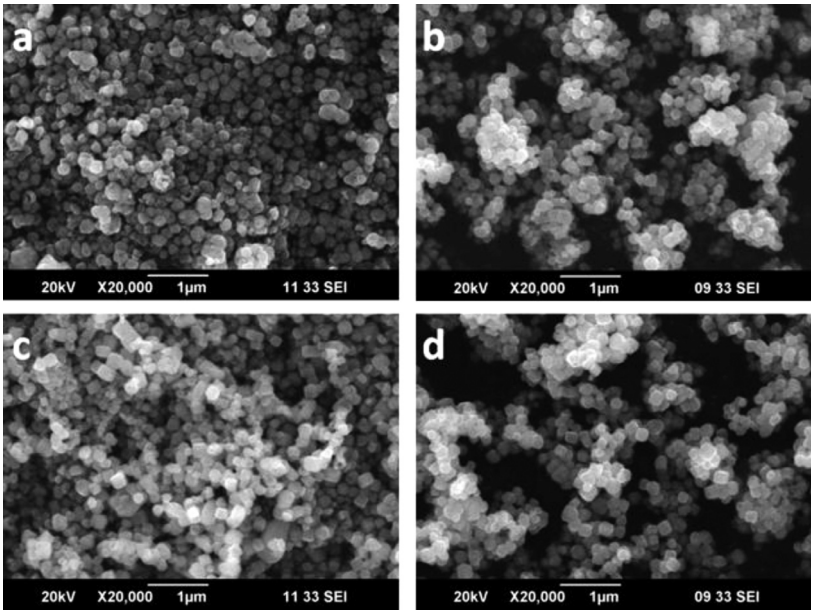

Figure 4: SEM images of $BaTiO_3$ synthesized in water vapour at 350 °C and 16 MPa for: a) 0 h, b) 3 h, c) 4 h, d) 20 h
Slika 4: SEM posnetki $BaTiO_3$, sintetiziranega v vodni pari pri 350 °C in 16 MPa po: a) 0 urah, b) 3 urah, c) 4 urah, d) 20 urah

size is reduced. This effect can be explained with the interaction of the excessive amounts of $Ba(OH)_2$ in the reacting mixture with the already formed $BaTiO_3$. It is known that the crystallite size from the Scherrer equation is sensitive to phase inhomogeneities.

In the SEM images of the synthesized samples the crystals of $BaTiO_3$ exhibit a narrow size distribution. The average crystal size slightly varies in a range of 150–188 nm without a distinct relation to the duration of the synthesis (**Figure 3**). There is a clear effect of the reaction time on the shape of the crystals. The samples processed for 0–3 h consist of sphere-shaped particles (**Figures 4a** and **4b**). A longer processing leads to a

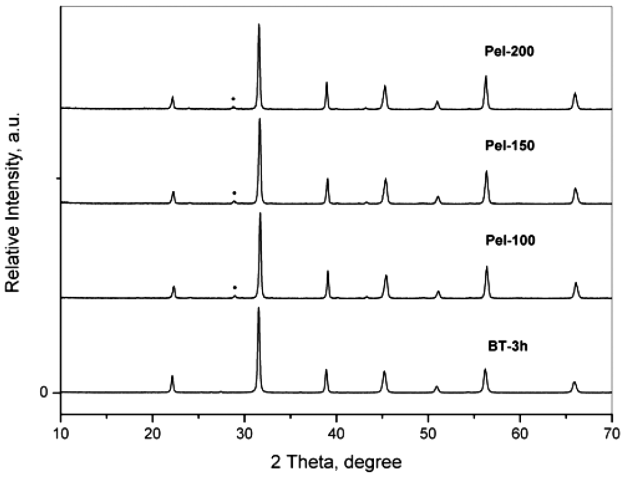

Figure 5: XRD patterns of the $BaTiO_3$ pellets pressed at 100–200 MPa and sintered at 1300 °C for 1 h and $BaTiO_3$ powder BT 3 h used as the raw material
Slika 5: Rentgenogram peletov $BaTiO_3$, stisnjenih pri 100–200 MPa in sintranih 1 uro na 1300 °C in prah $BaTiO_3$ po 3 urah, uporabljen kot surovina

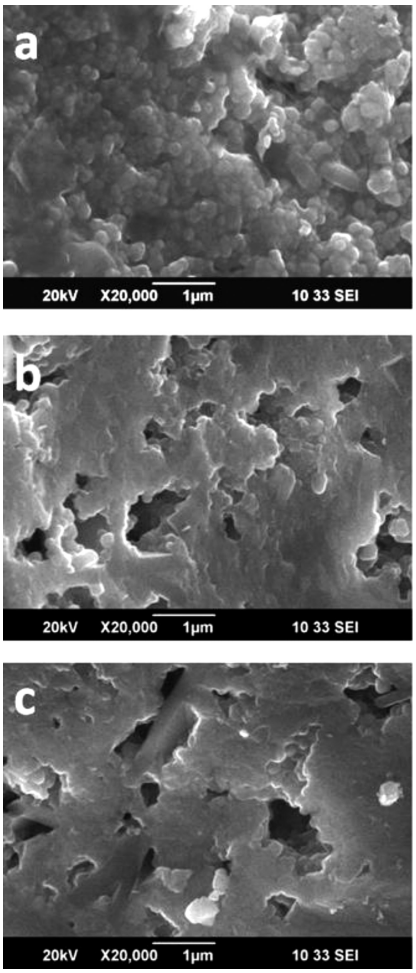

Figure 6: SEM images of the $BaTiO_3$ pellets pressed at: a) 100 MPa, b) 150 MPa, c) 200 MPa, and sintered at 1300 °C for 1 h
Slika 6: SEM posnetki $BaTiO_3$ peletov, stisnjenih pri: a) 100 MPa, b) 150 MPa, c) 200 MPa in sintranih 1 uro na 1300 °C

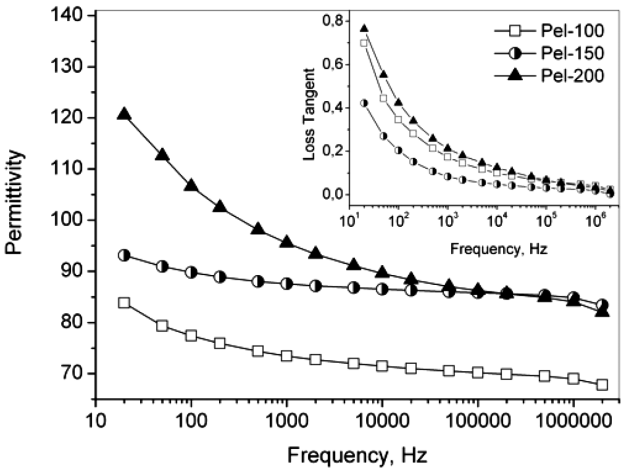

Figure 7: Frequency dependencies of the permittivity and loss tangent of the $BaTiO_3$ ceramic pellets pressed at 100–200 MPa and sintered at 1300 °C for 1 h

Slika 7: Frekvenčna odvisnost permitivnosti in tangenta izgub $BaTiO_3$ keramičnih peletov, stisnjenih pri 100-200 MPA in sintranih 1 uro na 1300 °C

formation of crystal facets. In the sample synthesized for 4 h cube-shaped particles could be observed among the sphere-shaped ones and, after 20 h, the sample mainly consisted of faceted crystals (**Figures 4c** and **4d**). The formation of the faceted crystals is related to the $BaTiO_3$ structure perfection due to its interaction with water vapour.

Ceramic pellets were manufactured from the $BaTiO_3$ powder sample synthesized in water vapour for 3 h, so that it consisted of pure, crystalline and sphere-shaped $BaTiO_3$ particles. Three pellets were shaped at different compacting pressures, while the temperature and duration of the sintering were taken from the literature.[19–23] The geometric density of the pellets was 84–86 % of the theoretical value of 6.01 g/cm^3 (**Table 1**) and it naturally rose with the increase in the compaction pressure. In addition to the $BaTiO_3$, the XRD analysis showed the presence of an impurity phase in every pellet at $2\theta = 29$ ° (**Figure 5**), which is a complex barium aluminate titanate originating from the milling process.

Table 1: Ceramic-processing conditions and density of the pellets

Tabela 1: Pogoji pri izdelavi keramike in gostota peletov

Pellet	Compacting pressure, MPa	Sintering temperature, °C	Density, g/cm^3	Relative density, %
Pel-100	100	1300	5.07	84
Pel-150	150		5.14	86
Pel-200	200		5.15	86

In the SEM images the pellets consist of the grains of 160–180 nm in size. Typical features of the pellet microstructure are sub- and micron-sized pores and plates (**Figures 6a** to **6c**). The presence of the plates shows that the recrystallization occurred during the sintering and suggests that the temperature of 1300 °C chosen on the basis of the reference literature is higher than the appropriate sintering temperature for the thermo-vaporous $BaTiO_3$ powder.

The frequency dependence of the dielectric permittivity and loss tangent is shown in **Figure 7**. The values of both parameters decrease with the increase in the frequency. This phenomenon is common for all dielectrics. The higher the frequency the less polarization can be realized in a dielectric.[24] As the permittivity is a parameter that shows the polarizability of a dielectric,[25] it is reduced with a frequency increase. Notably, the permittivity of the pellets shows a strong dependence on the compacting pressure. The permittivity of the pellet manufactured at 150 MPa exhibits the smallest variation in the range of 20 kHz–2 MHz in comparison with the other two pellets. Both the pellets made at 200 MPa and 100 MPa show a more pronounced variation in the permittivity (**Figure 7**). The loss tangent shows a similar tendency as the permittivity, depending on the frequency, and the pellet prepared at 150 MPa exhibits the lowest values of tg δ among the three examined pellets. Comparing these results, it can be concluded that 150 MPa is the most appropriate compacting pressure for thermo-vaporous $BaTiO_3$ ceramics.

4 CONCLUSION

The present work reports on the results of a thermo-vaporous synthesis and ceramic processing of crystalline $BaTiO_3$. The optimum duration of the synthesis in water vapour at 350 °C and 16 MPa is 3 h in order to obtain a raw material for ceramics. The study of the ceramic microstructure showed that the sintering temperature for the thermo-vaporous $BaTiO_3$ powder should be lower than 1300 °C. For the ceramics with the permittivity weakly dependent on the frequency in the range of 20 Hz–2 MHz and a low loss tangent, the compacting pressure of 150 MPa involving 1 % PVA as the binder is the most applicable.

Acknowledgements

This work was partly supported by the M. V. Lomonosov State University Program of Development. The authors are thankful to Dr. G. P. Muravieva for the help with the XRD analysis and S. A. Chernyak for the SEM study.

5 REFERENCES

[1] W. Maison, R. Kleeberg, R. B. Heimann, S. Phanichphant, Phase content, tetragonality and crystallite size of nanoscaled barium titanate synthesized by catecholate process: effect of calcination temperature, J. Eur. Ceram. Soc., 23 (**2003**) 1, 127–132, doi:10.1016/S0955-2219(02)00071-7

[2] D. H. Yoon, B. I. Lee, Processing of barium titanate tapes with different binders for MLCC applications – Part I: Optimization using design of experiments, J. Eur. Ceram. Soc., 24 (**2004**) 5, 739–752, doi:10.1016/S0955-2219(03)00333-9

[3] U. A. Joshi, S. Yoon, S. Baik, J. S. Lee, Surfactant-free hydrothermal synthesis of highly tetragonal barium titanate nanowires: a structural investigation, J. Phys. Chem. B., 110 (**2006**), 12249–12256, doi:10.1021/jp0600110

[4] D. Padalia, G. Bisht, U. C. Johri, K. Asokan, Fabrication and characterization of cerium doped barium titanate/PMMA nanocomposites, Solid State Sciences, 19 (**2013**), 122–129, doi:10.1016/j.solidstatesciences.2013.02.002

[5] Ch. Pithan, D. Hennings, R. Waser, Progress in synthesis of nanocrystalline $BaTiO_3$ powders for MLCC, Int. J. Appl. Ceram. Technol., 2 (**2005**) 1, 1–14, doi:10.1111/j.1744-7402.2005.02008.x

[6] D. H. Yoon, Tetragonality of barium titanate powder for ceramic capacitor application, Journal of Ceramic Processing Research, 7 (**2006**) 4, 343–354

[7] W. S. Jung, J. H. Kim, H. T. Kim, D. H. Yoon, Effect of temperature schedule on the particle size of barium titanate during solid-state reaction, Materials Letters, 64 (**2010**) 2, 170–172, doi:10.1016/j.matlet.2009.10.035

[8] V. Vinithini, P. Singh, M. Balasubramanian, Synthesis of barium titanate nanopowder using polymeric precursor method, Ceramics International, 32 (**2006**) 2, 99–103, doi:10.1016/j.ceramint.2004.12.012

[9] P. Duran, F. Capel, J. Tartaj, D. Gutierrez, C. Moure, Heating-rate effect on the $BaTiO_3$ formation by thermal decomposition of metal citrate polymeric precursors, Solid State Ionics, 141–142 (**2001**), 529–539, doi:10.1016/S0167-2738(01)00742-1

[10] A. Purwanto, W. N. Wang, I. W. Lenggoro, K. Okuyama, Formation of $BaTiO_3$ nanoparticles from an aqueous precursor by flame-assisted spray pyrolysis, J. Eur. Ceram. Soc., 27 (**2007**) 16, 4489–4497, doi:10.1016/j.jeurceramsoc.2007.04.009

[11] M. R. Mohammadi, D. J. Fray, Sol-gel derived nanocrystalline and mesoporous barium strontium titanate prepared at room temperature, Particuology, 9 (**2011**) 3, 235–242, doi:10.1016/j.partic.2010.08.012

[12] Y. B. Khollam, A. S. Deshpande, H. S. Potdar, S. B. Deshpande, S. K. Date, A. J. Patil, A self-sustaining acid-base reaction in semi-aqueous media for synthesis of barium titanyl oxalate leading to $BaTiO_3$ powders, Materials Letters, 55 (**2002**) 3, 175–181, doi:10.1016/S0167-577X(01)00642-5

[13] K. Y. Chen, Y. W. Chen, Preparation of barium titanate ultrafine particles from rutile titania by a hydrothermal conversion, Powder Technology, 141 (**2004**) 1–2, 69–74, doi:10.1016/j.powtec.2004.03.002

[14] S. G. Kwon, K. Choi, B. I. Kim, Solvothermal synthesis of nano-sized tetragonal barium titanate powders, Materials Letters, 60 (**2006**) 7, 979–982, doi:10.1016/j.matlet.2005.10.089

[15] M. N. Danchevskaya, Yu. D. Ivakin, S. N. Torbin, G. P. Muravieva, O. G. Ovchinnikova, Thermovaporous synthesis of complicated oxides, J. Mater. Sci., 41 (**2006**) 5, 1385–1390, doi:10.1007/s10853-006-7411-0

[16] Yu. D. Ivakin, M. N. Danchevskaya, G. P. Muravieva, Kinetic model and mechanism of $Y_3Al_5O_{12}$ formation in hydrothermal and thermovaporous synthesis, High Pressure Research, 20 (**2001**) 1–6, 87–98, doi:10.1080/08957950108206156

[17] A. A. Kholodkova, M. N. Danchevskaya, A. S. Fionov, Investigation of fine-crystalline barium titanate synthesized in water fluid, Abstr. of the XIV Inter. Scientific Conf. High-Tech in Chemical Engineering, Tula, 2012, 547

[18] A. A. Kholodkova, M. N. Danchevskaya, A. S. Fionov, Study of nanocrystalline barium titanate formation in water vapour conditions, Proc. of the 4th Inter. Conf. NANOCON 2012, Brno, 2012, 66–71

[19] W. Cai, C. Fu, Z. Lin, X. Deng, Vanadium doping effect on microstructure and dielectric properties of barium titanate ceramics, Ceramics International, 37 (**2011**), 3643–3650, doi:10.1016/j.ceramint.2011.06.024

[20] M. M. Vijatovic Petrovic, J. D. Bobic, T. Ramoska, B. D. Stojanovic, Electrical properties of lanthanum doped barium titanate ceramics, Materials Characterization, 62 (**2011**), 1000–1006, doi:10.1016/j.matchar.2011.07.013

[21] P. Kumar, S. Singh, M. Spah, J. K. Juneja, Ch. Pracash, K. K. Raina, Synthesis and dielectric properties of substituted barium titanate ceramics, J. of Alloys and Compounds, 489 (**2010**), 59–63, doi:10.1016/j.jallcom.2009.08.024

[22] S. B. Narang, D. Kaur, Sh. Bahel, Dielectric properties of lanthanum substituted barium titanate microwave ceramics, Materials Letters, 60 (**2006**), 3179–3182, doi:10.1016/j.matlet.2006.02.079

[23] L. J. Gao, X. L. Liu, J. Q. Zhang, S. Q. Wang, J. F. Chen, Grain-controlled barium titanate ceramics prepared from high-gravity reactive precipitation process powder, Materials Chemistry and Physics, 88 (**2004**), 27–31, doi:10.1016/j.matchemphys.2004.03.023

[24] T. Lee, I. A. Aksay, Hierarchical structure-ferroelectricity relationship of barium titanate particles, Crystal Growth & Design, 1 (**2001**) 5, 401–419, doi:10.1021/cg010012b

[25] B. M. Yavorskiy, A. A. Detlaf, Spravochnik po fizike, Nauka, Moscow 1974

UDK 669.721.5:621.793:620.197
Professional article/Strokovni članek

ISSN 1580-2949
MTAEC9, 49(3)453(2015)

HYBRID SOL-GEL COATINGS DOPED WITH CERIUM TO PROTECT MAGNESIUM ALLOYS FROM CORROSION

HIBRIDNI SOL-GEL-NANOSI, DOPIRANI S CERIJEM, ZA KOROZIJSKO ZAŠČITO MAGNEZIJEVIH ZLITIN

Noé Verner Murillo-Gutiérrez, Florence Ansart, Jean-Pierre Bonino, Marie-Jöelle Menu, Marie Gressier

Université de Toulouse UPS-INP-CNRS, Institut Carnot CIRIMAT, 118 Route de Narbonne, 31062 – Toulouse CEDEX 09, France
murillo@chimie.ups-tlse.fr

Prejem rokopisa – received: 2014-05-12; sprejem za objavo – accepted for publication: 2014-09-03

doi:10.17222/mit.2014.077

Hybrid coatings produced via the sol-gel route were deposited onto an Elektron 21 magnesium alloy. The sol consisted of tetraethyl-orthosilicate (TEOS) and 3-(trimethoxysilyl)propylmethacrylate (MAP) to which corrosion inhibitors were added. The influence of the cerium concentration on the anti-corrosion properties of the hybrid coating is presented. Furthermore, the morphology of the organic/inorganic coatings deposited on the magnesium alloy was determined with scanning electron microscopy (SEM). In parallel, the electrochemical behavior during the immersion in a 0.05 M NaCl corrosive solution was studied with electrochemical impedance spectroscopy (EIS). It was proven that the hybrid films exhibit a high impedance modulus during the first hours of the immersion and that an addition of cerium to the sol with a concentration of 0.01 M considerably increases the durability of the film, delaying its degradation during the immersion. In addition, this project especially focusses on determining the critical concentration of the cerium salt at which the impedance modulus of the hybrid coating strongly decreases during the immersion.

Keywords: magnesium, coating, sol-gel, corrosion inhibitor, EIS

Hibridni nanosi, pripravljeni s sol-gel-postopkom, so bili naneseni na magnezijevo zlitino Elektron 21. Osnova je bila tetraetil-ortosilikat (TEOS) in 3-(trimetoksisilil)propilmetakrilat (MAP), ki so ji bili dodani inhibitorji korozije. Predstavljen je vpliv koncentracije cerija na protikorozijske lastnosti hibridnega nanosa. Poleg tega je bila določena morfologija organskih/neorganskih nanosov na magnezijevo zlitino z vrstičnim elektronskim mikroskopom (SEM). Vzporedno je bilo preučevano elektrokemijsko vedenje med potopitvijo v korozijsko raztopino 0,05 M NaCl, z uporabo elektrokemijske impedančne spektroskopije (EIS). Dokazano je bilo, da izkazujejo hibridni nanosi visok impedančni modul med prvimi urami namakanja in da dodatek cerija osnovi v koncentraciji 0,01 M močno poveča zdržljivost nanosa z zadržanjem njegove degradacije med namakanjem. Ta projekt je bil usmerjen v določanje kritične koncentracije cerijeve soli, pri kateri se impedančni modul hibridnega nanosa močno zmanjša med namakanjem.

Ključne besede: magnezij, nanos, sol-gel, inhibitor korozije, EIS

1 INTRODUCTION

With a density equivalent to 2/3 of that of aluminium, magnesium and its alloys are interesting weight-saving materials for the automotive and aeronautics industries. However, compared to steel and aluminium alloys, magnesium alloys have a very low corrosion resistance. In order to prevent this problem, various surface treatments and coatings have been developed with different techniques over the last few years[1,2]. However, most of these processes make use of chromium (Cr VI) compounds, nowadays forbidden by international regulations since these are classified as carcinogen, mutagenic and reprotoxic compounds. The sol-gel route is an efficient method to produce "green" coatings and their anti-corrosion performances have been proven successful on steel and aluminium alloys.[3–5] This project aims to evaluate the anti-corrosive properties of a hybrid coating obtained via the sol-gel route and deposited on a cast Elektron 21 magnesium alloy (El21) and, secondly, to identify its mechanisms.

2 METHODOLOGY

2.1 Preparation of the materials and coatings

Samples with the dimensions of 40 mm × 20 mm × 6 mm were obtained by making cuttings from a cast Elektron 21 (El21) alloy. The chemical composition of this alloy is shown in **Table 1**. The samples were first mechanically polished with abrasive papers with a grit of up to grade 4000, then with alumina paste (3 μm and 1 μm) and finally they were rinsed with ethanol and dried under a flux of cold air.

Table 1: Chemical composition of the Elektron 21 cast alloy in mass fractions, *w*/%
Tabela 1: Kemijska sestava livne zlitine Elektron 21 v masnih deležih, *w*/%

Element	Nd	Gd	Zr	Zn	Other rare earths	Mg
w/%	3.1	1.7	1	0.5	< 0.4	Balance

The sols were produced by mixing the starting precursors consisting of tetraethyl-orthosilicate (TEOS) and

3-(trimethoxysilyl)propyl-methacrylate (MAP), deionized water and ethanol with a molar ratio of 11 : 1 : 60 : 80, under constant stirring and at room temperature. In order to adjust the pH of the sol to 4, nitric acid (HNO_3) was drop-added to the mixture when required. The production of cerium-doped sols was performed by adding cerium nitrate ($Ce(NO_3)_3 \cdot 6H_2O$) at four different concentrations: (0.005, 0.01, 0.05 and 0.1) mol L^{-1}. The addition of the cerium salt was carried out by previously dissolving this compound in the corresponding water volume of the formulation. After maturing for 24 h, the sols were deposited on the magnesium El21 substrates using the dip-coating technique, at a controlled withdrawal speed of 200 mm min^{-1}. They were then dried at 60 °C for 20 min.

2.2 Characterization techniques

The microstructures of the El21 substrate and the sol-gel coatings were analyzed with scanning electron microscopy (SEM) using a JEOL JSM-6510LV microscope, at an operating voltage of 20 kV. Electrochemical tests of the open circuit potential (E_{ocp}) and electrochemical impedance spectroscopy (EIS) were performed in 0.05 mol L^{-1} of a NaCl corrosive solution at room temperature, using a Bio-Logic SP-150 potentiostat. The electrochemical cell consisted of a one-chamber three-electrode cell, the working electrode having an exposed area of 2 cm^2, delimited with an insulating tape. The reference and auxiliary electrodes included a saturated calomel electrode (SCE) and a platinum-foil electrode, respectively. The EIS spectra were drawn using the potentiostatic mode and a frequency ranging from 100 mHz and 10 mHz, with an applied voltage oscillation of 10 mV vs. OCP. For each test, three samples were analyzed in order to check the reproducibility of the tests.

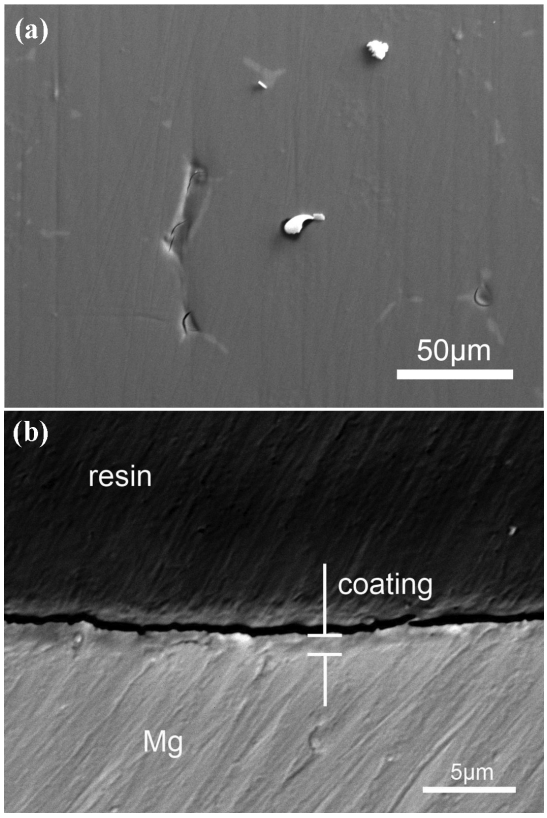

Figure 1: SEM images of the hybrid sol-gel coating on the El21 magnesium alloy: a) surface of the coating, b) cross-section of the substrate in the BSE mode

Slika 1: SEM-posnetka sol-gel hibridnega nanosa na magnezijevi zlitini El21: a) površina nanosa, b) prečni prerez podlage v BSE-načinu

3 RESULTS AND DISCUSSION

3.1 Morphology of the hybrid coatings

The microstructure of a hybrid sol-gel coating was first observed with SEM (**Figure 1**). The surface of the coating (a) shows a homogeneous surface, with the presence of some cracks and defects spotted in the neodymium-rich zones. The origin of these defects may be attributed to the formation of a galvanic couple between this intermetallic phase and the alpha phase of magnesium[2], and to the internal stresses of the hybrid coating that lead to fracture. A cross-sectional observation of the substrate in the BSE (back-scattered electrons) mode (b) allows the thickness of the hybrid coating to be measured at around 1 µm.

3.2 Electrochemical characteristics of the hybrid coatings

Firstly, the open-circuit potential of the samples was recorded during the immersion of the substrates in a corrosive solution containing 0.05 mol L^{-1} of NaCl (**Figure 2**). All the samples exhibit a similar behavior, except

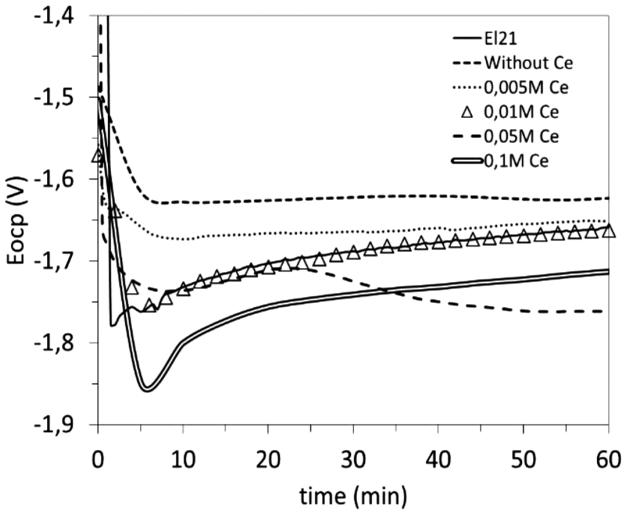

Figure 2: Evolution of the open-circuit potential (E_{ocp}) of the hybrid coatings doped with cerium of different concentrations, during the immersion in a corrosive solution of 0.05 mol L^{-1}

Slika 2: Razvoj potenciala odprtega kroga (E_{ocp}) hibridnega nanosa, dopiranega s cerijem v različnih koncentracijah, med namakanjem v korozijski raztopini 0,05 mol L^{-1}

the hybrid coatings that were non-doped or doped with 0.005 mol L^{-1} of Ce. These show a stabilized potential from the beginning of the immersion, at around –1.63 V and –1.65 V, respectively, attributed to the insulating effect of the protective coating. In contrast, the sol-gel coatings containing 0.01 mol L^{-1} or higher concentrations, present a behavior similar to that of the bare El21 alloy. This is related to the growth of the passive layer and corrosion products at the surface of the substrates, due to the reaction with the electrolyte.[6]

Secondly, the hybrid coatings were tested with EIS after 1 h of the immersion in the corrosive solution, right after the OCP recording. The Bode plots of the EIS spectra obtained for different protective systems are shown in **Figure 3**. It is worth noting that only the hybrid coating doped with 0.1 mol L^{-1} presents a behavior similar to that of the bare El21 substrate. The Bode phase-angle diagram (a) shows that the last group presents two time constants, at the high and low frequencies (10 kHz and 1 Hz, respectively). The first is normally attributed to the capacitive response of a hybrid sol-gel coating, which indicates that this film has a physical barrier effect.[7] The second time constant is attributed to the presence of a porous layer in the corrosion products.[8] It is important to observe that the phase angle of a hybrid coating is the highest when it is doped with 0.01 mol L^{-1} of cerium. On the other hand, the impedance modulus (b) obtained at a low frequency (10 mHz) is typically assigned to the resistance of the electrochemical system, and so to its corrosion resistance.[9] The cerium concentrations lower than 0.1 mol L^{-1}, especially 0.01 mol L^{-1}, exhibit higher impedance values. **Figure 4** presents the evolution of a hybrid coating doped with 0.01 mol L^{-1} during its immersion in the corrosive solution. The time constant attributed to the coating gradually disappears with the immersion time (**Figure 4a**, the time constant at 10 kHz), simultaneously with the shift of the time constant at a low frequency from 1 Hz to 20 Hz. After 48 h of immersion, both curves, representing the bare El21 substrate and the hybrid coating, are superimposed, meaning that the coating lost its protective properties. However, the corrosion resistance of the hybrid film, depicted by the impedance modulus at a low frequency (**Figure 4b**) shows a progressive decrease with the time.

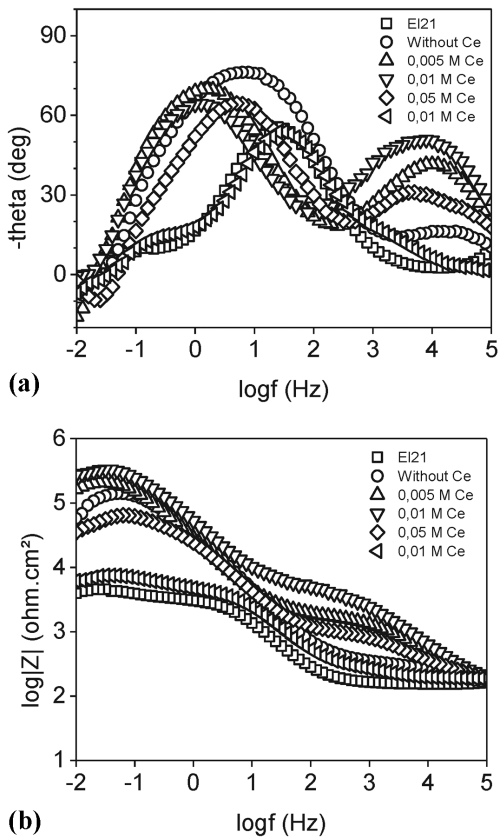

Figure 3: EIS spectra of the El21 magnesium alloy covered with the hybrid coating, doped with different concentrations of cerium. Results obtained after 1 hour of immersion in 0.05 mol L^{-1} of NaCl: a) phase-angle diagram, b) impedance modulus.

Slika 3: EIS-spektri magnezijeve zlitine El21 s hibridnim nanosom, dopiranim z različnimi koncentracijami cerija. Rezultati, dobljeni po 1 h namakanja v 0,05 mol L^{-1} NaCl: a) fazni kotni diagram, b) impedančni modul.

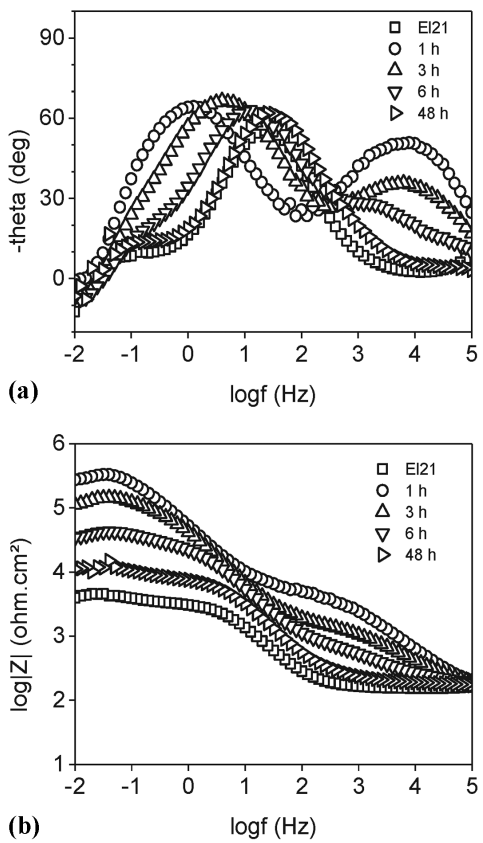

Figure 4: Bode plots of the results obtained with EIS for the hybrid coating doped with 0.01 mol L^{-1} of cerium, during immersion in the corrosive solution (0.05 mol L^{-1}): a) phase-angle diagram, b) impedance modulus

Slika 4: Bodejev diagram rezultatov, dobljenih z EIS hibridnega nanosa, dopiranega z 0,01 mol L^{-1} cerija, med namakanjem v korozijski raztopini (0,05 mol L^{-1}): a) fazni kotni diagram, b) impedančni modul

Here, it is proven that the hybrid coating doped with 0.01 mol L^{-1} of cerium has the best corrosion resistance. Higher or lower concentrations of cerium decrease the coating resistance and capacitance, which leads to a rapid loss of the protective properties.[10] The inhibiting properties of this element are strongly determined by the ion concentration inside the hybrid film,[11] showing the existence of the optimum cerium concentration. This is due to the formation of insoluble compounds such as CeO_2 and $Ce(OH)_3$ [12] that temporally block the passage of the corrosive species through the hybrid coating to the metallic substrate.

4 CONCLUSION

A hybrid sol-gel coating offers a slight protection to a magnesium substrate during the first hours of an immersion. Moreover, an addition of cerium inside the coating with the optimum concentration of 0.01 mol L^{-1} leads to the increase of its anti-corrosion properties. This is due to the corrosion-inhibiting effect of cerium ions that allows a formation of insoluble compounds, enhancing the resistance of the hybrid coating to corrosive species.

Acknowledgments

The FDA and the OSEO are gratefully acknowledged for the funding provided for this project. The authors would like to thank the partners in the FUI CARAIBE project and its coordinator: the SAFRAN group.

5 REFERENCES

[1] J. E. Gray, B. Luan, Journal of Alloys and Compounds, 336 (**2002**), 88-113, doi:10.1515/bmt-2014-4495

[2] R. G. Hu, S. Zhang, J. F. Bu, C. J. Lin, G. L. Song, Progress in Organic Coatings, 73 (**2012**), 129-141, doi:10.1016/j.porgcoat.2011.10.011

[3] E. Certhoux, F. Ansart, V. Turq, J. P. Bonino, J. M. Sobrino, J. Garcia, J. Reby, Progress in Organic Coatings, 76 (**2013**), 165-172, doi:10.1016/j.porgcoat.2012.09.002

[4] H. B. Lu, Y. Hu, M. H. Gu, S. C. Tang, H. M. Lu, X. K. Meng, Surface and Coatings Technology, 204 (**2009**), 91-98, doi:10.1016/j.surfcoat.2009.06.035

[5] N. C. Rosero-Navarro, L. Paussa, F. Andreatta, Y. Castro, A. Duran, M. Aparicio, L. Fedrizzi, Progress in Organic Coatings, 69 (**2010**), 167-174, doi:10.1016/j.porgcoat.2010.04.013

[6] G. Baril, N. Pebere, Corrosion Science, 43 (**2001**), 471-484, doi:10.1016/S0010-938X(00)00095-0

[7] S. V. Lamaka, G. Knornschild, D. V. Snihirova, M. G. Taryba, M. L. Zheludkevich, M. G. S. Ferreira, Electrochimica Acta, 55 (**2009**), 131-141, doi:10.1016/j.electacta.2009.08.018

[8] I. A. Kartsonakis, A. C. Balaskas, E. P. Koumoulos, C. A. Charitidis, G. Kordas, Corrosion Science, 65 (**2012**), 481-493, doi:10.1016/j.corsci.2012.08.052

[9] G. W. Walter, Corrosion Science, 26 (**1986**), 27-38, doi:10.1016/0010-938X(86)90120-4

[10] P. S. Correa, C. F. Malfatti, D. S. Azambuja, Progress in Organic Coatings, 72 (**2011**), 739-747, doi:10.1016/j.porgcoat.2011.08.005

[11] W. Trabelsi, P. Cecilio, M. G. S. Ferreira, M. F. Montemor, Progress in Organic Coatings, 54 (**2005**), 276-284, doi:10.1016/j.porgcoat.2005.07.006

[12] M. F. Montemor, M. G. S. Ferreira, Electrochimica Acta, 52 (**2007**), 7486-7495, doi:10.1016/j.electacta.2006.12.086

UDK 669.715:621.791
Professional article/Strokovni članek

ISSN 1580-2949
MTAEC9, 49(3)457(2015)

INFLUENCE OF THE TOOL GEOMETRY AND PROCESS PARAMETERS ON THE STATIC STRENGTH AND HARDNESS OF FRICTION-STIR SPOT-WELDED ALUMINIUM-ALLOY SHEETS

VPLIV GEOMETRIJE ORODJA IN PARAMETROV PROCESA NA STATIČNO TRDNOST IN TRDOTO PRI VRTILNO-TORNEM TOČKASTEM VARJENJU PLOČEVIN IZ Al-ZLITINE

Hande Güler

Uludag University, Faculty of Engineering, Department of Mechanical Engineering, 16059 Gorukle-Bursa, Turkey
handeguler@uludag.edu.tr

Prejem rokopisa – received: 2014-06-07; sprejem za objavo – accepted for publication: 2014-07-22

doi:10.17222/mit.2014.087

In this study, the effects of the tool geometry and welding parameters on the friction-stir spot-welding properties of AA 5754-H111 were studied. Two different tool-pin geometries were used and tensile shear tests were carried out to compare the weld strength. Hardness observations were also done. The optimum tool geometry for the mentioned material was determined as the circular pin tool and the tapered pin tool gave the lowest tensile shear load.

Keywords: Al-alloys, friction-stir spot welding, mechanical properties, hardness

V tej študiji so bili preučevani vplivi geometrije orodja in parametrov varjenja na torno- vrtilno točkasto varjenje zlitine AA 5754-H111. Dve različni geometriji konice orodja sta bili uporabljeni in opravljeni so bili natezni strižni preizkusi za primerjavo trdnosti zvara. Opravljene so bile tudi meritve trdote. Za ta material je bilo ugotovljeno, da je optimalna geometrija orodja v obliki okrogle konice, pri stožčasti konici orodja pa je bila ugotovljena najmanjša strižna trdnost.

Ključne besede: Al-zlitine, torno-vrtilno točkasto varjenje, mehanske lastnosti, trdota

1 INTRODUCTION

Friction-stir spot welding (FSSW) is an alternative method for spot welding of lightweight alloys that was developed by Mazda Motor Corporation and Kawasaki Heavy Industries in 2003.[1] The FSSW method consists of three phases: plunging, stirring and retraction. In these phases, a cylindrical rotating tool plunges at a specific rate into the overlapping sheets to a predetermined depth. It is then retracted at a rapid rate either immediately or after a dwell period. The heating is achieved with the friction between the tool and the workpieces causing a plastic deformation of the workpieces. The localized heating softens the material around the pin and the forging pressure applied with the tool shoulder results in the formation of an annular, solid-state bond around the pin. The retraction of the pin leaves a characteristic exit hole.[2]

The significant parameters that determine the strength of FSSW joints are the rotational speed, the dwell time and the tool plunge depth and this method has been successfully applied to aluminum, magnesium, advanced high-strength steel and polymers.[3] There have been several papers relating to different FSSW process parameters and different materials.

Külekçi[4] investigated the effects of the FSSW parameters such as the tool rotation, the dwell time and the tool-pin height on the tensile shear strength of an EN AW 5005 aluminium alloy and determined the optimum parameters. Tozaki et al.[5] proposed a new tool which uses a scroll groove to displace the material in the vertical direction instead of the profiled pin and compared it with the conventional convex-shoulder tool with a cylindrical pin. They found that the new tool exhibited equal, or superior, results compared with the conventional tool.

FSSW of an Al-alloy 6016-T4 sheet was evaluated by Yuan et al.[6] using the conventional pin tool and off-center feature tool. Different parameters were investigated to determine the lap-shear separation load and they found that the tool rotational speed and plunge depth influenced the shear strength. Badarinarayan et al.[7] studied the effects of the shoulder and pin geometry on the hook formation, and the material flow of a friction-stir spot-welded 5754-O aluminum alloy was investigated. Külekçi et al.[8] explored the hardness distribution and the tensile shear strength of FSSW welds of the EN AW 5005 aluminum alloy and compared them with resistance spot welding.

The effects of three tool shapes (threaded-pin tool: TPT; cylindrical tool: CT; cylindrical tool with projection: CTP) and the tool penetration depth on the joint strength of a FSSW commercial AA 5J32 alloy with a nominal composition in mass fractions (w/%) of Al-5.54Mg-0.03Si-0.07Fe-0.32Cu-0.03Ti-0.01Zn was investigated by Choi et al.[9] The CTP (cylindrical tool

Table 1: Chemical composition of the investigated material in mass fractions, *w*/%
Tabela 1: Kemijska sestava preiskovanega materiala v masnih deležih, *w*/%

	Si	Fe	Mn	Mg	Cu	Ti	Cr	Zn	Al
Chemical composition	0.071	0.251	0.19	2.834	0.022	0.003	0.024	0.049	Balance

with projection) showed the best mechanical properties compared to the other tool shapes.

Karthikeyan and Balasubramanian[10] aimed at optimizing the welding parameters to attain the maximum lap-shear tensile strength of a friction-stir spot-welded AA2024 aluminum alloy. For this purpose, an empirical relationship was developed to predict the tensile shear-fracture load.

In this work, the FSSW process was used with the objective to investigate the effects of different welding parameters and tool geometry on the mechanical performance of thick AA 5754-H111 1 mm. This alloy has been widely used in shipbuilding, the vehicle, chemical and nuclear industries.[11]

However, a literature review indicated that there is only one paper about the thick AA 5754-H111 1 mm.[12] Güler[12] studied the FSSW process of the thick AA 5754-H111 1 mm using only circular pinned tool. In this context, the effects of the tool design and process parameters on the weld strength and hardness distribution were studied and the effects of FSSW process were compared using the tools with circular and tapered pins.

2 EXPERIMENTAL DETAILS

Commercially available aluminium-alloy plates (AA 5754-H111) with a thickness of 1 mm were used to fabricate the joints. The chemical composition of the material is presented in **Table 1**. The tensile strength, the yield strength and the elongation are 207 MPa, 117 MPa and 21 %, respectively. The samples for the tensile shear test were machined out with the dimensions of 105 mm × 45 mm × 1 mm according to the ISO 14273 standard. The specimens were lap positioned with a 45 mm × 45 mm overlap area (**Figure 1**). The welded samples were loaded on a universal testing machine with a constant crosshead of 5 mm/min and with a load capacity of 250 kN.

FSSW was performed using two different tools made of hot-work tool steel having different pin profiles: a circular one, designated as FSSW-C and a tapered one, designated as FSSW-T. The tools with different pin geometries were selected to ensure simple manufacturing with a small amount of tool wear. As shown in **Figure 2**, each tool had a shoulder with a diameter of 15 mm and a pin length of 1.7 mm. The circular pin had a diameter of 5 mm and the tapered pin had the diameters of 5 mm at the bottom and 7 mm at the pin shoulder.

The prepared samples were joined by FSSW using different tool rotational speeds and dwell times. FSSW was performed at three tool rotational speeds, ranging from 500 r/min to 1500 r/min, while the plunge depth of the tool pin was 1.8 mm and the dwell time ranged from 6 s to 21 s. Considering each parameter, five joints at different tool rotational speeds and dwell times were produced and tested. Some samples of the FSSW joints are shown in **Figure 3**.

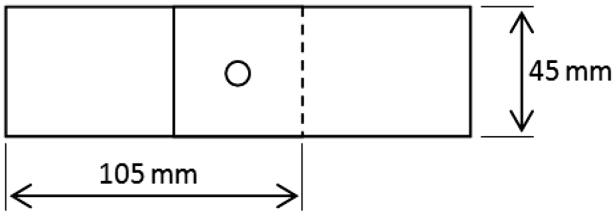

Figure 1: Lap-shear specimen
Slika 1: Vzorec s prekrivanjem za strig

3 RESULTS AND DISCUSSION

3.1 Tensile shear strength

Figure 4 shows a comparison of the shear load versus the dwell time obtained during the shear tensile testing at a constant tool rotational speed. According to **Figure 4a**, both the dwell time and the shear load of the FSSW-C welds increased, while the shear load of the FSSW-T welds remained almost constant. When using the tapered tool with a combination of a tool rotational speed 500 r/min and dwell time 6 s, the shear load increased by 55 %. Besides, at the other dwell times, the shear loads of the FSSW-C welds were higher compared to those of the FSSW-T welds.

Figure 2: Two types of tool used for FSSW: FSSW-T (tapered pin, left) and FSSW-C (circular pin, right)
Slika 2: Dve vrsti orodja, uporabljeni za FSSW: FSSW-T (konica v obliki prisekanega stožca, levo) in FSSW-C (okrogla konica, desno)

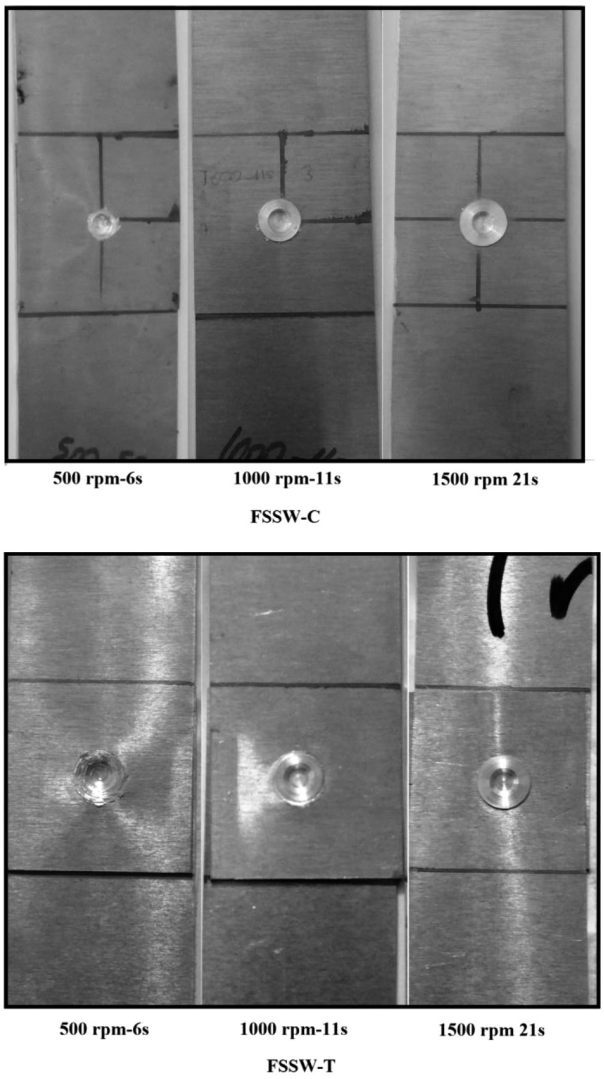

Figure 3: Samples of friction-stir spot-welded joints
Slika 3: Vzorci vrtilno-torno točkasto zvarjenih spojev

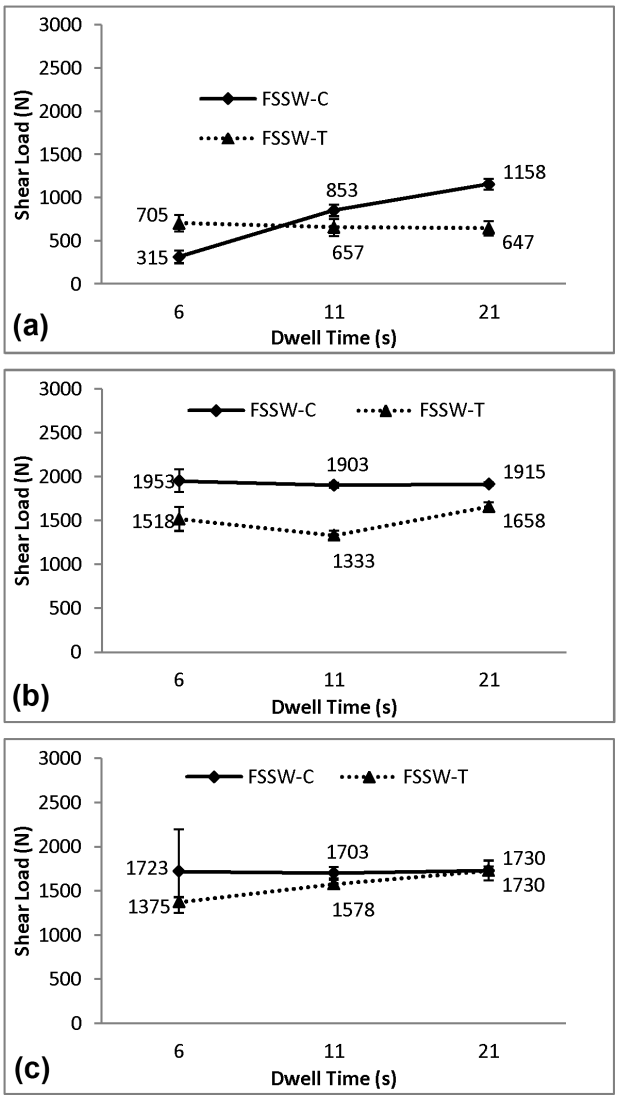

Figure 4: Shear load as a function of dwell time for both FSSW-C and FSSW-T welds at a tool rotational speed: a) 500 r/min, b) 1000 r/min, c) 1500 r/min
Slika 4: Strižna obremenitev v odvisnosti od časa zadrževanja za obe varjenji: FSSW-C in FSSW-T pri hitrosti orodja: a) 500 r/min, b) 1000 r/min, c) 1500 r/min

Figure 4b shows the shear-load values at a tool rotational speed 1000 r/min. According to the figure, the average shear loads of the FSSW-C welds are higher than the ones of the FSSW-T welds. With the combination of the tool rotational speed 1000 r/min and dwell time 11 s, the maximum increase was observed when using the circular tool which increased the shear load by approximately 43 %.

The tensile-shear-test results for 1500 r/min are given in **Figure 4c**. An increase in the dwell time from 6 s to 21 s increased the tensile shear load of the FSSW-T welds by 26 %, while the tensile shear load of the FSSW-C welds remained almost constant. On the other hand, the shear-load values were higher when a sample was welded with the FSSW-C tool compared with the FSSW-T tool.

According to all the tensile shear results, the specimens welded with the FSSW-C tool exhibited an increase in the shear load. The results of the previous investigations[7,13,14] stated that the tool-pin geometry significantly affects the hook geometry and thereby the shear-load capacity of FSSWs. An increase in the tensile shear load may be explained with the microstructural changes due to the heat generation at a stirring location.[4] When using a FSSW-T tool, the materials may be stirred severely and extensively. When the amount of the material stirred is large, the size of a bonded region also becomes large, resulting in a higher separation load.[14]

3.2 Microhardness

Hardness measurements were performed on a Vickers microhardness tester focusing at the medium-thick area of the upper sheet with a load of 100 g, dwell time of 10 s and spacing of 1 mm. The microhardness-distribution examples of the FSSW-C and FSSW-T welded joints are

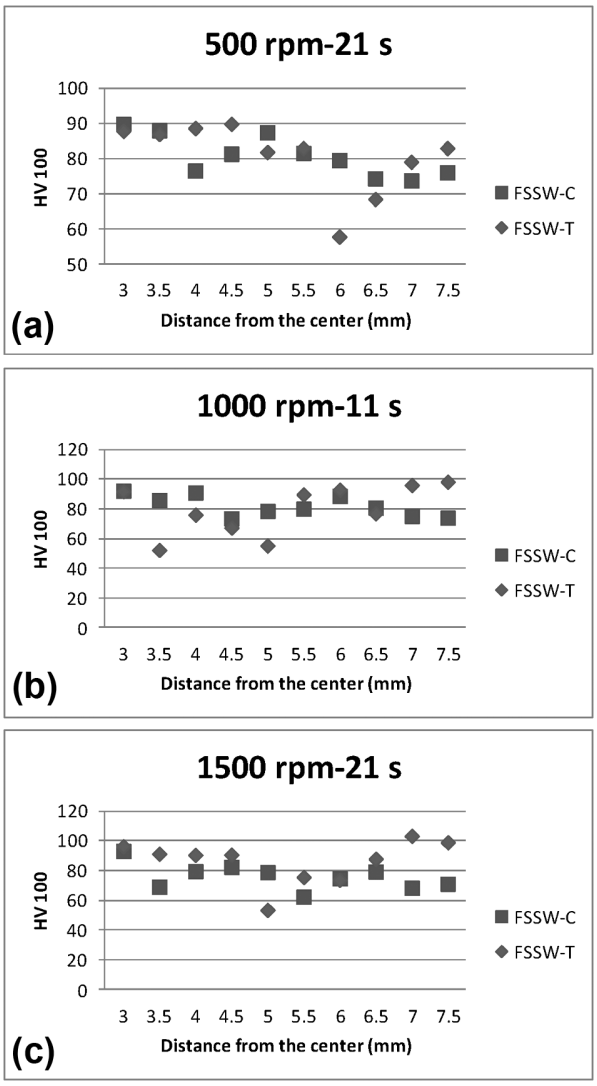

Figure 5: Hardness distribution for both FSSW-C and FSSW-T welds with a combination of: a) 500 r/min and 21 s, b) 1000 r/min and 11 s, c) 1500 r/min and 21 s

Slika 5: Razporeditev trdote za oba zvara FSSW-C in FSSW-T pri kombinaciji: a) 500 r/min in zadržanju 21 s, b) 1000 r/min in 11 s, c) 1500 r/min in 21 s

given in all the hardness profiles, and a higher Vickers microhardness was observed close to the keyhole because of a higher plastic deformation, which also caused very fine, dynamic recrystallized grains. On the other hand, in the region close to the keyhole, the FSSW-T weld had a slightly higher hardness than the FSSW-C weld. This situation occurred because of the presence of a finer grain structure observed in the stir zone of the FSSW-T weld.[13] In addition, on the basis of **Figures 5a**, **5b** and **5c**, it was concluded that the hardness distribution was somewhat scattered without a noticeable trend. There was no obvious influence of the process parameters on the hardness distribution.[4]

4 CONCLUSIONS

In this work, the mechanical properties of the AA 5754-H111 aluminum-alloy material were investigated during the FSSW process. The welding process was performed using two different types of designed tools (FSSW-C and FSSW-T), compared to each other. After analyzing the experimental results, the following conclusions can be drawn:

1. At the tool rotational speed 500 r/min, the dwell time is an influential factor in determining the tensile shear load of the FSSW-C welds, while the tensile shear loads remain almost constant at the other tool rotational speed. When using the FSSW-T tool at the rotational speed 1500 r/min, the tensile shear load increases if the dwell time increases.

2. Higher shear-load values are found for the sample welded with the FSSW-C tool, compared to the FSSW-T tool, because of a better stirring procedure.

3. There are no noticeable effects of the tool geometries and welding parameters affecting the hardness of the mentioned material.

4. As future work, different failure modes occurring during the lap-shear test could be studied to determine their effects on the tensile shear-load capacity.

5 REFERENCES

[1] W. Ratanathavorn, Hybrid Joining of Aluminum to Thermoplastics with Friction Stir Welding, Master of Science Thesis, Department of Materials Science and Engineering, KTH – Royal Institute of Technology [cited 2014-07-06], available from http://kth.diva-portal.org/smash/get/diva2:515154/FULLTEXT01.pdf

[2] S. Lathabai, M. J. Painter, G. M. D. Cantin, V. K. Tyagi, Scripta Materialia, 55 (**2006**), 899–902, doi:10.1016/j.scriptamat.2006.07.046

[3] X. Song, L. Ke, L. Xing, F. Liu, C. Huang, The International Journal of Advanced Manufacturing Technology, 71 (**2014**) 9–12, 2003–2010, doi:10.1007/s00170-014-5632-y

[4] M. K. Külekçi, Archives of Metallurgy and Materials, 59 (**2014**) 1, 221–224, doi:10.2478/amm-2014-0035

[5] Y. Tozaki, Y. Uematsu, K. Tokaji, Journal of Materials Processing Technology, 210 (**2010**), 844–851, doi:10.1016/j.jmatprotec.2010.01.015

[6] W. Yuan, R. S. Mishra, S. Webb, Y. L. Chen, B. Carlson, D. R. Herling, G. J. Grant, Journal of Materials Processing Technology, 211 (**2011**), 972–977, doi:10.1016/j.jmatprotec.2010.12.014

[7] H. Badarinarayan, Y. Shi, X. Li, K. Okamoto, International Journal of Machine Tools & Manufacture, 49 (**2009**), 814–823, doi:10.1016/j.ijmachtools.2009.06.001

[8] M. K. Külekci, U. Esme, O. Er, Mater. Tehnol., 45 (**2011**) 5, 395–399

[9] D. Choi, B. Ahn, C. Lee,Y. Yeon, K. Song, S. Jung, Materials Transactions, 51 (**2010**) 5, 1028–1032, doi:10.2320/matertrans.M2009405

[10] R. Karthikeyan, V. Balasubramanian, Int. J. Adv. Manuf. Technol., 51 (**2010**), 173–183, doi:10.1007/s00170-010-2618-2

[11] T. S. Mahmoud, T. A. Khalifa, JMEPEG, 23 (**2014**), 898–905, doi:10.1007/s11665-013-0828-0

[12] H. Güler, JOM, 66 (**2014**) 10, 2156–2160, doi:10.1007/s11837-014-1117-6

[13] H. Badarinarayan, Q. Yang, S. Zhu, International Journal of Machine Tools & Manufacture, 49 (**2009**) 2, 142–148, doi:10.1016/j.ijmachtools.2008.09.004

[14] N. Pathak, K. Bandyopadhyay, M. Sarangi, S. K. Panda, Journal of Materials Engineering and Performance, 22 (**2013**), 131–144, doi:10.1007/s11665-012-0244-x

UDK 677
Professional article/Strokovni članek

ISSN 1580-2949
MTAEC9, 49(3)461(2015)

THE STABILIZATION OF NANO SILVER ON POLYESTER FILAMENT FOR A MACHINE-MADE CARPET

STABILIZACIJA NANODELCEV SREBRA NA POLIESTRSKEM VLAKNU ZA STROJNO IZDELAVO PREPROG

Khashayar Mohajer Shojaei, Ali Farrahi, Hossein Farrahi, Ahmad Farrahi

Farrokh Sepehr Kashan Company (Farrahi Carpet), Kashan, Iran
Khashayar045@yahoo.com

Prejem rokopisa – received: 2014-07-20; sprejem za objavo – accepted for publication: 2014-09-02

doi:10.17222/mit.2014.113

Nowadays, polyester filament yarns with permanent anti-bacterial characteristics are known as an innovative yarn in the textile industry for machine-made carpets and garments. Different methods, such as chemical modification, entrapment and encapsulation, have been applied to stabilize the silver nanoparticles on polyester filament yarn for use in machine-made carpets. In this article we modified the nano-silver particles by a chemical reaction in order to produce a polyester filament yarn with permanent anti-bacterial characteristics using a spraying method. The anti-bacterial tests were carried out on the nano-silver-coated machine-made carpet according to ATCC 27853, 25923 and 25922 some 72 h before and after the washing process. The results showed that the nano-silver-coated polyester machine-made carpet has a permanent anti-bacterial characteristic.

Keywords: anti bacterial characteristic, polyester filament yarn, machine-made carpet, DLS method, washing processes, bacteria, surfactant, Mac Farlen

Dandanes je preja iz poliestrskih vlaken s trajno protibakterijsko odpornostjo poznana kot inovativna preja v tekstilni industriji za strojno izdelavo preprog in oblačil. Različne metode, kot so kemijska obdelava, ujetje in enkapsulacija, so bile uporabljene za stabilizacijo nanodelcev srebra na vlaknih poliestrske preje za strojno izdelavo preprog. Članek predstavlja modifikacijo nanodelcev srebra s kemijsko reakcijo z napršević za izdelavo vlakna poliestrske preje s stalno protibakterijsko odpornostjo. Protibakterijski preizkusi so bili opravljeni na strojno izdelani preprogi, prekriti z nanodelci, skladno z ATCC 27853, 25923 in 25922, 72 h pred pranjem in po njem. Rezultati so pokazali, da ima strojno izdelana preproga iz poliestra, prekritega z nanodelci srebra, trajno protibakterijsko odpornost.

Ključne besede: protibakterijske lastnosti, preja iz poliestrskih vlaken, strojno izdelana preproga, DLS-metoda, postopek pranja, bakterija, površinska aktivnost, Mac Farlen

1 INTRODUCTION

Microbial organisms, bacteria and micro-organisms are the main reasons for sickness, infections and bad odours, etc. In fact, increasing death rates in many underdeveloped countries, such as many African countries, led to the legislation of global and social policies in order to overcome this challenge. Such problems and needs have led to a resurgence in the use of silver- and copper-based antiseptics that may be linked to broad-spectrum activity and a far lower propensity to induce microbial resistance than antibiotics[1].

The anti-bacterial characteristics of silver and silver salts have been observed since antiquity[2]. Silver is currently used to control bacterial growth in a variety of applications, including dental work, catheters and burn wounds[3,4].

In fact, it is well known that Ag ions, Ag-based compounds, copper and brass compounds have a strong biotical effect on many bacteria species, such as *E. coli*, *P. aeruginosa* and *S. aureus*[5].

A lot of information is available about the practical use of nanoparticles for food safety and hygiene, the disinfection of water in swimming pools and hospitals, wound healing, air disinfection and surface sanitation[6–8]. It is believed that the germicidal property of metals, especially heavy metals, is due to oligodynamic effect in which the metal and metal compounds, when introduced into the interior of bacterial cells, have the ability to change and then kill them in a specific way. Copper and silver are the most studied metals for oligodynamic action[9]. The data from silver suggest that its ions denature the proteins in the bacterial cells by binding to the reactive groups, resulting in their inactivation[10].

Different factors influence the efficiency of silver- and copper-based compounds, such as the particle size and particle size distribution. In these cases, a reduction of the particle size of silver and copper nanoparticles is a reliable solution to improve their efficiency and biocompatibility. In this field, nanotechnology has a direct effect on the elimination of particle size limitations and changing the world outlook regarding science[10,11].

In this study we investigated the stabilization of nano silver on polyester filament yarn in order to produce a machine-made carpet with permanent antibacterial characteristics.

2 MATERIALS

A nano-silver colloid was obtained from US Research Nano Material Company. The polyester filament yarns as a pile, warp and weft in a machine-made carpet were provided by the Farrokh Sepehr Kashan Textie Company. Gluteraldehyde (cross linking agent) and α-amino propyl tri-etoxy silane were provided by the Sigma-Aldrich Company on a laboratory scale. An amphoteric surfactant based on amino betaine was provided by the Carp Company.

3 METHODS

Nano-silver colloids, including a cross-linking agent and amphoteric surfactant in different concentrations, were applied to the polyester filament yarn and the back of a machine-made carpet using a spraying method. The nano-silver-coated polyester filament yarn and polyester machine-made carpet were dried and cured in the stenter at 130 °C for 6 min.

4 ANALYSIS

To predict the stability of the anti-bacterial characteristics, the nano-silver back-coated polyester machine-made carpets were analysed according to ATCC 27853, 25923 and 25922 some 72 h before and after a washing process in the Pasteur Institute of Iran.

The anti-bacterial characteristic of the nano-silver-coated machine-made carpet were measured based on the growth of different bacteria, such as *E. coli*, *P. aeruginosa* and *S. aureus* with respect to the reference sample.

The stability of the nano-silver colloids and their particle size distribution were analysed using the DLS (dynamic light scattering) method at 25 °C (Malvern seri nano (zeta sizer) model DLS).

The FTIR analysis of the obtained solution from washing the nano-silver-coated polyester filament was carried out using Fourier-transform spectroscopy in the range 300 cm^{-1} to 4000 cm^{-1}.

The distribution of nano-silver on the back of the polyester-filament machine-made carpet was analysed using the FESEM method in 1.89 KX (Philips model FESEM).

5 PREPARATION METHOD

The Mac Farlan solutions of different bacteria such as *P. aeruginosa* (ATCC 27853), *S. aureus* (ATCC 25923) and *E. coli* (ATCC 25922) at a concentration of 1.5×10^8 CFU/mL were prepared in the first stage.

During the next stage, the nano-silver-coated machine-made carpet and the reference machine-made carpet were put in contact with the Mac Farlen solution of different bacteria for 24 h. After the cultivation and incubation process for 72 h at 37 °C, the growth of the bacteria were analysed.

6 RESULTS AND DISCUSSION

6.1 Particle size distribution of nano-silver colloid

The particle size distribution of the nano-silver colloid was measured using the DLS method. The results showed that the average size of the nano-silver colloid and the Pdi constant were about 49.08 nm and 0.408 nm, respectively. **Figure 1** shows the size distribution of the nano-silver.

6.2 Stability of the nano-silver colloid

The stability of the nano-silver colloid was measured using the DLS method according to the zeta-potential value. The results showed that the nano-silver colloid has

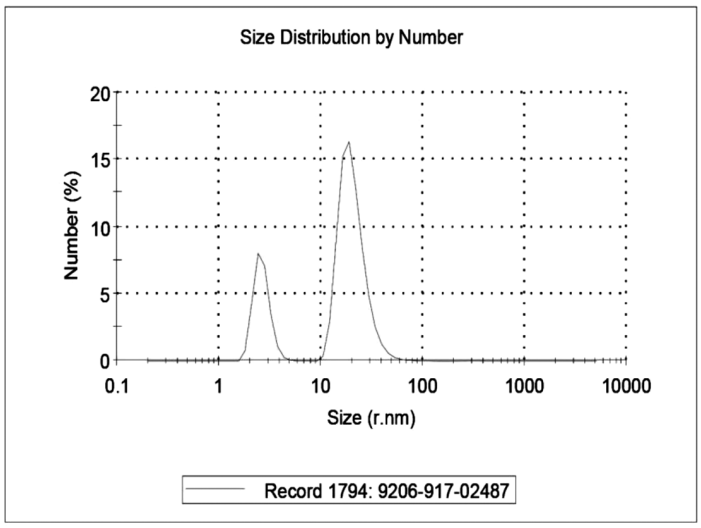

Size r.nm	Number %	Size r.nm	Number %
0.2000	0.0	34.03	2.5
0.2316	0.0	39.41	1.3
0.2682	0.0	45.64	0.6
0.3106	0.0	52.85	0.3
0.3597	0.0	61.21	0.1
0.4166	0.0	70.89	0.1
0.4825	0.0	82.09	0.0
0.5587	0.0	95.07	0.0
0.6470	0.0	110.1	0.0
0.7493	0.0	127.5	0.0
0.8678	0.0	147.7	0.0
1.005	0.0	171.0	0.0
1.164	0.0	198.0	0.0
1.348	0.0	229.3	0.0
1.561	0.0	265.6	0.0
1.808	0.8	307.6	0.0
2.093	4.2	356.2	0.0
2.424	8.0	412.5	0.0
2.807	7.1	477.7	0.0
3.251	3.4	553.2	0.0
3.765	1.1	640.7	0.0
4.360	0.3	741.9	0.0
5.050	0.1	859.2	0.0
5.848	0.0	995.1	0.0
6.772	0.0	1152	0.0
7.843	0.0	1335	0.0
9.083	0.0	1545	0.0
10.52	0.4	1790	0.0
12.18	2.9	2073	0.0
14.11	9.1	2400	0.0
16.34	15.2	2780	0.0
18.92	16.3	3219	0.0
21.91	12.9	3728	0.0
25.37	8.4	4317	0.0
29.39	4.8	5000	0.0

Figure 1: Size distribution of nano silver colloid
Slika 1: Razporeditev velikosti nanodelcev srebra v koloidu

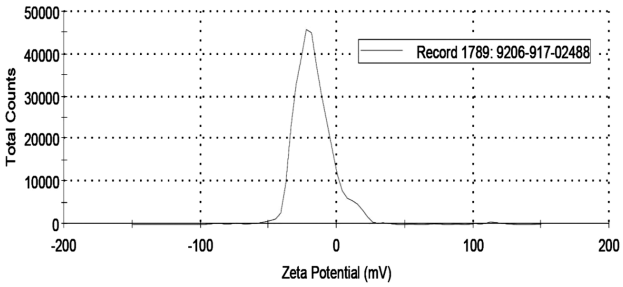

Figure 2: Zeta-potential distribution of nano-silver colloid
Slika 2: Zeta potencial razporeditve nanodelcev srebra v koloidu

a suitable stability under normal conditions. In **Figure 2**, the zeta-potential distribution of the nano-silver is shown. According to **Figure 2**, the zeta-potential for a nano-silver colloid is about –17.2 MV. In addition, the nano-silver particle colloid has a suitable stability against sedimentation.

6.3 Distribution of nano-silver on the back of polyester machine-made carpet

The distribution of the nano silver on the back of the machine-made carpet is shown in a FESEM micrograph in 1.89 KX. According to **Figure 3**, it can be concluded that the anti-bacterial characteristics of the polyester-filament machine-made carpet is due to the nano-silver material that was applied on the polyester filament yarn and the back of the machine-made carpet.

6.4 Anti-bacterial test

The nano-silver back-coated machine-made carpets before and after washing were tested according to ATCC 27853, 25923 and 25922 in 72 h. In **Tables 1** and **2**, the concentration of bacteria before and after the washing processes are presented.

The results showed that the nano-silver-coated polyester-filament machine-made carpet before and after

Figure 3: SEM micrographs of samples: a) polyester-filament yarn, b) nano-silver-coated polyester-filament yarn
Slika 3: SEM-posnetka vzorcev: a) vlakna poliestrske preje, b) z nanodelci srebra prekrita vlakna poliestrske preje

Table 1: Anti-bacterial characteristics of samples before washing
Tabela 1: Protibakterijske lastnosti vzorcev pred pranjem

Name of test bacteria	Bacteria concentration (CFU/mL)	The growth of bacteria after 72 h (CFU/mL)	
E. coli (ATCC 25922)	1.5×10^8	Sample control	1.5×10^6
		Anti bacterial sample	8.5×10
P. aeruginosa (ATCC 27853)	1.5×10^8	Sample control	1.5×10^6
		Anti bacterial sample	7.5×10
S. aureus (ATCC 25923)	1.5×10^8	Sample control	1.5×10^6
		Anti bacterial sample	7.5×10

Table 2: Anti-bacterial characteristics of samples after washing
Tabela 2: Protibakterijske lastnosti vzorcev po pranju

Name of test bacteria	Bacteria concentration (CFU/mL)	The growth of bacteria after 72 h (CFU/mL)	
E. coli (ATCC 25922)	1.5×10^8	Sample control	1.5×10^6
		Anti bacterial sample	8.5×10
P. aeruginosa (ATCC 27853)	1.5×10^8	Sample control	1.5×10^6
		Anti bacterial sample	7.5×10
S. aureus (ATCC 25923)	1.5×10^8	Sample control	1.5×10^6
		Anti bacterial sample	7.5×10

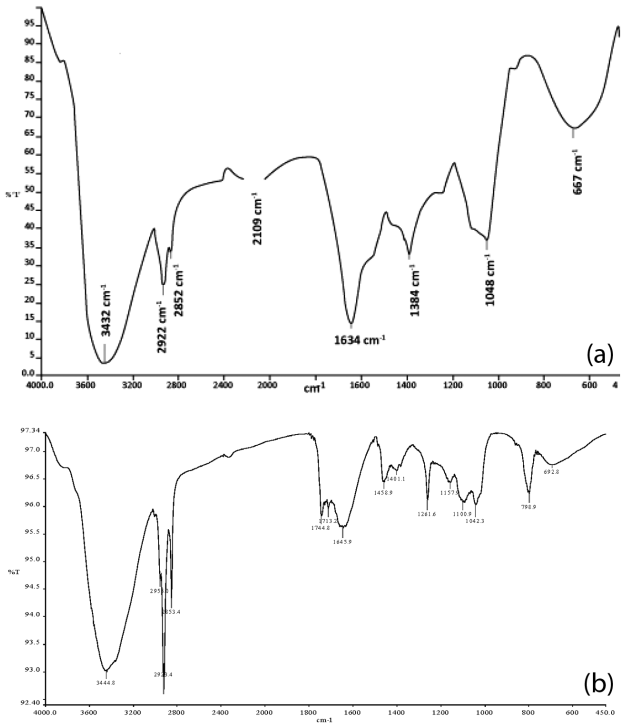

Figure 4: FTIR analysis a) nano silver b) solution from washing
Slika 4: FTIR-analiza, a) nanodelci srebra, b) raztopina pri pranju

washing has suitable anti-bacterial characteristics against *E. coli*, *P. aeruginosa* and *S. aureus* (99.9 % anti-bacterial characteristic).

6.5 FTIR analysis of nano-silver-coated polyester-filament machine-made carpet

In order to demonstrate the permanence of the anti-bacterial characteristic in a polyester-filament machine-made carpet, FTIR analyses carried out on a nano-silver colloid and the obtained solution from washing the nano-silver-coated polyester-filament machine-made carpet. **Figure 3** shows the FTIR analysis of the nano-silver colloid and the obtained solution from washing the nano-silver-coated polyester-filament machine-made carpet (**Figure 4**).

According to **Figure 4a**, the sharp peaks at 1634 cm^{-1} and 1384 cm^{-1} indicate the formation of asymmetric and symmetric stretching modes of metal carbonyl groups. This is due to the stabilization of the silver nano particles by the –COO- group of amino betaine (as an amphoteric surfactant). The peaks at 3432 cm^{-1} and 2922 cm^{-1} are related to the C-H stretching bond of the propyl and the amine groups of the α-amino propyl tri-etoxy silane[12].

According to **Figure 4b**, the sharp peaks at 3444 cm^{-1} and 2934 cm^{-1} are related to the O-H and C-H groups of the soap solution, which are used for washing the nano-silver-coated polyester-filament machine-made carpet.

Moreover, the lack of any peak at 1634 cm^{-1} and 1384 cm^{-1} indicates that the washing process had no effect on removing the silver nanoparticles from the anti-bacterial polyester-filament machine-made carpet.

7 CONCLUSION

The results showed that the nano-silver-coated polyester-filament machine-made carpet has a permanent anti-bacterial characteristic. This is due to the modification process carried out on the nano-silver before applying it to polyester-filament yarn and the back of the machine-made carpet. Having permanent anti-bacterial characteristics in the machine-made carpet make it more suitable for use in crowded places by removing the bad smells in a machine-made carpet due to the direct contact of people with machine-made carpet's surface.

Acknowledgement

This work was done in the Farrokh Sepehr Kashan Company. Mr. Ali Farrahi and Mr. Ahmad Farrahi are grateful for the financial support.

8 REFERENCES

[1] S. A. Jones, P. G. Bowler, M. Walker, D. Parsons, Wound Repair and Regeneration, 12 (**2004**) 3, 288–294, doi:10.1111/j.1067-1927.2004.012304.x

[2] S. Silver, L. T. Phung, Annu. Rev. Microbiol., 50 (**1996**), 753–789, doi:10.1146/annurev.micro.50.1.753

[3] M. Catauro, M. G. Raucci, F. De Gaetano, A. Marotta, J. Mater. Sci. Mater. Med., 15 (**2004**) 7, 831–837, doi:10.1023/B:JMSM.0000032825.51052.00

[4] J. H. Crabtree, R. J. Burchette, R. A. Siddiqi, I. T. Huen, L. L. Hadnott, A. Fishman, Perit. Dial. Int., 23 (**2003**) 4, 368–374

[5] G. Zhao, S. E. Stevens Jr., Biometals, 11 (**1998**) 1, 27–32, doi:10.1023/A:1009253223055

[6] C. E. Santo, N. Taudte, D. H. Nies, G. Grass, Appl. Environ. Microbiol., 74 (**2008**) 4, 977–986, doi:10.1128/AEM.01938-07

[7] S. A. Wilks, H. Michels, C. W. Keevil, International Journal of Food Microbiology, 105 (**2005**) 3, 445–454, doi:10.1016/j.ijfoodmicro.2005.04.021

[8] D. S. Blanc, P. Carrara, G. Zanetti, P. Francioli, J. Hosp. Infect., 60 (**2005**) 1, 69–72, doi:10.1016/j.jhin.2004.10.016

[9] A. J. Varkey, Scientific Research and Essays, 5 (**2010**) 24, 3834–3839

[10] M. Yamanaka, K. Hara, J. Kudo, Appl. Environ. Microbiol., 71 (**2005**) 11, 7589–7593, doi:10.1128/AEM.71.11.7589-7593.2005

[11] J. S. Kim, E. Kuk, K. N. Yu, J. H. Kim, S. J. Park, H. J. Lee, S. H. Kim, Y. K. Park, Y. H. Park, C. Y. Hwang, Y. K. Kim, Y. S. Lee, D. H. Jeong, M. H. Cho, Nanomedicine: Nanotechnology, Biology, and Medicine, 3 (**2007**) 1, 95–101, doi:10.1016/j.nano.2006.12.001

[12] R. Augustine, K. Rajarathinam, Int. J. Nano Dim., 2 (**2012**) 3, 205–212

UDK 621.742.48:621.742.43
Professional article/Strokovni članek

ISSN 1580-2949
MTAEC9, 49(3)465(2015)

EVALUATION OF THE THERMAL RESISTANCE OF SELECTED BENTONITE BINDERS

OCENA TOPLOTNE UPORNOSTI IZBRANIH BENTONITNIH VEZIV

Jaroslav Beňo[1], Jiřina Vontorová[2], Vlastimil Matějka[3], Karel Gál[1]

[1]Department of Metallurgy and Foundry Engineering, Faculty of Metallurgy and Material Engineering, VŠB-Technical University of Ostrava, 17. listopadu 15/2172, 708 33 Ostrava – Poruba, Czech Republic
[2]Department of Chemistry, Faculty of Metallurgy and Material Engineering, VŠB-Technical University of Ostrava, 17. listopadu 15/2172, 708 33 Ostrava – Poruba, Czech Republic
[3]Nanotechnology Centre, VŠB-Technical University of Ostrava, 17. listopadu 15/2172, 708 33 Ostrava – Poruba, Czech Republic
jaroslav.beno@vsb.cz

Prejem rokopisa – received: 2014-07-29; sprejem za objavo – accepted for publication: 2014-09-03

doi:10.17222/mit.2014.126

Bentonite is one of the most widely used clays associated with various applications. In the case of foundry technology, bentonite is primarily used as a binder for the mold manufacture. The thermal resistance of bentonite binders, also called the thermal stability, is a natural property of clay minerals, depending on the source, the mineralogical and chemical composition of clay and it is also closely connected to the bentonite structure (various interlayer ions, the level of ion substitution of montmorillonite). Generally, there are various methods for evaluating this property. This contribution describes various methods of determining the bentonite thermal stability based on the evaluation of the technological parameters of bentonite molding mixtures and their comparison. These methods were chosen on the basis of a background research and practical experiences. For the experiments the bentonites commonly used in the foundries of the Czech and Slovak region were selected.

Keywords: bentonites, clay minerals, thermal stability, dehydration, dehydroxylation

Bentonit je ena najpogosteje uporabljanih glin, povezanih z različno uporabo. V livarstvu se bentonit uporablja predvsem kot vezivo pri izdelavi form. Toplotno upornost bentonitnih veziv imenujemo tudi toplotna stabilnost in je naravna lastnost mineralov glin, odvisna je od izvora, mineraloške in kemijske sestave gline in je tudi tesno povezana s strukturo bentonita (različni ioni med plastmi, nivo nadomestila ionov v montmorilonitu). Obstaja več metod za oceno te lastnosti. Ta prispevek opisuje različne metode določanja toplotne stabilnosti bentonita, ki temeljijo na oceni tehnoloških parametrov bentonitnih mešanic za forme in njihovo primerjavo. Te metode so bile izbrane na podlagi raziskav ozadja in praktičnih izkušenj. Za preizkuse so bili izbrani bentoniti, ki se uporabljajo v livarnah na Češkem in Slovaškem.

Ključne besede: bentoniti, minerali glin, toplotna stabilnost, dehidracija, dehidroksilacija

1 INTRODUCTION

Bentonite as a natural and abundant soil is being widely used in a large range of industrial applications. A high CEC, the swelling ability and a high surface area of bentonite predetermine it for utilization in ceramics, cosmetics, nanocomposites, environmental protection, waste-water treatment, nuclear-waste deposits or manufacture of foundry molds and cores.[1–6]

As a rule, bentonites consist of the montmorillonite clay with the amount of the montmorillonite mineral higher than mass fractions w = 70 % to 75 %, which means that it contains up to 30 % of other minerals, above all aluminosilicates and also micas and carbonates. Individual bentonite localities also differ with their genesis. In principle, the bentonites do not differ in the chemical composition, but their behaviors are quite different (because of their mineral composition, physical characteristics, etc.). Nowadays the required properties are achieved by mixing the bentonites from different localities.

The thermostability of bentonite is connected with the temperature of the clay dehydroxylation, i.e., with liberating the OH^- groups from the octahedral network in the form of H_2O (g). The residual oxygen remains in the structure. At the same time the binding properties are gradually lost and the "burnt-out bentonite" is formed. The whole process is endothermic and it can be well monitored with a thermal analysis (DTA). The thermostability and its testing methods were studied by Jelínek et al.[7] In the bentonites of a mean quality the endothermic reactions are present in the temperature region from 450 °C to 550 °C. The bentonites with a high thermostability (a loss of crystallic water, dehydroxylation, occurs in the range from 700 °C up to 750 °C) often even have two peaks, at 500 °C and 700 °C. This state is explained as follows:

- a substitution of ions in montmorillonite octahedrons and tetrahedrons (the influence of Fe)[8]
- defects in the lattice (vacancies)
- a difference in the size of montmorillonite particles[9].

The influence of Fe on dehydroxylation has not yet been unambiguously explained. A low concentration of Fe (< 8 %)[7] results in a low dehydroxylation temperature; Fe-rich bentonites have higher dehydroxylation

temperatures[10]. On the contrary, Grefhorst[11] and Kaplun[12] give an opinion that with the increasing Fe_2O_3 content the dehydroxylation temperature is falling (in the range of 2–14 %) and in the presence of black coal the fall is even more intense.

Due to the thermal exposure of the mold buildup of bentonite during metal casting, the amount of the active bentonite decreases and the non-reactive (burnt-out) bentonite is formed. For each cycle of the mold preparation the used mixture is reactivated with an addition of fresh bentonite in order to maintain the portion of active bentonite (replacing the burnt-out bentonite in the sand). The burnt-out bentonite amount of the foundry sand is affected by the thermal stability of bentonite. The thermal stability of bentonite is usually determined as the temperature of dehydroxylation or, more precisely, the temperature of the crystal-lattice destruction and/or the measure of the loss of its plasticity.

The objectives of this study are: i) an evaluation of the basic physical and chemical properties of the bentonites from the Czech and Slovak region commonly used in the foundry industry, and a comparison of the parameters of these bentonites with natural Na^+ – the bentonite of the Wyoming type; ii) an evaluation of the impact of the bentonite chemical composition on its thermal stability with respect to its utilization in the foundry industry (with an emphasis on Fe and Mg contents); iii) a determination of the thermal stability of bentonite samples evaluated with the methods based on an evaluation of the technological parameters of the bentonite molding mixtures; iv) a comparison of individual methods and an assessment of the optimum method for determining the bentonite thermal stability.

2 MATERIALS AND METHODS

Four commonly used binders supplied as soda-activated foundry bentonites and one natural sodium bentonite of the Wyoming type were used for the experiments within this research.

The studied bentonites comprise the following groups of bentonites: i) two bentonites mined and produced in the Czech Republic (assigned as Sa and K, from the West Bohemian region), ii) two bentonites from the Central Slovakia region, assigned as B and S; and iii) a natural sodium bentonite of the Wyoming type (USA), assigned as P, was used as the standard material.

The following general parameters (**Table 1**) commonly used for the characterization of bentonites were determined: a) the moisture under the temperature of 105 °C up to the constant weight; b) pH and conductivity of water suspension (a 1 : 10 solid-liquid ratio); c) the loss of ignition (LOI) of dried samples (105 °C up to the constant weight) at 900 °C/2 h.

The chemical compositions of the studied samples were determined using energy dispersive fluorescence spectrometer (XRFS) SPECTRO XEPOS (SPECTRO Analytical Instruments GmbH) equipped with a 50 W Pd X-ray tube. The samples for the analysis were prepared in the form of pressed tablets (wax was used as a binder) for this measurement.

The thermal stabilities of the selected bentonite samples were determined as the ratio of the values of the selected technological properties (splitting strength, wet tensile strength, determination of the methylene-blue consumption – an active clay test) before and after the annealing of the bentonite molding mixture.

The samples of the bentonite molding mixture were prepared with a 5 min homogenization of the mixture of the studied bentonite with silica sand, in the constant weight ratio of 8 : 100 and with an appropriate amount of water ensuring a constant compactibility of (45 ± 3) % using an MK 00 sand mill. The prepared mixtures were processed into standard cylinders (Ø 50, a height of 50 mm) to obtain the samples for the determination of the technological parameters.

The splitting strengths were measured using a WADAP testing machine of the LRU-1 type, while the wet tensile strength was measured using a +GF+ testing machine of the SPNF type.

3 RESULTS AND DISCUSSION

The basic bentonite-binder parameters are summarized in **Table 1**. The natural moisture of the samples determined at 105 °C (as the loss of weight) varied a lot, ranging from 6.93 % (K) to 11.69 % (standard – P). The conductivity of the elements prepared from the studied bentonites varies significantly in the range from 457 µS/cm to 2800 µS/cm, measured for samples P and S, respectively. The lowest conductivity as well as the lowest pH value obtained for bentonite P are connected with the fact that bentonite P is a natural bentonite (not activated by soda).

Table 1: Basic parameters of the studied bentonite samples
Tabela 1: Osnovni parametri preiskanih vzorcev bentonita

Sample	moisture	pH	conductivity	LOI
	w/%	(–)	µS/cm	*w*/%
Sa	7.16	10.27	1422	16.30
K	6.93	10.16	1067	13.60
B	8.21	10.43	1456	12.60
S	10.46	10.50	2800	16.30
P	11.69	9.54	457	12.20

The values of the loss of weight at the ignition (up to 900 °C) of individual samples ranged from 12.20 (P) up to 16.30 % (Sa). The LOI values reached the values typical for the amount of water present in the interlayer space of montmorillonite (approximately w = 12 %).

The chemical compositions of the studied samples were evaluated with XRFS, whereas the amounts of the analyzed elements were recalculated to the amounts of oxides and resumed in **Table 2**. The most important

elements associated with the bentonite-binder behavior under high temperatures (mainly Fe and Mg) were selected.

Table 2: Technological parameters of the basic salt-core mixtures
Tabela 2: Tehnološki parametri osnovnih slanih mešanic za jedra

Composition (*w*/%)/Bentonite	Sa	K	B	S	P
Na_2O	2.00	< 1.00	2.50	3.05	< 1.00
Al_2O_3	11.80	15.80	16.40	17.16	16.70
SiO_2	44.30	53.90	60.20	59.01	59.10
CaO	4.69	2.40	1.49	1.34	1.22
MgO	3.20	2.50	2.20	1.72	2.20
Fe_2O_3	12.88	8.50	2.16	1.77	4.31

Although sample K should be rich in the Na^+ content (the sample is a soda-activated bentonite), the chemical analysis performed with XRFS showed the amount of Na_2O to be bellow the detection limit; the same situation was observed for bentonite P activated without soda.

The lowest amount of Na_2O, measured for samples K and P, is in good agreement with the measured conductivity of their water suspensions (**Table 1**).

From the background research, mentioned above, it is evident, that the thermal resistance of bentonite binders to higher temperatures is closely connected to the Mg and Fe contents. According to the chemical analysis of the studied samples there is no significant difference between the Mg contents of the bentonite samples.

The Mg content ranged from 1.72 % (sample S) up to 3.20 % (sample Sa). On the other hand, the Fe content differs significantly. The highest value of the Fe content was obtained for sample Sa (12.88 %), while the lowest value of the Fe content was detected for sample S (1.77 %). On the basis of the results of the XRFS analysis, it can be assumed that the highest thermal resistance will be obtained for samples S, B or P.

For the determination of the thermal stability of the studied bentonite samples two methods were selected. The first procedure includes a determination of the thermal stability as the ratio of the mechanical properties of the fresh and annealed molding mixtures. The temperature of the thermal exposition of 550 °C/1 h was selected on the basis of the background research.[6–12]

The values of the splitting strength of the bentonite molding mixture with individual bentonite samples are summarized in **Figure 1**.

The evaluated values of the technological parameters significantly depend on the type of a bentonite sample as evident from **Figures 1** and **2**.

The optimum mechanical properties required for molds (high values of the splitting strength in the fresh state) were obtained for all the samples, but the highest values were found for sample Sa (31 kPa) and K (30 kPa), respectively.

However, the lowest thermal resistance, calculated as the ratio of the splitting strengths of the fresh and annealed bentonite molding mixtures was detected for bentonite Sa (a 100 % decrease in the splitting-strength values).

From this point of view, even though sample Sa in its fresh state suggested the best mechanical properties, the highest thermal stability was obtained for samples P and S, where no change was found.

A slight increase in the splitting-strength values detected for samples S (+5.6 %) and P (+4.3 %) was probably caused by a measurement error.

Generally, a more sensitive parameter for the evaluation of the bentonite-binder quality is the determination of the wet tensile strength of the bentonite molding mixture. The results of these experiments are summarized in **Figure 2**.

All the samples suggest satisfactory values of the wet tensile strength. In practice there is a rule, according to which the value of the wet tensile strength should be

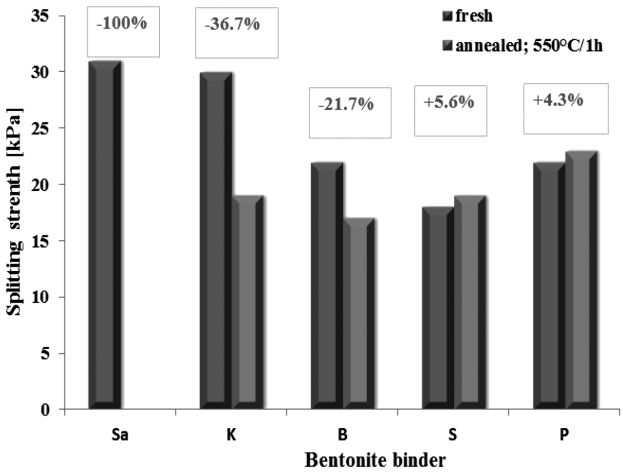

Figure 1: Thermal stability of the bentonites determined as the ratio of splitting strengths
Slika 1: Toplotna stabilnost bentonita, določena kot razmerje trdnosti pri cepljenju

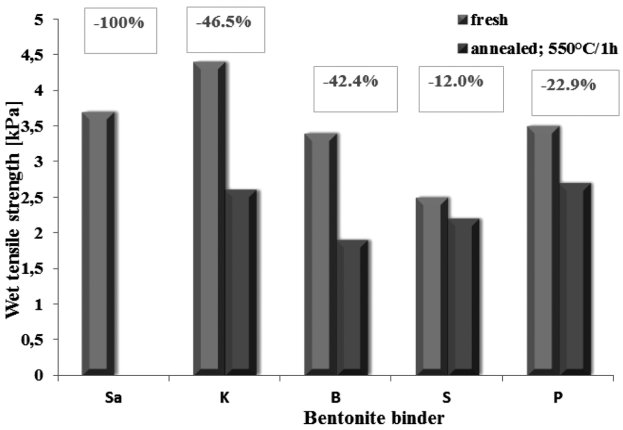

Figure 2: Thermal stability of bentonites determined as the ratio of wet tensile strengths
Slika 2: Toplotna stabilnost bentonitov, določena kot razmerje natezne trdnosti v vlažnem

higher than 2.0 kPa. In these experiments it ranges from 2.5 kPa (S) to 4.4 kPa (K). After the annealing the values of the wet tensile strength significantly decreased for all the bentonite samples.

The highest decrease was also detected for sample Sa (–100.0 %). The lowest decrease in the wet tensile strength was obtained for samples S (–12.0 %) and P (–22.9 %).

The second method of determining the bentonite thermal stability includes a preparation of two molding mixtures. The first mixture was prepared with 5 % dried bentonite and the second with 5 % annealed bentonite.

Then active-clay tests (a determination of the methylene-blue consumption) were carried out. The thermal stability was calculated as the ratio of the bentonite molding mixtures with fresh (dried, 105 °C) and annealed bentonites.

The results of these experiments are summarized in **Figure 3**.

The results of these experiments (the determination of active bentonite) suggested the same trend as the previous experiments based on the determination of the mechanical properties of the molding mixtures with individual bentonite samples.

The minimum (the lowest) thermal stability was also found for sample Sa (–53.8 %) and the maximum thermal stability was found for sample P (–8.5 %).

Finally, all the most important parameters based on the results of the thermal-stability determination for the individual bentonite samples are summarized in **Table 3**.

Table 3: Resume of the thermal stability of the studied bentonite samples

Tabela 3: Pregled toplotnih stabilnosti preiskovanih bentonitnih vzorcev

Parameter/Bentonite		Sa	K	B	S	P
Δ*STS*	(%)	–100.0	–36.7	–21.7	+5.6	+4.3
Δ*WTS*		–100.0	–46.5	42.4	–12.0	–22.9
Δ*ABT*		–53.8	–18.2	29.5	–18.4	–8.5
MgO		3.20	2.50	2.20	1.72	2.20
Fe_2O_3		12.88	8.50	2.16	1.77	4.31

Note: Δ*STS* – change in the splitting strength
Δ*WTS* – change in the wet tensile strength
Δ*ABT* – change in the active-bentonite test

The experiments carried out in order to evaluate the thermal stability of the selected bentonite binders commonly applied at the Czech and Slovak foundries show that, in all the cases, the lowest thermal resistance was observed for sample Sa. It is probably related to the highest amount of Fe (12.88 %). This fact is in line with our previous research[7].

Even if sample P is natural sodium bentonite (not soda activated) this sample shows the highest thermal stability. It also shows the minimum decrease in the mechanical properties and methylene-blue consumption applied for the evaluation of the thermal stability. It is in good accordance with the theory of clay binders.[4,7]

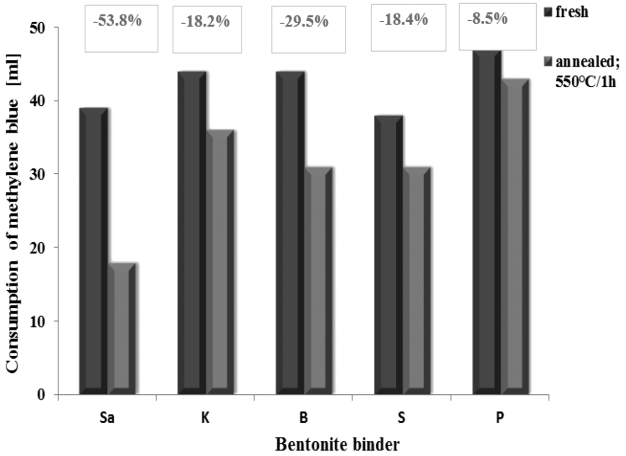

Figure 3: Thermal stability of bentonites determined as the ratio of the methylene-blue tests

Slika 3: Toplotna stabilnost bentonitov, določena kot razmerje preizkusov metilen modro

4 CONCLUSION

Thermal stability, the natural property of clay minerals, depends on the source, the mineralogical and chemical composition of clay and, thus, it is always necessary to evaluate the suitability of a given clay for a selected purpose.

The results obtained within this work clearly show the influence of the Fe amount on the thermal stability of bentonites as the highest thermal stability was observed for bentonite P which also shows almost the lowest iron amount. A high amount of iron was observed for sample Sa which demonstrates the lowest thermal resistance.

The optimum method for assessing the thermal stability of the bentonite binder appears to be the method based on a different methylene-blue consumption of the bentonite molding mixture with fresh and annealed bentonite. This method eliminates the potential problems with the preparation of a molding mixture and the natural loss of water (drying) from the mixture during the experiments, which can negatively affect the results of the measurements. This method is also more sensitive and more conclusive with respect to the evaluation of the thermal resistance of a bentonite binder.

Acknowledgement

The research was carried out within the frame of internal projects of the VŠB-Technical University of Ostrava, SP2014/61 and SP2014/62.

5 REFERENCES

[1] C. Paluskiewicz, M. Holtzer, A. Bobrowski, FTIR analysis of bentonite in moulding sands, Journal of Molecular Structure, 880 (**2008**) 1–3, 109–114, doi:10.1016/j.molstruc.2008.01.028

[2] V. J. Inglezakis et al., Removal of Pb(II) from aqueous solutions by using clinoptilolite and bentonite as adsorbents, Desalination, 210 (**2007**) 1–3, 248–256, doi:10.1016/j.desal.2006.05.049

[3] H. A. Patel et al., Preparation and characterization of phosphonium montmorillonite with enhanced thermal stability, Applied Clay Science, 35 (**2007**) 3–4, 194–200, doi:10.1016/j.clay.2006.09.012

[4] J. Madejova et al., Behaviour of Li+ and Cu2+ in heated montmorillonite: Evidence from far-, mid-, and near-IR regions, Vibrational Spectroscopy, 40 (**2006**) 1, 80–88, doi:10.1016/j.vibspec.2005.07.004

[5] F. Mikšovský, P. Lichý, The oolitization rate determination of bentonite moulding mixtures, Archives of Foundry Engineering, 8 (**2008**) 2, 103–106

[6] I. Vasková, J. Malik, P. Futáš, Tests of moulding mixture by using various clay binder granularity, Archives of Foundry Engineering, 9 (**2009**) 1, 29–32

[7] P. Jelinek et al., Thermostability of montmorillonitic clays, China Foundry, 11 (**2014**) 3, 201–207

[8] L. Heller et al., An approximation of the position of some cations in dehydroxylated montmorillonite, Clay Minerals Bulletin, 4 (**1961**) 25, 213–220

[9] R. Gauglitz, H. E. Schwiete, Thermochemical investigations on montmorillonite with regards to type, grain size, and cation loading, Berichte Deutsche Keramik Ges, 38 (**1964**), 43–49

[10] P. Wu, C. Ming, The relationship between acidic activation and microstructural changes in montmorillonite from Heping, China, Spectrochimica Acta A, 63 (**2006**) 1, 85–90, doi:10.1016/j.saa.2005.04.050

[11] C. Grefhorst, Investigation of bentonites, Giesserei, 93 (**2006**) 5, 26–31

[12] V. I. Kaplun et al., New studies of Čerkas bentonite, Litějnoje proizvodstvo, 6 (**2006**), 12–15

UDK 519.61/.64:621.78:621.73.043
Professional article/Strokovni članek

ISSN 1580-2949
MTAEC9, 49(3)471(2015)

DEVELOPMENT OF NUMERICAL MODELS FOR THE HEAT-TREATMENT-PROCESS OPTIMISATION IN A CLOSED-DIE FORGING PRODUCTION

RAZVOJ NUMERIČNIH MODELOV ZA OPTIMIZACIJO POSTOPKA TOPLOTNE OBDELAVE PRI PROIZVODNJI ODKOVKOV V ZAPRTIH UTOPNIH ORODJIH

Ladislav Maleček[1], Mikuláš Fedorko[1], Filip Vančura[2], Hana Jirková[2], Bohuslav Mašek[2]

[1]COMTES FHT a.s., Průmyslová 995, 334 41 Dobřany, Czech Republic
[2]University of West Bohemia in Pilsen, Výzkumné centrum tvářecích technologií – FORTECH, Univerzitní 22, 306 14 Plzeň, Czech Republic
ladislav.malecek@comtesfht.cz

Prejem rokopisa – received: 2014-08-15; sprejem za objavo – accepted for publication: 2014-09-04

doi:10.17222/mit.2014.196

The paper describes a numerical simulation of the current technology of heat treatment of closed-die forgings made of the 25CrMoS4 steel. The aim of this simulation was to create a temperature model enabling a temperature analysis of closed-die forgings during the heating to the austenitization temperature. This model would permit the heating and soaking times to be reduced. The paper also describes a numerical simulation and material/technological modelling of the current forming technology and the subsequent still-air cooling of a selected type of closed-die forgings for the automotive industry. This numerical simulation provides information on the material flow, the part size and the deformation rate during forming and on the temperature conditions during handling, forming and subsequent still-air cooling. Using the material/technological modelling, samples corresponding to the selected locations of a forging can be obtained. By combining these two techniques, controlled cooling of closed-die steel forgings will be developed and optimized as a substitute for heat treatment. It is also possible to optimize the process in terms of both quality and energy consumption. Both numerical simulations were applied to the technology of forming and heat treatment of closed-die forgings of microalloyed steel, chromium-molybdenum 25CrMoS4, at the company of Kovárna VIVA a.s.

Keywords: 25CrMoS4, MARC, DEFORM, closed-die forging

Članek opisuje numerično simulacijo sedanje tehnologije toplotne obdelave odkovkov iz jekla 25CrMoS4 v zaprtih orodjih. Namen te simulacije je bil postavitev temperaturnega modela, ki bi omogočil temperaturno analizo odkovkov, kovanih v zaprtih utopih, med ogrevanjem na avstenitizacijo. Ta model naj bi omogočil skrajšanje ogrevanja in zadrževanja na temperaturi. Članek opisuje tudi numerično simulacijo in materialno-tehnološko modeliranje sedanje tehnologije preoblikovanja in ohlajanja na mirujočem zraku izbranih utopnih izkovkov za avtomobilsko industrijo. Ta numerična simulacija omogoča informacijo o toku materiala, o velikosti delov in hitrosti deformacije med kovanjem in o temperaturnih razmerah med manipuliranjem, preoblikovanjem in ohlajanjem na mirujočem zraku. Z materialno-tehnološkim modeliranjem se lahko dobijo vzorci, ki ustrezajo izbranemu položaju kovanja. S kombiniranjem teh dveh tehnik bo razvito in optimirano kontrolirano ohlajanje izkovkov v zaprtih utopih kot nadomestilo za toplotno obdelavo. Proces je mogoče optimirati tudi s stališča kvalitete in porabe energije. Obe numerični simulaciji sta bili uporabljeni pri tehnologiji preoblikovanja in toplotne obdelave izkovkov iz krom-molibdenovega mikrolegiranega jekla 25CrMoS4 v zaprtih utopnih orodjih v podjetju Kovárna VIVA, a. s.

Ključne besede: 25CrMoS4, MARC, DEFORM, zaprto utopno kovanje

1 INTRODUCTION

The production of closed-die steel forgings involves a series of forming operations and the subsequent heat treatment. The forming process typically consists of several operations. The ones most frequently used are upsetting, preforming, finish-forging and trimming. Trimmed forgings are transferred with a conveyor to a container where they cool down to the ambient temperature. In order to attain the desired mechanical properties, the cooling is followed by re-heating the concerned parts in a continuous-tunnel furnace and by quenching them. Today's closed-die-forging plants strive to shorten this cycle or even omit some of the operations.

Several approaches are available for achieving this goal. One of them involves the use of numerical simulations. The present paper focuses on two possible applications of a numerical simulation to optimise the production of closed-die forgings. The first one aims at optimising the heating and soaking of forged parts prior to quenching. The other uses a numerical simulation for constructing a material/technological model in order to develop a new method of the thermomechanical treatment of forged parts.

The goal of the first application was to construct a temperature model. It would be used for predicting the temperature fields in the forged parts during heating and soaking at the quenching temperature in the existing heat-treatment process. Knowing the temperature distribution, it is possible to adjust the process and potentially reduce the tact time in the production.

Table 1: Chemical composition of 25CrMoS4 steel in volume fractions, φ/%
Tabela 1: Kemijska sestava 25CrMoS4 jekla v prostorninskih deležih, φ/%

Element	C	Mn	Si max.	P max.	S	Cr max.	Mo max.
Content	0.22–0.29	0.60–0.90	0.40	0.035	0.02–0.04	0.90–1.20	0.15–0.30

With respect to the second application, the development of the material/technological model, the paper describes a comprehensive numerical simulation of a forming process, including the subsequent still-air cooling. The forged part in question belongs to a larger group of products of a similar shape. The paper also presents the results of physical modelling of the forging process on a thermomechanical simulator. It compares the properties of the resulting specimens with the conditions of the corresponding locations within the actual forged part.

2 NUMERICAL MODELLING OF HEAT TREATING A FORGED PART

The objective of the numerical simulation of the heat treatment was to map the effects of the radiant heat from the furnace lining on the forgings and the effects of the radiant heat between the forgings themselves. The forged parts were made of the 25CrMoS4 material (**Figure 1** and **Table 1**). In the process, these forgings were arranged in a charging basket passing through a continuous heating furnace.

The model was constructed with the use of the data obtained from the heat-treatment lines. The computation was carried out using the MSC.MARC/MENTAT software. This software employs the finite-element method and is suitable for solving multiphysical problems[1].

The simulation of the heat treatment was an iterative process. The goal was to fine-tune the simulation to match the data obtained from the heat-treatment lines. The iterative approach consisted of a gradual refinement and an addition of the input data to the computational model. The computational model comprised three types of bodies (groups of objects forming a single entity): the furnace, the charging basket and the forgings (**Figure 2**). The CAD models provided the input data for generating the mesh in individual bodies.

The meshes used for solving the problem consisted of hexagonal elements for the furnace and the basket and tetragonal elements for the complex-shaped forgings. The element size was changing in all the bodies as the computation was gradually made more accurate. There were two reasons for it. One was related to the total number of the elements and the other to the element size ratio with respect to the view-factor setting. The view factor is used in analysing the heat transfer by radiation. It defines the proportion of the radiation from surface A that reaches surface B. In the model, the view factor indicates the visibility of the face elements of the individual bodies in the furnace to one another and to the elements of the inner surface of the furnace chamber. As a rule, the more elements there are in a computational model, the more accurate the results are – and the more face surfaces of the elements there are. With these numbers increasing, the computation time of the furnace heating simulation increases as well. For this reason, the analysis was first tried out using a simplified thermal model shown in **Figure 3**. The goal was to examine the effect of the view factor on the heat transfer by radiation between two simplified objects.

The meshed objects were assigned material properties. The properties (the thermal conductivity and the specific heat) were measured for the forgings using thermophysical measurement methods. The material properties of the basket and the furnace were retrieved from the material data library of the software. The computation was fine-tuned by defining a permanent thermal contact between the basket and the forged parts. The

Figure 1: Shape of a forging – a 3D view
Slika 1: Oblika izkovka – 3D-pogled

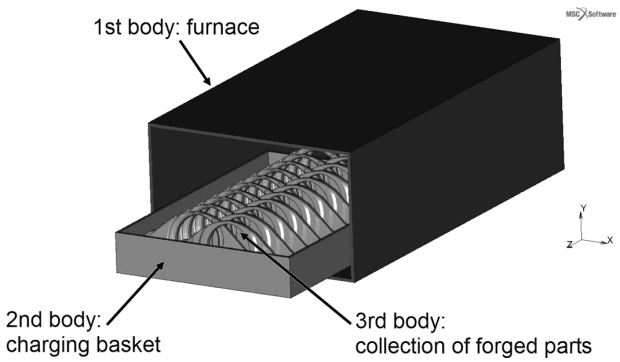

Figure 2: Bodies used in computing a temperature model in the MARC software environment
Slika 2: Telesa, uporabljena za izračun temperaturnega modela v okolju programske opreme MARC

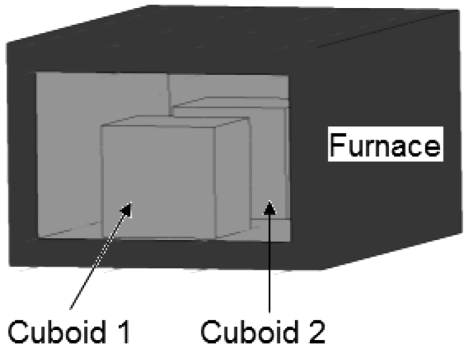

Figure 3: Trial model (examination of the effect of the view factor between two simple objects: cuboids)

Slika 3: Preizkusni model (preiskava vpliva faktorja videza med dvema enostavnima kvadratastima objektoma)

initial temperature of the forgings was 20 °C. At the start of the simulation, the furnace temperature was 690 °C. It changed during the simulation in accordance with the schedule used. The furnace heating and soaking schedule was constructed in accordance with the real-world conditions. It was applied to the side walls and the top wall of the furnace chamber. Heating by radiation was first modelled using the MONTE-CARLO method which, however, did not yield adequate results. Therefore, the HEMI_CUBE method was employed. This method uses a pre-defined hollow space, within which the heat is reflected from or absorbed by the objects. The hollow space is a numerical zone where the outer elements of the bodies constitute a working space within which the view factor is computed.

Due to the increasing computation time, some aspects that substantially complicated the simulation were neglected and certain preconditions were defined. The variation in the position of the basket inside the furnace was neglected, as it can be taken into account by adjusting the thermal schedule. The wire basket was substituted with a solid metal-sheet container in order to shorten the computation of the view factor. The temperature field inside the furnace was considered to be uniform, although the actual temperature field is not constant. It is affected by opening the furnace door, by the transitions between its zones with different temperatures, the types of heating and the temperature-measurement methods. The results of the FEM simulation were compared with the temperature curves obtained in the selected locations of the real-world forgings in the production (**Figure 4**).

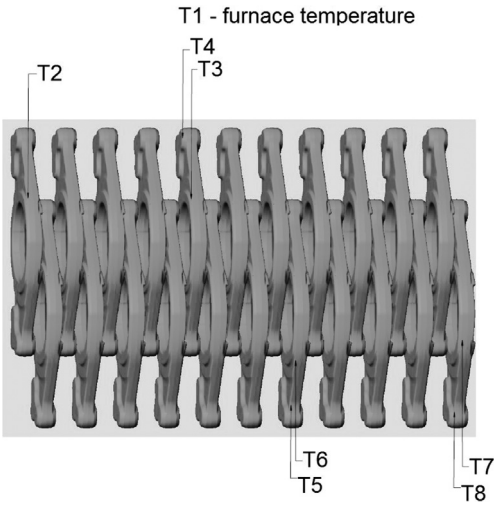

Figure 4: Layout of forged parts in the furnace with thermocouple locations. The layout was also used for the simulation of heat treatment (quenching).

Slika 4: Razporeditev izkovkov v peči s položajem termoelementov. Razporeditev je bila uporabljena tudi za simulacijo toplotne obdelave (kaljenja).

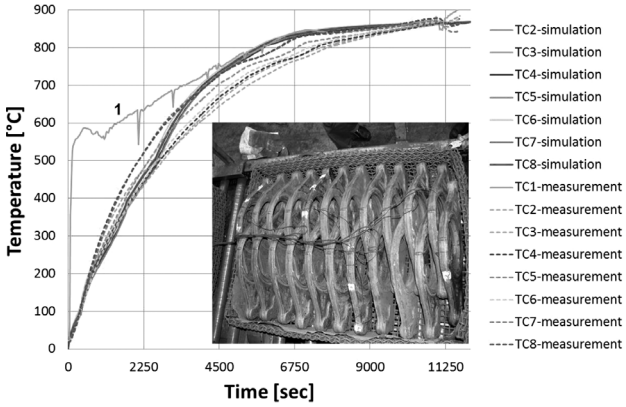

Figure 5: Comparison between the temperatures found with the numerical simulation and the field measurement (curve 1 shows the furnace temperature)

Slika 5: Primerjava med temperaturami, dobljenimi z numerično simulacijo in z meritvami (krivulja 1 prikazuje temperaturo peči)

Simulation results (**Figure 5**) were in agreement with the temperature curves obtained for the forged parts in the continuous furnace. Therefore, the numerical model is suitable for this type of analysis. It can be used for predicting the temperatures of the forged parts during heating and soaking before quenching.

3 NUMERICAL SIMULATION OF FORMING AND COOLING A SPECIFIC TYPE OF FORGED PARTS

A numerical simulation of forging a selected type of forged part (**Figure 1**) was carried out using DEFORM 3D, a program developed for modelling forging processes. The input data for the simulation was obtained by measuring the mechanical and thermophysical properties of the 25CrMoS4 steel, the material of the forged part. The goal of the measurement was to obtain an accurate description of the plastic and temperature behaviours of the material for the numerical simulation. The plastic behaviour of the forged material was described with the flow stress/temperature (T), flow stress/strain (e) and flow stress/strain rate ($\dot{e}$) relationships in the form of curves. The flow-stress levels were found using the Rastegaev test[2,3]. The temperature behaviour of the workpiece, i.e. the changes in the temperature field within the

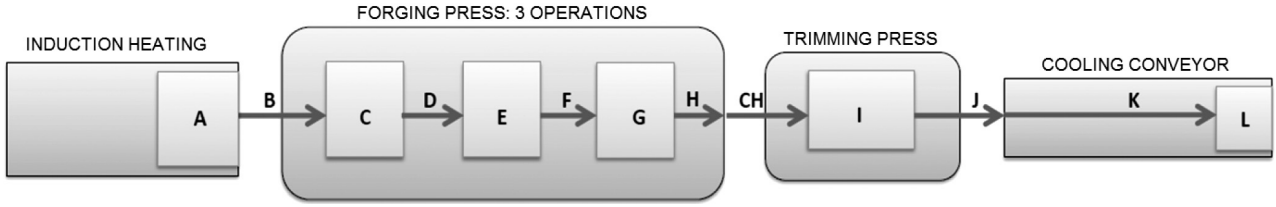

Figure 6: Block diagram of the manufacturing process of the forged part
Slika 6: Blok-diagram izdelavnega procesa izkovkov

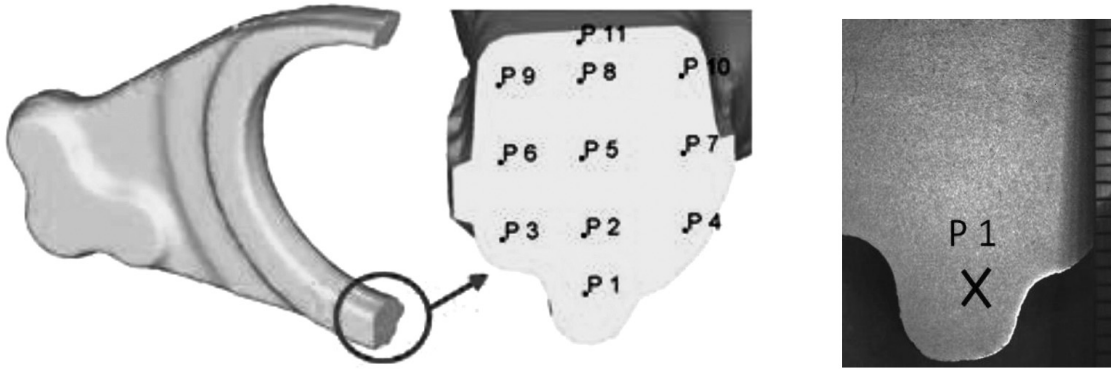

Figure 7: Tracked points on the cross-section of the FEM model of the forged part (left) and a micrograph of the P1 location on the real-world forged part (right)
Slika 7: Spremljane točke na prerezu FEM-modela izkovka (levo) in mikrostruktura položaja P1 v realnem izkovku (desno)

forged part during forming, was described using the measured specific-heat and thermal-conductivity values, as in the previous simulation of heat treatment. A kinematic model of the LMZ 2500 press, in which the actual forged part was made, was developed. The simulation was based on the forging-sequence description provided by the company of Kovárna VIVA a.s., as well as on the manufacturing-route analysis and on the field measurement (**Figure 6**).

The model comprised all the forming operations. Their sequence consisted of: upsetting – preforming – finish-forging – trimming. After the trimming, the forging cooled in still air to the ambient temperature. All the relevant handling times were taken into consideration, including the duration of the transfer of the forged part by the conveyor to the container.

The goal of the numerical modelling was to obtain the strain and temperature versus the time plots which were going to be used as the input data for the thermo-mechanical simulator (for the material/technological modelling). The material/technological modelling allows the entire process model to be validated using real specimens and also permits the microstructure evolution and mechanical properties to be mapped[4]. The point-tracking method was employed to determine the temperature-versus-time and strain-versus-time curves for the selected locations during the production of the forged part (**Figure 7**). A single representative point (P1) was selected for the physical simulation. The information obtained for this point of the forged part, i.e. the

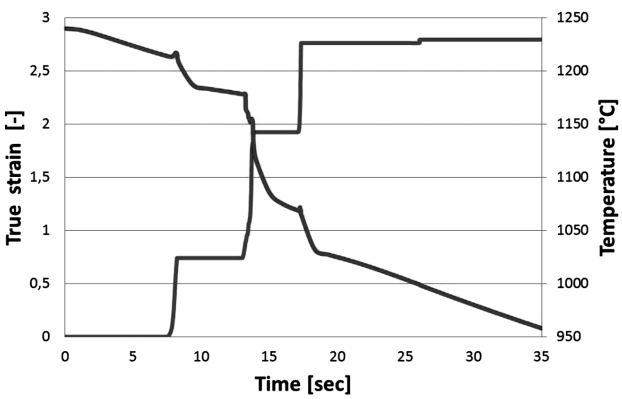

Figure 8: Strain and temperature plots for the tracked point
Slika 8: Diagram napetosti in temperature za preiskovano točko

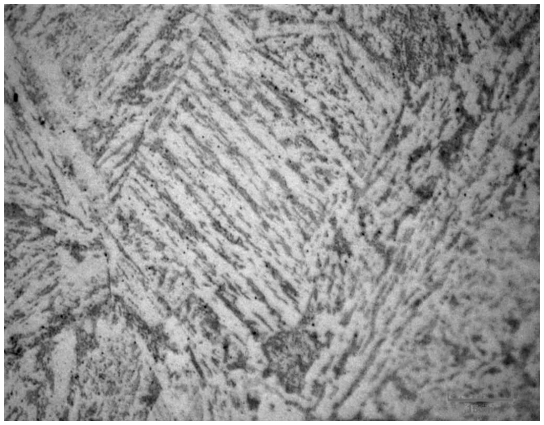

Figure 9: Bainite-ferrite microstructure of the forged part (HV 284)
Slika 9: Bainitno-feritna mikrostruktura izkovka (HV 284)

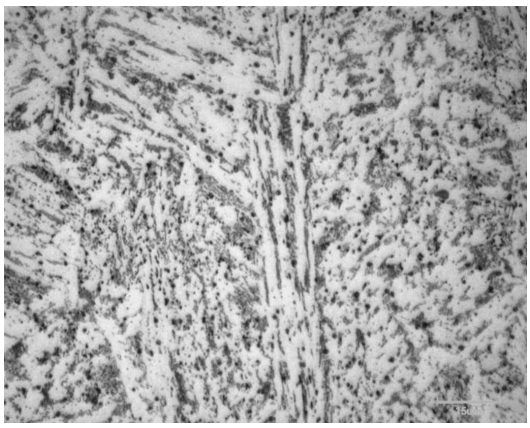

Figure 10: Bainite-ferrite microstructure of the physical-simulation specimen (HV 270)
Slika 10: Bainitno-feritna mikrostruktura v fizikalno simuliranem vzorcu (HV 270)

strain-time and temperature-time curves, is shown in **Figure 8**.

Using this data, a schedule for the thermomechanical simulator was developed and applied to an actual specimen. The microstructure of the real-world part (**Figure 9**) was then compared with the specimen microstructure upon the physical simulation (**Figure 10**) conducted for the selected point (P1). In both cases, the microstructure consisted of bainite and a portion of ferrite. For the sake of comparison, the measured Vickers-hardness values are shown as well.

4 CONCLUSIONS

Finite-element-method-based simulation is a powerful tool that can provide information about the variables that are difficult to measure otherwise: the strain and temperature curves for particular points of a forged part. The knowledge of these values is the key to optimising the existing processes and developing new procedures and materials. This is, however, impossible without verified models, required for a reliable analysis of the process. The present work deals with two applications of a FEM simulation to analysing the manufacturing routes in closed-die forging.

The first application of the numerical simulation involved constructing a temperature model. It described the temperature changes in closed-die forgings during the heating to the austenitizing temperature before the quenching. Using this model, the heating and soaking times of the forgings in the furnace can be shortened, the optimum layout of the forgings in the furnace can be found and various types of problems solved.

In the model, all the heat-transfer modes were taken into consideration. The most effective method of the solution was sought, taking account of the accuracy of the results. Due to the complexity of the problem, the computation times of the simulation variants were on the order of hundreds of hours. The sizes of database files even exceeded 100 GB. For this reason, this model will continue to be developed in an effort to shorten the computation times and reduce the data storage requirements. Gradual improvement in the accuracy of the model is a matter of course.

The second application of the numerical simulation involved an analysis of a closed-die forging process for a selected forged part. This model was developed to obtain the temperature and strain data to be used as the input data in constructing a material/technological model. Such a model combines the findings from the numerical and physical simulations for assessing the feasibility of substituting the existing hardening process. The available alternative is the thermomechanical treatment (combining forming and the subsequent controlled cooling).

It was found that thermomechanical treatment can produce practically identical properties of a workpiece as conventional hardening. However, such results should be interpreted with caution and this finding should be supported by a larger body of statistical data. In future efforts, the FEM simulation of forming processes will be refined, e.g., using Johnson-Cook model for describing the plastic behaviour of a forged part instead of the curve plots employed so far.

Acknowledgement

This paper reports the results obtained under project TA02010390 "Innovation and Development of New Thermo-Mechanical and Heat Treatment Processes of Die Forgings by the Transfer of Findings Obtained from Material-Technological Modelling". The project runs in the framework of the ALFA programme and is funded from the specific resources of the state budget for research and development through the Technology Agency of the Czech Republic.

5 REFERENCES

[1] Marc® 2012, Volume A: Theory and User Information, User's manual

[2] I. Poláková, T. Kubina, Flow stress determination methods for numerical modelling, 22nd International Conference on Metallurgy and Materials, METAL 2013 , Brno, Czech Republic, 2013, 273– 278

[3] S. L. Semiatin, T. Altan, Measurement and Interpretation of Flow Stress Data for the Simulation of Metal-Forming Processes, Materials and Manufacturing Directorate, Air Force Research Laboratory, Wright-Patterson Air Force Base, Ohio, USA, 2010, 1–57

[4] V. Pileček, F. Vančura, H. Jirková, B. Mašek, Material-Technological Modelling of the Die Forging of 42CrMoS4 Steel, Mater. Tehnol., 48 (**2014**) 6, 869–873

IN MEMORIAM

Alojz Prešern, dipl. inž. metalurgije (1920–2015)

Alojz Prešern se je rodil 23. 12. 1920 v Globokem pri Poljčanah. Na Montanistiko na Univerzi v Ljubljani se je vpisal leta 1939, študij metalurgije pa je končal leta 1943 v Leobnu. Konec vojne je dočakal v Prekomorski brigadi NOV. Leta 1946 se je zaposlil kot asistent v jeklarni Železarne Ravne, maja 1947 je bil prestavljen v Železarno Jesenice, leta 1948 pa v Železarno Zenica, nato pa je prišel ponovno v Železarno Jesenice, kjer je ostal do avgusta 1963. Povojni čas je bil čas največjega vzpona jeklarstva pri nas, pri katerem je Alojz Prešern intenzivno sodeloval. Postal je vodja vseh topilnic v Železarni Jesenice in bil hkrati med največjimi strokovnjaki za jeklarstvo v Sloveniji ter tudi širše v Jugoslaviji. Takrat so se uvajala nova jekla za gradnjo energetskih objektov, predelovalno industrijo, strojegradnjo in ladjedelništvo. Velik dosežek v tedanjem času je bil prehod iz generatorskega plina na mazut pri kurjenju Siemens-Martinovih peči. Jeklarna na Jesenicah je bila takrat šola jeklarstva za vso Jugoslavijo. Za svoje strokovne in organizacijske dosežke je bil Alojz Prešern odlikovan z redom dela III. stopnje.

Leta 1963 se je zaposlil na Metalurškem inštitutu kot tehnični direktor, nato pa je bil leta 1966 imenovan za direktorja inštituta. Ponovno je bil imenovan za direktorja Metalurškega inštituta še v letih 1970, 1974, 1978 in 1982. Pri svojem delu na inštitutu si je prizadeval inštitut bolj vključiti v tehnološki razvoj slovenske metalurgije in je sodeloval v prizadevanjih pri združevanju slovenskih železarn. Leta 1968 je bil sklenjen dogovor o sodelovanju med tremi slovenskimi železarnami in delovnimi organizacijami barvne metalurgije. Kot direktor je Alojz Prešern ves čas ohranjal in negoval vezi inštituta s slovenskimi železarnami in drugimi podjetji, ker se je zavedal, da je to edina trdna garancija za obstoj inštituta. Njegova velika zasluga je tudi, da se je leta 1973 Metalurški inštitut pridružil SOZD-u Slovenskih železarn kot samostojna delovna organizacija, obenem pa je inštitut ohranil status osrednje raziskovalne organizacije za vso slovensko metalurgijo.

Kljub mestu direktorja inštituta je Alojz Prešern vse do leta 1978 intenzivno delal tudi kot raziskovalec na področju jeklarskih tehnologij in kemizma reakcij v staljenem jeklu. Področja njegovih raziskovanj so bila: rekonstrukcije peči, gorilniki in zgorevanje, vakuumske tehnologije, vpihovanje argona in prašnih snovi, emisije, površinske napake na gredicah, predvsem pa korelacije med dezoksidacijskimi postopki in nekovinskimi vključki v jeklu. Upokojil se je leta 1986.

V zasebnem življenju je bil Alojz Prešern skrben oče sinu in hčeri, ki sta oba uspešna, vsak na svojem področju. V prostem času se je ukvarjal tudi s slikarstvom in zapustil obsežno zbirko svojih slikarskih stvaritev.

Direktorja Alojza Prešerna, dipl. inž. metalurgije, je odlikovala strokovna, raziskovalna in poslovodna sposobnost, obenem pa tudi pristnost, tovarištvo, neposrednost in preprostost v odnosih do sodelavcev. Zato se ga bomo spominjali tudi kot dobrega prijatelja, tovariša in sodelavca.

Dr. Matjaž Torkar,
Glavni in odgovorni urednik revije
Materiali in Tehnologije